Measurement of the Pion Absorption Cross-Section with the ProtoDUNE Experiment

Inauguraldissertation
der Philosophisch-naturwissenschaftlichen Fakultät
der Universität Bern

vorgelegt von

Francesca Stocker

von Zürich

Leiter der Arbeit
Prof. Dr. Antonio Ereditato
Dr. Francesco Pietropaolo

Albert Einstein Centre for Fundamental Physics
Laboratory for High Energy Physics
Physics Institute

Measurement of the Pion Absorption Cross-Section with the ProtoDUNE Experiment

Inauguraldissertation
der Philosophisch-naturwissenschaftlichen Fakultät
der Universität Bern

vorgelegt von

Francesca Stocker

von Zürich

Leiter der Arbeit
Prof. Dr. Antonio Ereditato
Dr. Francesco Pietropaolo

Albert Einstein Centre for Fundamental Physics
Laboratory for High Energy Physics
Physics Institute

Von der Philosophisch-naturwissenschaftlichen Fakultät angenommen.

Bern, 22. November 2021

Der Dekan:
Prof. Dr. Zoltan Balogh

To the best memory of my good friend Martin Auger.

1983 – 2021

ABSTRACT

Understanding the nature and origin of matter in the universe is one of the fundamental questions in modern particle physics. In consequence, the particle physics community strives to reveal why matter actually dominates anti-matter. The Sakharov conditions state the necessity of violation of the charge parity symmetry (CP-violation) to explain the matter-dominated universe. The phenomenon of neutrino oscillations holds the key to reveal CP-violation in the leptonic sector. A concerted international effort is therefore underway to construct next-generation neutrino oscillation experiments able to address this complex issue and eventually measure CP-violation. To reach the necessary sensitivity and revealing CP-violating physics, systematic uncertainties need to be controlled at the percent level. Neutrino experiments rely on interactions of neutrinos with bound nucleons inside the detector medium nuclei. Current interaction models used to simulate neutrino interactions with event generators, lack understanding and precise modeling of the hadronic and nuclear physics involved in the processes. Specific measurements of hadron-nucleus interactions can help constrain and improve the models resulting in reduced systematic uncertainties for CP-violation searches. This thesis presents a first preliminary measurement of the pion absorption cross-section in the relevant pion kinetic energy range of 450 to 950 MeV with the ProtoDUNE-SP detector. The results of this thesis indicate that the measurements agree within their systematic uncertainties with model predictions. However, they suggest a systematically lower cross-section which could open the way to interesting future developments.

CONTENTS

LIST OF FIGURES

LIST OF TABLES

ACRONYMS

TPC Time Projection Chamber

LAr Liquid Argon

LArTPC Liquid Argon Time Projection Chamber

DUNE Deep Underground Neutrino Experiment

SP Single Phase

MIP Minimum Ionising Particle

PMT Photomultiplier Tube

PDS Photon Detection System

UV Ultra Violet

DAQ Data Acquisition

ADC Analog Digital Converter

NIM Nuclear Instrumentation Standard

TTL Transistor-Transistor Logic

AC Alternating Current

DC Direct Current

HV High Voltage

CPA Cathode Plane Assembly

FC Field Cage

EW End Wall

APA Anode Plane Assembly

GP Ground Plane

BP Beam Plug

TCO Temporary Construction Opening

CE Cold Electronics

FRP Fibreglass Reinforced Plastic

DSS Detector Support System

PS Power Supply

FT FeedThrough

WIB Warm Interface Board

FEMB Front End Mother Board

RCE Reconfigurable Cluster Elements

BI Beam Instrumentation

SCE Space Charge Effect

PID Particle Identification

MC Monte Carlo simulations

INTRODUCTION

Neutrinos are the lightest and most abundant matter particle in the universe: the discovery of nonzero neutrino masses through the process of neutrino oscillation has been awarded the 2015 Nobel Prize. In fact, neutrino oscillations might hold the key to understanding the fundamental question of the origin of the observed matter dominance over anti-matter, *i. e.* CP-violation.

Today, neutrino physics is entering the era of high precision physics: to discover CP-violation it is crucial to quantitatively improve the measurements of neutrino properties and control systematic uncertainties at the percent level. CP-violating physics has been declared as one of the main science drivers in the particle physics community. Harvesting more neutrino data, as well as improving current and future detectors in terms of stable operation, exposure, measurement precision, and sensitivity are crucial to paving the way for discovering CP-violation. As part of a large international effort to measure CP-violation, the Deep Underground Neutrino Experiment (DUNE), located in the USA, is foreseen to start data taking during this decade. It will be an improved and larger version of its predecessors serviced by a more intense neutrino beam to uncover the still outstanding neutrino unknowns.

The DUNE project has adopted the Liquid Argon Time Projection Chamber (LArTPC) technology, providing high-precision, three-dimensional imaging, and calorimetry with the same detector. DUNE will invoke the technology at large scales using $\mathcal{O}(40\text{ kt})$ of liquefied argon. Inside the liquid, outgoing charged particles of a neutrino interaction ionise and excite atoms along their trajectory in the detector. The ionisation process leaves a track of electrons along the particle trajectory and the de-excitation of the argon atoms emits instant scintillation light. An electric field and photon detectors allow to production of 3D images of the interactions and hence provide particle identification.

ProtoDUNE-SP is the first large-scale DUNE prototype and the largest LArTPC built to date, holding 700 t of liquefied argon and validating several aspects of LArTPCs as used in DUNE. ProtoDUNE-SP construction started in 2017 at CERN. Operations started in summer 2018 and the first beam particle data was recorded over a period of 3 months in the fall of 2018. The detector was operated successfully for 2 years until mid-2020. The particle beam allowed for testing of calibration schemes and precise calorimetry, as well as the collection of an invaluable data set of hadron interactions with argon at various beam momenta. These data are used to improve event reconstruction algorithms and provide unique hadron-interaction measurements on liquid argon to ultimately quantify and reduce current systematic uncertainties in view of DUNE.

In the framework of this PhD-thesis, I was a key member of the core team for the construction and operation of the ProtoDUNE-SP HV system and electric field cage. During detector operation, I was appointed expert for the high voltage system and operation of the full detector. From September to November 2018, ProtoDUNE-SP took charged particle data from a hadron beam in the momentum range of 0.5 to 7 GeV/c. As a final scope of my PhD thesis, I measured the cross-section of a specific pion interaction channel on argon: the pion absorption cross-section.

Pions are common products of neutrino interactions. To identify and characterise neutrino interactions, the knowledge of the inclusive cross-section, as well as the cross-sections of the various exclusive interaction channels are very important. The data on these interactions with liquefied argon is scarce and current models are based on interpolations from historical measurements on lighter and heavier nuclei than argon. Dedicated measurements of exclusive pion interaction cross-section channels can provide constraints on the current models, avoiding interpolations and providing insight into the nuclear structure of argon.

The thesis is structured as follows. In the first chapter, I provide the historical context of neutrinos and their role in the standard model. Neutrino oscillation physics is reviewed and the open questions which will be answered by the next generation of neutrino experiments are discussed. The second chapter focuses on the DUNE Neutrino Program and testifies the interest in choosing LArTPCs as neutrino detectors. Further, measurements on neutrino interactions in argon, specifically hadron cross-section measurements, are motivated. An overview of the existing pion interaction measurements from various experiments is given and the strategy of the pion absorption cross-section measurement is outlined. The third chapter is a comprehensive summary of the ProtoDUNE-SP construction and all components. I took part in numerous construction steps of the detector. Chapter four focuses on signal processing, the major space charge effect in ProtoDUNE-SP, and the calibration of the data necessary to produce a reliable measurement. The first step, *i. e.* the adoption of an event selection that I developed for pion absorption event candidates, is detailed in chapter five. An estimation of the systematic uncertainties affecting my measurement is given in the 6th chapter. To perform the measurement, I developed a novel energy slicing method circumventing the limitations of the spatial distortions by the space charge effects in ProtoDUNE-SP. Chapter seven, finally, includes the validation of the new method, the final measurement and an unfolding procedure to compare the measured pion absorption cross-section to the prediction of the model in the event generator of the simulation.

1

STATE OF THE ART IN NEUTRINO PHYSICS

The opening chapter of this thesis provides the historical background and basic information as well as the state-of-the-art in neutrino physics. The discovery of neutrinos and the various experiments until nowadays are summarised in Section 1.1. Section 1.2 and Section 1.3 outline the role of neutrinos in the Standard Model of Particle Physics (SM) and present the theoretical underpinning of neutrino oscillation. The open questions and opportunities for new physics with neutrinos are highlighted in Section 1.4. The quest of the next generation neutrino experiments is to provide answers to those questions. Note, Section 1.1 and Section 1.3 are largely based on [1, 2, 3]. They are reproduced in parts from my master thesis [4].

1.1 NEUTRINOS IN THE HISTORICAL CONTEXT

In 1914 Chadwick measured the β-decay spectrum to be continuous instead of discrete a result that was confirmed by Ellis and Wooster in 1927 [5, 6]. The result was irritating and could not be explained at first, N. Bohr even suggested dropping the fundamental law of energy conservation. In 1930 Pauli found a solution to this problem proposing that another undetected particle carried away the *missing* energy. The particle should be a neutral weakly interacting fermion, at those times called *neutron*. The broad electron energy spectrum implies that the particle is very light or even massless [7].

By 1932 Chadwick had discovered the neutron thus, Fermi then renamed in 1933 the Pauli particle to be called *neutrino* "the little neutral one". He developed the theory of β-decay (precursor of weak interaction theory) in analogy with quantum electrodynamics in 1934 [1]. Today the fundamental β-decay process is

$$\mathrm{n} \rightarrow \mathrm{p}^{+} + \mathrm{e}^{-} + \overline{\nu}_{e}. \tag{1.1}$$

It was only in 1956 that electron antineutrinos were detected using the inverse β-decay in water containing dissolved cadmium chloride by Reines and Cowan. In the inverse β-decay an antineutrino can produce a positron via interaction with a proton. The method to detect the inverse β-decay is a delayed coincidence measurement. As neutrinos only interact extremely weakly with matter to conduct this experiment an intense antineutrino flux was required, which was provided by the Savannah River nuclear reactor in South Carolina.

The Goldhaber experiment measured the helicity of the neutrinos in 1957 using the inverse beta decay of samarium atoms. For neutrinos the spin is anti-parallel to the momentum, this corresponds to negative helicity [8]. In the limit of massless neutrinos, negative helicity neutrinos are the same as left-handed neutrinos. Therefore, only left-handed neutrinos and right-handed antineutrinos couple to the weak force.

In 1962 the second neutrino ν_μ was discovered at the Brookhaven National Laboratory (BNL) by L. M. Lederman, M. Schwartz, and J. Steinberger [9]. This demonstrated the doublet structure of the then known two lepton families: $(\nu_e,\ e)$ and $(\nu_\mu,\ \mu)$. After the detection of the τ lepton by M. Perl in 1975 [10] the existence of the ν_τ was assumed.

The solar neutrino problem arose in 1968 when Davis Jr., Harmer, and Hoffman measured the solar neutrino flux [11]. The total accumulation was only about a third of the predicted value by Bahcall's solar model [12], this discrepancy had been known as the solar neutrino problem.

In 1968 B. Pontecorvo proposed that the solar electron neutrinos transformed in flight to other neutrino species like the muon neutrino. Davis' experiment was insensitive to ν_μ and therefore had missed those neutrinos. This mechanism is today known as the *neutrino oscillation*, the theory was finally developed in 1975 by Bilenky and Pontecorvo [13]. Neutrino oscillation implies neutrinos to be massive and mixed.

Super-Kamiokande, a water Cerenkov detector, studied the neutrino oscillations of atmospheric neutrinos in 1998. Atmospheric neutrinos are produced from the primary cosmic rays (protons) that collide with nuclei in the upper atmosphere creating mostly pions. The pions decay into muons and muon neutrinos and the muons further into $\nu_\mu,\ \nu_e,\ e^-$. The model-independent evidence of neutrino oscillations was obtained by looking at the zenith angle dependence of the electron and muon events, which are induced by the corresponding neutrino [14].

In 2002 neutrino oscillation was confirmed experimentally and the solar neutrino problem was solved. The Sudbury Neutrino Observatory SNO collaboration was able to measure the total solar neutrino flux and the component of the electron-neutrino flux [15]. The discrepancy between the total solar neutrino flux and the electron neutrino flux implies the flavour change for neutrinos. Thus, neutrinos have non-zero mass, as implied by the oscillation theory. In the last two decades, neutrino oscillations have been extensively studied in many other experiments. KamLAND has been running since 2002 measuring the disappearance of reactor neutrinos $\bar{\nu}_e$. Accelerator neutrinos were studied by the experiments KEK to

Kamioka (K2K) and Main Injector Neutrino Oscillation Search (MINOS). Both are long-baseline accelerator experiments $\mathcal{O}(100\text{km})$ with a near and far detector. Significant distortion of the initial neutrino or antineutrino spectrum was observed in all three experiments [16, 17, 18].

A non-zero value for the oscillation parameter Θ_{13}, which would allow CP violation in the leptonic sector ($\delta_{CP} \neq 0$), was observed by Daya Bay, RENO and Double Chooz with reactor neutrinos [19, 20, 21]. As mentioned in the introduction of the thesis, CP violation is required to meet the Sakharov conditions [22] and explain the matter-antimatter asymmetry in the Universe.

In 2020 the T2K Collaboration presented the first constraints with a significance of 3σ on the CP-violating phase δ_{CP} with accelerator-based neutrino oscillation. δ_{CP} is cyclic repeating every 2π. For the so-called normal mass ordering the CP violation was constrained to lie within [-3.41, 0.03] and for the inverted mass ordering in the interval of [-2.54, -0.32] with a significance of 3σ [23]. The-next generation neutrino experiments will aim to measure CP violation with a 5σ significance and determine the neutrino mass hierarchy.

1.2 NEUTRINOS IN THE STANDARD MODEL OF PARTICLE PHYSICS

The Standard Model (SM) of particle physics includes all known elementary particles and their interactions through the fundamental strong, weak and electromagnetic forces. Theoretically, the SM is a quantum field theory with fundamental objects described through fields changing only in discrete portions corresponding to the observed particles. Many predictions of the SM have been proved by experiments. More importantly, elementary particles like the Higgs Boson have been discovered after their prediction by the SM. However, assumptions that the SM is part of a more general theory, the theory of everything, is valid: it fails to include the gravitational force, dark matter, and dark energy, as well as the non-zero masses of the neutrinos that are confirmed by the neutrino oscillation phenomenon [24, 25].

The SM of particle physics splits the fundamental particles into two groups the Fermions and Bosons. The Fermions are 12 elementary matter particles with spin-1/2, each with a corresponding antiparticle. Six of the fermions carry a color and flavour charge. Their flavours are: up u, down d, charm c, strange s, top t, and bottom b. They can come with each flavour in three colors and are called quarks. The other six are leptons and their defining property is their flavour: electron e, electron neutrino ν_e, muon μ, muon neutrino ν_μ, tau τ, and tau neutrino ν_τ. The leptons do not possess a color charge. All quarks and the e, μ, τ also carry an electric charge. The neutrinos do not carry an electric charge. The fermions are divided into three generations, each generation with a pair of quarks and leptons. The members of each generation have a larger mass than the corresponding particles of the generation before. They are indicated in Figure 1.1 by I, II, and III [1].

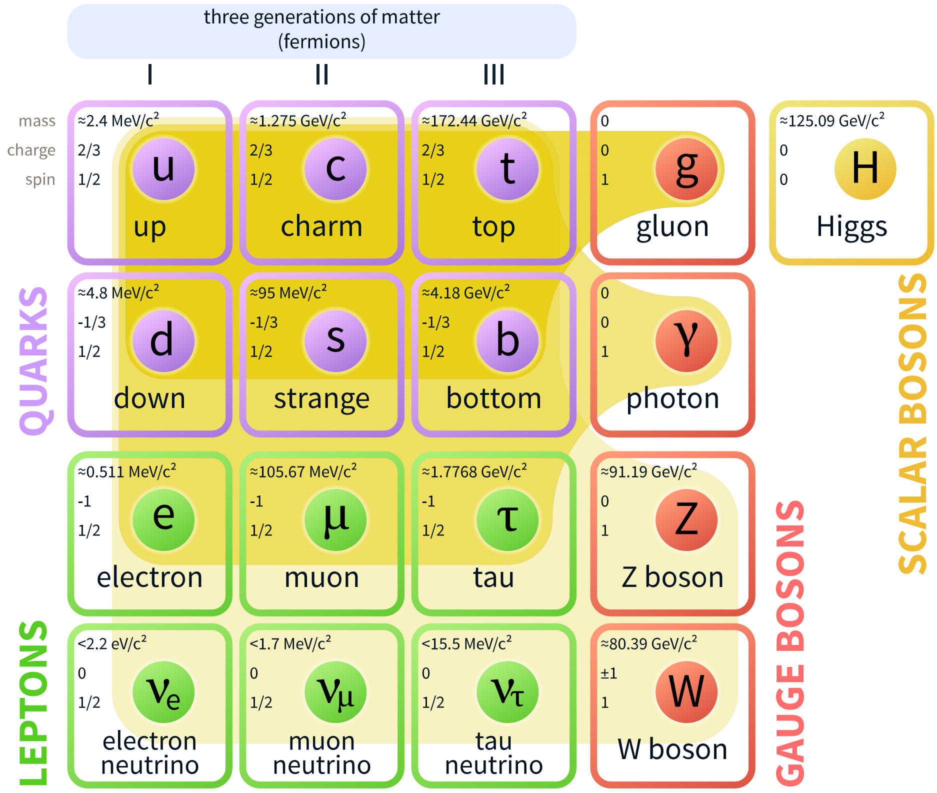

Figure 1.1: The elementary particles described in the Standard Model, taken from [26].

The Bosons are elementary particles with integer spins. The photon γ, gluon g, $W^{\pm}$, and Z^0 are spin-1 particles. The Higgs boson H carries spin-0. The spin-1 bosons are the mediators of the three fundamental forces, the strong, weak, and electromagnetic force. Only quarks can interact via the strong force which is mediated by the gluons. All electrically charged fermions can interact via the electromagnetic force mediated by the γ. Finally, all 12 fermions can interact via the weak force which is mediated by the $W^{\pm}$ and Z^0 bosons. Note, neutrinos only interact via the weak force as they carry no color and no electromagnetic charge. The Higgs boson does not mediate a force but is responsible for the mass of all elementary particles apart from the photon and gluon who have no mass. All massive elementary particles interact through the gravitational force which is not covered by the SM. Figure 1.1 shows the 12 elementary fermions and the five bosons.

The weak interactions can be split into two types: the charged current type which is mediated via the $W^{\pm}$ and the neutral current type mediated via the Z boson. The

Feynman graphs for the weak interactions are shown in Figure 1.2. The concept of handedness of a particle describes the projection of the particle spin vector onto the direction of motion. If both directions are the same, a particle is right-handed, if they are opposite the particle is left-handed [2].

Charged current interactions only act on left-handed quarks and leptons, as well as on right-handed antiquarks and antileptons. They are the only interactions that allow flavour change of quarks and leptons and thus, explain radioactive decays. For example, in the β-decay (Equation 1.1) one of the down quarks within the neutron is changed into an up quark and therefore, converting a neutron into a proton. Another example are interactions where the charged leptons are converted to their corresponding neutrino under emission of a W^-: $\nu_\mu + \mu^- \rightarrow e^- + \overline{\nu}_e$. Thus, charged weak interactions only allow for observation of left-handed neutrinos and right-handed antineutrinos.

Neutral current interactions act on left- and right-handed quarks, leptons, antiquarks and antileptons. Example are given by neutrino electron scattering $e^- + \nu_\mu \rightarrow e^- + \nu_\mu$ or proton neutrino scattering $p + \nu_\mu \rightarrow p + \nu_\mu$.

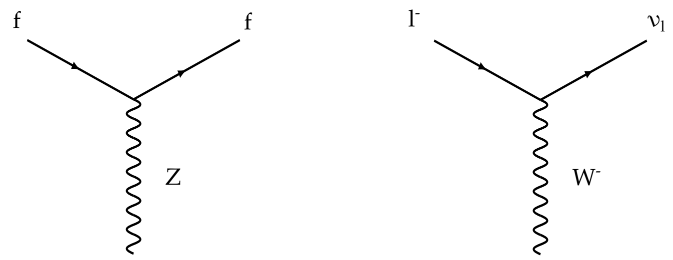

Figure 1.2: Feynman graphs for neutral and charge current interactions. f can be any quark or lepton. The charged current interaction is described including neutrinos.

1.3 NEUTRINO MIXING AND OSCILLATION

The concept of neutrino oscillation is described in this section. The derivation and discussion are largely based on [1, 2, 3, 4]. Summarizing the historical background of neutrino physics from the previous section, today we know that neutrinos are neutral-charged fermions with spin 1/2. There are three flavours of neutrinos and antineutrinos existing as doublets with the charged leptons: (ν_e, e^-), (ν_μ, μ^-) and (ν_τ, τ^-). Neutrinos have very small (unmeasured) masses and are the most abundant elementary particles. There are several natural sources of neutrinos as stars, supernovae, the earth's atmosphere, radioactive decays, and cosmogenic, *i.e.* the big bang. Neutrinos and antineutrinos only interact with two fundamental forces:

- weak interaction coupling to the $W^{\pm}$ and the Z^0 bosons
- gravity

Only left-handed neutrinos and right-handed antineutrinos couple to charged current interactions and can be observed.

Neutrino oscillation is a quantum-mechanical phenomenon where the three eigenstates of the weak interaction ($\nu_e,\ \nu_\mu,\ \nu_\tau$) are connected via a unitary 3×3 mixing matrix to the three eigenstates of the free-particle Hamiltonian which are known as the mass eigenstates[1] ($\nu_1,\ \nu_2,\ \nu_3$). The mixing matrix is the Pontecorvo-Maki-Nakagawa-Sakata (PMNS) matrix. The relation between the weak eigenstates and the mass eigenstates is

$$\nu_\alpha = \sum_{i=1}^{3} U_{\alpha i}\nu_i \quad \alpha = e, \mu, \tau \quad , \tag{1.2}$$

where U is the PMNS matrix and can be parametrised by 6 parameters as follows

$$U = \begin{pmatrix} c_{12}c_{13} & s_{12}c_{13} & s_{13}e^{-i\delta} \\ -s_{12}c_{23} - c_{12}s_{23}s_{13}e^{i\delta_{CP}} & c_{12}c_{23} - s_{12}s_{23}s_{13}e^{i\delta} & s_{23}c_{13} \\ s_{12}s_{23} - c_{12}c_{23}s_{13}e^{i\delta_{CP}} & -c_{12}s_{23} - s_{12}c_{23}s_{13}e^{i\delta} & c_{23}c_{13} \end{pmatrix} \cdot \mathrm{diag}(e^{i\Phi_1}, e^{i\Phi_2}, 1), \tag{1.3}$$

where $s_{ij} = \sin\theta_{ij}$ and $c_{ij} = \cos\theta_{ij}$. θ_{ij} are the three mixing angles, δ_{CP} the CP violation phase and $\Phi_1,\ \Phi_2$ the two Majorana phases. The Majorana phases allow a different description for the neutrino masses than the other massive fermions which are described by the Dirac mechanism [27]. If the CP phase is non-zero neutrino oscillations violate CP symmetry.

An ultrarelativistic neutrino of the flavour α will evolve in time as a superposition of the mass eigenstates

$$|\nu_\alpha(t)\rangle = \sum_{i=1}^{3} U^*_{\alpha i} |\nu_i(t)\rangle \,. \tag{1.4}$$

The amplitudes of $|\nu_\alpha(t)\rangle$ to be a $|\nu_i(t)\rangle$ are given by $U^*_{\alpha i}$. $|\nu_i(t)\rangle$ propagate as a plane waves

$$|\nu_i(t)\rangle = e^{-iE_i t} |\nu_i(0)\rangle \,. \tag{1.5}$$

The projection of the flavour state $|\nu_\beta\rangle$ on the time evolution of the flavour state $|\nu_\alpha\rangle$, reveals the amplitude for the $\nu_\alpha \to \nu_\beta$ oscillation as

1 The number i of neutrinos in equation 1.2 can be bigger than 3 if there exist sterile neutrinos that mix with the weak eigenstates [24]

$$\text{Amplitude}(\nu_\alpha \to \nu_\beta) = \langle \nu_\beta | \nu_\alpha(t) \rangle = \sum_{i,j} U^*_{\alpha i} U_{\beta j} \langle \nu_j | \nu_i(t) \rangle . \tag{1.6}$$

The oscillation probability is then given by the squared absolute value of the oscillation amplitude

$$P(\nu_\alpha \to \nu_\beta) = | \langle \nu_\beta | \nu_\alpha(t) \rangle |^2 = \left| \sum_{i,j} U^*_{\alpha i} U_{\beta j} \langle \nu_j | \nu_i(t) \rangle \right|^2 . \tag{1.7}$$

Using the ultra relativistic approximation $E_i = \sqrt{p^2 + m_i^2} \approx p + \frac{m_i^2}{2p}$, setting $p = E$ and exploiting orthonormality of the eigenstates $\langle \nu_i | \nu_j \rangle = \delta_{ij}$, careful calculation leads to the probability of neutrino oscillation in vacuum:

$$P(\nu_\alpha \to \nu_\beta) = \delta_{\alpha\beta} - 4 \sum_{i>j} \Re(U^*_{\alpha i} U_{\beta i} U_{\alpha j} U^*_{\beta j}) \sin^2 \left(\frac{\Delta m^2_{ij} L}{4E} \right) \tag{1.8}$$

$$+ 2 \sum_{i>j} \Im(U^*_{\alpha i} U_{\beta i} U_{\alpha j} U^*_{\beta j}) \sin \left(\frac{\Delta m^2_{ij} L}{2E} \right) . \tag{1.9}$$

Equation 1.8 holds for any number of neutrino mass eigenstates and is valid also for $\alpha = \beta$. Further the equation shows that neutrinos oscillate only if $\Delta m^2_{ij} \neq 0$, as the oscillation probability is zero if $\Delta m^2_{ij} = 0$. This implies that neutrinos have mass and that their masses are different. The Majorana phases cancel and can not be observed in neutrino oscillations. Oscillations do not occur for $L \ll 4E/\Delta m^2_{ij}$ since they have not enough time to develop and $P = \delta_{\alpha\beta}$. The second sum with the imaginary parts is the CP-violating contribution, it has opposite signs for neutrinos and antineutrinos. The PMNS matrix can be written as a product of three rotations around the three mixing angles and a diagonal matrix containing the Majorana phases which are given in equation 1.10.

$$U = \begin{pmatrix} 1 & 0 & 0 \\ 0 & c_{23} & s_{23} \\ 0 & -s_{23} & c_{23} \end{pmatrix} \cdot \begin{pmatrix} c_{13} & 0 & s_{13} e^{-i\delta} \\ 0 & 1 & 0 \\ -s_{13} e^{i\delta} & 0 & c_{13} \end{pmatrix} \cdot \begin{pmatrix} c_{12} & s_{12} & 0 \\ -s_{12} & c_{12} & 0 \\ 0 & 0 & 1 \end{pmatrix} \cdot \text{diag}(e^{i\Phi_1}, e^{i\Phi_2}, 1) \tag{1.10}$$

The first matrix can be investigated in atmospheric neutrino oscillations and long-baseline neutrino oscillations. The parameters of the second matrix are measured in reactor neutrino oscillations and also in long-baseline neutrino oscillations. Furthermore, the second matrix contains the CP-violating phase with $e^{-i\delta}$. The third matrix is sensitive to solar neutrino oscillations and reactor neutrino oscillations. As mentioned before, the Majorana phases can not be investigated in neutrino oscillations, they can be tested in neutrinoless double-beta decay.

So far the three mixing angles and the differences in the squares of the masses have been determined by current neutrino experiments. The values are given in Table 1.1. The current experiments have not been sensitive enough to measure the CP phase, they have only been able to put limits as published by the T2K collaboration in 2020 [23]. In addition, there is no experimental determination of the sign of Δm^2_{32}. The two different signs for Δm^2_{32} imply two possible mass spectra for the neutrinos. The *normal ordering* which is determined by $\Delta m^2_{32} > 0$ has the definite masses ordered as follows: $m_1 < m_2 < m_3$. The *inverted ordering*, determined by $\Delta m^2_{32} < 0$ gives $m_3 < m_1 < m_2$ the numbering of the neutrinos is convention. There is also the possibility that $m_1 \cong m_2 \cong m_3$, then the mass spectrum is called quasi-degenerate [24].

PARAMETER	BEST-FIT	3σ
Δm^2_{21} $[1/10^{-5}\ \mathrm{eV}^2]$	7.42	$6.82 \rightarrow 8.04$
$\lvert\Delta m^2\rvert$ $[1/10^{-3}\ \mathrm{eV}^2]$	+2.517	$+2.435 \rightarrow +2.598$
	(-2.498)	$(-2.581 \rightarrow -2.414)$
$\sin^2\theta_{12}$	0.304	$0.269 \rightarrow 0.343$
$\sin^2\theta_{23}$	0.573	$0.415 \rightarrow 0.616$
	(0.575)	$(0.419 \rightarrow 0.617)$
$\sin^2\theta_{13}$	0.02219	$0.02032 \rightarrow 0.02410$
	(0.02238)	$(0.02052 \rightarrow$ - $0.02428)$
$\delta_{CP}[1/^\circ]$	197	$120 \rightarrow 369$
	(282)	$(139 \rightarrow$ - $352)$

Table 1.1: Neutrino oscillation parameters best fit values and the 3σ ranges. For the δ_{CP}-phase the best fit value and the allowed 3σ range is given. Values that are not in brackets correspond to $m_1 < m_2 < m_3$, *i.e.* the *normal ordering*. Values in (brackets) correspond to $m_3 < m_1 < m_2$, *i.e.* the *inverted ordering*. The values are taken from the most recent (2020) oscillation parameter fits at [28, 29].

1.4 OPEN QUESTIONS: MASS HIERARCHY AND CP VIOLATION

The Update of the European Strategy for Particle Physics 2020 [31], as well as the 2014 Strategic Plan for U.S. Particle Physics [32] and the Japanese particle physics community identified research in neutrino physics as science drivers of the future. The aim of the next generation neutrino experiments is

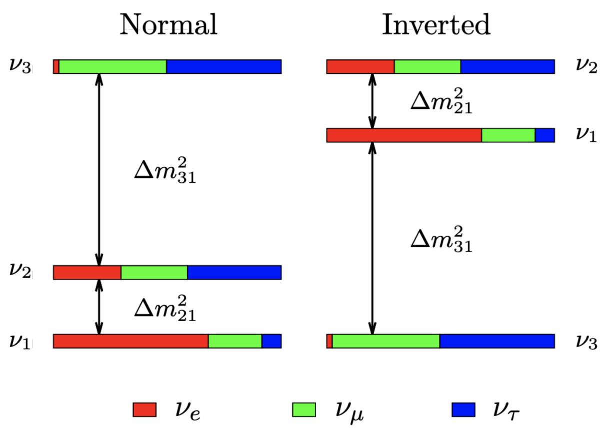

Figure 1.3: Schematic of the neutrino mass hierarchy [30].

- to measure δ_{CP}
- determine the neutrino mass hierarchy

Current neutrino experiments are limited by their available data, thus a concerted international effort is underway foreseeing two future leading-edge long-baseline neutrino oscillation experiments: the Deep Underground Neutrino Experiment (DUNE) located in the USA and Hyper-Kamiokande (Hyper-K) located in Japan. DUNE and Hyper-K are expected to take first data in 2026 and 2027, respectively [33, 34]. The two experiments utilise different technologies. DUNE will be based on the Liquid Argon Time Projection Chamber LArTPC technology and Hyper-K will use the Water Cerenkov technology. Both will be an order of magnitude larger than their predecessors and served by more intense neutrino beams $\mathcal{O}$(MW). These improvements will overcome the limits of current neutrino experiments.

As mentioned in Section 1.3, long-baseline neutrino oscillation experiments are sensitive to $\sin^2(\theta_{23}), \sin^2(\theta_{13})$, and δ_{CP}. As shown in Equation 1.8 probability of neutrino oscillation $P(\nu_\alpha \to \nu_\beta)$ depends on the ratio of $\sin^2(\Delta m^2_{ij} L/4E)$, *i. e.* the ratio of oscillation distance over neutrino energy. Thus, oscillation experiments maximise sensitivity by choosing accordingly L/E to increase the oscillation probability. Figure 1.4 shows the oscillation probability for a flavour change of an initial ν_μ (blue) to a ν_e (black) or a ν_τ.

There are two possible methods to investigate neutrino oscillations: *appearance* and *disappearance* measurements. In the first method, one looks for a different flavour of charged leptons from an initially pure flavoured neutrino beam. The latter looks for missing charged leptons from an initial beam. DUNE and Hyper-K will both look for the appearance of ν_e from an (almost) pure ν_μ beam. By studying

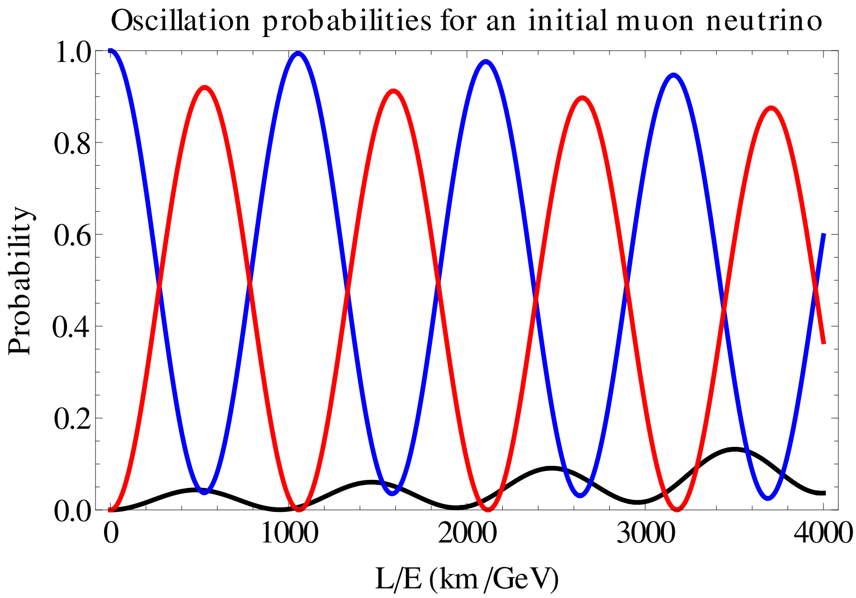

Figure 1.4: Oscillation probability for an initial ν_μ (blue) as a function of L/E. The black coloured curve represents the ν_e and the red coloured curve the ν_τ. DUNE will have a baseline of 1300 km and the neutrino energy peaks at 2-3 GeV. In consequence, L/E is located at 430-650. This is exactly in the region where the ν_μ disappearance is maximal. In that region the ν_τ appearance is maximal, however, the energy threshold for a charged current τ lepton appearance is of 3.5 GeV and greatly suppressed at low energies because of the relative large m_τ. Hence, DUNE will look for the ν_e appearance which is also maximal in the pointed out region of L/E. This plot was computed with [35].

NEUTRINO SOURCE	L [km]	E [GeV]	$\lvert\Delta m^2\rvert$ [eV^2]
Solar	10^7	10^{-3}	10^{-10}
Atmospheric	10^1 - 10^4	10^{-1} - 10^2	10^{-1} - 10^{-4}
Reactor	SBL 10^{-1} - 1	10^{-3}	10^{-2} - 10^{-3}
	LBL 10^1 - 10^2		10^{-4} - 10^{-5}
Accelerator	SBL 10^{-1}	1 - 10	>0.1
	LBL 10^2 - 10^3		10^{-2} - 10^{-3}

Table 1.2: Characteristic values for L and E for different experiments studying various neutrino sources and corresponding ranges of the difference of the mass squares. SBL refers to short base-line and LBL to long base-line, courtesy of [24].

the same appearance of $\bar{\nu}_e$ in a $\bar{\nu}_\mu$ beam δ_{CP} can be directly tested as it describes the asymmetry of matter and antimatter.

Long-baseline experiments consist in general of a Near Detector (ND) placed in proximity of the neutrino source and a Far Detector (FD) at the distance L defining the baseline. To shield the FD from cosmic radiation, *i. e.* unwanted activity in the detector usually they are located underground in industrial mines. The mass hierarchy can be tested in long baselines (L =1200 km) because the neutrino beam traverses the earth mantle and will be subject to matter effects revealing the neutrino mass ordering. A list of past, ongoing, and future neutrino long-baseline experiments is given in Table 1.3.

Experiment	Beam Line	Far Detector	L [km]	E_ν [GeV]	Year
K2K	KEK-PS	Water Cerenkov	250	1.3	1999 - 2004
MINOS	NuMI	Iron-scintillator	735	3	2005 - 2013
MINOS+	NuMI	Iron-scintillator	735	7	2013 - 2016
OPERA	CNGS	Emulsion	730	17	2008 - 2012
ICARUS	CNGS	Liquid Argon TPC	730	17	2010 - 2012
T2K	J-PARC	Water Cerenkov	295	0.6	2010 -
NOνA	NuMI	Liquid scint. + tracking calorimeter	810	2	2014 -
DUNE	LBNF	Liquid Argon TPC	1300	2 - 3	expected 2026
HYPER-K	J-PARC	Water Cerenkov	295	0.6	expected 2027

Table 1.3: List of accelerator based long-baseline neutrino experiments [24].

2

DUNE - THE NEXT GENERATION NEUTRINO PROJECT

It cannot be stressed enough that long-baseline neutrino oscillation experiments can probe directly the asymmetry between matter and antimatter, *i. e.* δ_{CP} and reveal the neutrino mass hierarchy. This chapter introduces the Deep Underground Neutrino Experiment DUNE [33] hosted by the Fermi National Accelerator Laboratory (Fermilab) in Illinois, USA. The main subject of this thesis is the construction, data taking, and a final measurement of the hadronic pion absorption cross-section with the ProtoDUNE-SP detector. As the name states, ProtoDUNE-SP is the first prototype for one of the DUNE detectors utilising the LArTPC technology. Therefore, the benefits of using liquid argon as a detector medium are detailed in Section 2.2. The basic working principle of LArTPCs is described in Section 2.3. Section 2.4 and Section 2.5 describe neutrino interactions in argon and motivate measurements on hadronic cross-section in argon. Finally, the derivation of the energy-slicing method and the general measurement strategy for the pion absorption cross-section are outlined in Section 2.6.

2.1 SCIENTIFIC GOALS AND OUTLINE OF THE DUNE NEUTRINO PROGRAM

The international DUNE experiment is a long-baseline next-generation neutrino oscillation experiment that is expected to start operation by 2026. The goals of DUNE are to search for CP-Violation, determine the neutrino mass hierarchy, detect supernova neutrinos and conduct searches for nucleon decays. The experiment is composed of a far detector (FD) complex located 1.5 km underground at the Sanford Underground Research Facility (SURF) in South Dakota, USA. The FD complex is composed of 4 independent FD modules (40 kt in total) based on the LArTPC technology. By 2035 the exposure of the DUNE detectors will reach a *120kt * MW * year* exposure and 1.2MW beam power from a high-intensity neutrino beam produced at Fermilab, located at $\sim$1300 km baseline away from SURF. At the beam production site at 570 m distance, a near detector (ND) complex will monitor and characterize the beam intensity and energy with high precision[36]. Figure 2.1 shows a cartoon illustrating the DUNE experiment.

The in-depth science goals of the DUNE experiment are summarised as follows:

- Measurement of the CP-Violation through high precision measurements of ν_μ and $\overline{\nu}_\mu$ oscillations. This might answer the fundamental question on the

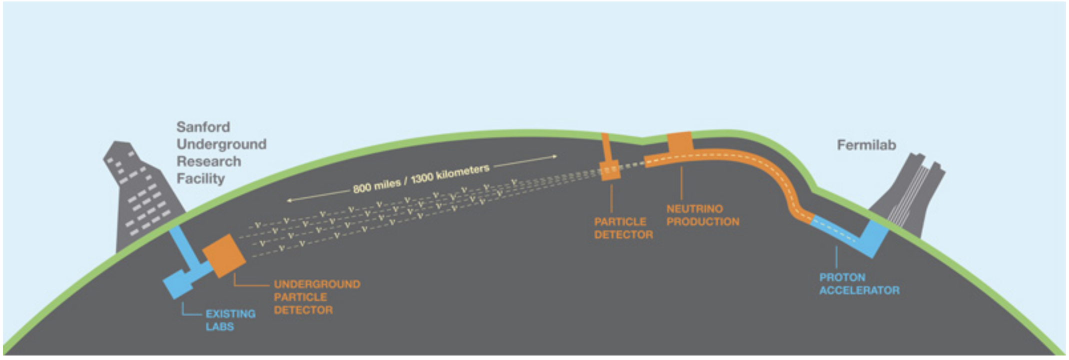

Figure 2.1: Cartoon of the DUNE experiment setup. The long-baseline neutrino experiment is hosted by Fermilab, IL-USA, and SURF, SD-USA. A high-intensity $\nu_\mu / \overline{\nu}_\mu$ beam is produced at Fermilab. The far detector complex located 1.5 km underground at SURF will study the oscillation of the neutrinos over 1300 km. A near detector at Fermilab located at 570 m of the neutrino beam production is responsible for the characterisation and measurement of the neutrino beam energy spectrum. Taken from [33].

matter-antimatter asymmetry in particle physics and cosmology. Figure 2.2 shows the significance of the δ_{CP} measurement as a function of the DUNE exposure time in years if $\delta_{CP} \neq 0$ or π.

- Determination of the neutrino mass hierarchy also through ν_μ and $\overline{\nu}_\mu$ oscillation measurements. If $\delta_{CP} = \pi/2$ a 1 year exposure is sufficient to determine the mass hierarchy. For all other δ_{CP} values mass hierarchy will be determined with a 5σ significance after 2 years of exposure.

- Nucleon decay searches. The impact of observing proton decay is a requirement for the grand unification theories (GUTs) aiming to unify the electromagnetic, weak, and strong force at high energies.

- Observation of the ν_e fluxes from core-collapse supernovae, this would provide new insight about the physics processes in early stages of a star collapse and black hole formation

Among the main scientific goals for DUNE lie many more opportunities for interesting physics measurements: at the neutrino beam source with the ND, using the FD complex for studies of atmospheric neutrinos, dark matter searches for different signatures at the far and near detectors, beyond standard model (BSM) particle searches, and precision studies of neutrino interactions and neutrino cross-sections as well as nuclear effects at the near detector [36].

DUNE is a classical accelerator-based neutrino experiment where the muon neutrino beam is produced by boosted pion decays $\pi^+ \rightarrow \mu^+ + \nu_\mu$ or $\pi^- \rightarrow \mu^- + \overline{\nu}_\mu$

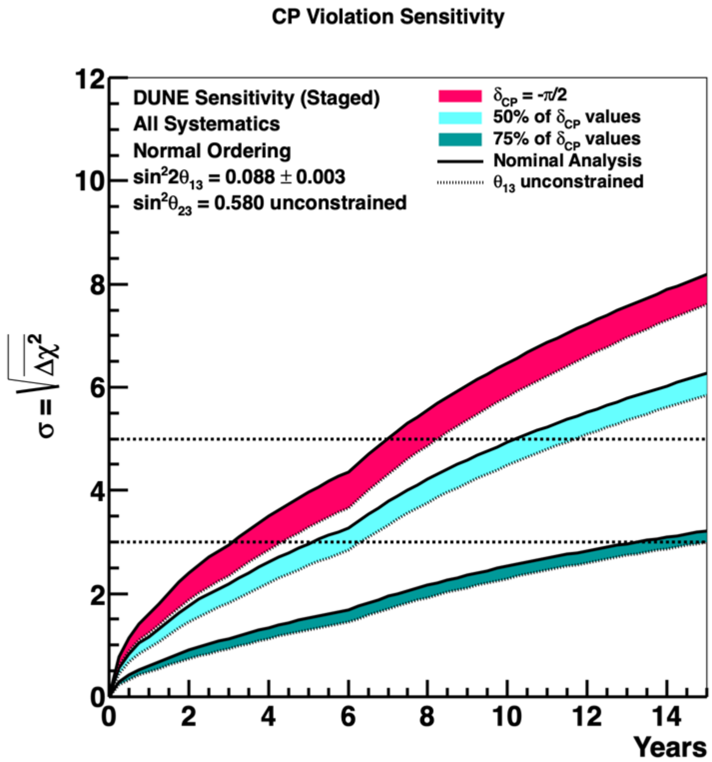

Figure 2.2: Significance of determination for δ_{CP}. The different FDs come online one by one and the beam power is increased after 6 years with a planned upgrade. These stages influence the trajectories of the significance. After about 7 years CP violation can be observed with a 5σ certainty if if $\delta_{CP} = \pi/2$. For other 50% of possible values the significance is reached after 10 years and for 75% of the possible values 3σ can be reached within 14 years. Taken from [33].

with a branching ratio of 99.98%. Primary protons produced in the Fermilab accelerator facility are shot on a target where mainly secondary pions and kaons are produced. Through focusing magnetic horns the secondary particles can be charge and energy-selected. This controls the *sign* of the neutrino beam, *i. e.* whether it carries neutrinos or anti-neutrinos. After selection, the secondary beam is conducted through a decay pipe at a length of 194 m. The length of the decay pipe is chosen in a way to maximise the number of pion decays and keep the number of muon decays low as they introduce other, unwanted neutrino types to the beam. A beam dump at the end of the decay pipe absorbs the remaining hadrons and leptons. The neutrino beam continues through the earth mantle in the direction of the FD complex as shown in Figure 2.1.

The predicted beam composition of the ν_μ and $\overline{\nu}_\mu$ beam for DUNE as a function of its energy spectrum is shown in Figure 2.3. The energy spectrum is chosen in order to maximise the $\nu_\mu / \overline{\nu}_\mu$-oscillation probability depending on L/E. The beam energy peaks at 2 - 3 GeV. In 10 years of operation, the DUNE FD complex will collect a few thousand images of neutrino interactions. The number of neutrino interactions is a product of the beam intensity, the neutrino oscillation probability, the neutrino interaction cross-section, and the detector mass.

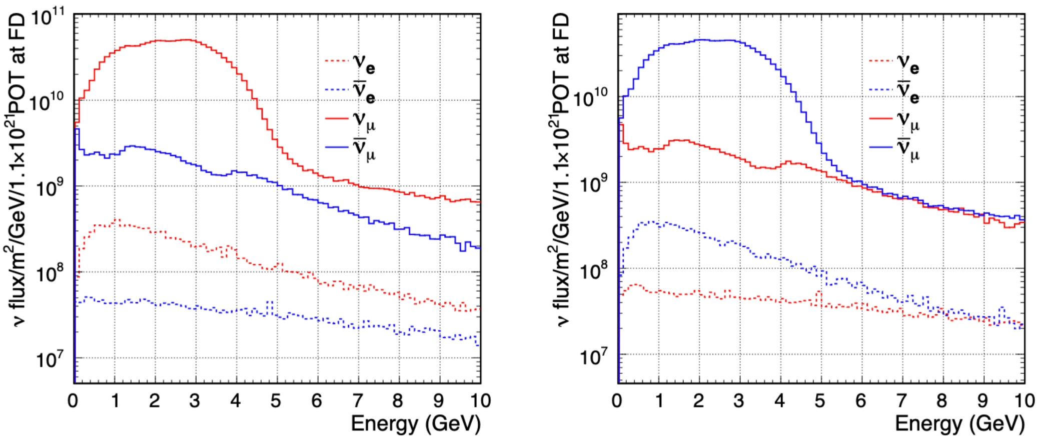

Figure 2.3: Predictions for the beam flux composition of DUNE in neutrino and antineutrino mode. The neutrino energy peaks at 2-3 GeV for the preferred muon (anti)neutrino type. The contaminations from wrong sign neutrinos and electron neutrinos are due to muon decays in the decay pipe. Left: ν_μ beam composition. Right: $\overline{\nu}_\mu$ beam composition. Taken from [36].

The DUNE FD is composed of four independent cryostats holding a total of 70 kt of LAr at a temperature of 88 K (-185°C). Each cryostat will host a detector module based on the LArTPC technology with an active detector volume of about 10 kt each, totaling to 40 kt of sensitive FD volume for DUNE. The inner dimensions of one DUNE FD cryostat are approximately 15.1 m in width, 14.0 m in height, and 62 m in length. The FD detectors will rely on LArTPC technology. It has excellent neutrino energy reconstruction and imaging capabilities. The benefits of using LAr as a detection medium are included in Section 2.2. The working principle of LArTPCs is explained later in Section 2.3.

The FD complex is required to guarantee safe and stable detector operation during several years of data taking. Thus, a strong research and development effort is ongoing to meet the requirements for DUNE. The ProtoDUNE-SP detector located at CERN in Geneva, Switzerland, is the first completed large-scale prototype of the first DUNE FD module. Its construction, performance, and physics data are the main focus of this thesis.

2.2 LIQUID ARGON AS NEUTRINO DETECTION MEDIUM

In particle physics detectors rely on the fact that particles under study either interact electromagnetically (producing charge and /or light) or produce particles that then subsequently interact electromagnetically and allow for conclusions about the particles in question. 125 years after its discovery, argon offers in its liquefied state compelling properties to facilitate powerful detectors with cutting-edge technology for neutrino physics measurements and rare event phenomena in particle physics.

Charged particles traversing liquid argon produce ionisation electrons, positive ions, as well as excited argon nuclei along their trajectory. The excited nuclear states de-excite under emission of light in the deep UV region at 128 nm also known as scintillation light. Thanks to a stokes shift where the positions of the band maximum of the emission and the absorption spectra do not coincide, liquid argon is transparent to its own scintillation light and it remains available for detection. Without an electric field the ionisation electrons and ions recombine under further emission of scintillation light. Strong electric fields can be facilitated in LAr due to its high dielectric constant. In presence of an electric field the recombination effects are suppressed and the ionisation electrons are available for charge signal detection and reproduction of the track topology. The ratio of the ionisation electrons and scintillation light varies as a function of electric field the relation is shown in Figure 2.4a. The electron drift velocity is shown in Figure 2.4b and varies as a function of electric field in the mm/μs region.

Challenging aspects of liquid argon are the cryogenic temperature of the liquid state from 84 to 87 K ($\sim$ -188°C), as well as the liquid argon purity. The first challenge can successfully (and expensively) be addressed by using membrane cryostats based on a proprietary technology [40]. They are well suited to keep $\mathcal{O}(\sim$kt) volumes of LAr at stable temperatures and pressure. Electronegative impurities in the argon limit the performance of liquid argon based detectors reading out the ionisation electron charge signals. Impurities, for example, oxygen and water contamination reduce the ionisation electron quantity. In consequence, it is necessary to implement purification circuits cleaning and maintaining the liquid argon purity to profit of the excellent detector capabilities. Table 2.1 lists the basic properties of liquid argon.

Argon makes about 1.3% of the earths atmosphere mass with a high molar mass of 40 u and is the most abundant noble gas. Its density of 1.39 g/cm^3 is high enough to achieve a large target mass and remains low enough to distinguish charged particle track topologies and measure the charge deposition per unit length enabling particle identification. Besides the highlighted challenges, LAr provides outstanding imaging and calorimetric capabilities for neutrino detection. Its

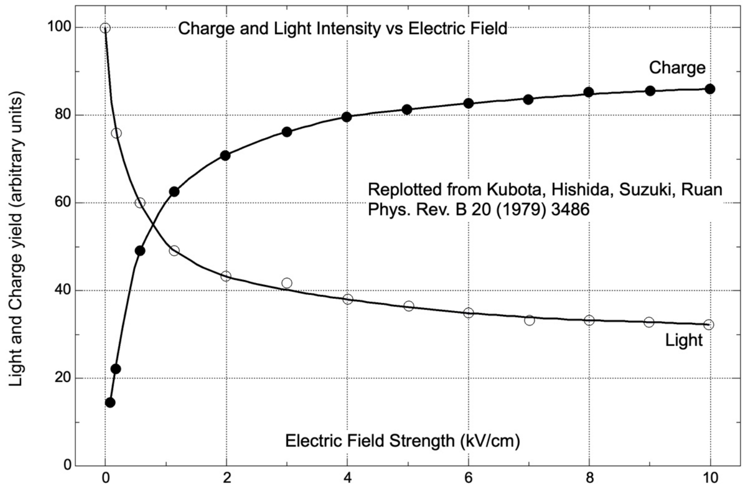

(a) Charge and light as function of electric field

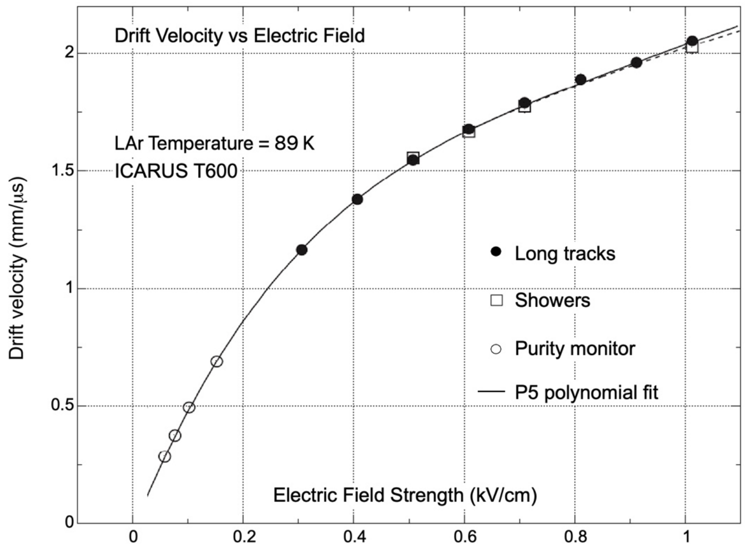

(b) Electron drift velocity.

Figure 2.4: Left: The complementarity between the amount of free charge and the amount of light as measured with 1 MeV electrons, data from [37]. Note that the y-axis is arbitrary units and while the argon light scale is 100 at its maximum, the argon charge is not 100 at its maximum. Right: Measurement of the drift velocity at different electric field strength [38]; the solid line is a fit, the dashed line is from the prediction of [39]

industrial production and abundance in the atmosphere make it cheap enough to construct detectors with target masses in the kilo-tonne range.

2.3 PRINCIPLE OF A LIQUID ARGON TIME PROJECTION CHAMBER

The concept of Time Projection Chambers (TPC) was proposed by David Nygren in 1974 [45] as a successor of multiwire proportional chambers invented by Georges

QUANTITY	SYMBOL	VALUE	
Atomic number	Z	18	
Molar mass	M	39.948(1)	g/mol
Atmospheric abundance	η_{atm}	0.934	%vol.
Boiling point (BP)	T_{BP}	87.26	K
Melting point (MP)	T_{MP}	83.8(3)	K
Density at normal BP	ρ_{BP}	1396(1)	$\mathrm{kg/m^3}$
Dielectric constant	ϵ_r	1.505(3)	
Ionization energy	I	13.84	eV
Effective ionization potential	I_c	188	eV
W-value for ionization	W_i	23.6(3)	eV/pair
W-value for scintillation	W_s	19.5(10)	eV/photon
Radiation length	X_0	14.0	cm
Nuclear interaction length	λ_I	85.7	cm
Mean specific energy loss	$\langle dE/dx \rangle$	2.12	MeV/cm
Critical energy (e^-)	E_c	32.84	MeV
Scintillation emission peak	λ_s	128	nm
e^- drift velocity	v_e	1.60(2)	mm/μs
e^- mobility	μ_0^e	518(2)	$\mathrm{cm^2/(Vs)}$
Ar^+ drift velocity	v_i	8.0(4)	mm/s
Ar^+ mobility	μ_0^i	$6.0 \cdot 10^{-4}$	$\mathrm{cm^2/(Vs)}$

Table 2.1: Liquid argon properties [41, 42, 43]. T_{BP} and T_{MP} are at a pressure of 1 atm. W_i, W_s and $\langle dE/dx \rangle$ are obtained for minimum ionizing particles. μ_0^e, μ_0^i and v_e, v_i are specified at T_{BP} and $E = 00\,\mathrm{kV\,cm^{-1}}$ and $E = 0.5\,\mathrm{kV\,cm^{-1}}$ [44].

Charpack in 1968 [46]. The multi wire proportional chambers were awarded the Nobel Prize in Physics in 1992. At times, TPCs marked a new era of ionisation detection thanks to the use of electronic readout capability for particle detection. First TPCs were used with noble gas as a detection medium. In 1977 however, Carlo Rubbia [47] proposed liquefied argon as detector medium for the reasons specified in Section 2.2 and thus, the LArTPC concept was born and developed to be one of the most powerful particle imaging detector types nowadays.

LArTPCs are imaging detectors with the capability to produce 3D images at exquisite resolutions of $\mathcal{O}$(mm), perform calorimetric measurements, and particle identification. This all is possible by exploiting the compelling properties of liquefied argon maximally. The central part of a LArTPC detector is a set of two parallel planes enclosing a gap of $\mathcal{O}$(m). One plane, the cathode, is biased with a high negative electric potential. The other plane, the anode, is held at ground. The setup gives rise to the drift electric field in the gap between the planes. The gap size defines the drift distance from cathode to anode for ionisation electrons of charged particles. Typically, the field intensities are held at 500 V/cm to have reasonable electron mobility, charge, and light yields (see Figure 2.4).

In the detector volume, outgoing charged particles of neutrino interaction ionise and excite the argon atoms along their trajectory in the detector. Thanks to the electric field, the ionisation tracks are drifted towards a readout at the anode classically composed of several sensing wire planes. To maintain the interaction topology of the charged particle tracks, a homogeneous electric field is crucial. A field cage, composed of field-shaping electrodes placed in equal spacing between the anode and cathode planes. Each electrode is biased with a tuned potential evenly stepping down the strong negative potential from the cathode to the anode. This is achieved by a highly resistive ohmic resistor chain.

The anode is composed of two or three parallel sets of sensing wire planes. Each wire plane is composed of spatially separated conductive wires spanning the full plane. The wire planes are oriented at different angles and carry a bias potential in a way such that the wire plane furthest from the anode, collects ionisation charges. When the ionisation electron tracks arrive at the sensing wires, they will induce on the first (two) plane(s) bipolar induction signals and are collected on the last plane leaving unipolar collection signals. Thus, each plane records a projection of the ionisation tracks which are reconstructed to a 2D image.

The third component to reconstruct the 3D image from a LArTPC is obtained through detecting the scintillation light of the excited argon nuclei. Several photon detectors are placed looking into the detector volume. The prompt scintillation light is collected and serves as a timestamp t_0. The difference in the arrival time of the ionisation charge at the sensing wires and the recorded scintillation light allows us to derive the location of the origin of the interaction event within the drift volume. The schematic in Figure 2.5 shows the working principle of a LArTPC.

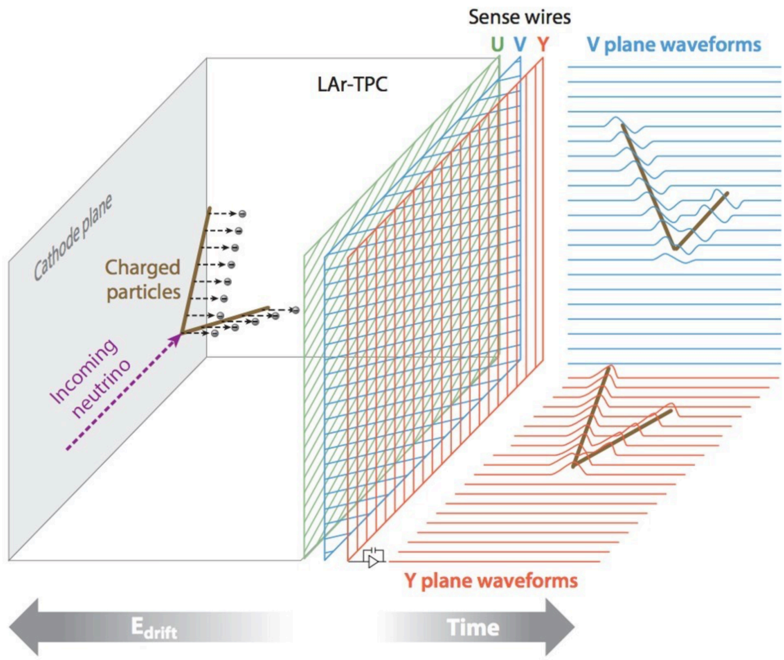

Figure 2.5: Basic working principle of a Liquid Argon Time Projection Chamber (LArTPC). A LArTPC consist of two paralle planes, cathode (left) and anode (right). The cathode is biased with a negative high potential and the anode is set to ground. The resulting electric field is used to drift ionisation tracks produced by charged particles passing through the volume. At the anode the ionisation tracks induce signals on sensing wires at the anode. Further, produced scintillation light is recorded by photon detectors. The signals on the sensing wires in combination with the light signals from the photon detectors, allow for 3D image reconstruction with a resolution of mm. The integrated charge of the signals allows for determination of the deposited energy per unit track length to perform particle identification. Taken from [48].

Energy Deposition by Charged Particles in LArTPCs

The energy loss per unit track length of a particle is measured in a LAr TPC. The amount of ionisation charge produced by a charged particle passing through LAr depends on the particle type and energy. Hence, the measured mean energy loss dE/dx is measured to perform particle identification.

The mean energy loss to ionisation per unit length of charged particles is described by the Bethe Bloch formula [24] as given in Equation 2.1.

$$-\frac{dE}{dx} = K\frac{\rho Z}{A}\frac{z^2}{\beta^2}\left[\frac{1}{2}\ln\left(\frac{2m_e c^2\gamma^2\beta^2 W_{max}}{I^2}\right) - \beta^2\right] \tag{2.1}$$

The density of the medium is given by ρ, Z and A are the atomic number and mass of the medium. z is the charge of the incident particle and m_e the electron mass. The effective ionization potential is given by I and the constant K has the value $K = 0.307$ MeV g^{-1} cm^2. β is the ratio of the velocity v and velocity of light c and γ the Lorentz factor. W_{max} is the maximum energy transfer for a particle with mass M and given in equation 2.2. For LAr the values of ρ, Z, A, I, W are noted in Table 2.1.

$$W_{max} = \frac{2m_e c^2\beta^2\gamma^2}{1 + 2\gamma m_e/M + (m_e/M)^2} \tag{2.2}$$

For non-relativistic particles, the expression in the brackets of Equation 2.1 varies slowly. In rough approximation, the energy loss per unit density of the medium and unit track length is a function of $\beta\gamma$. Figure 2.6 shows the dE/dx for different charged particles in the momentum range of 100 MeV to 10 GeV. The energy loss for a minimum ionising particle (MIP) in LAr is 2.1 MeV/cm.

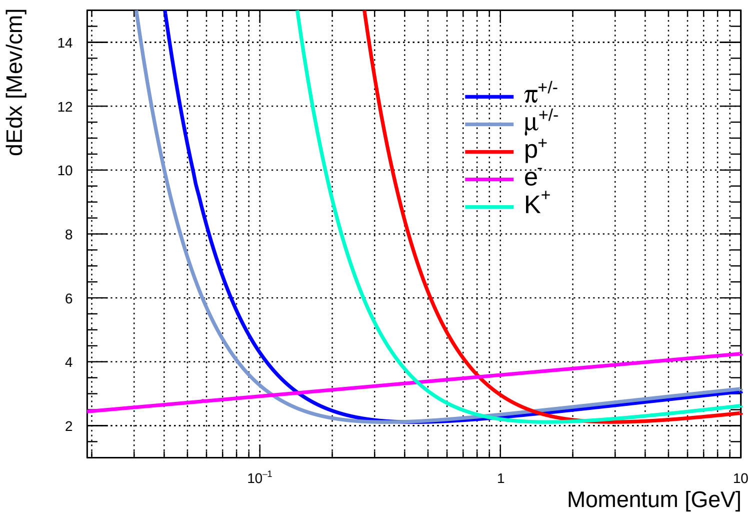

Figure 2.6: Distributions of the mean energy loss (dEdx) of particles in LAr. Theoretical prediction with the Bethe Bloch equation of the mean energy loss in LAr as a function of momentum.

Recombination Effect

During the production of the ionisation electrons, they may recombine with the parent ion due to its Coulomb field influence or with other nearby electronegative ions, for example coming from impurities. Based on [49] the dominant recombination process is the reattachment to the parent ion. The amount of recombined ionisation electrons varies as a function of energy and the impinging particle energy. Different models have been validated for LArTPCs especially in the ICARUS [50] and ArgoNEut [51] experiments.

Recombination effects have been studied for varying dE/dx and electric field variations $\mathcal{E}$. For ICARUS data the recombination is well described by the Birks model [52]. The behaviour for $\mathcal{R}_{ICARUS}$ is noted and the stopping power dE/dx is described as function of $\mathcal{R}$ in Equation 2.3.

$$\mathcal{R}_{ICARUS} = \frac{A_B}{1 + k_B \frac{dE}{dx} \frac{1}{\mathcal{E}}} \quad \text{and} \quad \frac{dE}{dx} = \frac{1}{\mathcal{R}} \frac{1}{W_{ion}} \frac{dQ}{dx}, \tag{2.3}$$

where $A_B = 0.8 \pm 0.003$ and $k_b = 0.0486 \pm 0.0006$ kV/cm$\times$ g/cm^2 /MeV. Thus, dE/dx can be described as

$$\frac{dE}{dx} = \frac{dQ/dx}{A_B/W_{ion} - k_B(dQ/dx)/\mathcal{E}}. \tag{2.4}$$

Values for dE/dx can become large if the denominator approaches 0 which poses technical difficulties for large dQ/dx values. However, this is not the case for the inverse Box model [51] with an exponential form described as

$$\frac{dE}{dx} = \frac{(exp(\beta W_{ion}(dQ/dx)) - \alpha)}{\beta}. \tag{2.5}$$

The Box model circumvents the technical difficulties of the Birks formula, however, it does not adequately describe the stopping power at low values. By allowing $\alpha < 1$ the inaccuracies can be avoided as shown in Figure 2.7 resulting in the modified Box model.

2.4 NEUTRINO INTERACTIONS IN ARGON

Neutrino experiments rely on detecting neutrino interactions with matter. The detection of the products of neutrino interactions with matter is the only way to determine the neutrinos presence, its flavour, if the interaction is of the charged current type, and reconstruct the neutrino energy. The expected DUNE neutrino energy spectrum peaks in the region of around 2-3 Gev. In this energy region, there are three categories of neutrino interactions: quasi-elastic (QE), resonant (RES), and deep inelastic (DIS) scattering. The occurrence of the three interaction categories as a function of increasing neutrino energy is shown in Figure 2.8. The QE process is described in Equation 2.6 where the neutrinos scatter off nuclei under emission of the nucleon and the flavour-corresponding charged lepton. RES Interaction types produce nucleon excited states (Δ resonances) decaying mostly to nucleons and a

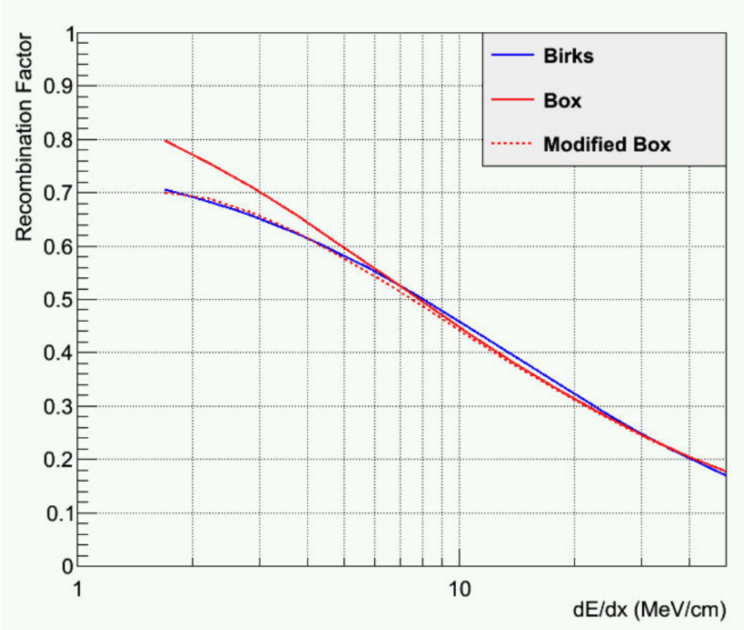

Figure 2.7: Recombination factor as a function of dEdx for the Birks, the Box and the modified Box model. The determination of the recombination values for the Birks estimate was done by using ICARUS parameters. The modified Box model has been adjusted to match the low dEdx values of the Birks model with $\alpha = 0.93$. Taken from [51].

single pion which are available for detection in the final state as shown in Equation 2.7. DIS interactions become more dominant at rising energy. They describe head-on collisions between neutrinos and the partons inside the nucleons. Interaction products are several mesons and nucleons, as described in Equation 2.8.

$$\text{CC-QE} \qquad \nu_\mu + N \to \mu^- + p \tag{2.6}$$

$$\text{CC-RES} \qquad \nu_\mu + A \to \mu^- + \Delta/N^* \to \mu^- + \pi + N' \tag{2.7}$$

$$\text{CC-DIS} \qquad \nu_\mu + N \to \mu^- + n/p + \pi^+ s \tag{2.8}$$

The classification of QE, RES, and DIS works rather well for light nuclear targets. The heavier the nuclei of the experiments, the more complex their nuclear structure. Thus, long baseline experiments like DUNE profit from higher signal yields by using argon as target nuclei. However, they have to face challenges due to the presence of significant nuclear effects impacting the interaction cross-sections and the particle final state topologies [53]. Further, nuclear effects influence the prediction and measurements of neutrino event rates, the reconstruction of neutrino energy, as well as the ratio of neutrinos/antineutrinos. If uncertainties from nuclear effects (currently in the range of 5–10%, see Section 2.5) are not well controlled results from neutrino oscillation experiments are affected.

For example, QE scattering with heavier nuclei can include intra-nuclear effects where produced hadrons rescatter within the nucleus. This can lead to the emission of additional nucleons affecting the final state topologies and kinematics. For the RES and DIS case, the produced mesons undergo hadronic interactions and can complicate the final state topologies even more.

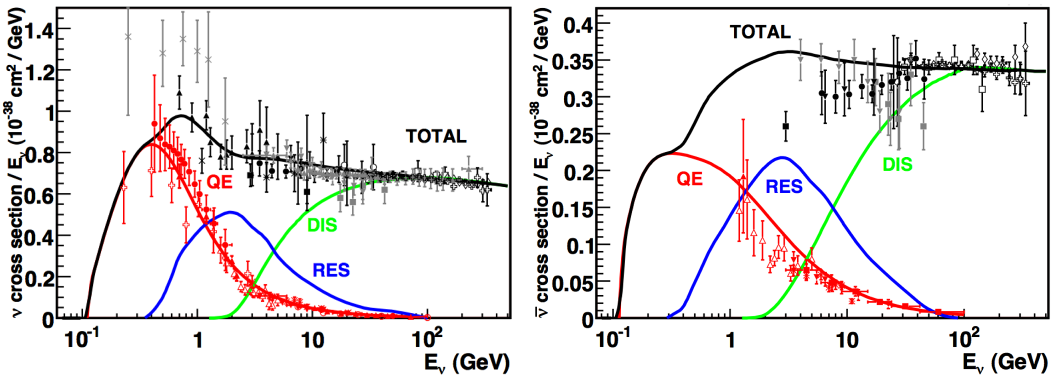

Figure 2.8: On the left the prediction of the total cross-section for neutrino charged current interactions is shown as a function of neutrino energy. Ther right hand side plot shows the cross-section in the antineutrino case. Taken from [53].

2.5 MOTIVATING HADRONIC CROSS-SECTION MEASUREMENTS IN ARGON

Pions appear especially in processes of resonant scattering and DIS. Current systematic uncertainties on neutrino-nucleus interactions lie in the range of 5–10% [54, 55]. With a large contribution coming from uncertainties of pion (re-)interactions inside the target nucleus, *e.g.* pion re-scattering, charge exchange, and absorption. There is interest in reducing the current systematic uncertainties on the neutrino-nucleus interactions with a direct impact on the run-time duration for future experiments to determine the CP-violating phase.

To understand and interpret measurements on neutrino oscillations, neutrino experiments rely on Monte Carlo (MC) simulations. In the neutrino landscape different neutrino event generators such as GENIE[56], NEUT[57], NuWro[58], and/or GiBUU[59], are used to simulate neutrino interactions. The presence of pions in the interactions expected for neutrino oscillation experiments requires an in-depth understanding of pion-nucleus interactions to precisely model the pion behaviour inside the target nuclei and its propagation in the detector medium. Simulations are based on theoretical models to determine the final distributions and kinematics of outgoing particles from a neutrino interaction. They are prone to inaccuracies and biases which lead to a model-dependent reconstruction of the incoming neutrino energy and ultimately impact the measurements of neutrino oscillation parameters. It is crucial to have precise theoretical models describing neutrino-nucleus interactions taking into account energy-dependent cross-section and nuclear effects contributing to the observed final state particles from a neutrino interaction. Experimental measurements of hadronic cross-section on argon nuclei are important contributions to constrain and improve current nuclear models in view of DUNE.

The Δ and excited nucleus states N^* in resonant scattering (see Equation 2.7) will undergo hadronic decays inside the nucleus as described in Figure 2.9. Δ decays produce pairs of protons and pions or neutrons and pions inside the nucleus. Before exiting the nucleus the hadrons have many chances to re-interact inside. The MC event generators implement intra nuclear cascade models to describe the processes within a nucleon.

Intra Nuclear Cascade Models

When a bullet particle, *i. e.* a pion, interacts with a nucleus the intra-nuclear cascade model steps the bullet particle through the nucleus. At each step, a path length is selected as a function of the free particle-particle cross-sections and region-dependent nucleon densities. When a nucleon is struck, its momentum, the reaction type, and products as well as the four-momentum are determined. The cascade is continued by stepping the products through the nucleus. At each step, the model is updated. When all particles that can escape the nucleus have done so, the cascade is stopped under the condition that energy conservation laws are respected. The particles escaping the nucleus are listed as secondary (daughter) particles of the primary (parent) beam particles at the event generator level. An illustration of the intra-nuclear cascade model is shown in Figure 2.9 for a neutrino interaction. The intra-nuclear cascade model is also used in neutrino event generators for the propagation of final state particles.

Pion Hadronic Interaction Measurement Landscape

In the past, several experiments have studied pion interactions on different targets with light and heavy nuclei such as Li, C, Al, Fe, Sn, and Pb in energy ranges of 65 to 320 MeV, *i. e.* the Δ resonance region [62]. The experimental results from the 1970ies are reported in Figure 2.10. The results were produced with *thin targets*, *i. e.* with thickness smaller than the pion interaction length in the material. At low energies the resonant peak is visible. It is more pronounced for lighter nuclei. The peak broadens and is shifted towards lower energies with an increasing atomic

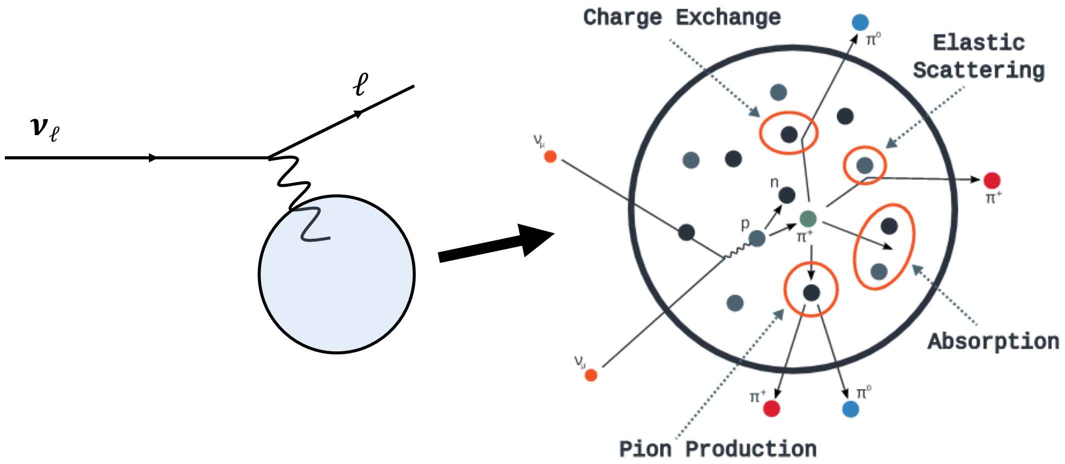

Figure 2.9: Illustration of the intra-nuclear cascade model for neutrino final state particles. In neutrino event generators like GENIE [56], final state pions in neutrino interactions with a nucleus are propagated according to the Bertini intra-nuclear cascade model [60] inside the nucleus. Not always the final state particles make it out of the nucleus in order to be available for detection as is shown in the schematic taken from [61].

number of the probed target nuclei. This is due to the resonance kinematics and its propagation inside the target nucleus. In consequence, extrapolations from lighter to heavier nuclei include contributions of uncertainties from theoretical models.

Current simulations of pion interactions on argon are based on interpolations from the existing measurement on other nuclei [62, 64] and the intra-nuclear models like the Bertini Cascade model [60].

Pions in the sub-GeV range have an interaction length of about $\sim$80 cm in LAr. Thus, only considerably sized LArTPCs with an impinging hadronic beam can reliably produce measurements on pion interactions on argon nuclei. To date, only LArIAT[65] and ProtoDUNE-SP have collected a set of pion interactions on argon in the energy range of interest. First results on the π^+ total cross-section in LAr for an energy range of 100 to 700 MeV have recently been published by LArIAT [63]. The results of the LArIAT measurement on the total negative pion cross-section are shown in Figure 2.11. The predictions from the GEANT4 Bertini Cascade model are in agreement with the measured cross-section. At energies higher than 500 MeV the measurements are slightly higher than the model predictions.

The total pion interaction cross-section can be split in several exclusive channels defined through their topology. The channels are listed in Equation 2.9 and a description of the topologies and final states of the pion interactions is given in Table 2.2 and Figure 2.12.

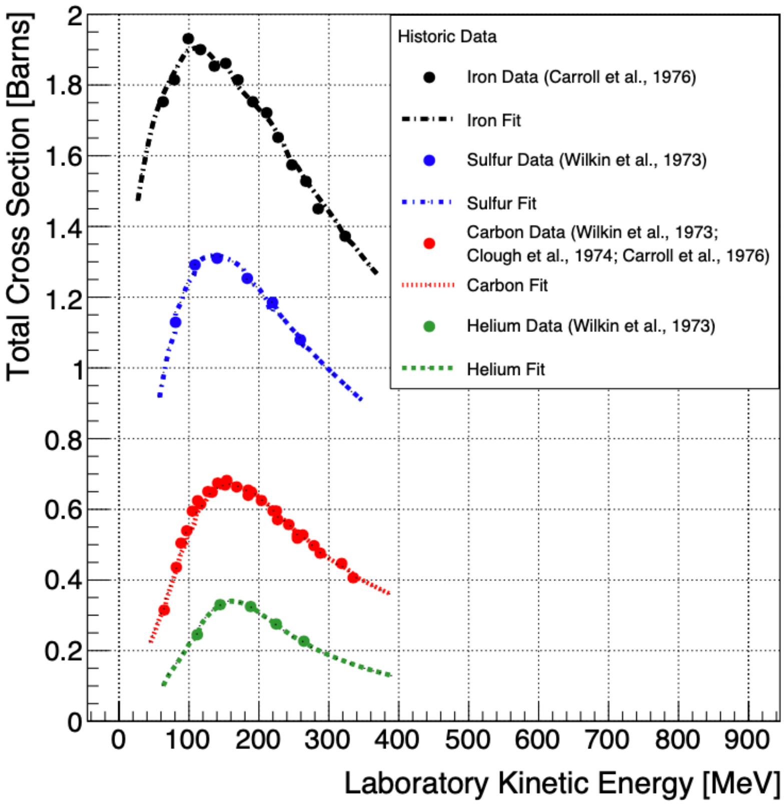

Figure 2.10: Reproduced pion cross-section plot for different target nulcei (Fe, Sn, C, He) taken from [63]. Pion scattering data from [62].

$$\sigma_{total} = \sigma_{elastic} + \sigma_{reaction} = \sigma_{elastic} + \sigma_{inel} + \sigma_{abs} + \sigma_{chex} + \sigma_{\pi prod}. \quad (2.9)$$

Not only are measurements of the total pion interaction cross-section on argon of particular interest for future neutrino experiments, but also the different exclusive interaction channels are important to better understand the underlying physics of the interactions. Especially the pion absorption interaction channel is of particular interest for two reasons: the first, coming from the fact that due to momentum and energy conservation a pion cannot be absorbed by one nucleon. The pion absorption process involves coupled states of at least two nucleons as shown in Table 2.2. Measuring the absorption interactions provides direct insight into the nuclear structure of the target nuclei [64]. Secondly, and more interesting for future neutrino experiments, is the appearance of pions in neutrino RES interactions at neutrino energies in the 1–3 GeV range. If the produced pion is absorbed within the argon nucleus or directly after exiting, the pion may not be detected. Thus, a RES interaction can be misidentified as a QE interaction and the kinematic infer-

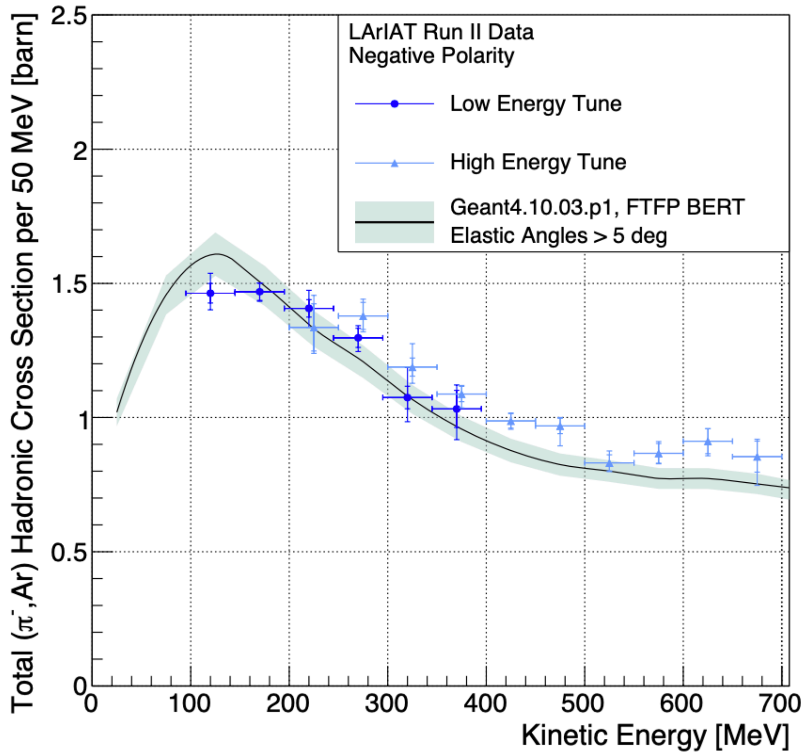

Figure 2.11: Negative pion-argon total hadronic cross-section measured in the LArIAT experiment in the pion kinetic energy range from 100 to 700 MeV. The model prediction by GEANT4 Bertini Cascade is visible in green. Taken from [63].

ence of the neutrino energy is biased. Furthermore, the misidentified event is a background to neutrino QE interaction measurements.

Specific measurements to extract the exclusive pion absorption cross-section on argon have been performed on N, Ar, and Xe at the Paul Scherrer Institute at pion energies in the delta resonance region by the LADS collaboration [66]. The measurements of the argon data have been performed at 70, 118, 162, 230, and 330 MeV pion energies and are reproduced in Figure 2.13.

The extensive amount of ProtoDUNE-SP pion interaction data and the excellent performance of the detector offer the opportunity to perform pion exclusive interaction cross-section measurements directly on argon with a LArTPC. This thesis aims to extract an exclusive measurement of the π^+ absorption cross-section on argon for 1 GeV/c beam pions. The kinetic energy range of 450 to 950 MeV will be covered with ProtoDUNE-SP data. Figure 2.13 shows the LADS data points for the pion absorption cross-section on argon and the GEANT4 pion cross-section for the different interaction types as a function of pion kinetic energy. The ProtoDUNE-SP simulations are generated with these GEANT4 input cross-section models. The

Channel Name	Topology	Comments
PION ELASTIC	$\pi + N \rightarrow \pi + N$	Elastic scattering, target is left in ground state
PION INELASTIC	$\pi + p \rightarrow \Delta^0 \rightarrow \pi + p$ $\pi + n \rightarrow \Delta^- \rightarrow \pi + n$	Nucleons are knocked out or nuclear break-up is possible
PION ABSORPTION	$\pi + (np) \rightarrow nn$ $\pi(nnp) \rightarrow nnn$ $\pi(npp) \rightarrow pnn$ $\pi(nnpp) \rightarrow pnn$	Due to energy conservation the process happens on at least two-nucleon systems
PION CHARGE EXCHANGE	$\pi + p \rightarrow \Delta^0 \rightarrow \pi^0 + n$	Pion converts into neutral pion
PION PRODUCTION	$\pi + N \rightarrow 2\pi + p/n$	If pion kinetic energy $\leq$ 500 MeV

Table 2.2: Definition of π^+ inelastic interactions as a function of outgoing secondary particles.

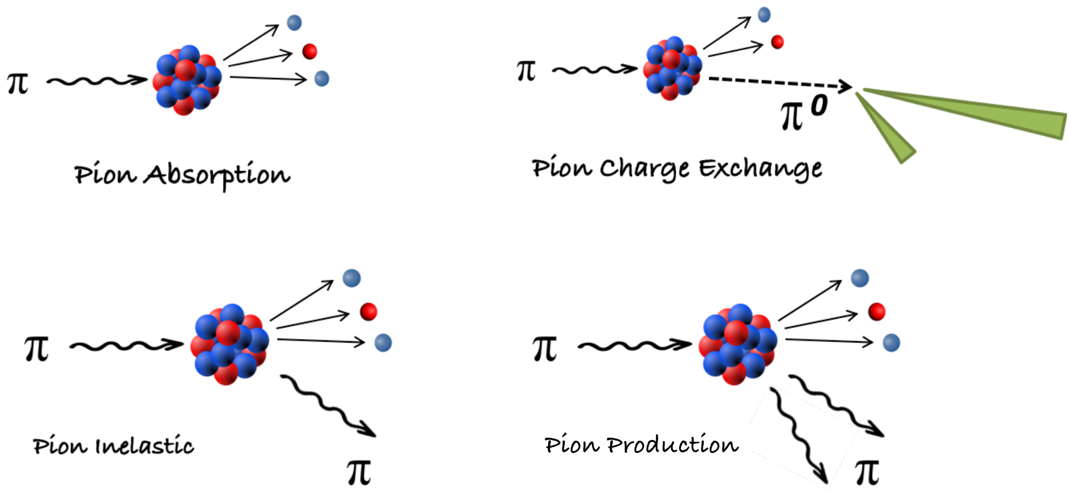

Figure 2.12: Cartoons of the different pion interaction topologies. Upper left: In the π^+ absorption process the incoming pion is absorbed by the nucleus and nucleons (protons and/or neutrons) can be emitted. Upper right: The π^+ charge exchange includes a π^0 which subsequently decays in two photons which are seen as showers, as well as nucleons that can be emitted. Lower left: The π^+ inelastic interaction includes an outgoing charged π^+ and nucleons. Lower right: If multiple π^+ are produced in the interaction it is called pion production.

measurements of the LADS experiment suggest the pion absorption cross-section be significantly lower in the energy range of the resonance. The measurement of this thesis can extend the LADS measurement region and study the behaviour of the pion absorption cross-section at slightly higher pion kinetic energies.

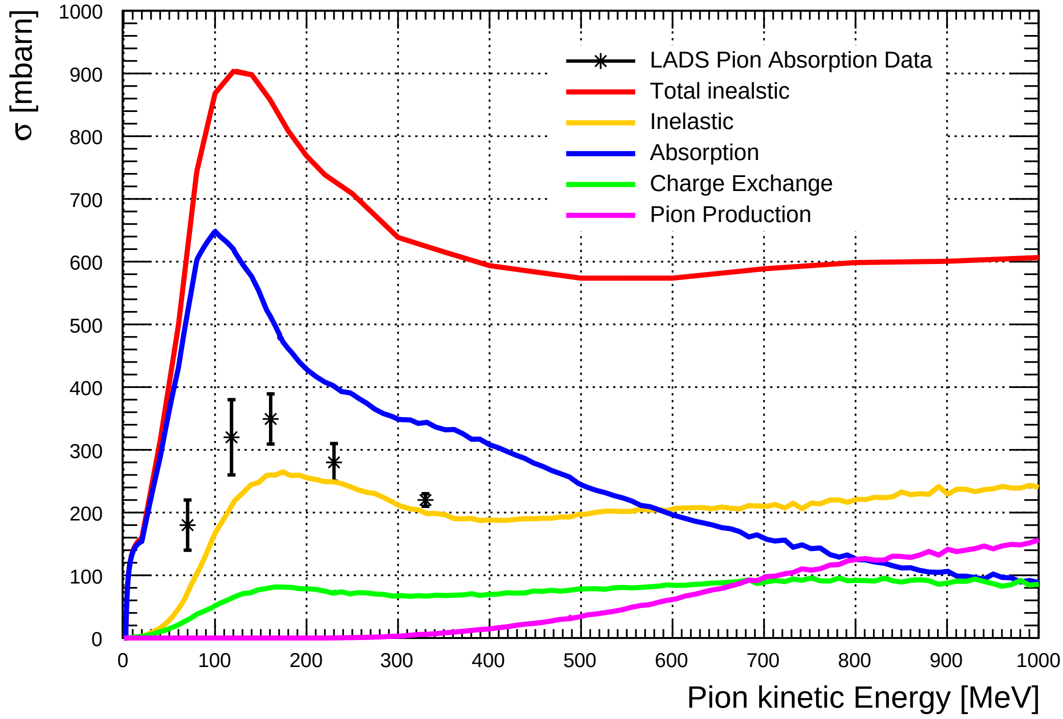

Figure 2.13: Exclusive π^+ cross-section as a function of π^+ kinetice energy implemented in the ProtoDUNE-SP MC simulations based on GEANT4. In comparison the results from pion-absorption interactions on argon from the LADS experiment [66] have been reproduced. The simulations rely on the Bertini cascade model [60]. The red curve, representing the total inelastic cross-section is the sum of the absorption, inelastic, charge exchange, and pion production interactions. At low momenta the pion absorption cross-section is dominant. The pion production process is only possible from π^+ kinetic energies above 500MeV, hence the rise only at higher momenta. The measurements of the LADS data suggest the model predictions by GEANT4 overestimate the pion absorption cross-section in the energy range of 70 - 330 MeV.

2.6 TOWARDS A MEASUREMENT OF THE PION ABSORPTION CROSS-SECTION

In my PhD thesis, I present the measurement of the pion absorption cross-section as a function of the pion kinetic energy on liquid argon. The measurement is performed on beam pions impinging ProtoDUNE-SP with 1 GeV/c momentum and will cover the range of 450 to 950 MeV pion kinetic energy. This section gives an overview of the measurement by defining and introducing the derivation of the cross-section formula, as well as outlining the necessary steps to perform the measurement. The different components to complete the measurement will be detailed in the following chapters of the thesis.

The cross-section σ describes the probability of a particle at given energy to interact. This is valid for any interaction type or the total sum of all interaction types. In general, the cross-section depends on the incoming particle energy and is related to the average distance of a particle traveling in a medium with a given density:

$$\sigma = \frac{1}{n\lambda}, \tag{2.10}$$

where λ is the mean free path in cm, n the number density composed of the density ρ of the medium in g/cm^3, the Avogadro constant N_A in 1/mol and the atomic mass A in g/mol

$$n = \frac{\rho N_A}{A}. \tag{2.11}$$

One can describe the probability of a pion interacting in an infinitesimal volume of $(L \times L \times dx)$ as the ratio of the net area of the available atoms with respect to the area of the infinitesimal volume, as shown in Figure 2.14. The net area of atoms that the pion can interact with depends on the cross-section, the number density n, and the infinitesimal thickness dx as noted in Equation 2.12. This can be done for multiple infinitesimal volume slabs. The interaction probability between the slabs is assumed to be independent of what happened before

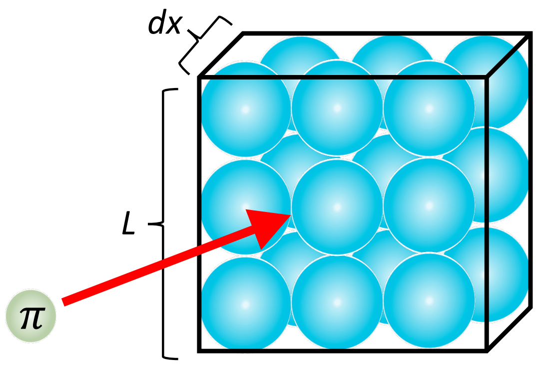

Figure 2.14: Illustration of a pion interaction in an infinitesimal volume with thickness dx.

$$P_{interaction} = \frac{A_{atoms}}{A_{slab}} = \frac{\sigma n L^2 dx}{L^2} = \sigma n dx. \tag{2.12}$$

The change in number of pions after traversing the infinitesimal volume, can be described as the number of pions entering N_π multiplied by the interaction probability, resulting in

$$dN_\pi = -N_\pi \sigma n dx. \tag{2.13}$$

Measuring the cross-section as function of the particle energy means, that we are interested in the loss of pions dN_π due to an interaction with respect to their deposited energy dE. Using Equations 2.13 and 2.11 and the ability to measure precisely dE/dx with a LArTPC one obtains the following expression:

$$\frac{dN_\pi}{dE} = \frac{dN_\pi}{dx}\frac{dx}{dE} = -N_\pi \sigma \rho \frac{N_A}{A}\left(\frac{dE}{dx}\right)^{-1}. \tag{2.14}$$

The measurement of the Pion Absorption cross-section is performed as a function of the pion kinetic energy, we go from $d \rightarrow \Delta$ and can write:

$$\frac{\Delta N_\pi}{\Delta E} = \left(\frac{dE}{dx}\right)^{-1} N_\pi \sigma \rho \frac{N_A}{A}, \tag{2.15}$$

where now ΔN_π is the number of interacting pions (from now on $N_{\pi Interacting}$) for the deposited energy ΔE and N_π the total number of incident beam pions (now $N_{\pi Incident}$). So far, cross-sections in LArTPCs have been measured using the *Thin Slice Method* [63]. It introduces the wire pitch z (4.79 mm) through associating it with the slab thickness. Thus, ΔE is the energy deposited per slab with a thickness of the wire pitch. Hence, the cross-section is measured by a geometric entity of the detector that can be affected by spatial distortions coming from accumulation of space charge distorting the drift electric field.

ProtoDUNE-SP is subject to high spatial distortions from strong space charge effects (SCE) as described in Section 4.3. The SCE effects cause an increase of the wire pitch which is stronger at the boundaries than in the bulk region of the LArTPC. The local effects in the beam entry region are difficult to reproduce precisely in simulations. Therefore, it is best to avoid SCE-affected observables in a measurement. Another reason to avoid using the wire pitch is the fact that the cross-section is measured as a function of energy. There is no benefit from inserting another variable in the final cross-section equation with an associated uncertainty if it is possible to directly remain in the energy domain. In consequence, the measurement I propose in this thesis is a novel and more simple approach by just directly slicing in the energy phase space. The new method is called *E-Slice Method*. ΔE is the energy bin width chosen for the cross-section measurement. This leads to the final equation for the cross-section at the i-th energy bin

$$\sigma(E_i) = \frac{A}{N_A \rho \Delta E}\frac{dE}{dx}(E_i)\frac{N_{\pi Interacting}(E_i)}{N_{\pi Incident}(E_i)}, \tag{2.16}$$

if $N_{\pi Interacting}(E_i)! \ll N_{\pi Incident}(E_i)$ the more accurate formula is given through

$$\sigma(E_i) = \frac{A}{N_A \rho \Delta E} \frac{dE}{dx}(E_i) \ln\left(\frac{N_{\pi Incident}(E_i)}{N_{\pi Incident}(E_i) - N_{\pi Interacting}(E_i)}\right). \tag{2.17}$$

The first fraction of Equation 2.16 is a constant, the second fraction is the mean energy loss per unit length for the given energy bin E_i. The mean energy loss per unit length is calculated using the Bethe Bloch formula for 1 GeV/c momentum pions as introduced in Section 2.2. The last fraction in Equation 2.16 is the bin-by-bin division of two measured histograms in bins of energy from data. The denominator $N_{\pi Incident}$ is built from the sample of all incident beam pions in the LArTPC. It is also referred to as the *incident histogram*. $N_{\pi Interacting}$ is the subsample of the denominator sample. It includes only pions of the interaction process of interest for the cross-section measurement and is referred to as *interacting histogram*. The more accurate formula for cross-section extraction is given in Equation 2.17 and is the one used for the measurement as it is better suited for bins where the number of interacting pions is not much smaller than the number of incident pions in that bin. A proof of principle of the E-Slice method is shown in a closure test with the truth quantities of simulated ProtoDUNE-SP data in Section 7.1.

Populating the Incident and Interacting Histograms

The essential part of the measurement lies in the step of populating incident and interacting histograms with events to perform the measurement. The event selection, described in Chapter 5, provides a sample of beam pions and a subsample of selected absorption events. The first is used to fill the incident histogram and the latter for the interacting histogram. For each pion, the initial kinetic energy and the kinetic energy at its interaction point are measured with the beamline instrumentation and LArTPC data (Section 7.2) are determined. An incident pion will contribute with an entry in the incident histogram from its starting point to each energy bin fully crossed including the energy bin of interaction. A pion interacting inelastically, decaying, or producing multiple neutral or charged pions will not contribute to the interacting histogram. The interacting histogram is populated only with the selected sub-set of pion absorption event candidates. Each event contributes with only one entry in the interacting histogram at the energy bin of interaction. Thus, the incident histogram describes for every energy bin how many pions have traversed without interacting. The interacting histogram records for every energy bin how many pions have interacted via the pion absorption process in the corresponding bin.

Figure 2.15 illustrates how the incident and interacting histograms are filled. The liquid argon inside the detector is sliced in ΔE. Pions enter the detector at 1 GeV/c momentum and interact at different points. Pions interacting with a green rhombus are of type absorption. They contribute to the interacting and incident histogram. Pions with an orange interaction point do not undergo absorption and only contribute to the incident histogram. Note, the incident histogram is similar to an integral of a histogram where the interaction of all pions is noted. The histograms are correlated and their ratio is proportional to the cross-section as shown in Equation 2.16.

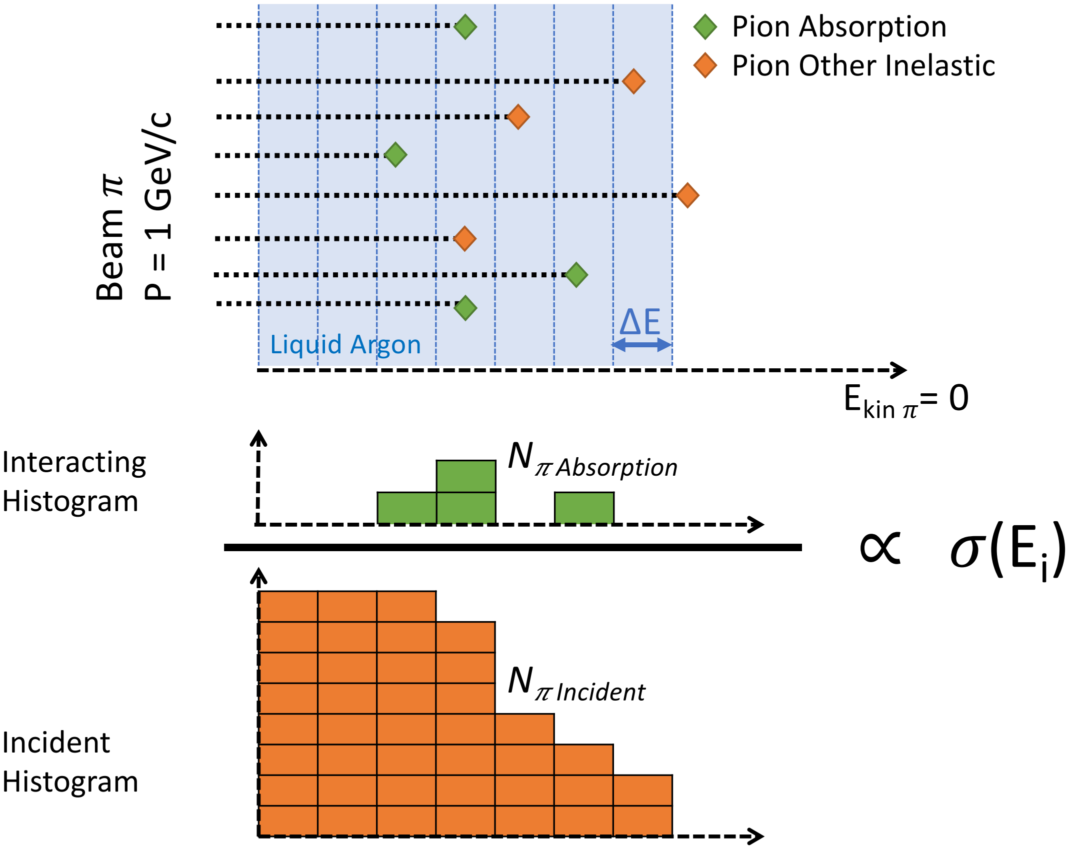

Figure 2.15: Top: pions entering the LAr of the TPC volume from the ProtoDUNE-SP beam. The pions travel a certain distance in the detector until they are either absorbed or interact in a different process. The bin-by-bin ratio of the *interacting* and *incident histogram* is proportional to the cross-section, as shown in Equation 2.16. The histograms are filled in the following way: Each beam pion impinging in ProtoDUNE-SP contributes to the incident histogram. An incident pion will contribute to an entry for each energy bin in the incident histogram that was crossed from its initial kinetic energy at the TPC entry until (and including) the kinetic energy at the interaction point. A pion undergoing an absorption process will contribute in the same way to the incident histogram and with only one entry at its interacting kinetic energy to the interacting histogram.

The selection of the energy bin width for the histograms is done carefully by considering certain aspects of energy resolution in the LArTPC, the beam momentum spread, and momentum resolution of each particle from the beam instrumentation. Once the incident and interacting histograms are computed from the selected data events, the next step is to correct for the efficiencies and purities of the various steps in the event selection. The values are reported in Section 5.6 and are extracted from the simulations.

When measuring a cross-section, the ulterior goal is to compare the measurement to theoretical values from models to constrain them. The distributions for the incident and interacting histograms are measured in pion kinetic energy. The observable is inevitably subject to detector effects introducing an energy smearing. The measured energy in the detector is smeared to a certain degree with respect to the true deposited energy of the particle. The smearing can arise from different effects such as longitudinal and transversal diffusion, charge recombination, spatial resolution, and other effects. The more relevant effects were introduced in Section 2.3. Removing detector effects from a measurement can be done through iterative Bayesian unfolding. Unfolding provides a measurement free of detector effects and allows to compare the measurement of the cross-section with the model predictions as shown in Figure 2.13. Both, measured incident and interacting histograms are unfolded to obtain the *true* underlying distributions. The limits of detector unfolding approaches are discussed in the final chapter of this thesis.

To complete the measurement, the evaluation of the major systematic uncertainties is done in Chapter 6. They arise from uncertainties on the measurements of the beam momentum, reconstruction resolution, model-dependent uncertainties from the simulations. Each uncertainty is described, evaluated, propagated, and included in the final result of the pion absorption cross-section measurement which is shown in Section 7.5.

3

ON THE WAY TO DUNE: THE PROTODUNE SINGLE PHASE DETECTOR

In the previous Chapter 2 the LBNF/DUNE neutrino program has been introduced and the fundamental working principles of a LArTPC have been discussed. Moreover, the necessity of thorough, efficient, precise, and DUNE-tailored prototyping has been highlighted to guarantee the success of this important international next-generation neutrino experiment. The neutrino community can already profit from experiences made with different LArTPC experiments over the last decades in the field [50, 67, 48]. This chapter describes in detail the design and construction of the first single-phase (SP) detector prototype for the first out of four DUNE far detector modules, the so-called ProtoDUNE-SP. The main deliverables of ProtoDUNE-SP are to validate the following points on hardware, software, and physics aspects of DUNE:

- Certify the membrane cryostat technology providing a vessel capable of holding the liquid argon at a stable temperature of ∼83 K and overpressure of ∼1000 mbar
- Prototype the full-scale detector components of the first DUNE far site module
- Test production and installation procedures
- Verify the design with detector performance
- Act as a test stand for the computing infrastructure for collecting data from a charged particle beam (0.5 – 7 GeV)
- Benchmark reconstruction performance with beam data
- Characterise the detector response and develop calibration procedures for precise calorimetry
- Provide hadronic cross-section measurements in order to quantify and significantly reduce systematic uncertainties for DUNE far detector measurements
- Demonstrate stable operation over long periods
- Study the detector behaviour under varying experimental conditions

Figure 3.1: Overview of the EHN1 extension in the north area of CERN. ProtoDUNE-SP, the DAQ system, the cryogenic system and the beam line are indicated [40].

Nevertheless, ProtoDUNE-SP is a significant experiment in its own right. The detector is in the CERN North Area and is the largest LArTPC built and operated to date with its active volume of 6 x 7 x 7.2 m^3. More precisely, ProtoDUNE-SP is located in the extension of the EHN1 hall alongside other fixed-target experiments with a dedicated charged particle test beamline as part of the prototyping program. Figure 3.1 shows an overview of the EHN1 extension. Alongside ProtoDUNE-SP also ProtoDUNE-DP (dual phase), utilising different LArTPC technology was built and is visible in the figure.

In June 2015 ProtoDUNE-SP was put forward to the CERN SPSC as part of the program of the Neutrino Platform (NP) and approved by December 2015 as CERN experiment NP-04. Construction and installation of the detector were finalized by July 2018 and after filling the detector with the liquid argon and commissioning, the first test beam data was received on August 29, 2018. By November 11, 2018, the beam run was completed and detector operations continued through to July 19, 2020. The operation time and data collection over 2 years (long endurance run) allowed us to assess the above-mentioned deliverables thoroughly and further explore the operational parameters.

I should like to note, that I dedicated my first two PhD years (2017 – 2019) to the construction, assembly, and commissioning of the detector with a special focus on the high voltage (HV) system and the field cage (FC) components which are described in detail in Section 3.2. Working directly on the completion and successful operation of ProtoDUNE-SP has proved to be an asset: I've had the privilege to become an expert on the detector and the in-depth knowledge earned during the construction and commissioning phase paved the way to build a deep understanding of the detector properties during operation.

3.1 DETECTOR DESIGN AND CONSTRUCTION

In size, ProtoDUNE-SP represents a self-sufficient LAr TPC that is at 1:20 of the size of a full DUNE far site module. The detector components however are replicas scaled to size with those used in DUNE. Thus, one DUNE far detector module will consist of 20 ProtoDUNE modules in a configuration of 2 x 2 x 5 ProtoDUNEs. Even though the ProtoDUNE-SP components are built to scale with DUNE components, they are themselves composed of smaller units, this approach simplifies various aspects of such a large scale experiment:

- Assembly above ground
- Underground transportation of the small modules
- Repetition of assembly and installation procedures underground

The ProtoDUNE-SP detector is designed with a close to cube-like geometry, with dimensions of 7.2 m along the drift direction (x coordinate), 6 m in height (y coordinate) and 7 m following the charged particle beam (π, p, e) direction (z coordinate), as shown in Figure 3.2. The full detector is suspended through the Detector Support Structure (DSS) from the cryostat roof and submerged in the LAr. Table 3.1 gives an overview of the key design and operation parameters of ProtoDUNE-SP.

ProtoDUNE-SP consists of two drift volumes separated by the Cathode Plane Assemblies (CPAs) which are located in the middle of the detector spanning the $y-z$ plane. The ionisation charge produced in the drift volume by the impinging beam particles is drifted to the wire plane readout and projections of said particle tracks are recorded on the wires as electric signals. The CPA carries the high voltage (HV) that provides the drift electric field with a target nominal intensity of 500 V/cm.

The two drift volumes are contained on each side (extremities of the x coordinate and parallel to the CPA) by the Anode Plane Assemblies (APAs) collecting the ionisation charge on wire planes. The detector is sealed in the $y-x$ plane by the End Walls of the Field Cage (FC EW). The top and bottom are sealed by the Top and Bottom Field Cages. The right-handed coordinate system on the figure is placed such that the z coordinate points in the direction of the beam that enters through the Beam Plug (BP) shown with the pink arrow. The coordinate origin is

Parameter	Value
LArTPC (active) dimensions ($h \times w \times l$)	6 m $\times$ 7.2 m $\times$ 7 m
LArTPC (active) mass	0.77 kilo tons
LAr temperature	86.9 - 88.2 K
Number of anode planes	6
Active dimensions ($h \times w$)	5.984 m $\times$ 2.300 m
Anode planes spacing	4.75 mm
Wire pitch collection plane (X) and grid (G)	4.790 mm
Wire pitch induction planes (U,V)	4.669 mm
Wire angle (w.r.t. vertical) (U,V)	35.7°
Wire angle (w.r.t. vertical) (X,G)	0°
Wire material	Beryllium copper, $d = 150\,\mu\text{m}$
Design wire tension	5.0 N
# wires / APA	2560
# wires / plane	960 (X), 960 (G), 800 (U), 800 (V)
Photon detector slots / APA	10
Cathode voltage (operational)	-180 kV
Bias voltages (G,U,V,X)	-665 V, -370 V, 0 V, 820 V
Drift-field	500 V/cm
# top & bottom field cage modules	6 (top), 6 (bottom)
# end wall planes	2
# end wall field cage modules (per plane)	8
# field cage profiles per module	57
Profile-to-profile voltage step	3 kV
Profile-to-profile distance (center to center)	6 cm
Ground plane to field cage distance	20 cm
Support structure material	G-10, FR4
Cryostat outer dimensions ($h \times w \times l$)	10.8 m $\times$ 11.4 m $\times$ 11.4 m
Cryostat inner dimensions ($h \times w \times l$)	7.9 m $\times$ 8.5 m $\times$ 8.5 m
Material outer structure	Prefabricated steel modules S460ML [68]
Overall inner vessel thickness	800 mm
Primary membrane thickness	1.2mm
Primary membrane material	Stainless steel
Cryostat leak tightness	$\sim$ 2-3 $\times$ 10^{-6} mbars l/s
Absolute pressure inside vessel	970-1100 mbar
Beam run start date	August 29, 2018
Beam run end date	November 11, 2018
End of detector operation	July 19, 2020

Table 3.1: ProtoDUNE-SP design parameters, operating conditions and dates [40, 69]

fixed to the bottom point where the CPA starts. The x coordinate is pointing in the drift direction, the drift volume that receives the beam is associated with the negative x coordinate component and is usually called the beam right side, as it extends to the right if one is looking in the beam direction. The other drift volume is referred to as the beam left side. Throughout the thesis I will talk of upstream and downstream placed components, referring to the beam entry point. Upstream is closer to the beam entry, downstream is further away.

The detector structure composed of FC and APAs acts like a Faraday cage to maintain a homogeneous electric field within the drift volumes and shield it from the nearby cryostat walls that would induce distortions and therefore compromise the detector performance. The cathode plane (CPA) is biased at a high potential of -180 kV. The potential is brought to the CPA through a high voltage located at the downstream side of the TPC, as shown in Figure 3.2.

The Photon Detection System (PDS), serving to collect timing information of the TPC signals, is composed of bar-shaped photon detectors and is embedded within the APAs. The Cold Electronics (CE) that amplify and transmit the signals from the collection planes to the Data Acquisition System (DAQ) is mounted on top of the APAs and is also submerged in LAr. The advantage of putting the CE in this hostile environment of -190°C lies in the signal amplification and transmission at cryogenic temperatures responsible for a substantial noise reduction of the waveforms. Stable and constant performance of all CE is crucial for the success of the experiment as the electronics become inaccessible once the detector is filled with LAr.

As DUNE is foreseen to take data for many years to meet its physics goals, the CE needs to function reliably during the whole period. At all times during detector operation, it is important to monitor various detector parameters, such as LAr temperature, pressure and purity, and the state of the FC, and possible electric discharges. Therefore, the space between the detector boundaries and the cryostat membrane is equipped with different cryogenic instrumentation including purity monitors, temperature sensors, and video cameras.

All the components of ProtoDUNE-SP have been designed and built with the scope of testing close to the final designed pieces for the first DUNE far detector module. The Beam Plug (BP) is the only component that is not included in the DUNE design. However, it is needed to meet the ProtoDUNE-SP physics goals of performing physics hadronic cross-section measurements, as I propose in this thesis. The details for the BP design choice and physics motivations are given in Section 3.2.

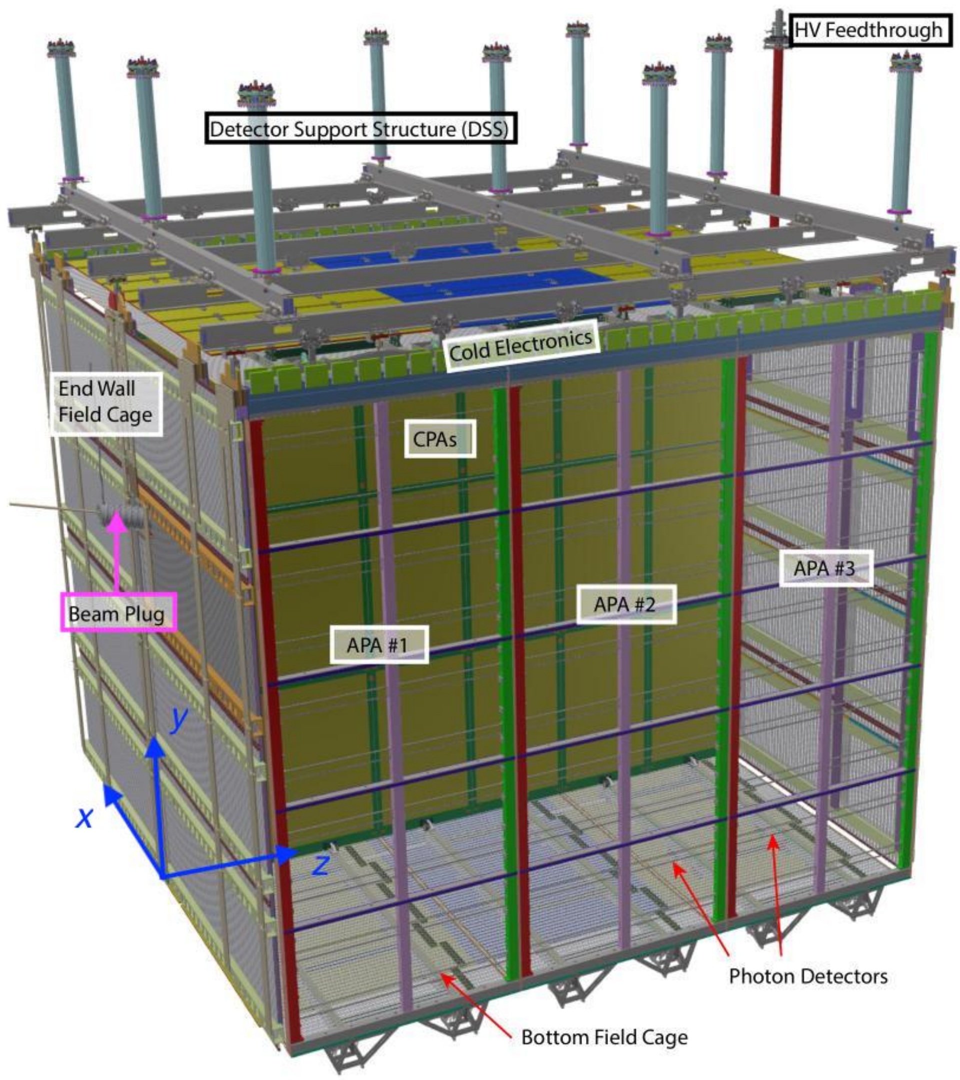

Figure 3.2: Drawing of the ProtoDUNE-SP detector. The central detector components are indicated in the figure. They include the Cathode Plane Assembly (CPA), the Anode Plane Assemblies (APA), the Cold Electronics (CE) sitting on top of the APAs, the Field Cage top, bottom and end walls, the Photon Detector System (PDS) and the Beam Plug (BP). The detector is suspended from the support system which is attached to the cryostat top. The charged particle beam (π, p, e) enters from the left side through the BP [69].

Modular Design

The design of ProtoDUNE-SP is as close as possible to the final configuration of the first DUNE far detector module. Components such as the CPA, FC, and APA are full-scale DUNE preliminary modules. The maximum drift distance of 3.6 m is identical to that of DUNE. Due to practical limitations, however, ProtoDUNE-SP is only half the height (1 APA high) of the first DUNE far detector module which is designed with a height of 12 m, *i. e.* 2 APAs stacked on top of each other.

Figure 3.3 shows the modular build of ProtoDUNE-SP. One APA is 6 m in height and 2.4 m in width. ProtoDUNE-SP uses six APAs that equip the two drift volumes, the charge collection plane of one drift volume is built by three APAs, side-by-side. The choice of placing three APAs next to each other was motivated to test whether the middle APA signal is affected by undesired effects of crosstalk. If crosstalk happens, the signal transmitted to the channels of one APA can be affected by the signals on the other APAs, it is usually caused by capacitive, inductive, or conductive coupling between circuits or channels. The APAs are described in more detail in Section 3.3.

The full cathode plane (7 m x 6 m) consists of 18 CPA modules of 2 m height and 1.2 m width. Three modules are stacked to a CPA column, the full plane, therefore, is built out of six columns. The relatively small size of the modules allows for easy transportation and handling. The bias voltage of -180 kV supplied to the CPA through the HV feedthrough is the same as planned for the first DUNE far detector module.

The FC surrounds the drift volume faces that are not covered by the APAs and completes the detector. It covers the top, bottom, upstream, and downstream faces. The top and bottom FCs consist of six assemblies matching the width of one APA and covering the drift distance from CPA to APA, hence with a width of 2.4 m by 3.6 m along the drift. The upstream and downstream sides are covered by the FC end walls (EW), each drift volume has two EW assemblies each made out of 4 panels (1.5 m in height and 3.6 m along the drift). The CPA, FC, and the HV system are described in detail in Section 3.2.

Construction

The different detector components, CPA modules, FC modules, APA, PDS system, and Cold Electronics (CE) were shipped to the EHN1 building in the CERN North Area. The components were partially built before shipping and finalised in the NP04 clean room in front of the ProtoDUNE-SP cryostat. The cleanroom satisfies the ISO-8 level of cleanliness. After assembly, the components are inserted into the cryostat. This happens through the cleanroom adjacent Temporary Construction Opening (TCO). The TCO is located at the upstream side of the cryostat, *i. e.* on the side where the test beam impinges into the detector as shown in Figure 3.4.

The cleanroom hosts a rail system on the roof where the detector components such as the CPA and APAs can be hanged and then further moved into the cold box for testing (APA) or directly through the TCO into the cryostat for final po-

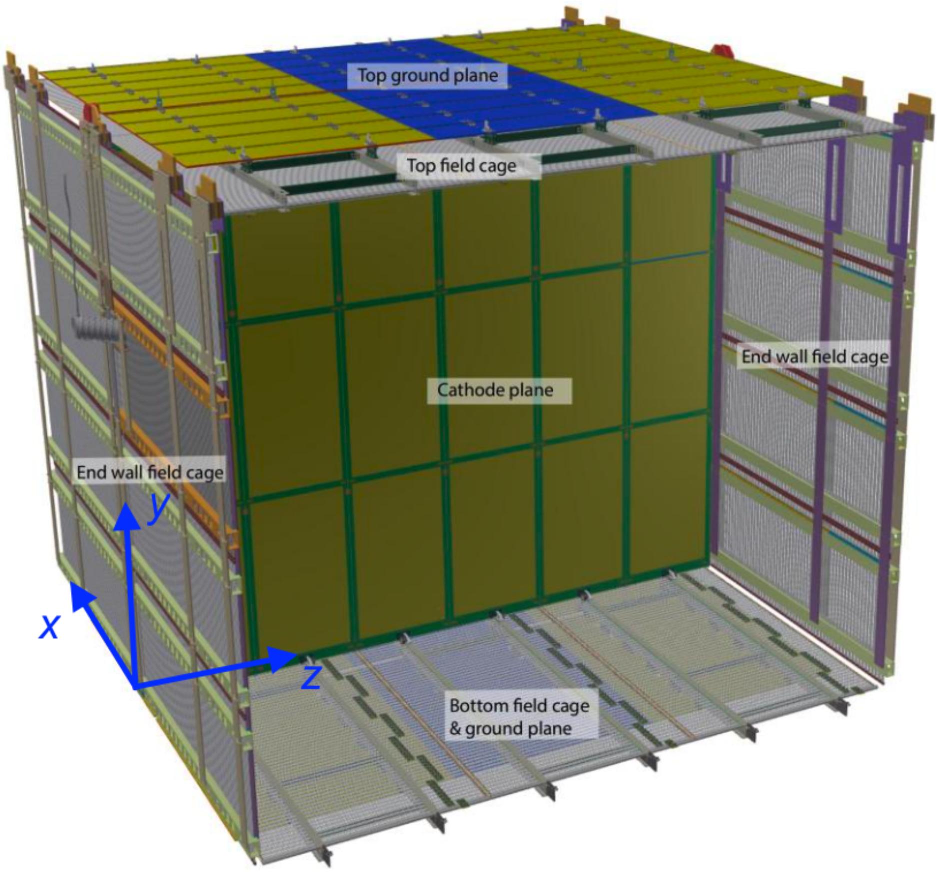

Figure 3.3: ProtoDUNE-SP's detector structure with the CPA modules and the FC modules visible [69].

sitioning. The materials for the detector and partially assembled components are lowered with the crane down through the "material sas" into the NP04 clean room. Figure 3.4 shows a schematic and photograph of the NP04 clean room.

Given the considerably "slim" opening of the TCO, the finalisation of the FC construction was only completed once the components were placed inside the cryostat. The components have to be arranged in a way such, to be slim enough to enter through the cryostat TCO. In the case of the APAs, this is not a problem as they are only 12 cm in thickness and hang vertically. The field cage, however, has the top and bottom modules which enclose the detector horizontally. This mechanical structure cannot fit through the TCO as it is in its final position. The top and bottom modules have to be inserted in a vertical position through the TCO before being placed horizontally closing the volume from CPA to APA inside the cryostat. For this reason, the CPA is designed to carry the load of the top and bottom modules which are installed vertically and snug onto the CPA, looking like a sandwich of FC-CPA-FC. Details of this procedure are described in Section 3.2. The resulting three sandwiches are then finally moved one by one through the TCO into the cryostat. The top and bottom modules are deployed from the CPA into their horizontal position as soon as the CPA is in its final position inside the cryostat. The end walls are also inserted through the TCO into the cryostat to close the detector.

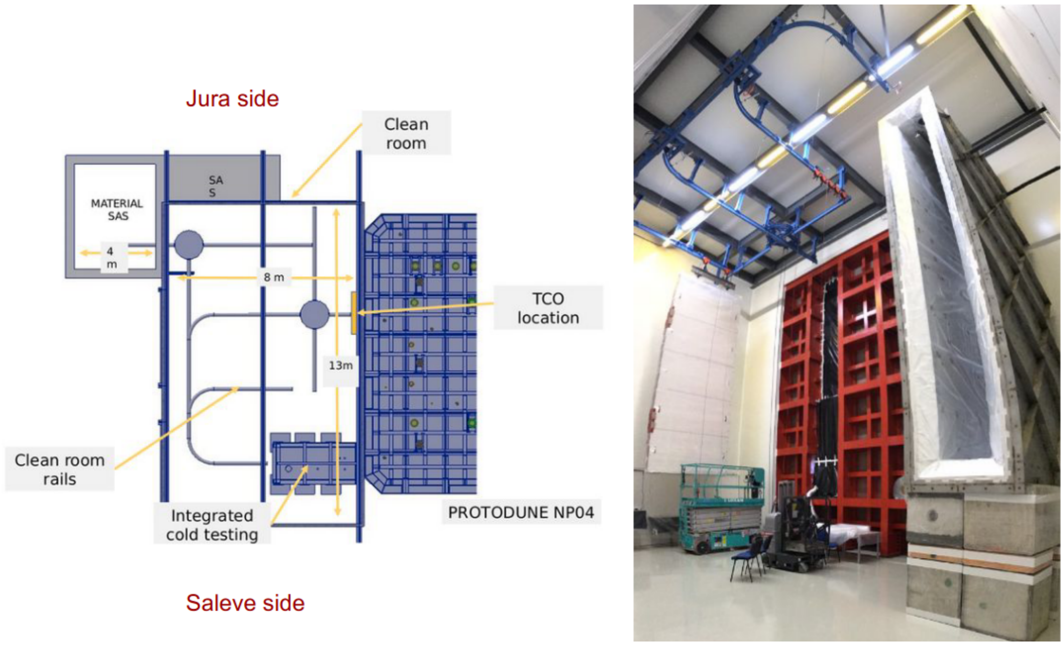

Figure 3.4: Schematics of the NP04 clean room with the integrated rail system for moving the hung detector components. The photo on the right shows the TCO on the red cryostat warm structure viewed from the cleanroom. On the right side of the picture, the cold box for the APA testing is visible and on top of the cleanroom, the rail system is also visible [40].

The major detector construction steps that took place inside the NP04 clean room were:

- CPA modules and CPA array construction
- Attachment of FC top and bottom assemblies on the CPA
- CE unpacking, testing, and mounting on the APAs
- PDS unpacking, testing, and embedding in the APA frames
- Integrated testing of APA with PDS and CE inside the cold box
- Displacement of the components through the TCO into the detector

The detailed steps of the full detector installation are given for the various components in their corresponding sections of this Chapter. Section 3.7 summarises step by step the full integration of ProtoDUNE-SP inside the cryostat. Once the full detector was nearly finalised inside the cryostat, the TCO was welded close from the inside. This changed the detector installation environment to become classified as a confined space. Working in this environment required special measures and education as it is prone to hazards. The inside of the cryostat was only accessible through a circular entry (manhole) and ladder on the top of the detector. In this configuration at all times that work was done in the confined space there had to be a member of the team at the manhole monitoring the people inside and establishing live contact. The detector was finalised and the cryogenic instrumentation, as well as other detector monitoring systems, were installed.

3.2 HIGH VOLTAGE SYSTEM DESIGN AND CONSTRUCTION

The High Voltage System of ProtoDUNE-SP consists of the Cathode Plane Assembly, the Field Cage top, bottom, and end walls, and the HV feedthrough. In a LArTPC, the cathode is the surface carrying the potential fixing the drift field at a nominal field intensity of 500 V/cm. The FC structure provides a graded voltage profile, *i. e.* the boundary conditions for a uniform drift electric field between CPA and APA. Finally, the HV feedthrough is the device that supplies the CPA with the -180 kV potential required to generate the electric field inside the LArTPC. A Heinzinger -300 kV 0.5 mA power supply is used to generate the high voltage outside of the cryostat. A brief overview of the modular design of CPA and FC is given in Section 3.1.

In the present Section, I discuss the ProtoDUNE-SP HV system and its construction phase in-depth as I was part of the team responsible for the installation, completion, and operation of this central detector component. Figure 3.5 shows a panoramic view of the two ProtoDUNE-SP drift volumes. The view is from the downstream face looking to the end walls upstream where the beam impinges on the beam right side, left side on the panoramic view. The Figure shows the CPA plane in the middle and the two drift volumes on each side of the CPA, closed by the two APA-planes on both left and right sides. The photograph shows the fully integrated HV system.

Cathode Plane Assembly

18 CPA modules of 1.2 m width and 2 m height that are assembled to form the central cathode plane visible in Figure 3.5. The modules are constructed from 6 cm thick fire-retardant, glass-reinforced epoxy laminate (FR4) frames that hold 3 mm thick FR4 sheets. Instead of using a classical set of interconnected metallic electrodes to form the cathode, the FR4 was chosen as it permits laminating the surface

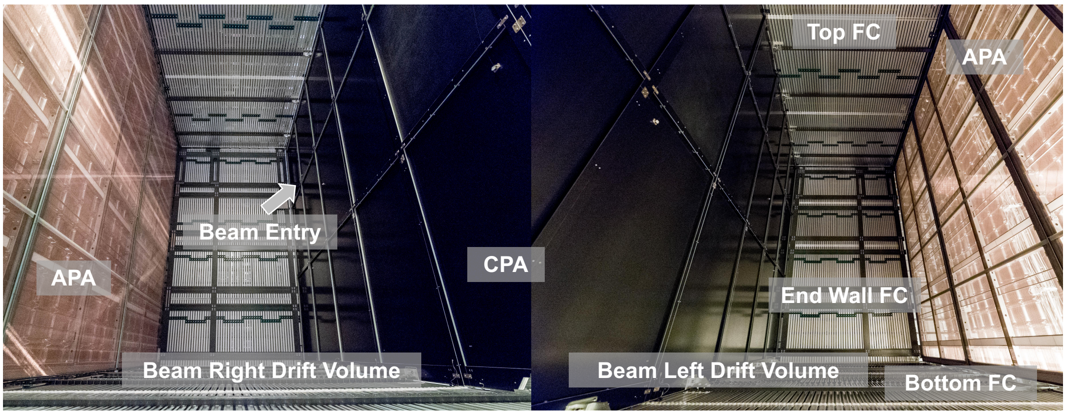

Figure 3.5: Photograph of the two ProtoDUNE-SP drift volumes in a panoramic view. The black cathode plane composed of the CPA modules is visible in the middle of the picture. The black colour comes from the resistive Kapton surface of the CPA. The drift volumes boundaries are given by the field cage (FC) with its distinct aluminum profiles and voltage dividers that are the key part of the FC. The detector is closed by the APA wire planes on the right and left side of the photograph, the wires are made out of copper as is visible from the APA colour. The so-called "beam right and beam left" sides are defined when looking into the detector in the beam direction. The pictures have however been taken facing the beam direction, thus left and right are reversed.

on both sides of the sheets with a highly resistive Kapton film of type D11261075 [70]. The FR4 frames holding the panels have field-shaping strips with the resistive material mounted on top.

To provide a drift field with a nominal value of 500 V/cm, the bias voltage is -180 kV, which is considered as high voltage. In case of a sudden energy release through a discharge, the integrity of the other detector components, especially the sensitive electronics of the DAQ system would be put in danger if conventional material like stainless steel would be used for the cathode. This eventuality is avoided by using the aforementioned resistive Kapton laminate, which has the advantage of providing the CPA with a long discharge time constant. In the case of an HV breakdown, the sudden change in voltage would be restricted to a considerably smaller and more localized area of the affected CPA module, whereas the rest of the CPA would keep the nominal potential and then gradually discharge to the ground because of the strong resistive material layer.

For excellent detector performance, a uniform electric field is crucial, and to mitigate the possibility of electric breakdowns, the electric field intensity must remain below 30 kV/cm. Special care has to be taken for the FR4 CPA frame and the CPA edges that can be a source of high field or irregularities. The aforementioned field-shaping strips are installed on the FR4 frames, biased differently than the CPA plane. The different bias voltage is chosen in a way such as to avoid distortions in the drift field.

High electric fields are most likely to happen around the CPA edges where the highest potential occurs, consequently, the edges of the CPA facing the cryostat wall are well covered with metal profiles that are also used for the FC. They are effectively a continuation of the FC that is mounted horizontally snug to the CPA frame. The profile shape and the reason for its choice are described later in this Section.

The bias voltage of -180 kV is brought through the HV feedthrough (described later in this Section) from the warm side into the cryostat. To receive the HV on the CPA receptacle, the *HV cup* is mounted on the CPA at the downstream side, far away from the beam entry point. The receptacle is visible in Figure 3.6. Its shape satisfies the same requirements of low field intensity as the CPA. The CPA modules upstream of the HV cup receive the bias voltage through the HV bus (Figure 3.6) that runs along with the CPA modules under the field shaping strips and interconnecting the modules. The HV bus is used to distribute the bias voltage providing a conductive path along with the CPA as the entire cathode is highly resistive. Connections on the CPA are made to be redundant to cope with possible HV bus or cable failures.

Three CPA modules are stacked vertically to build the full 6 m height of the CPA. The connected modules are shown lying horizontally in Figure 3.7. They are bolted together and the sheets are connected through metal plates on each side ensuring redundant electrical contact. The array of three modules is suspended by the insulating FR4 lifting bar from the Detector Support System (DSS), as shown in Figure 3.6. Each array is connected to its neighbouring ones through pin-and-slot connections. They are designed in a way to allow for relative movement due to the thermal contraction of the various detector components when cooling down to LAr temperature (83 K).

Two arrays of 3 CPA modules are connected and build the structure to mechanically hold on both sides of the surfaces one top and bottom FC module corresponding to one-third of the full ProtoDUNE-SP detector. When mounting the CPA modules together, special care had to be taken by visually inspecting the full surface of the resistive Kapton laminate. Any scratch or damage to the Kapton surface could be a source of distortion to the electric field or act as a weak point in case of electrical discharge. Furthermore, throughout the full construction of all the HVS components, if present, sharp edges, scratches, or small damage that occurred during construction and installation had to be addressed by either replacement of the affected component or covering scratches with insulating epoxy glue.

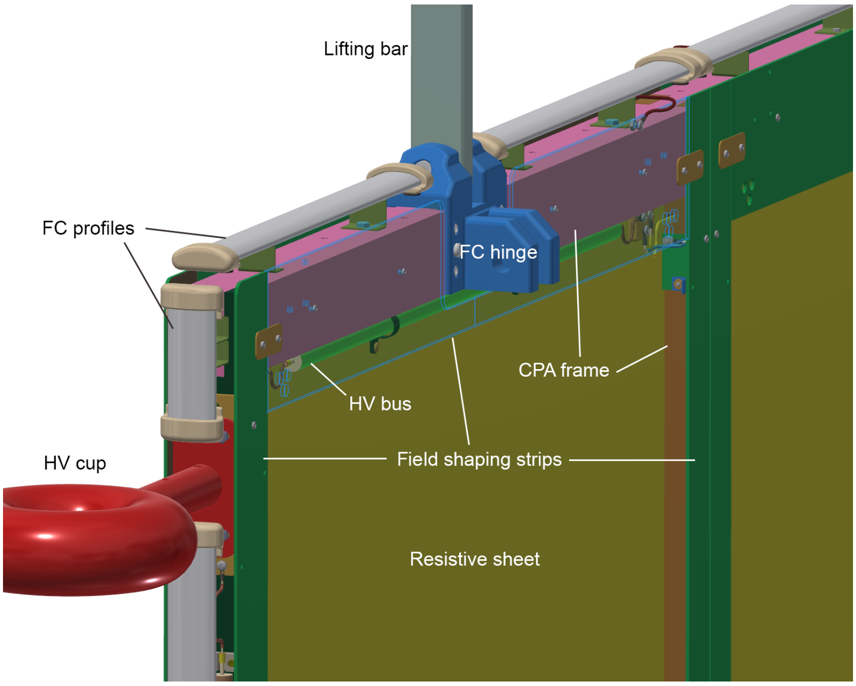

Figure 3.6: Close up of the downstream upper CPA edge. The drawing shows the CPA planes with the resistive sheet, framed by the CPA frames that hold the field shaping strips. The HV cup receives the bias voltage from the HV feedthrough and the FC profiles take care of limiting the field intensity below 30 kV/cm around the CPA edges. The lifting bar is made from insulating FR4 material hanging the structure from the Detector Support System (DSS) [40].

The two top and two bottom modules are hung onto two connected CPA arrays forming a sandwich build as shown in Figure 3.8. It hangs on movable trolleys from the clean room rail system shown in Figure 3.4. Three CPA-FC sandwiches are pushed into the cryostat through the TCO. The deployment of the top and bottom FCs is only done once all CPA + FC sandwiches and the FC end walls are inside the cryostat.

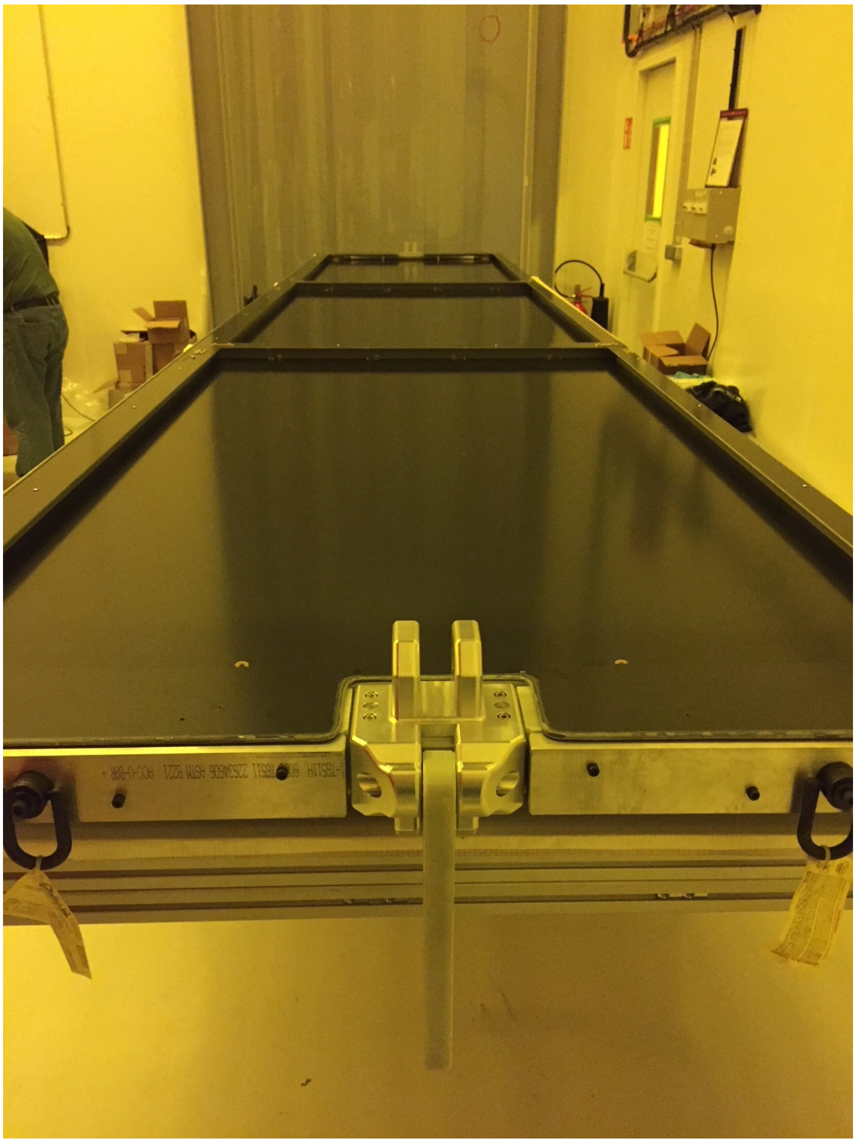

Figure 3.7: Three CPA modules completely built lying horizontally. They are bolted together to form one array spanning the full height of the CPA. Later in the construction process the array is lifted to hang vertically and connected to a second array to build a third of the full cathode plane. Two connected arrays build the structure to accept on each side of the array one top and one bottom FC module.

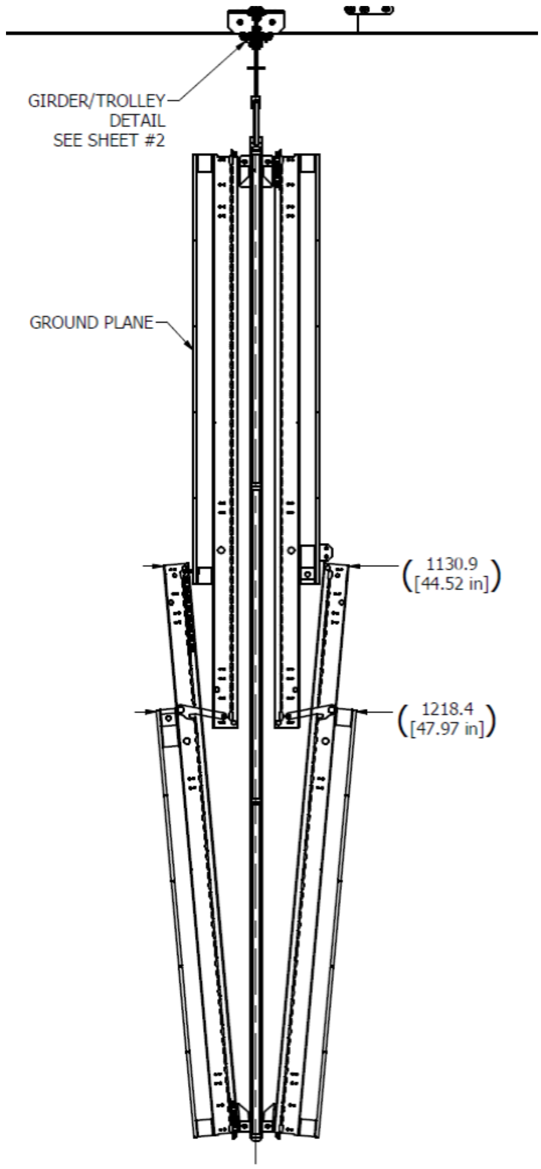

Figure 3.8: Drawing of two connected cathode plane arrays with two top and two bottom field cage assemblies attached. This cathode field cage sandwich hangs on trolleys from the rail system in the NP04 clean room. The field cage assemblies are mounted snug onto the cathode planes in order to facilitate pushing the build through the temporary cryostat opening into their final position [40].

Field Cage

The volume between the CPA and the APA is the electron drift region, as shown in Figure 3.5. The ionisation tracks are subject to the drift electric field transporting the electrons onto the APA wire planes. The drift distance, *i. e.* the distance between CPA and APA, is 3.6 m. The field cage (FC) takes care of closing the remaining open sides: top, bottom and the upstream and downstream side in the beam direction. Furthermore, a regularly graded voltage profile is provided as boundary condition for the uniform electric drift field. The FC structure is composed of:

- Six top FC modules 2.4 m wide and 3.6 m along the drift direction with ground planes
- Six bottom FC modules 2.4 m wide and 3.6 m along the drift direction with ground planes
- Two end wall planes made out of four end wall panels, each panel is composed of four stacked FC modules with 1.5 m in height and 3.5 m along the drift

The design principles are similar for all FC types:

- An insulating fibreglass-reinforced plastic (FRP) I-beam and box beam structure for the mechanical support of the FC. FRP has excellent mechanical strength at cryogenic temperatures and a low thermal expansion coefficient
- 57 aluminium profiles that are installed parallel to each other and held by the support structure
- Voltage divider boards composed of resistors interconnecting the parallel profiles facilitating the voltage gradient along the profiles
- Ground planes (GP) on the top and bottom FC shield the cryostat wall from the high field regions of the detector, hence preventing the occurence of discharges.
- Attachment fixtures for top and bottom FC to connect to CPA and APA
- One end wall module accommodates the beam plug

All FC modules are mechanically and electrically independent. This is another measure to limit detector damage in case of an electrical discharge as the stored energy is limited to the single FC module. Each FC module has its own voltage divider network, in consequence if a failure of a voltage divider board is present, field distortions would be limited to the concerned FC module.

Figure 3.9 shows a completed top/bottom FC module inside the NP04 clean room. The top and bottom FC design is more complicated as the modules are additionally equipped with Ground Plane (GP) panels. These panels are made out of perforated stainless steel sheets and run along the outside surface of top and bottom. The clearance between GP and the FC profiles is 20 cm and the GP are mounted onto the FC supporting FRP structure through FRP I-beams. As their name suggests, the GPs are electrically set to ground. They are necessary to limit high field regions extending into the gaseous LAr phase on top of the detector that contains grounded, sharp and conducting components, which could facilitate a breakdown if exposed to high field intensity. On the bottom FC the GPs are necessary to shield the cryogenic piping and cryostat floor from high field intensity.

Figure 3.9: A complete field cage module of the type top/bottom. The module is 2.4 m wide and 3.6 m in length along the drift direction. Each module holds 57 aluminium profiles in parallel which providing a regularly graded voltage profile from cathode to anode. The profiles face the inside of the active detector volume. The profiles are interconnected by voltage divider boards, the resulting voltage step from profile-to-profile is 3 kV. A module is electrically independent limiting detector damage in case of a discharge. Top and bottom field cage modules furthermore are equipped with the ground plane to prevent high electric field regions extending into the gas phase (top part of the detector) or to the cryogenic instrumentation (bottom).

The two end wall planes sit on two sides of the detector on the upstream side where the beam enters the active volume through the beam plug (BP), and on the downstream side opposed to the upstream side. They are marked in Figure 3.3 and Figure 3.5. They cover the full length (2.0×3.6 m) of the drift distance from

CPA to APA. Each end wall plane is made out of two end wall panels, one for each drift volume side.

One end wall panel is a stacked array of four end wall modules, as shown in Figure 3.10, the separation between the four modules is marked with white lines. The end wall module design drawing in Figure 3.11 shows the hanger plates out of G10 material on the top most end wall modules. These modules are simpler in design as the top and bottom modules because they come without the GPs. This is due to the fact that there is enough clearance between the end wall planes and the cryostat walls. A full end wall panel hangs from the hanger plates from the detector support system (DSS). Connecting plates are used to build the panel. They extend beyond the profiles and connect to the adjacent module through a shear pin and bolt arrangement. In the NP04 clean room the end walls were stored vertically on wheels to facilitate the building procedure that follows these steps:

1. Attach the top most end wall module (Figure 3.11) to an electric hoist
2. Lift the electric hoist to have enough clearance to proceed with the attachment of the second module
3. Lift the pair and proceed by attaching the third and fourth module in the same way

After completion of the end wall panel and ensuring its planarity, the full weight of the panel was transferred from the hoist onto trolleys on the rail system in order to move the completed plane into the cryostat vessel. There is one end wall that has a custom build as it was made to accommodate the beam plug (this will be described later on along with the BP).

Top, bottom and end wall FC modules make use of the same open extruded field shaping aluminium profiles. With the design, electric field intensity is minimised between the profiles and around their surface to maximally ~ 1.2 kV/cm, as shown in Figure 3.12. Each FC module has its own set of 57 profiles at a profile-to-profile distance of 6 cm. The profile length corresponds to the width of the modules. Both sides at the end of each profile have custom made UHMWPE (Ultra-High-Molecular-Weight Polyethylene) end caps shielding the sharp metallic ends. The caps withstand the full voltage across their thickness, preventing any possibility of breakdown in LAr. When finalising the FC modules and building the end wall panels it was very important to always visually examinate the FC profiles, as scratches in the aluminium could be sources of high electric field regions.

All FC module profiles are interconnected by a resistive divider chain providing a linear voltage gradient between cathode and anode planes. In order to maintain the detector drift electric field at 500 V/cm, the nominal voltage difference between

Figure 3.10: Complete field cage endwall panel made out of four modules [40].

two FC profiles spaced by 6 cm has to be 3 kV. The boards have resistive stages in series for each FC profile to provide the voltage difference. They consist of two 5 GΩ resistors in parallel. At each stage the circuit is protected by 3 varistors against HV discharge. Each divider chain draws about 1.2μA at the nominal field intensity setting. One resistive divider board is shown in Figure 3.13, covering 8 stages on a field cage module. On each FC module 7 divider boards were installed and the correct connection and voltage difference were controlled before and after installation.

HV Power Supply and Feedthrough

The cathode bias voltage is generated by a Power Supply (PS) of a brand Heinzinger (-300 kV, 0.5 mA) located outside of the cryostat vessel. A commercial HV rated cable and RC filters make the connection from the PS to the HV feedthrough (FT).

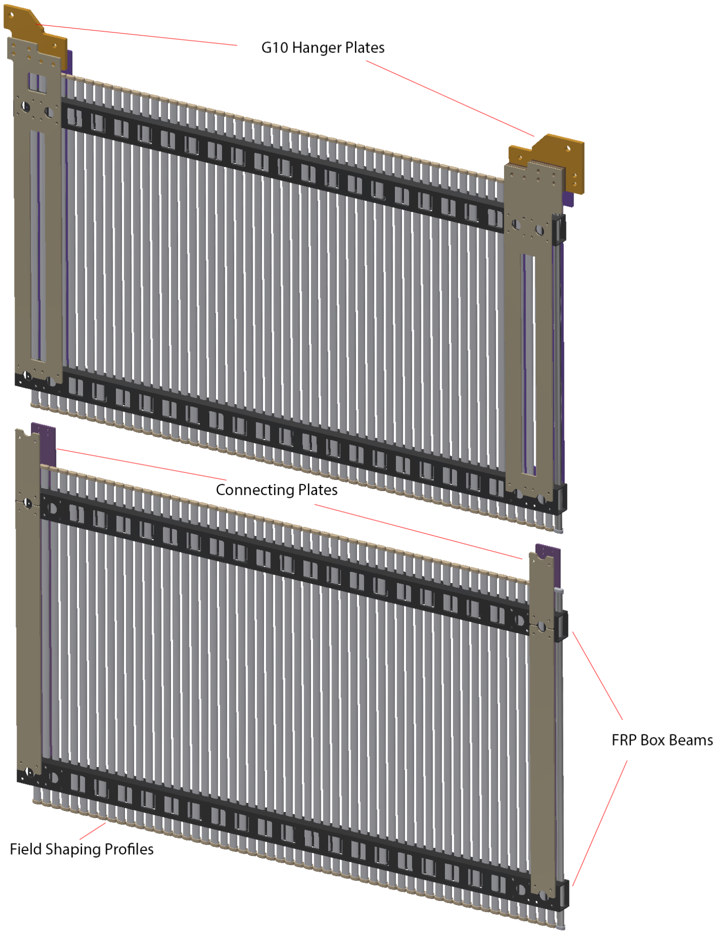

Figure 3.11: Top uppermost module of the endwall FC with hanger plates and regular end wall FC module below [40].

The FT builds the connecting tool from the HV cable into the cryostat and to the HV receptacle cup that is shown in Figure 3.6.

The FT design is based on the one presently used by the ICARUS experiment [50] adapted to ProtoDUNE-SP. It uses a cylindrical geometry and is shown in Figure 3.14 and is based on an inner stainless steel tube carrying the potential of -180 kV delivered by the PS. The tube is surrounded coaxially by ultra-high-molecular-weight polyethylene (UHMW PE) for insulation and followed by the outer conductor that is connected to ground. The outer conductor is made of a stainless-steel tube extending into the LAr in order to confine the electric field within the insulator.

In order to minimise the heat input inside the cryostat, the inner conductor was designed to be a tube instead of a rod. The tip of the FT is loaded with a spring and makes the connection to the receptacle cup that is mounted on the cathode (see Figure 3.6). Leak tightness at ultra high vacuum levels of the FT is required in

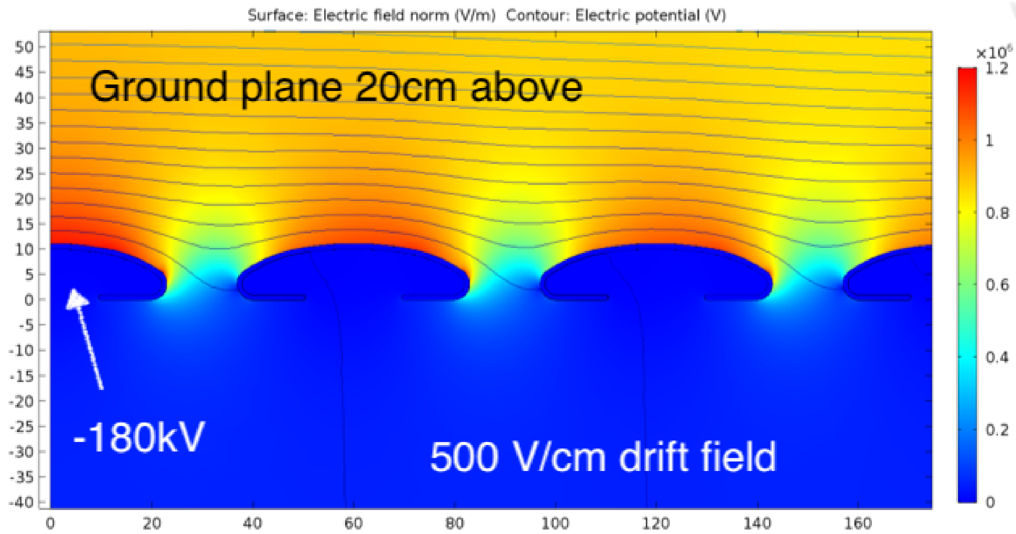

Figure 3.12: Electric field simulation around the extruded field shaping aluminium profiles used for the field cage modules. The maximum field intensity for spaces between the ground planes and profiles is around 1.2 kV/cm.

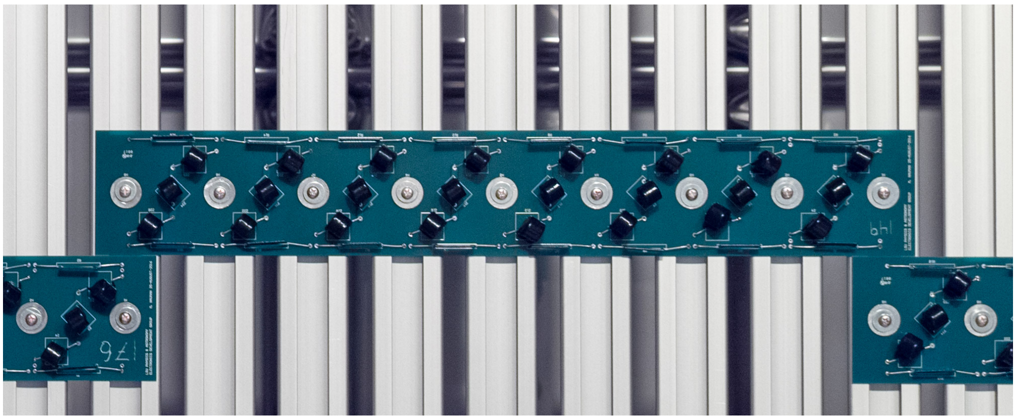

Figure 3.13: Voltage divider board mounted on the field cage modules. The resistive chain is equipped with two resistors in parallel per stage. Each stage of 6 cm between the profiles corresponds to a voltage difference of 3 kV. The black varistors protect the chain against high voltage discharge with a clamping voltage of 1.8 kV.

order to avoid any possibility of breakdown within the device. The full FT can be retrieved and replaced from the cryostat in case of issues. Before final installation the FT underwent various tests and was operated several days in a test stand with voltages up to 300 kV.

On the warm side the aforementioned RC filters that are connected to the HV cable and split the way in between the PS and the FT have two purposes:

- Reduce discharge impact by partitioning the stored energy of the system

- Act as a low-pass filter with the HV cable by reducing the 30 kHz voltage ripple on the output of the PS

The current can be monitored through the PS itself as it is able to read the current down to the nA level at a sampling frequency of about 3.3 Hz. For further monitoring purposes a toroid system was mounted on the HV cable, it is sensitive to fast changes in the current and the signal polarity indicates the location to be either upstream or downstream of the toroid. Other current monitoring devices are installed inside the cryostat:

- Pick-off points near the anode allow for precise monitoring of each voltage divider chain on the FC

- GPs are connected to a high-value resistor board that is sensitive in case of an emerging current path from FC to GP

As discussed, the full HV system of ProtoDUNE-SP is equipped with several monitoring devices that allow for precise observation and localisation in case of unexpected anomalies or discharges within the HV system.

Beam Plug

Between the beginning of the fiducial volume of the detector and the cryostat wall there are about 50 cm of LAr. If the beam hadrons were to travel through this argon volume before reaching the TPC, about 10% of their initial energy would lost prior to entering the active TPC volume. A substantial part would most likely already interact before the TPC and make precise cross-section measurements impossible. In order to bypass this inconvenience and warrant primary beam particle interactions to be recorded inside the fiducial volume, a beam plug (BP) was added to the ProtoDUNE-SP design.

The scope of this component is to provide a low density volume connecting the TPC fiducial volume with the cryostat membrane in the point where the test beam is directed to the warm side of the cryostat wall. The BP is a cylindrical device replacing the 50 cm of dense LAr volume with a dry nitrogen gas with a density three orders of magnitude lower. The design of the BP is quite complex as it requires a penetration of the FC but also should not compromise the operation of ProtoDUNE-SP. Before finalisation of the BP design it was crucial to thoroughly test its integration and omit any effect on the exact field configuration within ProtoDUNE-SP. The positions of the BP and the beam entry point are shown in Figure 3.2 and 3.5.

The BP is basically a cylindrical pressure vessel composed of glass fibre. It is about 50 cm in length and 22 cm in diameter, containing the nitrogen gas. It is

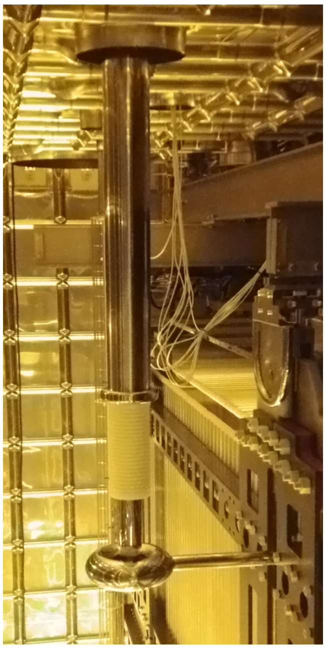

(a) Feedthrough in final position.

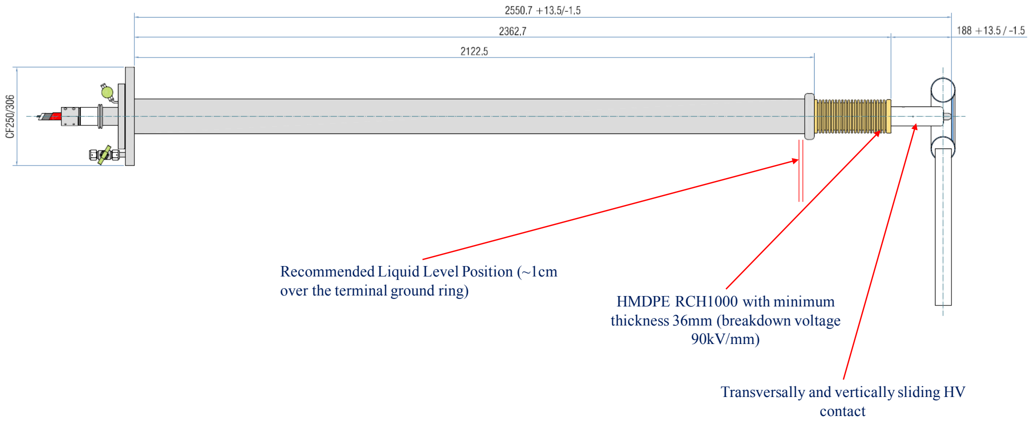

(b) Technical drawing.

Figure 3.14: The high voltage feedthrough is the interface between the power supply and the cathode of the TPC. It carries a potential of -180 kV. Top: Photograph of the high voltage feedthrough in its final position inside ProtoDUNE-SP. The receptacle cup that is connected to the cathode is well visible at the bottom of the picture. The outer conductor of the feedthrough (ground) comes through the cryostat roof. The feedthrough can be extracted from the cryostat after installation in case of issues [71]. Bottom: technical drawing of the high voltage feedthrough based on the ICARUS design [50].

connected through a nitrogen fill line to the top of the cryostat. On the outside a pressure release valve and burst disk are installed limiting the inside pressure to the specified safety level of the BP at 22 psi. Figure 3.15b shows how the beam plug is supported by the end wall FC it connects to. The front end of the BP extends into the fiducial volume by 5 cm. Figure 3.15a shows a detailed description of the BP components. The design consists of the fibre glass vessel which is collared by 7 voltage grading rings, connected in series with 3 parallel paths of resistor chains in order to overcome the potential difference of 165 kV between the first and last grading ring. The BP is electrically connected to the FC through the ring closest to the FC profiles, while the ring closest to the cryostat wall is grounded to the detector ground. The electrical design of the BP is made such to not interfere with the TPC electric field and induce any potential distortions.

3.3 CHARGE COLLECTION

The homogeneous electric field provided by the HV system (Section 3.2) drifts the ionisation charge created by the particles traversing the fiducial LAr volume to the anode plane. At the Anode Plane Assemblies (APAs) the drifted electrons are collected as a signal on the copper wires. As already described at the beginning of this chapter and visible in Figure 3.5, ProtoDUNE-SP is a detector with two drift volumes. The cathode sits in the middle of the field cage and two anode planes are placed parallel to the cathode on the boundaries of the field cage. Each of the two anode planes in ProtoDUNE-SP is composed of an array of three APAs that are 6.3 m high, 2.3 m wide and 0.12 m thick, thus the detector is equipped with six APAs in total. The sensing part of the APAs are 3 layers of wire planes wrapped around a frame of light rectangular stainless steel tubing. The signals are read out by the cold electronics boxes (CE) mounted on top of each APA. Each APA has 10 CE boxes reading out 2560 channels per APA. The CE is described later in Section 3.5.

Figure 3.16 shows a sketch of a ProtoDUNE-SP APA with the three sensing wire planes. The plane with an angle of $0°$ with respect to vertical is the collection (X-) plane coloured in blue on the sketch in Figure 3.16. The pitch of collection wires is of 4.79 mm and the X-plane has 960 wires per APA. The induction (U,V) planes are shown in magenta and green. They are at an angle of $35.7°$ with respect to vertical, a wire pitch of 4.67 mm and a total of 800 wires per plane. The sum of the wires per sensing plane results in the aforementioned total of 2560 channels per APA.

The location of signal hits and therefore a reliable reconstruction of the 2D projection of a particle track is retrieved by combining the induction and collection plane signals. The angle of U,V-plane with respect to the X-plane as well as the wire pitches are chosen such that an induction wire only crosses a collection wire once on the APA plane. By doing so ambiguities about the signal location on the

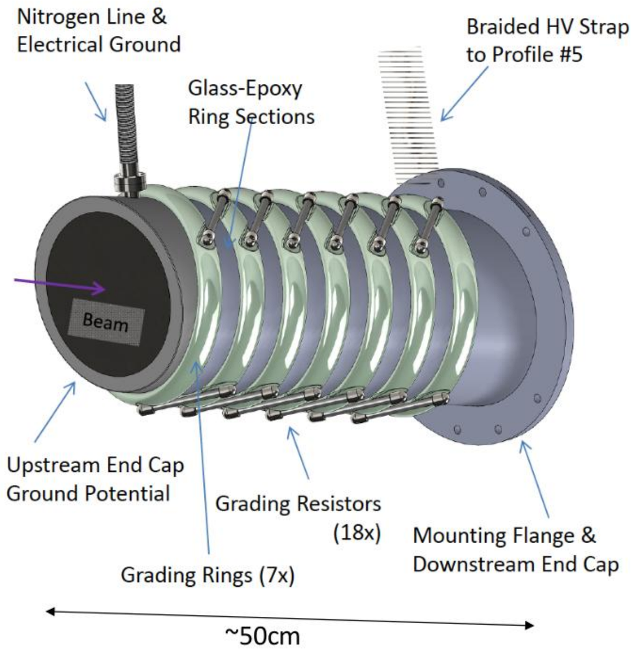

(a) Beam plug components.

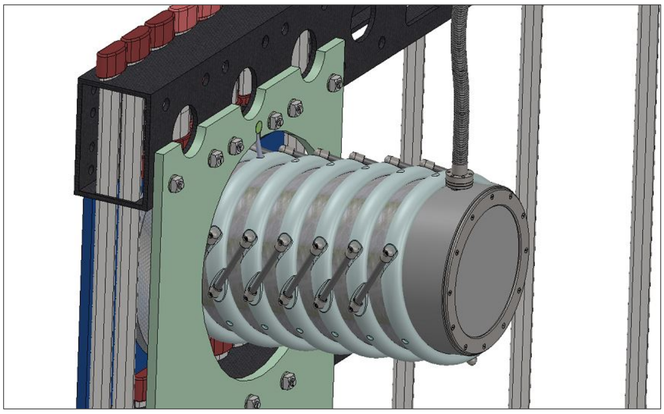

(b) Beam plug mounted to FC

Figure 3.15: The beam plug provides a low density (dry nitrogen gas) interface between the beam impinging point on the warm side of the cryostat and the active volume of the ProtoDUNE-SP detector, in order to minimise primary particle interactions before the TPC active volume. The beam plug is a cylindrical pressure vessel composed of fibre glass that is collared by voltage grading rings in order to maintain the homogeneous electric field. Figure 3.15a shows a detailed description of the beam plug with its components. Figure 3.15b shows the connection of the beam plug and to the field cage end wall.

wire plane are reduced, which allows to meet the required physics goals on the vertex resolution that need to be satisfied by the APA design, as listed in Table 3.2.

The three wire planes of the APA are operated at different voltages. The bias voltages are chosen in a way such that the U,V-planes are transparent to the drift

Figure 3.16: Left: Schematic of the APA with the three wire planes. Magenta and green represent the U,V (induction) wire planes. They are at an angle of 35.7° with respect to vertical and wrap around the structure of the APA. The X (collection) plane is drawn in blue and runs at an angle 0° with respect to vertical. The wire planes are biased in a way such that the U,V-planes record a bipolar signal and the X-plane records unipolar signals of the drift ionisation charge. Combining signals of the U,V and X-plane allows for reconstruction of a 2D projection of the ionisation tracks of particles inside the detector. The integral of the signals on the X-plane corresponds to the deposited charge. Right: Fotograph of an APA hanging in the clean room where the APA is prepared before insertion in the cryostat. Preparations include the mounting of the CE boxes and the cabling of those.

ionisation charge and the X-plane is opaque. In consequence, the signals from ionisation tracks on the U,V-planes are of a bipolar shape and unipolar at the X-plane. This also explains the common names of induction planes for U,V and collection plane for the X-plane. The integral of the unipolar signal on the X-plane corresponds to the amount of collected ionisation charge. The U and V planes are operated at -370 V and 0 V, respectively. The X-plane is operated at 820 V.

A reconstruction algorithm identifies clusters of wire signals that were produced by the same particle and stores them as 3D hits. Combining the hits to a track and measuring the amount of collected charge on every collection signal, allows for particle identification through track topology and energy deposition. Table 3.2 shows that the APA is required to deliver an energy resolution better than 5% for stopping hadrons.

SPECIFICATIONS	VALUE
MIP identification	100% efficiency
Charge reconstruction	$> 90\%$ efficiency for > 100 MeV particles
Vertex resolution (x, y, z)	1.5 cm, 1.5 cm, 1.5 cm
PARTICLE IDENTIFICATION (PID)	
Muon momentum resolution	$< 18\%$ for non-contained & $< 5\%$ for contained
Muon angular resolution	$< 1°$
Stopping hadron energy resolution	$1 - 5\%$
SHOWER IDENTIFICATION	
Electron efficiency	$> 90\%$
Photon mis-identification	$< 1\%$
Electron angular resolution	$< 1°$
Electron energy scale uncertainty	$< 5\%$

Table 3.2: Physics requirements that should be satisfied by the APA design [40, 69].

Every APA includes 10 slots within its frame that can accommodate the Photon Detection System (PDS) described in Section 3.4. A set of combs is installed on the APA at regular intervals ensuring the uniformity of the above mentioned track pitches for each wire plane. Otherwise the pitches could be deflected from gravity or electrostatic forces arising from the bias voltages. The combs are made out of insulating G10 with slots where the wires are supported. The APA wires are each tensioned at 5 N and held in place with no sag. It is essential for maximal performance of the charge readout as lose wires or snapped wires can influence reconstruction performance and plane transparency by distorting the field between the wire planes or causing short circuits if touching other wires. The contraction of the APA and subsequent further tensioning of the wires is considered within the chosen tensioning strength making sure that tension values do not exceed the manufacturer breaking value.

At the head of each APA the wires are grouped and terminated on wire boards that provide the connections to the CE boxes. They are immersed in the LAr and operate thus at cryogenic temperature, and provide signal processing. 20 CE boxes are placed on top of an APA in two arrays of ten boxes. Each CE box reads 128 wires, *i. e.* signal channels, of which 48 come from adjacent X-plane wires and 2×40

from U and V channels. Thus, the 20 CE boxes per APA cover the 2560 channels on the APA. Mounted CE boxes in their gray housing and the wire boards mounted on the APA are shown in Figure 3.17. The cables on the CE boxes are routed to the warm side through dedicated flanges.

Figure 3.17: Cold Electronics (CE) boxes installed on the head of the APA plane in order to read the wire signals in LAr. The wire boards (green) provide the connection from the APA wires to the CE boxes. 20 CE boxes are mounted on an APA, thus every CE box reads out 128 channels of the APA. The blue/white cables are routed through flanges to the warm side (outside) of the cryostat in order to transmit the signals to the data acquisition system.

Producing an electronic readout that works in liquid argon is challenging, although there are several advantages in processing the ionisation charge signals on the APA already at cryogenic temperature level and close to their generation, as low temperature minimises thermal electronic noise to the signal. Furthermore, placing the readout as close to the signal collection as possible reduces the capacitance and the connection length between wires and the electronics input.

One CE box takes care of 128 APA channels. The box acts like a Faraday cage and hosts a front-end motherboard (FEMB) onto which 8 ASIC chips with CMOS technology are mounted and shielded from noise. Thus, every ASIC chip serves 16 channels and the CE provide amplification, shaping, digitisation, buffering, and multiplexing.

The sampling rate of the CE is 2 MHz. The digitised signals are routed through highs peed data readout cable bundles (1 bundle per CE box), as shown in Figure 3.17, through flanges outside the cryostat to the warm side, where further processing is done at the Warm Interface Boards (WIBs). The cable bundles of the

20 CE boxes per APA are all routed outside through the same flange. The cables also serve the 20 FEMBs per APA with low-voltage power. Additionally, for every APA, the cables that provide the voltage for the wire bias and terminations for the FC are also routed through the flange. A schematic of the cable routing for one APA is shown in Figure 3.18.

On the warm side 5 WIBs receive the signals from one APA directly at the flange forming the interface to the DAQ system described in Section 3.5. One WIB is served with the signals coming from four FEMBs. The connection to the DAQ is provided by optical fibres that can transmit the data at a rate of up to 10.3125 Gbps.

APA Preparation and Tests in the Cold Box

The APAs are built at the Physical Science Laboratory of the University of Wisconsin, Madison and at the Daresbury Laboratory and packed in dedicated frames for shipping to CERN. The APAs arrived one by one at CERN and were extracted with a crane and turned by 90° into their vertical position. They are lowered and attached onto a series of rolling trolleys in the ProtoDUNE-SP clean room. A full inspection of each APA is done upon their arrival and placement in the clean room. This inspection includes an electrical integrity test, checking the wire tensions and a survey of the geometry in order to identify any damage caused by transportation.

The PDS (Section 3.4) bars are installed in the slots within the APA frame and mechanically attached to the frame. Every installed photon collector is tested immediately with the cables for signal routing. After the PDS installation, the CE is placed at the top of every APA frame. Installation requires two collaborators on an elevating platform at the height of the APA top. The CE boxes are connected to the matching electrical connectors on the FEMBs and mechanically fastened. Several tests of the installed CE boxes are performed at room temperature for noise and channel response. The cables connecting to the CE boxes are cut to length, bundled and attached to dedicated cable trays, as shown in Figure 3.17. Before insertion of the APA in the cryostat the APA and CE boxes are tested in cold with a dedicated cold box.

A dedicated large cold box was built in the clean room of ProtoDUNE-SP. The cold box is light tight and electrically isolated from its environment. It can accommodate an APA with the installed CE boxes and PDS in order to perform warm tests and the final cold test before inserting the APA in the cryostat. The tests asses functionality and electronic noise. The cold tests are performed during 48 h at roughly 150 K using cold nitrogen gas for cool-down.

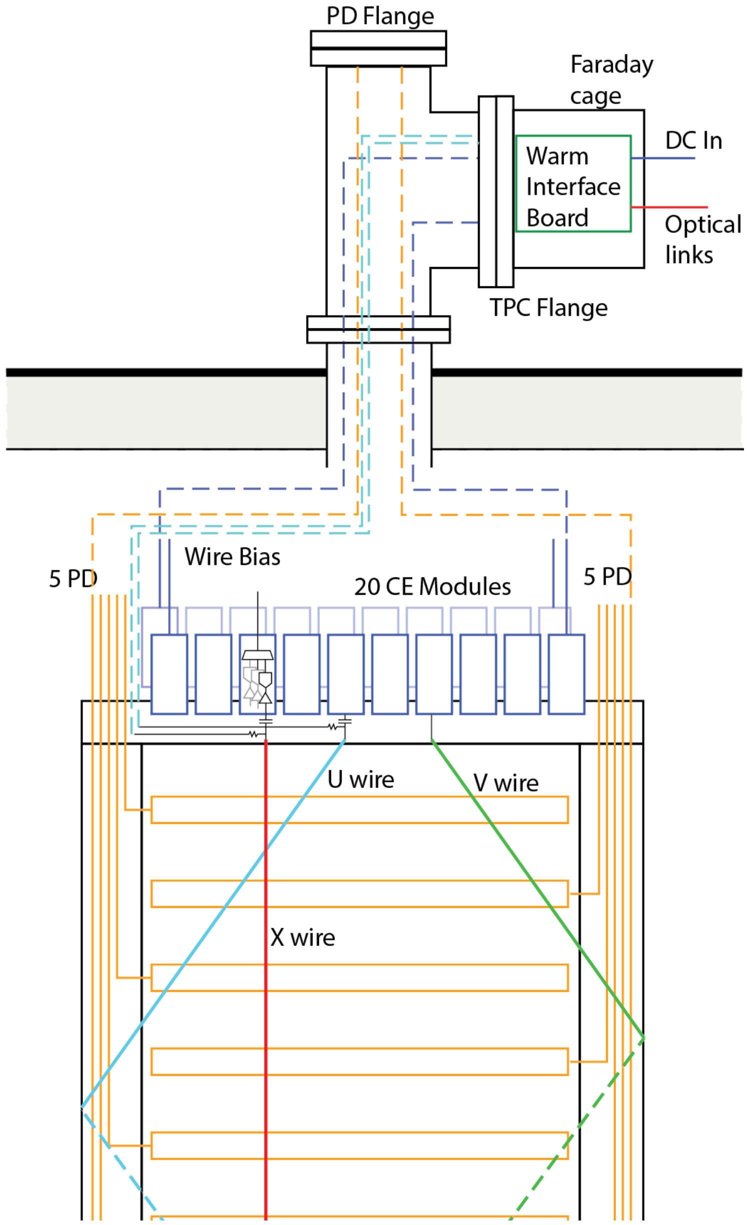

Figure 3.18: Schematic showing the readout and power cabling of an APA and the photon detection system. Signals coming from the wire planes (2560 channels) are amplified, shaped, digitised, buffered and multiplexed in the Cold Electronics (CE) modules. As their name suggest they operate in cold, *i. e.* the liquid argon. The CE modules connect through cables to the warm side of the cryostat (top of the schematic) and signals are streamed to five Warm Interface Boards (WIBs) through cable bundles - one for every CE module. The WIBs build the interface to the DAQ system through optical links.

3.4 LIGHT DETECTION SYSTEM

For each drift ionisation track the wire planes of a LArTPC are capable of producing a 2D projection. The third component required to produce a 3D image is

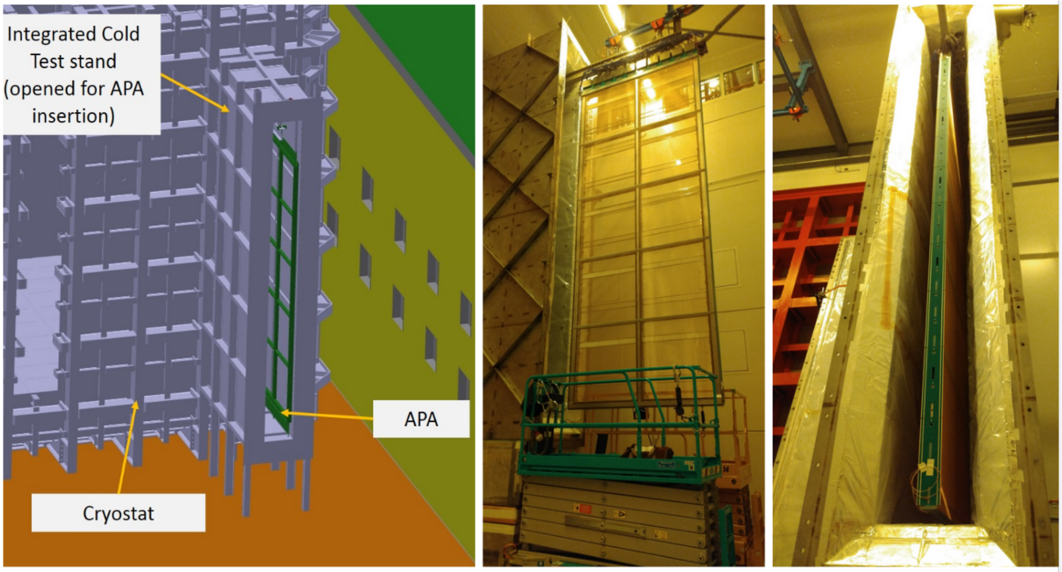

Figure 3.19: Photos and 3D model of the cold box facility inside the ProtoDUNE-SP clean room. The cold box is used to perform warm and cold tests of a fully instrumented APA with the PDS system and the installed cold electronics. The cold box is electrically isolated and light tight. The Equivalent Noise Charge (ENC) is measured in warm (room temperature) and cold temperature at differen gain settings for every APA [72]. Left: CAD model of the cold box. Middle: APA before insertion in the cold box. Right: Inserted APA before closing the cold box and testing.

timing. The wire plane signals alone do not give any information on where the interaction occurred within the LArTPC drift volume as drift times are up to $\mathcal{O}(\text{ms})$. A prompt timing signal (t_0) is then necessary. In ProtoDUNE-SP a timing signal is provided by the beam and also by the position of the beam entry point. However, for DUNE this will not be the case when locating interactions of neutrinos from supernova bursts or potential nucleon decays. For such events one can exhibit the scintillation light signals that were described in Section 2.2. In order to bench mark the performance of current PDS solutions and find a suitable system in view of DUNE, a prototype system has been deployed in.

In DUNE a PDS must provide large acceptance for light throughout the full detector volume and a timing resolution of mm-scale in order to located the drift ionisation charge precisely within the LArTPC. Furthermore, the PDS must be integrated in the detector respecting the design constraints and not disturb the operation of other detector components. It is desirable to keep the costs low, while maximising the light readout efficiency. A minimum photon yield of 0.5 PE/MeV at a maximum drift distance of 3.6 m and a minimum timing resolution of 100 ns are required for the physics goals of DUNE.

In ProtoDUNE-SP the PDS is located as mentioned in Section 3.3 inside the APA wire planes. Each APA can accommodate 10 PDS modules regularly spaced out in the vertical dimension, making up for a total of 60 PDS modules for the full detector. Within ProtoDUNE-SP three different PDS prototype module designs have been tested:

- 29 double-shift light guides
- 29 dip-coated light guides
- 2 ARAPUCA light traps

The three options of a photon collector and a photo sensor. The shape and mounting system of the photon collector for the three designs is the same, with dimensions of 2.3 cm$\times$11.8 cm$\times$209.7 cm. The modules are inserted through slots in the APA frame, as shown in Figures 3.16 and 3.18. In total the PDS covers up to 12.5% of the APA surface. The signals from the PDS are routed as shown in Figure 3.18 and directly synchronised and interfaced with the DAQ. Calibration is provided by UV LEDs that are placed on the CPA within the detector.

A charged particle traversing the LAr produces scintillation photons in the VUV spectrum at a wavelength of 128 nm. Commercially available silicon photon sensors (SiPM) reach acceptable light yield at around 400 nm wavelength. They are commonly used in the LArTPC technology. In order to match the SiPM sensitivity the photon collectors of the PDS need to reliably and efficiently perform wavelength-shifting (WLS) and act as light guides. WLS is performed by utilising chemical coatings that absorb high frequency photons and emit lower frequency photons. The three above mentioned light detectors perform WLS with three different techniques.

Dip-coated Wavelength-shifting Light Guide Photon Collector

A diamond-polished acrylic is used acting as the light guide of the system. It is dipped in a solution of tetraphenyl-butadiene (TPB)[73] and other solvants in order to attach a WLS coating on the acrylic light guide. TPB is the WLS chemical emitting the collected scintillation light of 128 nm at 430 nm. The blue light is guided through total reflection inside the acrylic light guide to the SiPMs that are mounted and readout at the end of the PDS modules.

The application of the WLS coating is done through dipping the acrylic light guide bar in a solution with ratios of 50 ml toluene, 12 ml ethanol and 0.1 g acrylic pellets. The toluene includes the wavelength-shifting TPB. Ethanol is added to slightly dissolve the surface of the acrylic light guide in order for the coating to better attach to the acrylic bar and acrylic pellets are added in order to match the coating index of refraction with the one of the bar (1.49) [74]. The dipping is performed mechanically using a dipping vessel for standardised and automated production. After dipping the bars are hung to dry for 30 minutes. The drying process is sensitive to humidity of the environment.

Uniform coating and quality is a challenge for this technique as the drying process is not immediate and thus can vary along the bar because of the hanging position. It is hard to measure the coating uniformity. Quality control is done by observing the attenuation of 200 nm light at room and LAr temperature. TPB coatings are sensitive to ambient light, more precisely the blue component of the spectrum which contributes to quality loss of the WLS property of the coating. Storage needs to be done in dry and dark or blue light filtered environment. Figure 3.20 shows a schematic of a dip-coated WLS light guide.

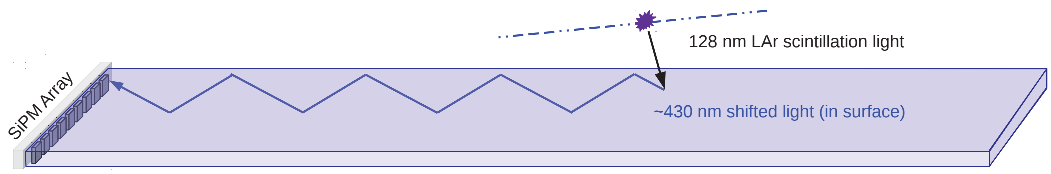

Figure 3.20: Dip-coated wavelength-shifting light guide. The acrylic light guide bar is coated with a solution of tetraphenyl-butadiene (TPB) acting as a wavelength-shifter. The scintillation photons of LAr with a VUV wavelength of 128 nm are absorbed in the (TPB) and emitted at a lower frequency, *i. e.* with a wavelength in the blue light spectrum of 430 nm. The blue light signals are collected by SiPM arrays at the end of the light guide [40].

Double-shift Wavelength-shifting Light Guide Photon Collector

As the name suggests, the double-shift WLS combines two stages of WLS. The first utilises, like the dip-coated WLS, a coating of TPB that takes care of the shifting from 128→430 nm. Another WLS is performed by the light guiding bar itself shifting the blue light from 430→490 nm in the green spectrum. The concept is shown in Figure 3.21. The double coated WLS benefit from increased signal efficiency of the SiPMs at 490 nm. The first WLS step is performed in plates that are placed on top of the WLS bar responsible for the second step. The TPB coated plates are done by hand and the WLS bars are made from Eljen EJ-280PSM cross linked polystyrene cut to fit the dimensions of the PDS module slots in the APAs.

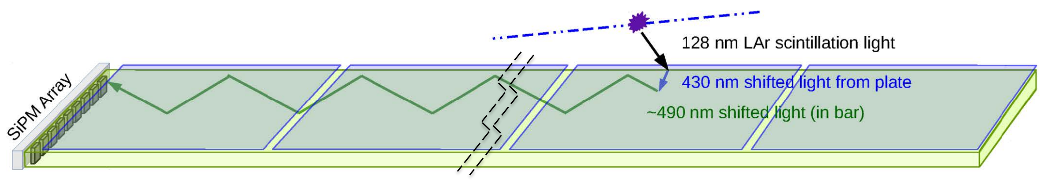

Figure 3.21: Double-shift wavelength-shifting light guide. The scintillation light from LAr is shifted in two steps from 128 nm VUV to blue at 430 nm and through WLS bars made out of cross linked polystyrene to 490 nm in the green light spectrum [40].

ARAPUCA Light Trap

The ARAPUCA [75] PDS prototypes follow a slightly different concept than the two aforementioned PDS options. The aim is to trap incident photons inside a highly reflective chamber until a sensor is reached. As opposed to the light guide designs, the ARAPUCA is segmented longitudinally into 12 cells per bar. The surface coverage for ARAPUCAs is smaller with respect to the dip-coated and double-shift WLS systems. However, it profits from a high detection efficiency. The chambers have a highly reflective surface and acceptance of light is unidirectional with a dichroic optical filter. The filter is placed between layers of WLS materials. The photon trap is built by coating the external face of the filter with a WLS emitting at a wavelength smaller than the cut-off wavelength of the filter. Photons passing through the first layer encounter a second WLS surface with an emission spectrum exceeding the cutoff wavelength thus the photons are trapped in the box below and reflect off the inner walls until they reach a sensor or are absorbed.

The SiPM sensors for the ARAPUCA are placed below the boxes and have a larger ratio of sensors with respect to the optical surface than the light guides. The probability of reaching a sensor before absorption in the chamber is very high. The cut-off wavelength of the dichroic filter is at 400 nm. The ARAPUCA concept and detailed view of the bar is shown in Figure 3.22. As opposed to the dip-coated and double-shifting WLS light guides, the ARAPUCA light trap includes SiPM arrays along the length of the bar and not its end.

Photon Sensors

Three different commercial photo sensors (SiPM) with an active area of $6/times6$ mm^2 were used:

- SensL Technologies, MicroFC-60035-SMT sensors with a pixel size of 35 μm of the A-Series and C-Series. Most of the WLS light guides were equipped with these two serie types of SiPMs

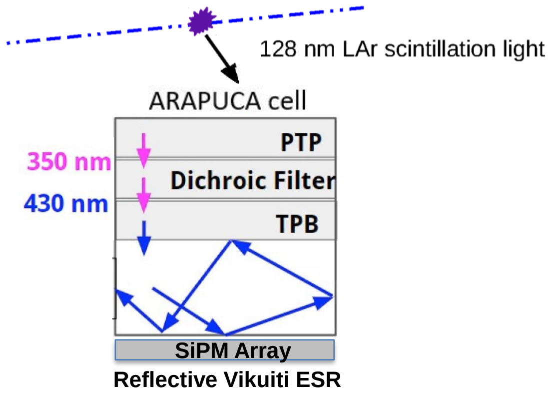

(a) ARAPUCA principle

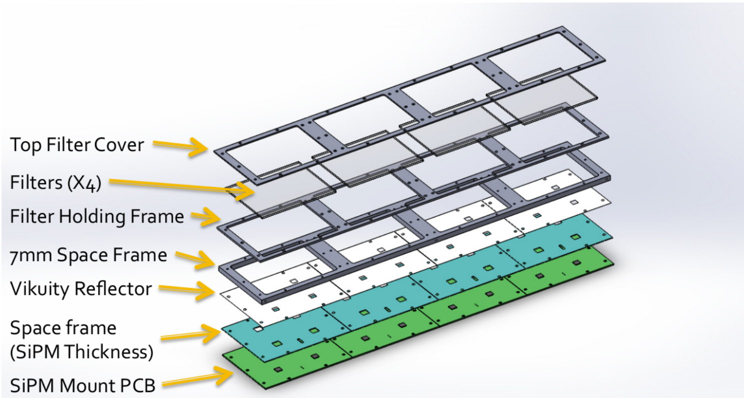

(b) Exploded view of an ARAPUCA module

Figure 3.22: The concept of ARAPUCA photon collection system. The VUV scintillation light in LAr is trapped by ARAPUCA cells using a dichroic filter placed between WLS materials creating o unidirectional acceptance of the light. The photons are trapped in a box with highly reflective inner walls, eventually they are absorbed by SiPMs placed at the bottom of the box. The probability of hitting a sensor is higher than the probability of photon absorption within the box, thus high signal efficiency is guaranteed. The exploded view on the right shows how the ARAPUCA cells are built. The cells are independent [75].

- Hamamatsu Photonics Multi-Pixel Photon Counter (MPPC) S13360-6050 with a quartz window (CQ) aimed to resist better thermal stress. All ARAPUCA cells are equipped with CQ MPPC
- Hamamatsu Photonics MPPC with through silicon via type (VE) have been used on several dip-coated and double-shift light guide desings

The performance of the PDS is fully characterised in [72]. The photo sensors installed on the ARAPUCA modules showed a signal-to-noise-ratio (SNR) of values around 6 while for the other SiPM sensors on the double-shift and dip-coated modules the SNR was better with a range of 10 to 12. The ARAPUCA cells are measured to have a photon detection efficiency of about 2% for a single area cell. 0.21% and 0.08% detection efficiency were measured for the the double-shift and dip-coated modules, respectively. If the full PDS system were to be equipped with ARAPUCA modules a light yield of 1.9 PE/MeV at 3.3 m from the anode is extrapolated exceeding the aforementioned DUNE requirements (0.5 PE/MeV at a drift distance of 3.6m) by almost a factor of four.

3.5 READOUT AND DATA ACQUISITION

In the previous sections the main detector components have been introduced individually. The TPC and PDS record the deposited ionisation charge and scintillation light inside ProtoDUNE-SP in order to produce 3D images of the impinging beam particles and cosmic rays. The whole data stream is managed from the Data Acquisition System (DAQ). The DAQ is responsible for collecting all the data from the sub detectors and includes the essential triggering system. When the DAQ is triggered, an associated time stamp t_0 is produced for every event and data is recorded during a time window of 3 ms corresponding to the drift time. The DAQ provides compression and organisation of the recorded data to files. The data files are locally stored and further transferred to permanent storage at CERN or FNAL. Within the DAQ system electronics configuration parameters, the run control and real time monitoring of data quality and DAQ performance are available.

The information on the ionisation charge coming from the APA dominates the data stream with 430 Gb/s. 30 WIBs are located on top of the cryostat, as shown in Figure 3.18. They collect the data of the six APAs inside the detector.

ProtoDUNE-SP was used as a test stand for two DAQ readout systems for the data coming from the APAs. The RCE (Reconfigurable Cluster Elements) an ATCA-based solution [76] and FELIX (Front-End LInk eXchange) a PCIe-based solution [77]. The RCE system is able to compress and buffer the raw data, sustaining a data rate of 1 Gb/s per RCE and a compressing factor of four. FELIX was designed to rely on commodity servers, networking and software in order to minimise customised hardware and firmware development. The FELIX PCIe card streams data to a PC through a continuous direct memory access transfer. After this step all the data process can be done by software on networked servers. FELIX bears the advantage of being a modular and flexible readout system. It is software based and therefore, allows even for basic on line hit finding and self-triggering which is essential for nucleon decay events and supernova bursts. During the two years of ProtoDUNE-SP data taking the full DAQ was switched to the FELIX solution. The system has been chosen as the baseline for the DUNE DAQ readout.

When an event is recorded, the DAQ is triggered at a t_0 and TPC data is readout taking 6000 consecutive samples of the ADC wire signals that are digitised in the CE at a rate of 2MHz in the cold. A readout window is in total 3 ms of time. The consecutive samples are spaced out with 500 ns and each sample ADC is called a "tick". The 3 ms window is wrapped around t_0 in a way such, that data from 250 μs before t_0 is recorded. This is put inplace to collect deposited charge from particles that "passed through" the detector earlier but the arrival of their charge falls into the trigger window. The coincident data from the PDS is saved as well. One event typically has a compressed size of 60 MB and the DAQ was able to stably sustain a trigger rate of 40 Hz. Studies of these "high-rate" trigger runs are shown in Chapter 4. During the beam period the trigger rate was about 1 Hz.

3.6 CRYOSTAT AND CRYOGENIC SYSTEM

The 700 t of LAr at a temperature between 86.2 K and 88.2 K and absolute pressure in the range of 970–1100 mbar, as well as the full ProtoDUNE-SP detector reside in the cryostat vessel. The cryostat acts like a fridge and insulates its inside from the environmental temperature in order to prevent the LAr from boiling off (normal boiling point at 87.303 K). The cryostat design is based on the commercial membrane technology that is used for storage and transport on tanker ships of liquefied natural gas. Its outer dimensions are 11.4 m$\times$11.4 m$\times$10.8 m (width, length, height). It is composed of an outer warm steel structure, a set of insulating layers and the cold inner membrane. The dimensions of the inner cryostat are 8.5 m$\times$8.5 m$\times$7.9 m.

The cryogenic system is responsible for initially filling the cryostat with LAr. Furthermore, it provides a LAr recirculation circuit where liquid is pumped out of the cryostat and purified in dedicated filters in the gas phase. It is re-liquefied by means of a separate cooling circuit using liquid nitrogen (LN) and fed-back into the cryostat. The connection of the cryostat to the cryogenic system is made through a set of dedicated penetrations.

Cryostat Structure

The mechanical support is provided through a steel structure composed of vertical beams alternating with a web of metal frames. The steel modules are prefabricated and come in three configurations:

- Standard modules that are used to construct the walls and floors
- Corner elements

- Web interlinks interconnecting the modules

The steel structure is also referred to as the warm vessel, as it is in contact with the "warm" ambient temperature of the detector hall. During detector construction the front wall of the cryostat was open through a wall section that was separately closed and sealed with the corresponding steel and insulation elements after finalisation of the ProtoDUNE-SP detector inside the cryostat. The opening is the so-called "Temporary Construction Opening" (TCO) with 7.3 m in height and 1.2 m in width.

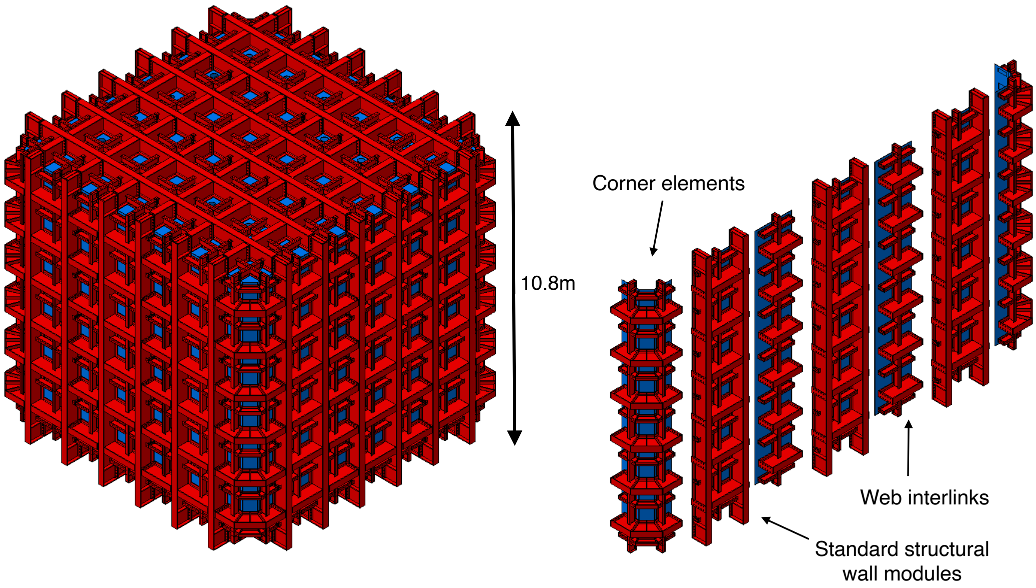

Figure 3.23: Three main structure components of the ProtoDUNE-SP cryostat. The outer dimensions are 11.4 m×11.4 m×10.8 m (width, length, height) [40].

Cryostat Inner Vessel

The 80 cm thick inner vessel is supported by the outer steel structure and is based on the membrane technology developed by GTT (Gaztransport & Technigaz [78]). The outermost layer, is a 10 mm thick stainless steel membrane referred to as the tertiary membrane providing an airtight barrier. This allows to flush the insulation volume with nitrogen gas preventing condensation and humidity in the insulation layer. The insulation layer is built in a sandwiched way: Two thick layers of foam from expanded polyurethane are separated by sets of plywood and a tight membrane acting as a containment layer, the GTT-proprietary Triplex.

The innermost part of the inner vessel, *i. e.* the primary membrane is made out of 1.2 mm thick stainless steel. It is the membrane in contact to the LAr and has a very characteristic configuration of special corrugations. The primary membrane acts like a balloon expanding and shrinking in a way such, that the cube like inner vessel is not under stress and strains causing damage to the sealed membrane. The membrane was delivered in multiple pieces which are then welded together at high precision and with the requirement to be airtight. Leak tests on the welding lines of the membrane are described further down in the section. An exploded view of the inner vessel structure is schown in Figure 3.24a and a photograph of the empty cryostat with the inner membrane and its typical corrugations is shown in Figure 3.24b. The average heat leak of the cryostat is of 8 W/m^2.

Penetrations in the Cryostat

A set of penetrations in the cryostat is necessary in order to power and extract the signals from detector components, operate several sub detectors for monitoring and safety devices, as well as ensure the LAr recirculation and purification of the full volume. Most of the penetrations (55) can be found on the roof of the cryostat, such as the flanges to route the LArTPC signals to the DAQ (Figure 3.18), safety valves, the high voltage feedthrough flange, monitoring system penetrations like cameras, and various sensors for pressure and temperature. Other penetrations are used for the detector support system and two manholes. The recirculation circuit extracts the LAr from a very low point on one of the cryostat side walls with LAr pumps. Extraction of LAr for purification from the bottom part of the cryostat is done in order to full fill the stringent requirement on a high LAr purity throughout the whole detector volume.

Another special penetration in the ProtoDUNE-SP cryostat is done at the charged particle beam entry point, the beam window. It is built to minimise the energy loss and scattering for beam particles and is adjacent to the beam plug described in Section 3.2. At the beam window the tertiary membrane (Figure 3.24a) is perforated and replaced by a 175 μm thick Mylar foil. The insulation foam is replaced by a lower density foam and the plywood is exchanged for a structure of a G10 and honey comb polymer sandwich. The polymer is Nomex and has a very high thermal and structural resistance. In total the beam window material is equivalent to 10% of a radiation length with 0.3 mm of G10 thickness and 0.3 mm of steel.

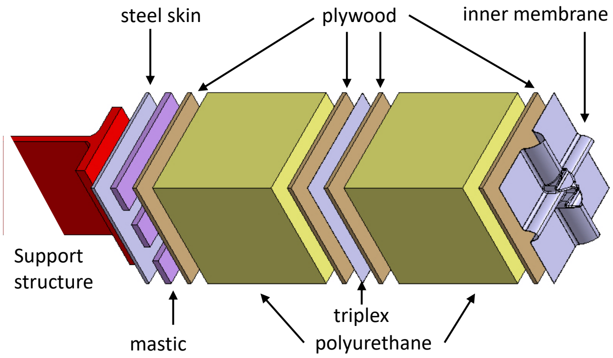

(a) Cross-section Inner Vessel [40]

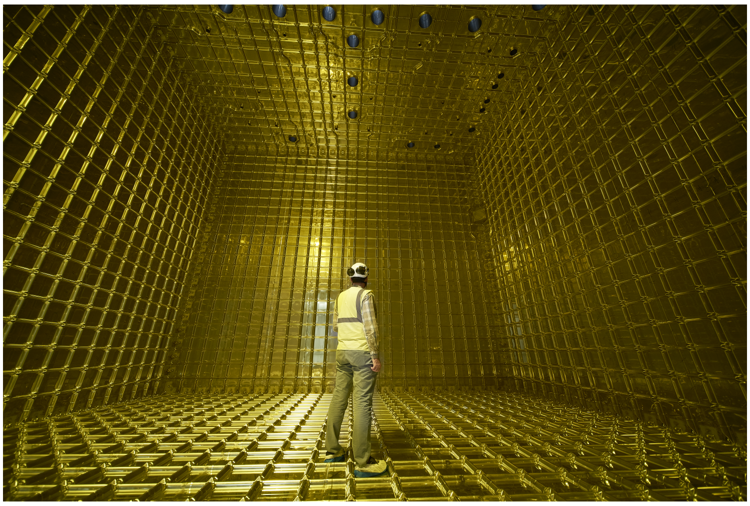

(b) Photograph of empty cryostat

Figure 3.24: A detailed break up of the inner vessel of the ProtoDUNE-SP cryostat. The space between the steel skin and the inner membrane is airtight. The outer polyurethane foam layer is flushed with nitrogen gas in order to prevent humidity and condensation inside the insulation layer. The photograph shows the inner membrane of the cryostat with the GTT-proprietary corrugations allowing the cryostat to expand and shrink without causing stress and damage on the inner membrane. The membrane is not golden as it appears on the picture, the yellow lightning comes from the fact the lightning inside the cryostat is filtered for its blue component in order to not damage the PDS system.

Assembly and Leak Tests

The installation of the ProtoDUNE-SP warm structure totalled 12 weeks and was carried out in the pit at the EHN1 hall in the CERN north area. The cryostat is built on a surveyed planar surface onto G10 strips providing seismic protection and electrical isolation. The walls are assembled flat individually, checked for planarity and then lifted into position by means of a crane and temporarily stabilised. The tertiary stainless steel membrane is welded and checked for leaks on every wall.

After the wall placement the corners are installed and the roof is put in place. The construction of the warm vessel is shown in Figure 3.25.

Upon finalisation of the welds of the tertiary membrane the inner vessel is installed. Precut insulation layer sections are lined from the inside onto the tertiary membrane as shown in Figure 3.24a. Voids in the inner vessel are filled in order to minimise circulation paths, *i.e.* thermal conduction. The primary membrane is installed as the last component piece by piece. The edges are connected by high precision welds subsequently tested for leak tightness.

Leak tests were performed on the tertiary stainless steel membrane and more thoroughly on the primary membrane. The tests are carried out on the welding seams of the membrane. A first global leak examination was carried out by the vendor, after flushing the insulation with N_2 gas it was evacuated down to 550 mbar and filled with helium until the pressure in the insulation matched the outside pressure. At two test holes in the primary membrane the helium presence was checked occasionally. A few minor leaks were found and repaired.

A second leak test campaign was carried out by collaborators of the experiment and members of the construction team, including myself. I participated in developing an optimised procedure of leak testing the welding seams section by section. The procedure foresees dedicated testing by pulling vacuum on a suction cup placed over the welding seams of the primary membrane, as shown in Figure 3.26. It tests the leak rate from the helium flushed insulation atmosphere on the other side of the welding seam. Several suction cups / vacuum boxes were produced in order to account for the various shapes of the primary membrane where the welding seams run. The welding seams run over flat parts, corners, and corrugations of different size.

The suction cups accommodate a silicon gasket that provides a tight contact to the primary membrane. Furthermore, they posses a connection that is attached to a vacuum pump and helium leak tester. The set-up for leak checking is shown in Figure 3.26. The procedure of leak checking with the suction cups is as follows:

1. Place the suction cup and silicon gasket appropriately on the membrane above the welded seam

2. Apply uniform pressure on the cup and evacuate it with the vacuum pump

3. Wait for a 10^{-3} mbar vacuum

4. Turn on the helium detector and check for helium leaking from the insulation through the weld down to 10^{-8} $\mathrm{L}\times\mathrm{mbar}\times\mathrm{s}^{-1}$

5. Continue the same procedure on the next welded section

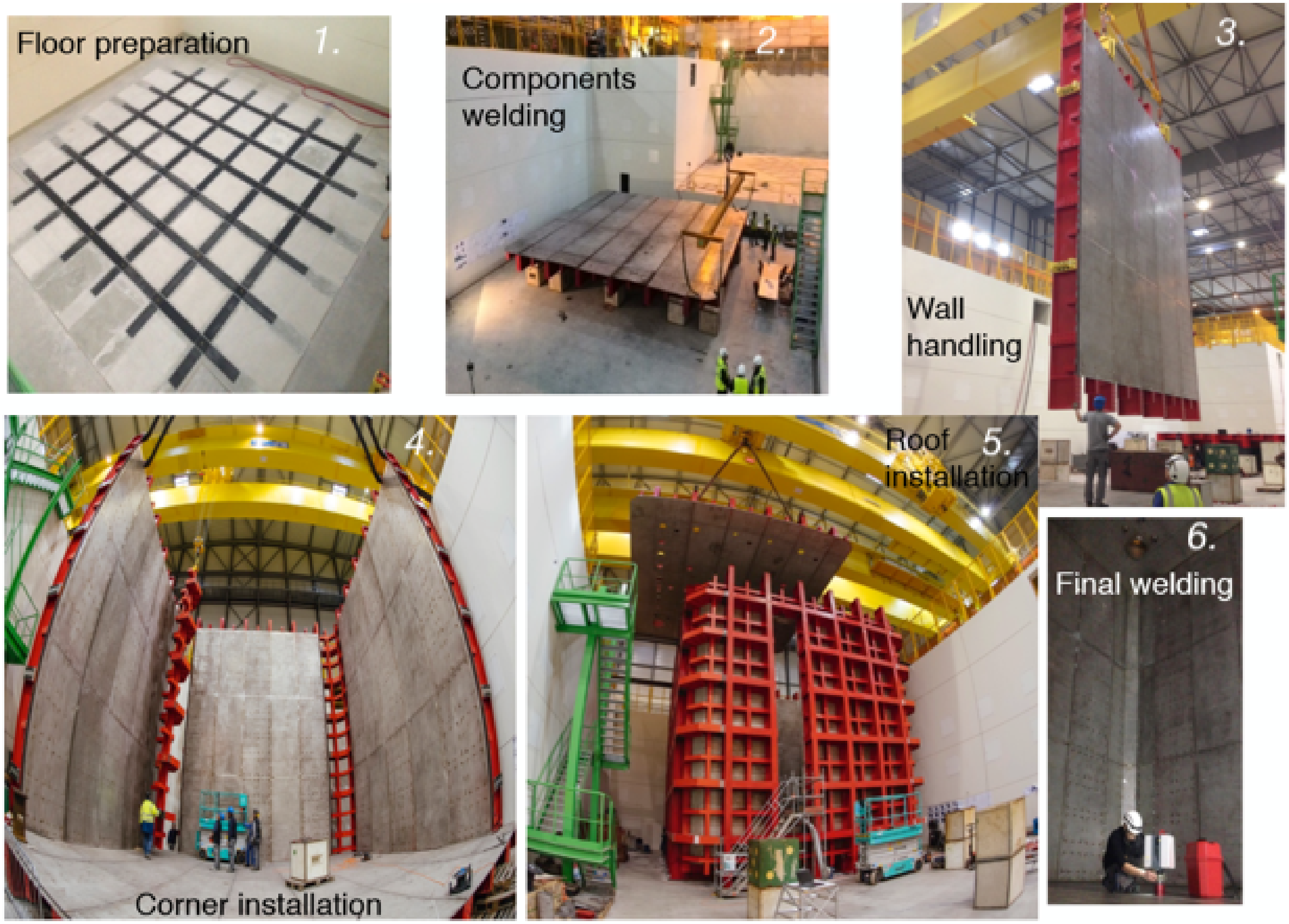

Figure 3.25: Photographs illustrating the assembly of the cryostat warm structure. The cryostat floor is placed on G10 in order to provide protection from seismic activity and electric insulation of ProtoDUNE-SP. The cryostat walls are assembled on flat and put in place with cranes and temporarily stabilised. The corners are installed after the side walls and replace the stabilisers. Finally the roof is of the cryostat is placed on top of the side walls and corners. The last parts of the stainless steel tertiary membrane are welded and checked for leaks [40].

A suction cup can take care of about 20 cm of welding seam. With this method about 80% of the welds on the primary membrane of ProtoDUNE-SP were tested over several weeks. No leaks larger than 10^{-8} L$\times$mbar$\times$s^{-1} were found, therefore the vendors testing procedure can be trusted and there is no need to perform the testing again within a DUNE-scale cryostat (which would require months!).

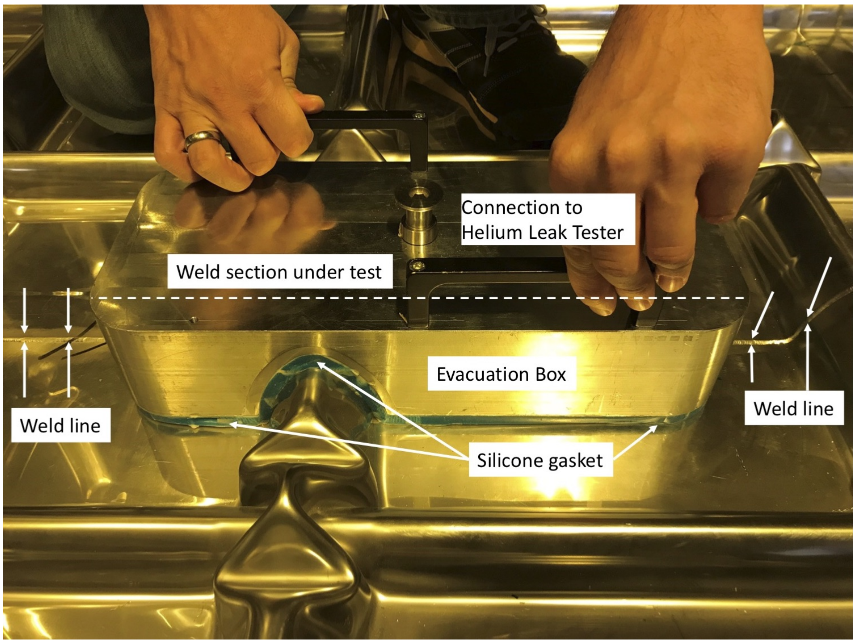

Figure 3.26: Detailed view of a custom made suction cup for leak checks on the welded sections of the primary membrane of ProtoDUNE-SP. The silicon gasket allows for placing the cup on the primary membrane and producing a vacuum inside the membrane. Behind the primary membrane is the helium flushed insulation, attaching a helium detector on the suction cup allows for checking whether the weld is tight and no helium is coming through. If helium is detected the weld presents a leak and would need repair. No leaks larger than 10^{-8} L$\times$mbar$\times$s^{-1} were found after having tested 80% of the welded seams in ProtoDUNE-SP [40].

Cryogenic Circuit, Cooling and Purification

The cryogenic system is fundamental for operations of a LArTPC experiment. It provides the facility to fill the detector and constantly recirculate the LAr inside the cryostat in order to remove impurities from oxygen and keep the impurity concentration below 20 ppt oxygen equivalent. The ProtoDUNE-SP cryogenic system can be split in three parts. The external, the proximity and the internal cryogenic system. A schematic is shown in Figure 3.27 and described in the following paragraphs.

The external cryogenic system is located outside of the EHN1 hall and includes the dewars that receive and store LAr (70 t capacity) and LN_2 (40 t capacity) deliveries. During the LAr filling phase of six weeks the LAr dewars were filled on a regular basis. The dewars connect to the proximity cryogenic system by means of cryogenic piping routed from outside to inside of the EHN1 hall.

The proximity cryogenic system is installed in proximity to ProtoDUNE-SP and hosts the recirculation system that takes care of LAr purification before directing the LAr flow into the detector. Through the aforementioned penetration at the bottom in the side wall of ProtoDUNE-SP LAr is continuously extracted with a cryogenic pump and directed to the filter system. The cold filters include three filter vessels with molecular sieve removing H_2, porous aluminium granules covered by copper for catalytic removal of O_2, and mechanical filters 15 μm after the copper filter [40].

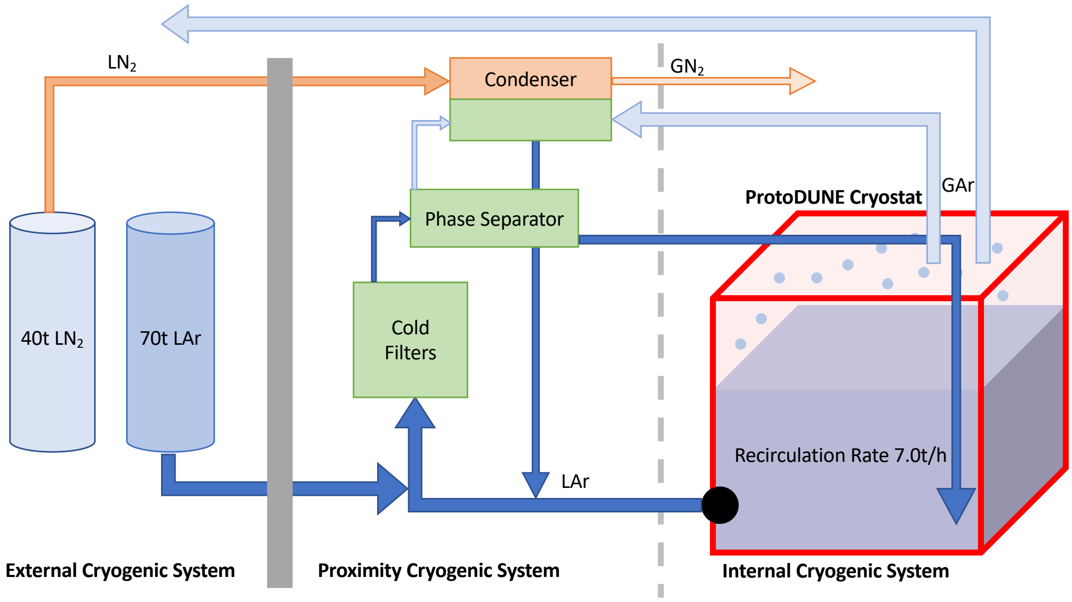

Figure 3.27: The scheme shows a simplified version of the cryogenic system for ProtoDUNE-SP. The cryogenic system can be separated in three sub systems: external, proximity and internal. The external is used initially when the cryostat is filled. The proximity system is responsible for the recirculation and purification of LAr inside the cryostat. By means of cryogenic pumps LAr is extracted at the bottom of the cryostat through a penetration in the side walls and fed to the cold filters. A phase separator and condenser are part of the system in order to only feed back LAr into the cryostat. The recirculation rate is 7.0 t/h, thus it takes 4.6 d to recirculate a full volume cycle. The cryogenic system is monitored at all times with temperature and pressure gauges, as well as flow metres. Alarms are issued in case of unexpected behaviours.

Cryogenic Parameters	Value
Liquid level	7.45 m
Liquid volume	540 m^3
Liquid mass	752.76 t
Normal operating pressure	1050.00 mbar

Table 3.3: ProtoDUNE-SP cryogenic parameters after commissioning [40].

A phase separator directs the LAr back into the cryostat and the GAr to a condenser. The condenser works through heat exchange using vaporization of LN_2 as cooling power to condense GAr $\rightarrow$ LAr and feed it back into the recirculation circuit. The GAr boil-off in the detector is liquefied in the condenser and fed into the purification circuit. About 15% of the boil-off are removed through purging pipes. The recirculation rate is about 7 t/h and the full LAr volume of ProtoDUNE-SP is recirculated over a period of 4.6 days.

The internal cryogenic system includes all cryogenic equipment inside the cryostat. Several pipes and openings are used for the cool-down phase and for LAr distribution during normal operations. Pipes where purified LAr is fed into the cryostat are positioned on the bottom of the cryostat opposite of the extraction point. Through several outlets on the pipe purified LAr is reinserted inside the cryostat. As consequence of the heat load on the cryogenic transfer lines the temperature of the purified LAr is 0.4 K warmer than the ambient LAr temperature inside the cryostat. The difference is essential in order to induce an upward flow of the freshly purified LAr and help to homogeneously mix the LAr.

Filling preparation includes pruging of the cryostat over a week with GAr. The duration of the purging process minimises the oxygen and water contamination to a sub-ppm and ppm level, respectively. The cool-down is started by delivering a mix of LAr and GAr through spray nozzles on the top of the cryostat. The maximum allowed cooling rate is 40 K/h with a maximum ΔT of 50 K between any two points inside the detector volume. After cool-down completion the filling starts. From the storage dewars outside LAr is purified in the proximity cryogenic system and inserted into ProtoDUNE-SP through the phase separators. The filling process takes about 6 weeks. After filling ProtoDUNE-SP enters the normal operation phase with the cryogenic parameters listed in Table 3.3.

During filling and operation the ProtoDUNE-SP cryogenic system is monitored at all times through temperature and pressure gauges, as well as flow metres. Safety valves are installed at various points of the system in case over-pressure is detected. The cryogenic control system allows for manual and automated operation and monitoring during all phases where cryogenics are involved. All installed hardware is electrically connected to the control system and can be operated and read such as valves, pumps and sensors. In total 630 signals are controlled by the system. If unexpected behaviour appears, software interlocks stop any further automatic actions and an expert of the cryogenic team is notified. The essential equipment of the cryogenic system is redundantly powered with uninterruptable power supplies and diesel generators.

3.7 DETECTOR INTEGRATION

In the previous Sections 3.2 and 3.3 the installation of the various components has been discussed. The current section describes the integration and final assembly of ProtoDUNE-SP. The CPA-FC sandwiches (Figure 3.8), the FC endwalls (Figure 3.10, Figure 3.11), and the APA with the installed PDS and CE boxes (Figure 3.19) are all finalised in the ProtoDUNE-SP clean room. Finalised components hang from the trolleys on rails and are inserted into the cryostat through the TCO and transferred onto the appropriate rail in the Detector Support System (DSS).

The six APAs are arranged in two arrays of three and put in position on the side of the cryostat and the cables from the CE boxes and PDS are routed through flanges on top outside of the cryostat. One APA array is bolted in place at that point already. Figure 3.28 shows the first APA array inside the ProtoDUNE-SP cryostat before it is transferred to its final position.

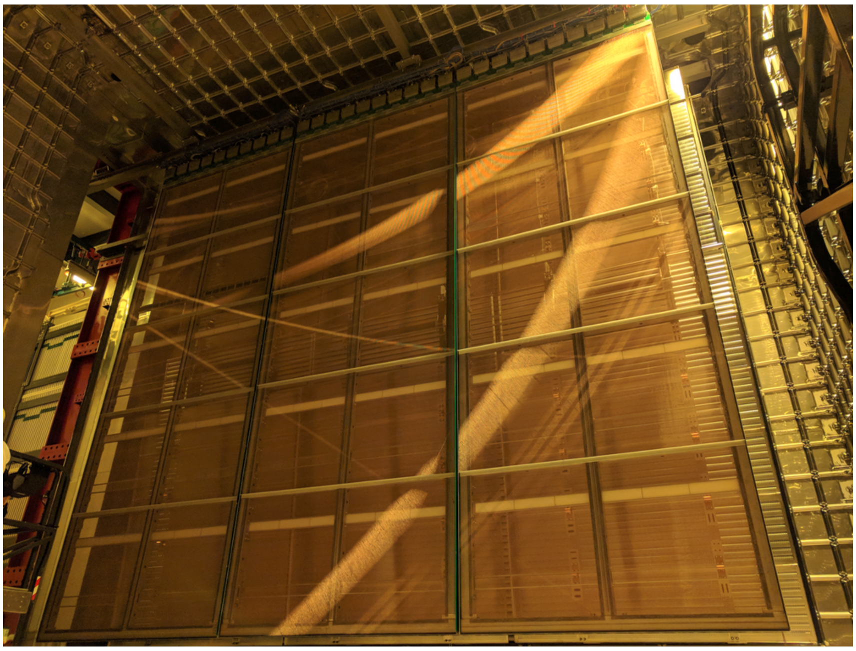

Figure 3.28: Array of three APAs to be put in their final position in the ProtoDUNE-SP cryostat. Three APAs readout one full drift volume of ProtoDUNE-SP [40]. Together they span 6 m along the detector z-coordinate.

The three CPA-FC sandwiches are strapped together and then inserted through the TCO into the cryostat. They are put in position in the middle of the cryostat and run parallel to the APA arrays. After bolting the CPA-FC sandwiches in place the FC endwalls are placed and also transferred onto the DSS. After this step one of the two ProtoDUNE-SP drift volumes is ready for completion.

The completion of a drift volume is done by deploying the top and bottom FCs attached to the CPA into their final horizontal position, closing the drift volume between APA and CPA with the FC. The deployment was a very delicate step in the construction of ProtoDUNE-SP. It was done mechanically by lowering first the bottom FC modules into position and subsequently lifting the top FC modules into position. The lowering and lifting process was carried out by a winch. The ends of the top and bottom FC modules have to be attached carefully to the APAs in foreseen points with latches and the electrical terminations for the FCs have to bee made. Figure 3.29 shows the procedure of the FC deployment in 5 photographs taken during the process. It shows the deployment of the first top FC module at the beam entry point.

After the finalisation of the first drift volume the TCO was welded close from the inside. A "dirt room" was built around the TCO in order to prevent detector exposure to any dust and dirt produced during the welding process. It was dismounted after completion of the welding work. With the sealed TCO, access through the cryostat was only possible through a manhole on the roof of the cryostat and a scaffolding put in place inside. Being a closed volume without natural air circulation the space became classified as a "confined space". Everyone working inside was required to have completed a set of special training courses. I was among the people of the team to enter the confined space and participate in completing the detector installation.

3.8 Cryogenic instrumentation

A dedicated detector like ProtoDUNE-SP is the core of a physics experiment, however it is not the only necessary part in order to guarantee the success of an experiment. Often along side a detector a set of monitoring devices or sub detectors are installed in order to observe the detector environment. In the case of ProtoDUNE-SP a set of instruments monitor several detector parameters. This is crucial in order to understand and diagnose the source of any changes during detector operation.

Temperature sensors and level metres observe the temperature throughout the detector and the level of the LAr. A set of purity monitors is put in place to swiftly and independently of the LArTPC evaluate the electron-drift lifetime. A system of internal cameras functioning at cryogenic temperatures is installed. This is helpful

Figure 3.29: Series of photographs showing the deployment of the top FC on the beam side. All images are from the same camera view showing the section of APA-corner-endwall-corner-CPA. Descriptions are from left to right, top to bottom. First image: Before starting the deployment operation. The top FC hangs on the CPA as it was positioned for insertion into the cryostat. The cable attaching the winch to the top FC lifting point is visible. Second image: Start of the deployment procedure. The winch slowly lifts the top FC module. Third image: Continuation of top FC deployment. Fourth image: Nearing the horizontal position. This is a very delicate moment as the top FC is now close to the APA wire plane. The arms of people from the installation team are visible. They stand on a scaffolding in order to manually perform the operations to attach the top FC modules with foreseen latches on the APA. Fifth image: Final position of the top FC closing the drift volume between APA and CPA on the top. It is attached via the latches on the APA and electrically connected. The deployment procedure is done 12 times for six top and six bottom FC modules [40].

to have means of visual inspection of detector components after cryostat sealing and filling. Figure 3.30 shows the placement of the cryogenic instrumentation inside ProtoDUNE-SP.

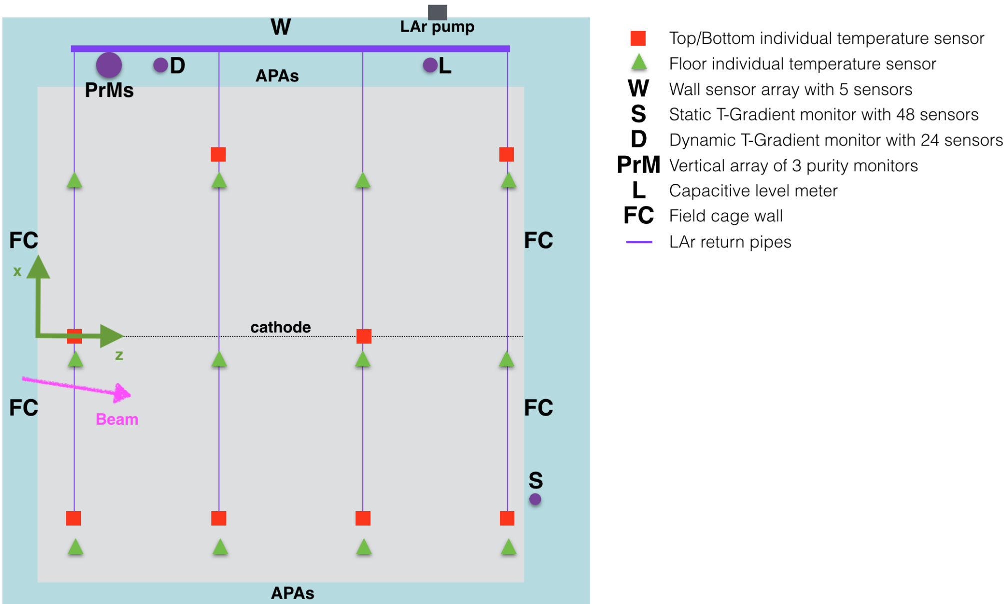

Figure 3.30: The location of the purity monitors, T-gradient monitors and level metres is shown in the top view of ProtoDUNE-SP [40].

Purity Monitors

In a LArTPC the electrons from the ionisation tracks of charged particles are drifted to the charge readout wire planes (APA). The maximum distance the electrons can cover is the drift distance from CPA to APA of 3.6 m. Ionisation electrons that are produced by charged particles in LAr are lost in parts through recombination, longitudinal and transverse diffusion and electronegative impurities. These affect track reconstruction and energy measurements particularly for tracks originating far away from the anode wire planes.

Recombination happens promptly at the generation of the ionisation track where some of the ionisation electrons recombine with the argon-ions. This process is modelled with the modified box model [51]. The longitudinal and transverse diffusion depend on the initial distance between the ionisation track and the APAs [79]. The concentration of electronegative impurities is inversely proportional to the electron lifetime. Oxygen and hydrogen are the main sources of electronegative impurities in LAr. It is possible to reduce electronegative impurities by recirculating LAr through dedicated filters as described in Section 3.6. For a successfull operation of ProtoDUNE-SP a long enough electron lifetime is crucial. Thus, LAr purity can be a limiting factor for operating LArTPCs. electron lifetime is parametrised as

$$N(t) = N_0 e^{-\frac{t}{\tau}}, \tag{3.1}$$

where N_0 is the initial number of ionisation electrons that were not subject to recombination. $N(t)$ is the number of electrons after a drift time t and τ is the electron lifetime. The nominal electric field of ProtoDUNE-SP is 500 V/cm, which results in an electron drift velocity of approximately 1.5 mm/μs [80]. In consequence, the drift time from cathode to anode for a maximum drift distance of 3.6 m results in roughly 2.3 ms. The signal attenuation can be described as

$$\frac{\Delta N}{N_0} = 1 - e^{-\frac{t}{\tau}}. \tag{3.2}$$

For a lifetime of τ = 10 ms and a signal originating at the cathode, the attenuation is less than 20%. Electron lifetime can be measured using cosmic rays inside the LArTPC or by purity monitors outside of the TPC volume.

Independent electron lifetime measurements in ProtoDUNE-SP are obtained by three purity monitors. They are installed at different depths within the LAr but outside of the TPC volume in order to see, whether the impurity concentration remains the same at different levels of height or if there are issues with the recirculation. In principle, a purity monitor is a miniature LArTPC: A photo cathode is illuminated via a deep UV-light generating a known amount of electrons Q_C. The electrons are drifted by means of an electric field over a known distance and collected at the anode Q_A. The signal attenuation between cathode and anode

$$\frac{Q_A}{Q_C} = e^{-\frac{t}{\tau}} \tag{3.3}$$

after drift time t, reveals the electron lifetime τ.

Figure 3.31 shows the design of a purity monitor following the original design of the purity monitors used in the ICARUS experiment [50]. The photo cathode, field shaping rings and anode are visible. To avoid interference with other parts of ProtoDUNE-SP the purity monitors are placed in a cylinder of stainless steel acting as a Faraday cage.

The measurable electron lifetime depends on the drift distance of the purity monitor and the electric field, *i.e.* the applied voltage. The purity monitors of ProtoDUNE-SP cover a electron lifetime measurement range of 35 μs to 10+ms. Purity monitor measurements are limited when the ratio of $Q_A/Q_C = 1$ as τ is infinity, meaning that the electron loss is minimal.

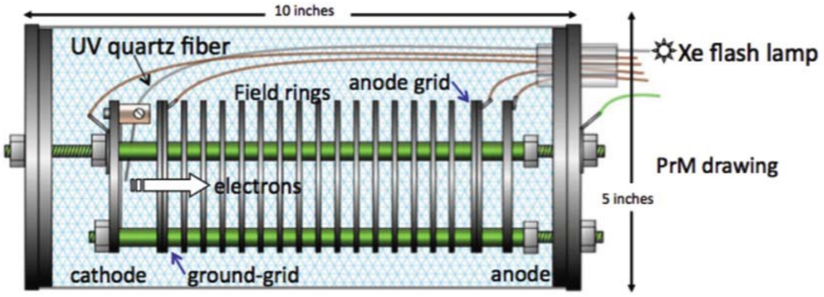

Figure 3.31: Schematic of the purity monitor design based on the original ICARUS design [50], taken from [81]. Via a deep UV quartz fibre a light flash is directed onto a photo cathode. A known amount of charged electrons (Q_C) is produced and drifted to the anode. The electric field uniformity is invoked by the field shaping rings that are speareted with resistors of 50 MΩ. At the anode the signal is read out Q_A. The ratio of Q_C/Q_A and the measured drift time between the signal generation at the cathode and signal arrival at the anode, reveals the electron lifetime τ [40].

The three purity monitors in ProtoDUNE-SP are located at 1.8, 3.7 and 5.6 m from the bottom of the cryostat. Operations of the purity monitors started in the commissioning phase in September 2018 and ran until July 2020. During ProtoDUNE-SP operation values of the ratio close to one were measured, *i. e.* the electron loss is very small and electron lifetime was measured to be greater than 70 ms on the top and greater than 30 ms on the bottom. During the beam run the impurity level for oxygen never exceeded 40 ppt [40]. For every beam run, purity monitor data was taken and results are included in the calibration data base for the TPC charge and energy calibration.

Figure 3.32 shows the electron lifetime data for the period of September 2018 to July 2020 from the purity monitors with the uncertainties. The uncertainties accounted for are fluctuations of the baseline of the signal waveform, cathode and anode RC constants, grid shielding inefficiencies and electron transparency of the anode grids. They are estimated individually for every purity monitor and are 1.9%, 2.2% and 3.9% from top to bottom. Dips in Figure 3.32 indicate pump failures, filter saturation and the initial low purity in the early commissioning phase of September 2018.

Temperature Sensors

In order to monitor the mixing of the LAr outside the TPC volume a set of temperature sensors is distributed. The sensors allow to create a 3D map of the temperature distributions. Temperature measurements are also used as input information for the computational fluid dynamic (CFD) model validation. If well done, CFD

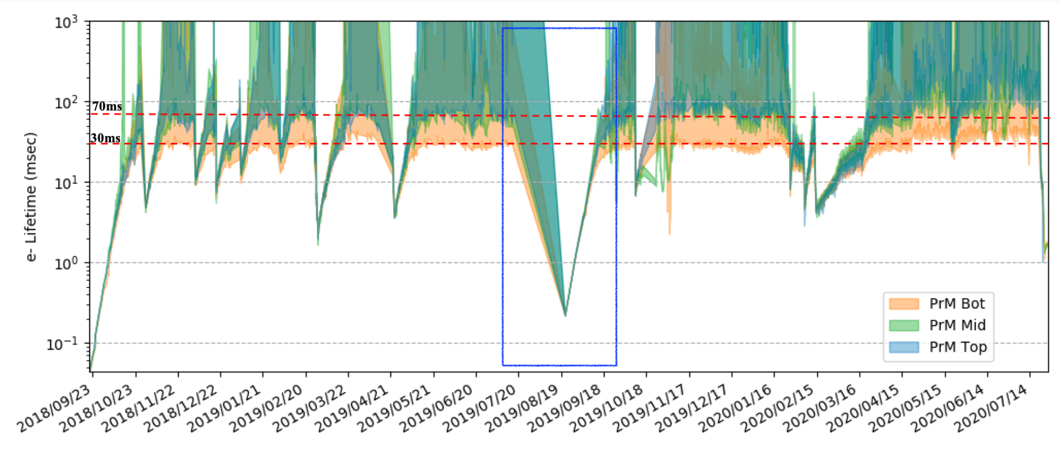

Figure 3.32: Purity monitor data for the period of September 2018 to July 2020. Every purity monitor measurement is shown with its uncertainties. The dips are due to pump stops (blue square), recirculation studies and initial LAr impurity as coming from the commercial delivery at the start of the commissioning phase in September 2018. During the beam run the oxygen impurity level never exceeded 40 ppt. The purity monitor data was taken on a run-by-run basis and is included in the calibration database for ProtoDUNE-SP data [40].

models can predict the purity of the LAr across the entire cryostat, especially the vertical coordinate is of interest as it reflects the homogeneity of the LAr recirculation.

In ProtoDUNE-SP high-precision temperature sensors are placed throughout the TPC. At the top and bottom of the cryostat 2D arrays of Lake Shore PT102 platinum sensors with 100 Ω resistance at 0° are placed. The sensors at the bottom are mounted on the LAr pipes and the ones on the top are installed on the ground planes of the top FC. The vertical coordinate is monitored by two vertical arrays of temperature sensors, the *static T-Gradient monitor* and the *dynamic T-Gradient monitor*. They are placed in proximity to the purity monitor array and 20 cm away from the lateral field cage as shown in Figure 3.30.

The static T-Gradient monitor is a vertical array of 48 sensors with 11.8 cm spacing for the 16 top and bottom and 23.6 cm for the 16 middle sensors. The sensors and cables are held by a U-shape fibre glass profile (FGP) and surrounded by a Faraday cage. Calibration was done in the laboratory beforehand by placing the sensors next to each other in LAr and assuming the same temperature for all. The calibration accuracy is estimated to be 2.6 mK.

The dynamic T-Gradient monitor is a motorised system. 24 temperature sensors are mounted on a carrier rod that is attached to a stepper motor. The five sensors on top and bottom are vertically spaced out with 10 cm in between. The remaining

14 sensors in the middle are spaced out by 50 cm. The rotational movement of the stepper motor is converted to a linear movement, moving the rod vertically. Thus, at various heights in the TPC the temperature can be measured. Offsets between the temperature sensors can all be calibrated out with respect to a single sensor.

The data from the temperature sensors and T-Gradient monitors have shown that the difference between any two sensors is within 3 mK. Therefore, it can be stated that the system is stable in standard operation conditions. Temperature measurements have also been taken in periods where the recirculation pumps were shut down in order to deepen the understanding and knowledge of the LAr circulation in the system, results are shown in Figure 3.33.

Cameras

Eleven cameras have been installed in ProtoDUNE-SP. Having a "set of eyes" inside the detector turns out to be very useful for certain reasons. Visual inspections during filling or critical operations, monitoring the movable parts inside the detector as for example the dynamic T-Gradient monitor, as well as looking for any visual hints when unexpected detector behaviour was registered. Furthermore, the cameras were also used to check the TPC alignments during cool-down and detect any detector instabilities like bubbles at the perforated ground planes for example. Figure 3.34a shows the location of the eleven cameras in ProtoDUNE-SP. The cameras that were placed in the lower part of the detector are referred to as *cold cameras*. The ones placed at the top of the detector are the *warm cameras*.

The cold cameras are in a fix position and planned for long-term use. The cameras are placed in an aluminium or acrylic enclosure with a heating element inside following the design used at EXO-100 [82]. Temperature is controlled via a thermocouple inside the enclosure. The cameras are operational at all times.

The warm cameras are deployed from the roof of the cryostat and only operate in case of specific operations or dedicated inspections such as examinations of the HV feedthrough and receiver cup. A set of commercial cameras has been used and the cameras are kept warmer than -150°C [83]. An air-tight acrylic tube is attached to a flange and inserted via one of the available penetrations on the cryostat roof. The camera sits inside the acrylic tube and thus can be extracted at any time for servicing.

The field of view for all cameras inside the detector was equipped with dedicated LED lightning at two wavelengths (IR and visible). LED models were chosen in order to minimise heat emission in the LAr they are only turned on when a visual inspection was necessary. Because of the light sensitive PDS system it was important to not operate the LEDs while the PDS was turned on. Eventually, a

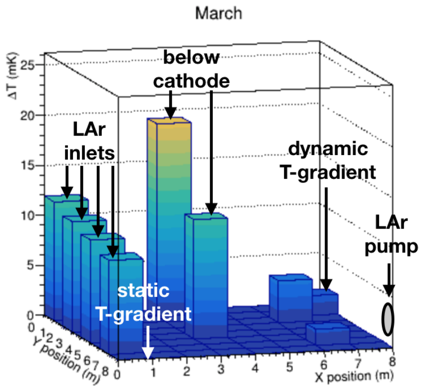

(a) Recirculation ON

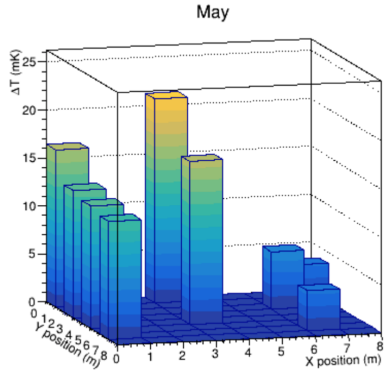

(b) Recirculation ON

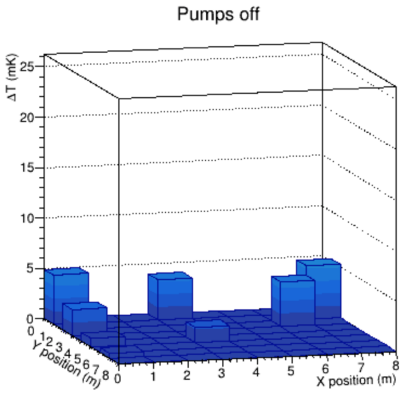

(c) Recirculation OFF

Figure 3.33: Results of the difference between the static T-Gradient bottom sensor and the 2D arrays of temperature sensors placed on the bottom of the cryostat. The 3D plots show the position of the sensors and the value of ΔT. The top left and top right plot are both produced with the recirculation system running and two months apart in the data campaign. The distribution and values of the temperature differences are similar, confirming the stability of the temperature distribution when the recirculation system is on. The bottom plot shows the temperature differences when the recirculation system is off and as expected a constant temperature distribution is visible [40].

software interlock was implemented in the detector control software preventing possible damage.

3.9 VERY LOW ENERGY BEAM LINE H4 AT CERN

Figure 3.1 indicates the location of the Very Low Energy (VLE) beam line within the extension hall of EHN1 in the CERN north area. The VLE beam line is a tertiary extension branch of the H4 beam line. 400 GeV/c primary protons are extracted

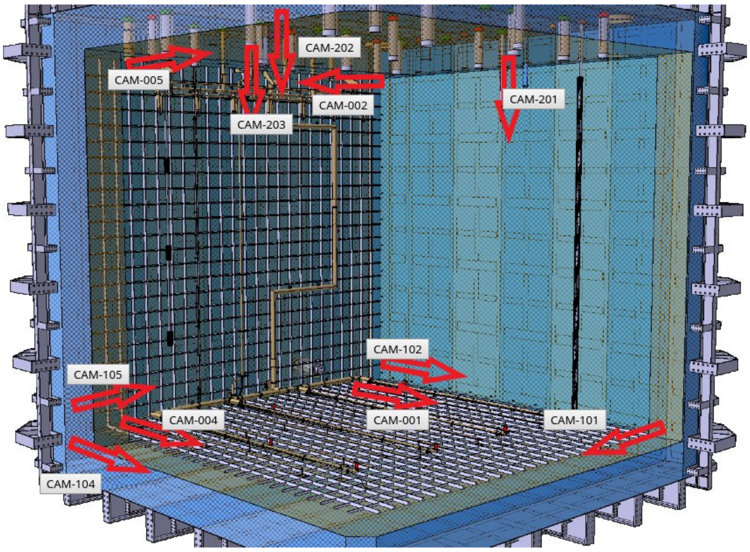

(a) Camera Locations in ProtoDUNE-SP

(b) View of purity monitor from cold camera.

Figure 3.34: Cameras for visual inspection are installed in ProtoDUNE-SP. They are either installed in the bottom region of the cryostat in specific aluminium or acrylic enclosures or inserted from top and operated in a ″warm″ environment inside an air-tight acrylic tube. The image of a camera that is shown is from camera 105, its location is indicated in the schematic on the lefthand side [40].

from the CERN Super Synchrotron (SPS) and aimed at a beryllium target producing a mixed hadron beam with a reduced momentum of 80 GeV/c. The secondary beam is subsequently directed onto a secondary target producing the tertiary VLE beam in a momentum range of 0.3–7 GeV/c. The secondary target is either copper or tungsten depending on the requested VLE beam parameters. Tungsten is used for beam momenta below 4 GeV/c and also increases the hadron content. Copper is used for the momentum range from 4 GeV/c to 7 GeV/c. The VLE beam is directed by three bending magnets to ProtoDUNE-SP and injected in the detector through the beam plug. A beam line length of less than 50 m is required in order to limit the decays of unstable low-energy hadrons such as pions and kaons. However the beam line has to be long enough in order to separate the high energy background and include the beam instrumentation (BI) components.

The BI provides trigger and particle identification capability, as well as momentum measurement on a particle-by-particle basis. It includes profile monitors "XBPF", trigger counters "XBTF" and two threshold Cherenkov counters "XCET". The arrangement of the various instrumentations is shown in Figure 3.35.

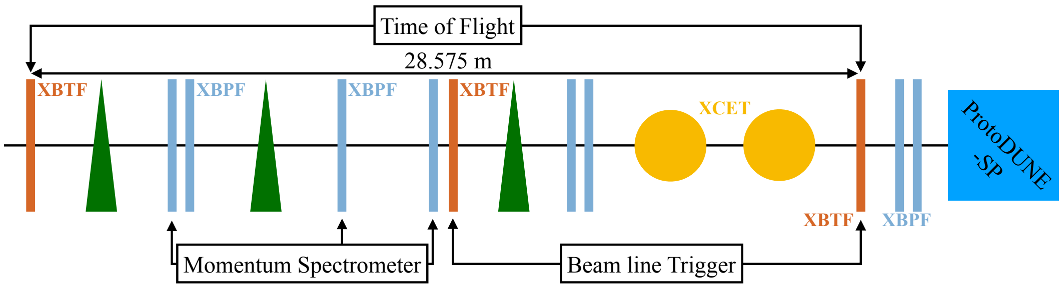

Figure 3.35: Schematic of the Very Low Energy (VLE) beam line providing charged particles (pions, protons, kaons and positrons) in the range of 0.3 to 7 GeV/c to ProtoDUNE-SP. The beam line includes three types of beam instrumentation components for triggering, particle identification and momentum estimation [84].

The XBPF are scintillating fibre detectors described in detail here [85]. 1 mm thick scintillating fibres are arranged on a square surface of 20×20 cm^2 in a planar configuration. The signals from 192 fibres are read individually by Hammamatsu SiPMs. Three pairs of XBPF are placed in several points of the beam line with 90° with respect to each other allowing for position tracking of every beam particle. The data from the XBPF is also used for momentum reconstruction. At the final XBPF detector pair the position information is used to extrapolate the particles entry coordinates inside ProtoDUNE-SP [72].

Three XBTF sensors allow for general triggers. The XBPF detectors are of a similar build like the XBPF detectors, however the planar configuration of fibres is bundled for readout offering no position resolution. The XBTF are separated by 28.575 m as is shown in Figure 3.35, thus their signals provide every beam particle's time of flight (TOF) with a resolution of 900 ps [84].

	1 GeV				2 GeV			
	e	π/μ	K	p	e	π/μ	K	p
TOF[ns]	0, 105	0, 110	–	110, 160	0, 105	0, 103	–	103, 160
XCET-L	1	0	–	0	1	0	–	0
XCET-H	–	–	–	–	–	–	–	–
	3 GeV				6 - 7 GeV			
	e	π/μ	K	p	e	π/μ	K	p
XCET-L	1	0	0	0	1	1	0	0
XCET-H	1	1	0	0	1	1	1	0

Table 3.4: The combination of the beam line instrumentation to correctly identify different particle types is summarised in this table. The TOF values are given for the lower and upper cuts and only used for the 1 GeV/c and 2 GeV/c beam runs. The value of 0 or 1 for the Cherenkov counters represent the absence or presence of the signal. XCET-L refers to the lower pressure Cherenkov counter, while XCET-H refers to the higher pressure Cherenkov counter as specified in Section 3.9. A dash is used if a certain beam line instrumentation detector is not used for PID at a given momenta [72] .

The last part of the beam instrumentation detectors are two Cherenkov counters XCET. A Cherenkov counter makes use of the fact that particles emit prompt photons when passing through a medium (here a radiator gas) with a velocity grater than the phase velocity of light in the medium. The XCET are filled with a radiator gas CO_2 and kept at different pressures. The first (Figure 3.35) at a pressure up to 15 bar tagging the low energy positrons and pions. At higher momenta above 5 GeV/c kaons and protons can be tagged. The second XCET is set to a pressure up to 5 bar and used to tag positrons at 1 and 2 GeV/c. Pions are the particles I use for my physics measurement. They are tagged by using the low pressure XCET above the positron threshold and the high pressure XCET below the proton threshold as described in Table 3.4.

The BI is used for its reliable and TPC-independent pre-selection of beam pion candidates for the analysis. The measured efficiencies are greater than 95% [72]. At momenta above 2 GeV/c the TOF measurements are not able to resolve the particle species any more. This is visible in Figures 3.36b and 3.36c. Therefore, at higher momenta only the two Cherenkov counters are used to tag beam particles. Due to their similar mass, beam pions (139 MeV) and muons (105.6 MeV) have indistinguishable TOF measurements, as shown in Figure 3.36.

Table 5.2 shows the recorded triggers and expected triggers issued by the beam instrumentation for the different particle types and momenta. The expected triggers are compiled from the MC simulations of the beam line. The analysis presented in this thesis uses the data of π^+ at 1 GeV/c. The measured momentum distribution for π^+ (and μ^+) like triggers from the beam instrumentation is shown for data and MC simulations in Figure 5.4. The predicted beam momentum spread from the beam line simulations underestimates the slightly the beam momentum spread that was measured in data as can be seen in the fit values in Figure 5.4. This is further discussed in Section 6.1.

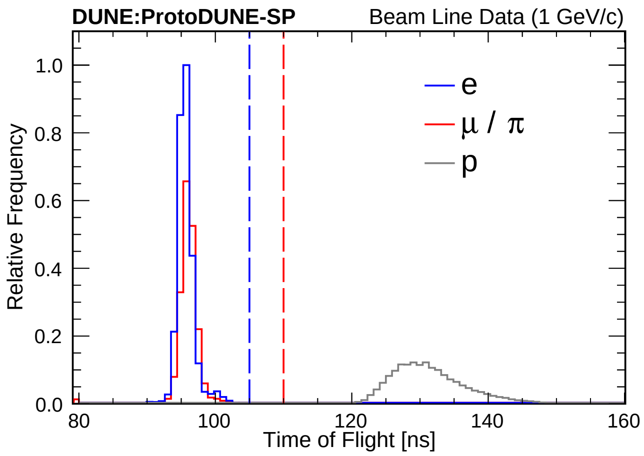

(a) TOF cut values for electrons (blue) and pions/muons (red) at 1 GeV/c, normalized distribution.

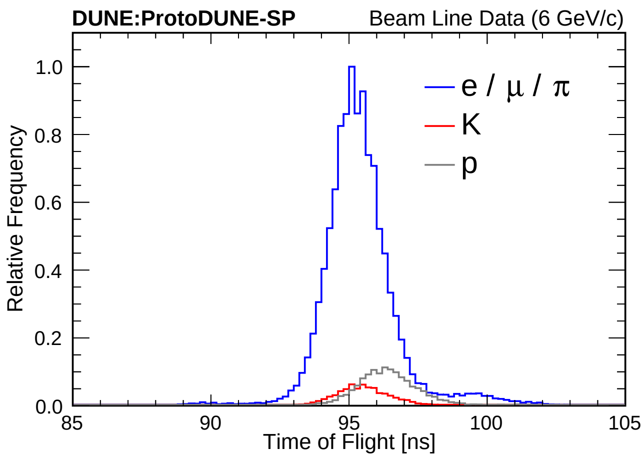

(b) At 6 GeV/c, the TOF values are not used for particle identification, normalized distribution.

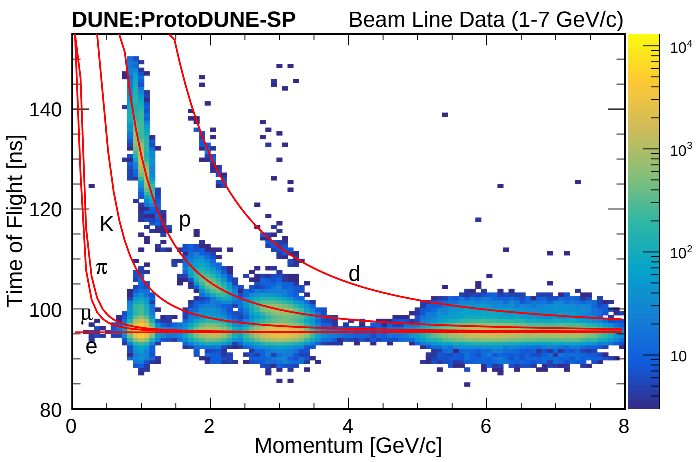

(c) TOF vs reconstructed beam momentum for particle types. The red curves are predictions for e, μ, π, K, p and deuterons (d). At higher momenta the time of flight becomes similar for all particles and cannot be used anymore for particle identification

Figure 3.36: Time of flight distributions for specific momenta and over all momenta for particle identification with the beam line instrumentation. The capability of PID with TOF measurements at lower momenta is well visible [72].

4

DETECTOR COMMISSIONING AND RESPONSE

The previous chapter has presented in detail the design and construction of the ProtoDUNE-SP detector. From 2017 to 2019 I was part of the core team constructing and commissioning the detector. The present chapter describes the commissioning phase, as well as the detector response. The signal detection and processing in ProtoDUNE-SP is described in Section 4.1 and an overview of the signal reconstruction is given in Section 4.2. ProtoDUNE-SP is subject to strong Space Charge Effects (SCE) offering the opportunity to study them with beam data and cosmic rays extensively but also limiting, as their description and simulation currently are not precisely modeled and they can influence ProtoDUNE-SP data analysis. SCE effects in ProtoDUNE-SP are discussed and quantified in Section 4.3. The calibration of several detector effects like the spatial and electric field distortions from SCE effects are discussed in Section 4.4.

4.1 SIGNAL DETECTION AND PROCESSING

As was introduced in Section 2.3 LArTPC signals rely on the conversion of the ionisation electrons to an electric signal on the sensing wire planes. The three wire planes in ProtoDUNE-SP are parallel with respect to each other and the two induction planes are at an angle of $\pm 35.7^\circ$ with respect to vertical. The wires on the vertical collection plane are spaced out with a pitch of 4.67 mm as described in detail in Section 3.3. Thanks to the carefully chosen bias voltages of the three sensing wire planes, the first two planes record bipolar signals from the drift ionisation charge and the collection plane collects at full transparency 100% of the drift ionisation charge and reads a unipolar signal. To reach 100% transparency the electric field increase between the wires should increase by more than 40% at each successive plane gap [86]. Figure 4.1 shows the electric field between 3 planes of sensing wires from simulations.

Section 3.5 described the trigger rates and ADC samples collected by the CE and sent through the WIBs to the DAQ system for signal processing and event reconstruction.

To facilitate event reconstruction a set of steps are performed called data preparation [72]. They include:

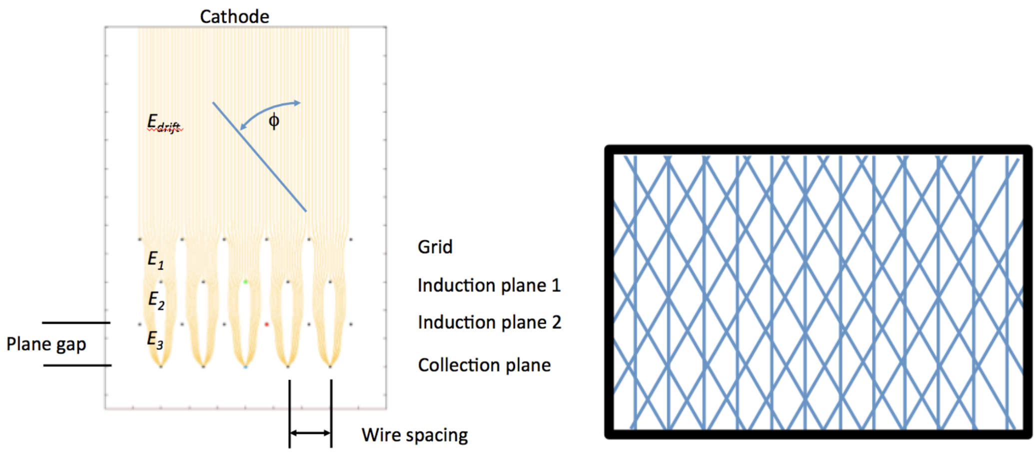

Figure 4.1: Schematic of the electric field between three sensing wire planes. Ionisation electrons from charged particle tracks follow the field lines and arrive at the anode sensing wire planes. The Induction plane 1 and 2 record bipolar signals and the collection plane records unipolar signals from the ionisation charge. The integral of the unipolar signals is proportional to the deposited charge by charged particles. A blue line at an angle ϕ with respect to the drift electric field is shown representing a particle track. On the right, the view of an area of the wire sensing plane is shown. Taken from [86].

1. before any data preparation steps are applied, the gains are calibrated for each channel. The gain in product with the integral of the ADC signal over a pulse on the collection should result in the deposited charge, *i.e.* $Q = gA$. ProtoDUNE-SP electronics can inject a known charge to all amplifiers of the 15360 channels. Apart from specifically noisy channels, the gains are contained in a narrow peak with RMS of 5.1% [72].

2. evaluation of the pedestal on a channel by channel basis. The 6000 ticks of one channel are histogrammed and the observed peak is fitted with a Gaussian and the RMS of the fit gives an estimate of the noise on the channel.

3. each channel is assigned with a gain and the charge waveforms for each channel are obtained by subtracting the estimated pedestal value.

4. specific channels have behaviours where some ADC values are preferred due to a transistor failure when digitising the signals. Other channels from 1 FEMB do not receive the master timing signal and therefore are corrected individually to match the timing of the other FEMBs.

5. alternate coupling through high-pass RC filters at the amplifier and ADC of each TPC channel introduce long tails of the opposite sign after a collec-

tion plane signal. The effect is less strong on the bipolar induction signals. Removal of the tails is obtained by using time-domain corrections.

6. ProtoDUNE-SP is subject to correlated noise at 45 kHz for groups of channels in the same FEMB. Thus, this noise is removed in waveforms and referred to as Correlated Noise Removal (CNR). In order to protect ionisation signals from electrons, specific Regions Of Interest (ROI) are defined where the CNR is not applied.

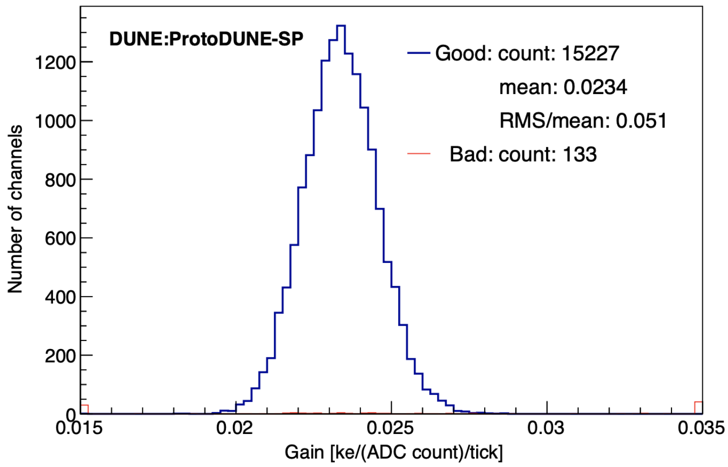

Figure 4.2: Fitted gains for 15227/15360 good channels in ProtoDUNE-SP. The bad, *i. e.* specifically noisy channels are shown in red. A mean of 23.4 e/(ADC count)/tick is obtained with a narrov RMS of 5.1%. Taken from [72].

The noise levels are well below the signals of charged track in nearly all ProtoDUNE-SP channels. After the aforementioned data preparation, the noise is evaluated. The noise is given in ENC (equivalent noise charge) and describes the standard deviation of the signal pulse height corresponding to the charge contained within the recorded signal. Before CNR the ENC on the collection plane is 530 e. It reduces to 430 e after. Correspondingly for the induction channels, it is reduced from 620 e to 500 e after CNR. This results in most probable values (MPV) for the Signal to Noise ratio (S/N) of 40.3 for the collection plane. The S/N values for the first and second induction planes are 18.6 and 15.1, respectively. They are reported in Figure 4.3. The difference of the S/N ratios is due to the electron drift velocity difference in the electric fields in the gaps between the wire planes [72].

Finally, the offline signal processing stage produces distributions of the charge signals and their arrival time, *i. e.* waveforms which are passed to the reconstruction algorithms to perform hit finding. Due to the linear response of the charge

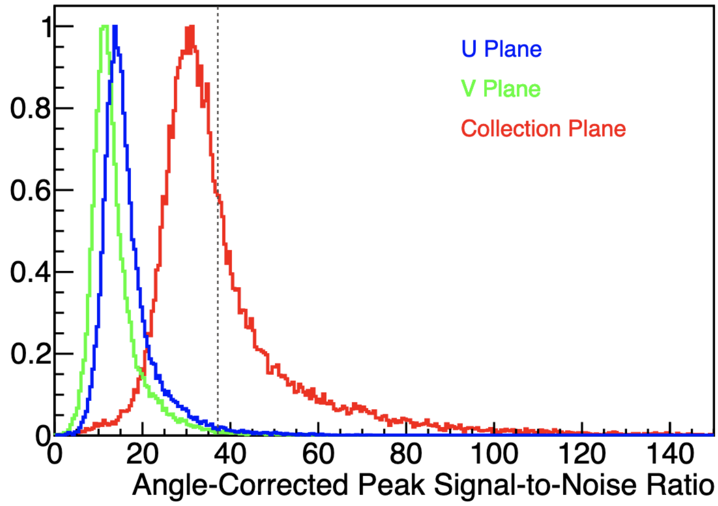

Figure 4.3: Angle corrected S/N for the three sensing wire planes of ProtoDUNE-SP. Taken from [87].

distributions, signal processing is based on deconvolution techniques detailed in [72].

4.2 OVERVIEW OF THE EVENT RECONSTRUCTION

The reconstruction of ProtoDUNE-SP events from beam particles or cosmic rays is separated into two steps: a hit finding and pattern recognition. The hit finding is composed of an algorithm fitting Gaussian shapes to peaks in the waveforms. Each hit is associated with a fitted peak and carries a time stamp. This is done regardless of whether the waveforms have been recorded by induction or collection wires. The signal shapes can vary as a function of the ionisation track orientation with respect to the wire plane orientations. Hit disambiguation happens at this stage where a pair of hits on induction wires can often be only matched to one collection plane signal. From simulations it is shown that more than 99% of the hits are associated with the correct wires [71].

The second step of pattern recognition is performed via the Pandora software package [88] which has been successfully used in MicroBooNE [48]. For reconstruction of ProtoDUNE-SP data some modifications have been added as the events under study are not from neutrinos but coming from a charged particle beam with a well-defined location in the detector. The isolation of the beam particle event candidates from the cosmic ray events is detailed in Section 5.1.

As a reminder, one drift volume of ProtoDUNE-SP is readout by 3 APAs. Charged particle tracks can cross APA boundaries or pass from one drift volume to the other by crossing the cathode. Pandora in a first step clusters in 2 dimensions the hits from each APA plane. After the clustering, the hits from one induction plane are matched to the collection plane views. Ambiguously matched clusters use the second induction plane for disambiguation.

Due to their long tracks, cosmic rays often cross APA boundaries or go from one drift side to the other through the CPA. They enter mostly from the top (and sides) of the detector and traverse through to the bottom or exit on a side face. A dedicated track stitching step is applied for identified cosmic ray candidates if they cross an APA boundary or the CPA as they will include gaps in the reconstructed track segments as shown in Figure 4.4. The stitched cosmic ray tracks especially the ones crossing the CPA also referred to as *cathode crossers* are of invaluable importance for the ProtoDUNE-SP detector calibration. As regions of the APA boundary and CPA are independently known within the detector, tracks passing through those regions can be assigned an unambiguous time stamp. Cathode crossing muons have t_0 values from -2500 μs to 500 μs. If they cross the anode their t_0 lies in the interval of -250 μs and 2750 μs within the 3 ms readout window.

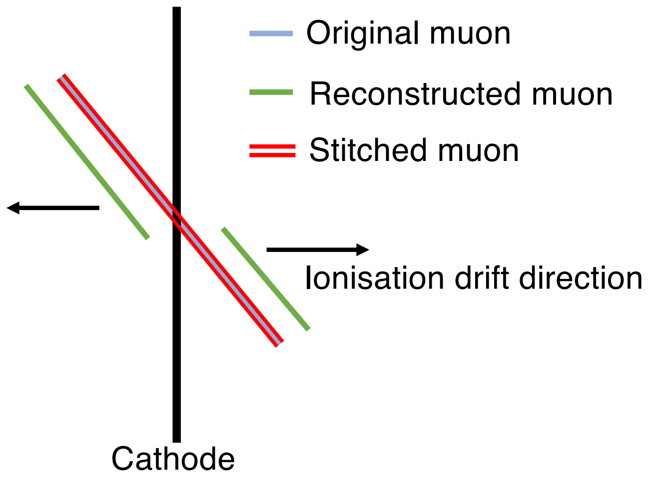

Figure 4.4: Schematic of a cathode crossing muon. The blue track is the original muon track as it crosses the cathode of ProtoDUNE-SP. The two split green tracks are the reconstructed track segments for each drift volume. The stitching algorithm recognises the tracks as they are both close to the cathode and have the same direction. The red line indicates the reconstructed muon track after the Pandora track stitching. Thus, the original muon trajectory was reproduce.

4.3 Space charge effects in ProtoDUNE-SP

As already mentioned in the previous section, cosmic rays are used for detector calibration. Due to its location on the surface, ProtoDUNE-SP is subject to a continuous flux of cosmic muons. The flux rate for 1-10^9 GeV muons is around 10^4 m^{-2}s^{-1}. While traversing the detector, the charged particles leave ionisation tracks. As discussed the ionisation electrons follow the electric field lines to the anode with a velocity of $\mathcal{O}$(mm/μs). The positive argon ions are drifted in the opposite direction to the cathode plane with a considerably slower drift velocity $\mathcal{O}$(mm/s). This leads to a substantial amount of positive charge built up in the region of the cathode which is constantly replenished by the steady cosmic muon flux rate [72, 89, 90, 91].

The accumulation of positive ions in the cathode region is enough to introduce magnitude and directional distortions in the ProtoDUNE-SP drift electric field. This is referred to as the Space Charge Effects (SCE). Distortions in the magnitude of the drift electric field can influence the recombination factor of electron and ion pairs as explained in Section 2.3 and Section 6.4. The higher the electric field, the less the effect on recombination. The spatial distortions affect trajectories of reconstructed particle tracks and electromagnetic showers. They are split into two effects: transversal squeezing of the track ends in the transverse direction of the LArTPC. Bowing of the ionisation track towards the cathode as the effect is stronger in the bulk of the TPC. Figure 4.5 shows a cartoon of the two effects on a cosmic muon traversing ProtoDUNE-SP. The view is from the top looking at the xz plane. SCE effects can bias the reconstruction of the particle position, energies, and dE/dx. Thus, careful characterisation and calibration of SCE effects is necessary.

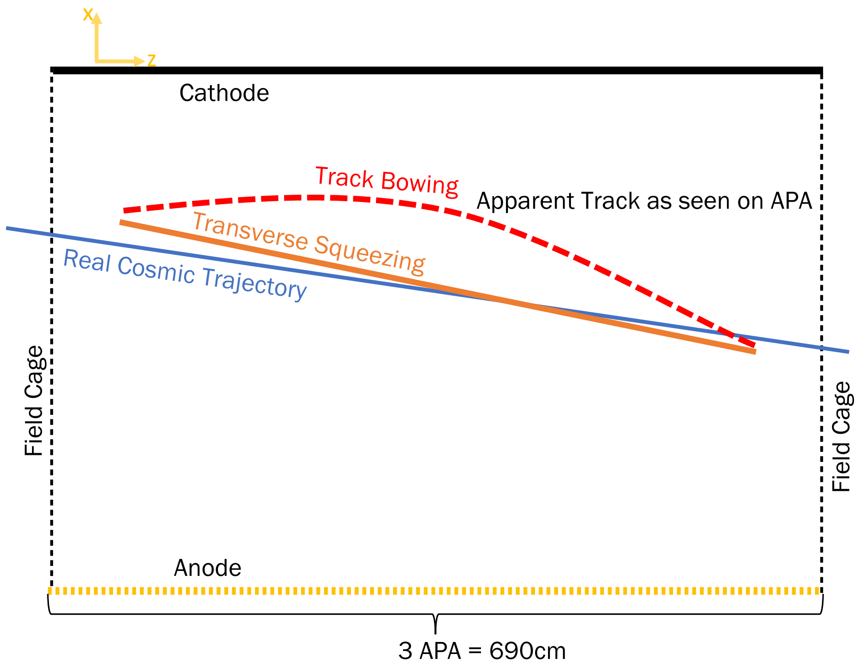

Figure 4.5: Schematic of the squeezing and bowing effects from accumulated positive ions in the bullk of the TPC.

The characterisation of the SCE effects can be done by using different types of tracks that have passed through independently known locations in the LArTPC. The unambiguously known positions within the drift coordinate x of the ProtoDUNE-SP detector are:

- $x = 0$ cm location of the cathode. Cosmic rays traversing the cathode will have prior to track stitching start and end points in the cathode boundary region.
- $x = \pm 360$ cm location of the anode.
- $x = -30$ cm location of the beam window entry point.

Tracks passing through any of these location points can be correctly placed within the drift time and used for SCE effect studies. They are called t_0-tagged tracks. Beam particles permit to measure very accurately the SCE effects in the region of the beam entry point, but only there. However, cosmic muons will pass through the cathode and anodes more often, entering ProtoDUNE-SP through the top or sides and exiting through the sides or the bottom mostly. A set of cathode crossing t_0-tagged muons is used and the distribution of the reconstructed start and entry points is plotted on the yx and xz projections of the LArTPC face. Without space charge effect the start/end points should be reconstructed on the black dashed lines along the field cage boundary where they originated. Figure 4.6 indicates a considerable positive ion density around the cathode which shifts the start/end points of the t_0-tagged tracks.

The t_0-tagged muons, as shown in Figure 4.8 are used to measure the squeezing effect of SCE by measuring the distance of the detector surface with respect to the reconstructed start/end of the cosmic track. The distance is considered orthogonal to the detector face of consideration. For example, a muon entering through the top face, crossing the cathode, and exiting through the bottom TPC face (xz coordinates) reveals information about the spatial distortions in the y-coordinate. This is equivalent for a cathode crossing track with a start or end point in the upstream or downstream TPC face (xy-coordinates), revealing information about the spatial distortion in the z-coordinate. Figure 4.7 shows a schematic drawing of how the offsets in the y and z-coordinate are measured from t_0 tagged tracks.

Figure 4.8 shows the track offset in Y and Z with respect to the ProtoDUNE-SP faces that are obtained from cathode crossing muons. The distortions offset tracks up to 40 cm from their original position at the TPC face and are largest in the area around the cathode at $x = 0$ while becoming smaller towards the anode planes. Tracks that originate close to the cathode, have a longer drift time of up to $\sim$3 ms

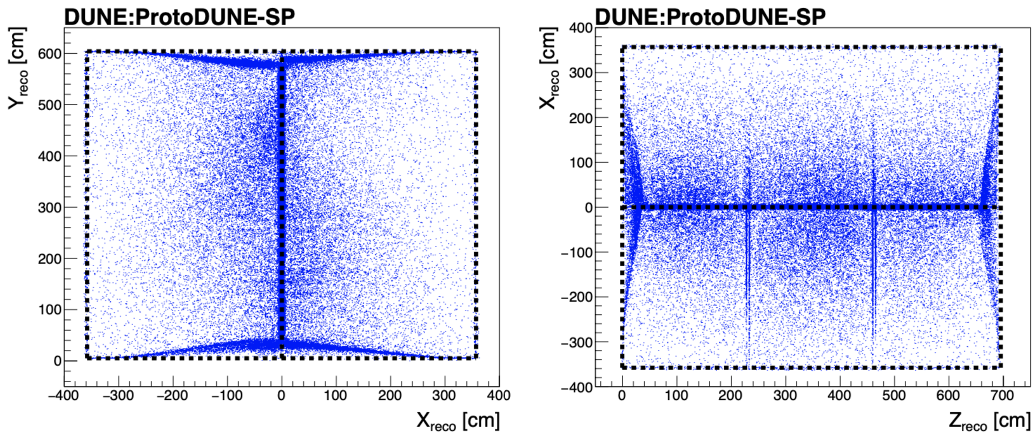

Figure 4.6: Cathode crossing cosmic muons are t_0-tagged. Their start and/or end points are projected onto the ProtoDUNE-SP surfaces in xy and xz. Without the SCE effects the track start and end points should follow the detector boundaries (dotted black lines). An apparent accumulation of positive charge in the bulk however pulls the ionisation charge inwards. Taken from [72].

and thus experience the space charge effect with a larger impact on their drift path [72].

ProtoDUNE-SP beam tracks enter the detector in the xy upstream face at $x \sim -$ 30 cm, y ~420 cm the Δz-offset they experience is of roughly 30 cm. Indeed, data beam tracks only start at around wire 68 as can be seen later in Figure 7.6. Further, it is very well visible that the behaviour of the spatial distortions is not symmetric in the two drift volumes as one would expect from the space charge model.

The asymmetry which is also inconsistent with the MC simulation (originally developed for MicroBoone [91]) of SCE shown in Figure 4.9. This is an effect from the liquid argon flow in the detector and the fact that the center of the field cage

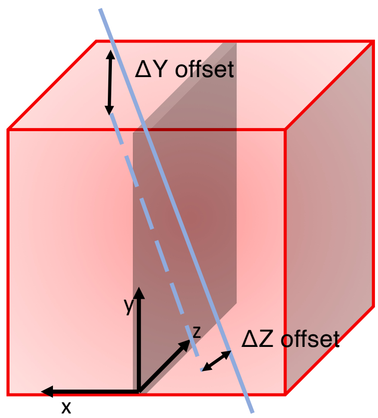

Figure 4.7: Schematic of offset measurement from the ProtoDUNE-SP xy and xz faces for t_0-tagged muons.

is not placed at the center of the cryostat, *i.e.* convective flows in the LArTPC are not symmetric for both drift volumes. Finite element models of the fluid flow for the liquid argon ProtoDUNE-SP show the flow velocity to be similar to the expected positive ion velocity in the range of mm/s. In order to test this, during 2019 I performed a set of studies where I turned off the purification system, *i.e.* the pumps pumping the LAr to the filters and introducing an extra fluid flow component to normal convection. Any observed changes in the SCE distributions would be directly correlated with the turned-off purification system. Taking data with cosmic rays while the pumps were off showed that the SCE is more symmetric when the LAr pumps were off. The studies were reported here: [92].

A comparison of the expected SCE effect from simulations with the observed effects from data under normal detector conditions also shows that the magnitude as measured from ProtoDUNE-SP data is up to two times larger. The cause for this has not yet been fully understood. Reasons can lie in using a wrong value for the drift velocities for the positive ions and a mismodeling for the fluid flow estimates.

As a consequence of the flaws in the purely simulated SCE maps a data-driven map of the SCE effects for the spatial and electric field distortions was developed. A more detailed description of the intermediate steps is given in the corresponding SCE Section in [72]. Finally, a set of 3D spatial distortions and electric field maps is obtained which is included in the ProtoDUNE-SP simulation. The relative difference of the electric field intensity with respect to the nominally expected 500 V/cm is shown for data and simulations in Figure 4.10. The slices are picked in the symmetry axis of ProtoDUNE-SP at z =347 cm and y =305 cm where the effects are strongest. For data, the electric field can vary up to 25% with respect to the nominal intensity. Given the entry coordinates of ProtoDUNE-SP beam candidates and the fact that they barely reach the bulk of the detector at 1 GeV/c momentum, the electric field distortions they encounter are maximally 10%, see Section 6.4 for more information.

4.4 DETECTOR CALIBRATION

A LArTPC can measure the deposited energy per unit length. In order to remove any detector effects from the measured quantity, it is important to correct the extracted LArTPC information for detector effects and calibrate it properly. The calibration takes care of converting the measured ADC signals to energy in MeV. The measured energy allows performing particle identification and energy measurements for reconstructed particle tracks.

For ProtoDUNE-SP data the MicroBooNE calibration scheme [93] is adopted. It follows two steps: first, the detector response is equalised throughout the TPC us-

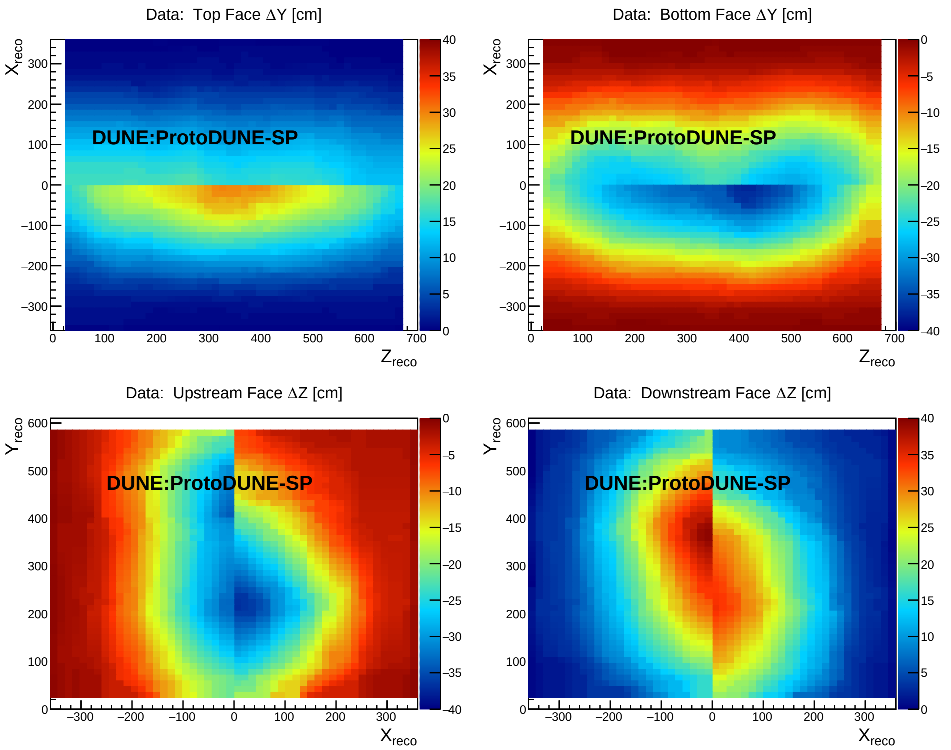

Figure 4.8: Projection of the measured offsets from the reconstructed entry and exit coordinates of cosmic muons crossing the cathode plane of ProtoDUNE-SP. In certain regions at the detector faces the offsets can be up to 40 cm. ProtoDUNE-SP beam particles enter through the upstream face at $x =-30$ cm and $y = 420$ cm, the measured offset δz in this region is of 30 cm. The asymmetry between the drift volumes is unexpected from the simulations. This is due to different fluid flow behaviour in the two volumes originating from the fact that the field cage is not placed centrally in the detector and the location of the purified LAr insertion and extraction flanges. Taken from [72]

ing crossing muons, second, the energy scale is determined with stopping muons as the energy deposition of minimum ionising particle is known better than 1%.

The deposited charge per unit length dQ/dx (ADC count × tick/cm) is subject to several detector-related effects such as gain variations in the electronics. They are taken care of in the signal preparations as discussed in Section 4.1. SCE affects the measured dQ/dx of tracks as the positions of the tracks are shifted and the local electric field may be different. The SCE effects are corrected by using the data-driven maps and applying scale factors for the electric field distortions [72]. Finally, after gain calibration and SCE correction, the residual non-uniformity of dQ/dx values are corrected for using a set of specifically selected cathode crossing muons.

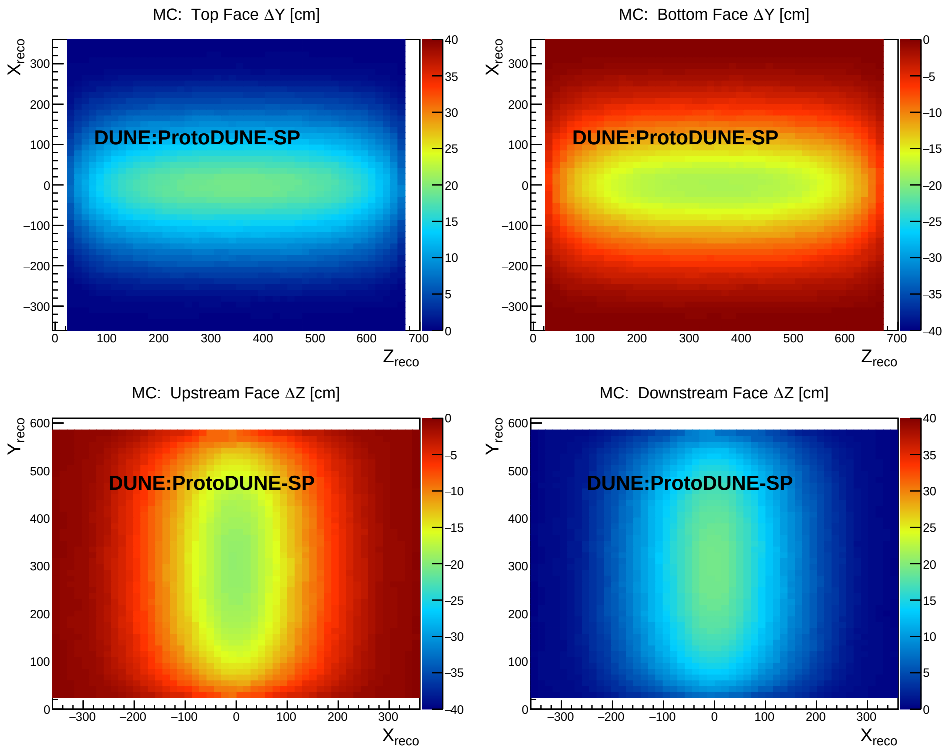

Figure 4.9: Simulated SCE offsets for ProtoDUNE-SP. The simulations suggest symmetric behaviour of SCE effects and offsets only up to 20 cm. In order to correct for the misestimated SCE effects in ProtoDUNE-SP, a data-driven map was produced in order to reproduce the measured SCE effects. Taken from [72]

The t_0-tagged muons are selected in specific TPC regions making sure the tracks cross the full volume of the detector and stay oriented in angular regions where the reconstruction of the track objects is well behaved filtering out tracks that are parallel to APA wires. Fluctuations of dQ/dx values in the yz plane arise from detector effects such as non-uniform wire response, dead channels, effects of electron diverters or transverse diffusion. A correction factor C_{yz} for the yz plane is developed by comparing local dQ/dx values in 5×5 cm^2 bins to the globally measured values.

In the drift direction, the measured dQ/dx is affected by the electron lifetime through attenuation and longitudinal diffusion. The measured dQ/dx value of a muon track segment close to the cathode will be lower than the dQ/dx value of a muon track segment close to the anode. After application of C_{yz} in a similar way a correction factor C_x is calculated by comparing 5 cm bins in x-direction to the globally measured values in the x-direction

$$\left(\frac{dQ}{dx}\right)_{calibrated} = N_Q C_x C_{yz} \left(\frac{dQ}{dx}\right)_{reconstructed}. \tag{4.1}$$

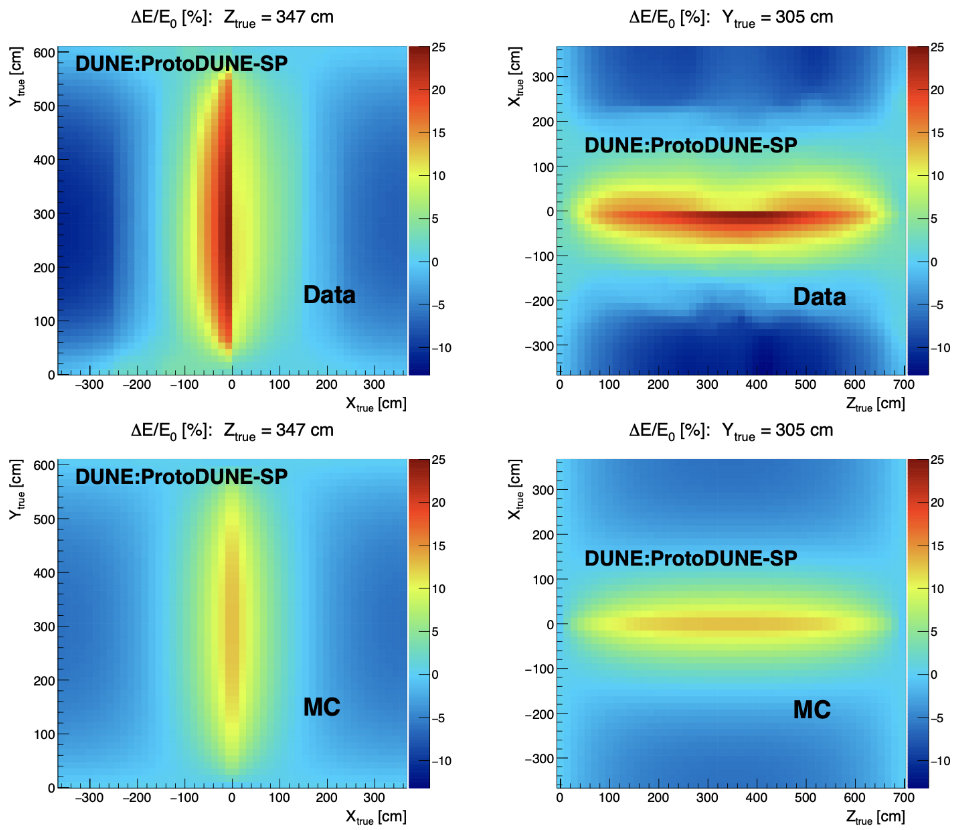

Figure 4.10: 2D projections in the z and y symmetry axis' for the relative field distortions in percent. The field distortions are expected to be strongest in the bulk of the detector where all the positive ions accumulate. The largest distortions can be up to 25% in data (upper two plots). The original simulations (down) only predict distortions of up to 12% which is in agreement with the wrongly predicted offsets of 20 cm as shown in Figure 4.9. Taken from [72]

A normalisation factor N_Q is applied in the end to reproduce the dQ/dx values observed at the anodes which are least subject to the detector effects as their drift distance is very short. The absolute energy scale is done by selecting cathode crossing stopping muons. They are found by requesting the track start to be in a larger fiducial volume and the track ends in a smaller volume inside the large volume. Again, angular regions are selected where the reconstruction is well behaved. A set of quality cuts remove broken tracks at APA boundaries, timing issues in the track hits, and track objects with Michel electron hits attached. A highly pure stopping muon sample remains after the cuts with a purity of 99.74% according to simulations [72].

In the MIP region of the stopping muon at around 120 to 200 cm from its stopping point from the calibrated dQ/dx values, the dE/dx values are fitted by using the modified Box model as described in Section 2.3 to correct for recombination effects, see Equation 4.2. C_{cal} is a freely varying parameter in the χ^2 minimisation of the fits. Effectively, it is a scaling factor accounting for residual effects that were not calibrated. Table 4.1 contains the values of the parameters in

$$\left(\frac{dE}{dx}\right)_{calibrated} = \left[\exp\left(\frac{\left(\frac{dQ}{dx}\right)_{calibrated}}{C_{cal}} \frac{\beta' W_{ion}}{\rho \mathcal{E}}\right) - \alpha\right]\left[\frac{\rho \mathcal{E}}{\beta'}\right]. \tag{4.2}$$

C_{cal}	Calibration constant used to convert ADC values to number of electrons
W_{ion}	23.6×10^{-6} MeV/electron (the work function of argon)
$\mathcal{E}$	E field based on the measured space charge map
ρ	1.38 g/cm^3 (liquid argon density at a pressure of 124.106 kPa)
α	0.93 [51]
β'	0.212 (kV/cm)(g/cm^2)/MeV [51]

Table 4.1: Parameters for the calibrated dEdx as described in Equation 4.2.

α and β' are the Modified Box model parameters which were measured by the ArgoNeuT experiment at an electric field strength of 0.481 kV/cm [51]. The calibration is performed on data and simulation Figure 4.11 shows the dQ/dx distribution for stopping muons before and after calibration as well as the final calibrated dE/dx for data and simulations normalised such that the maximum is one.

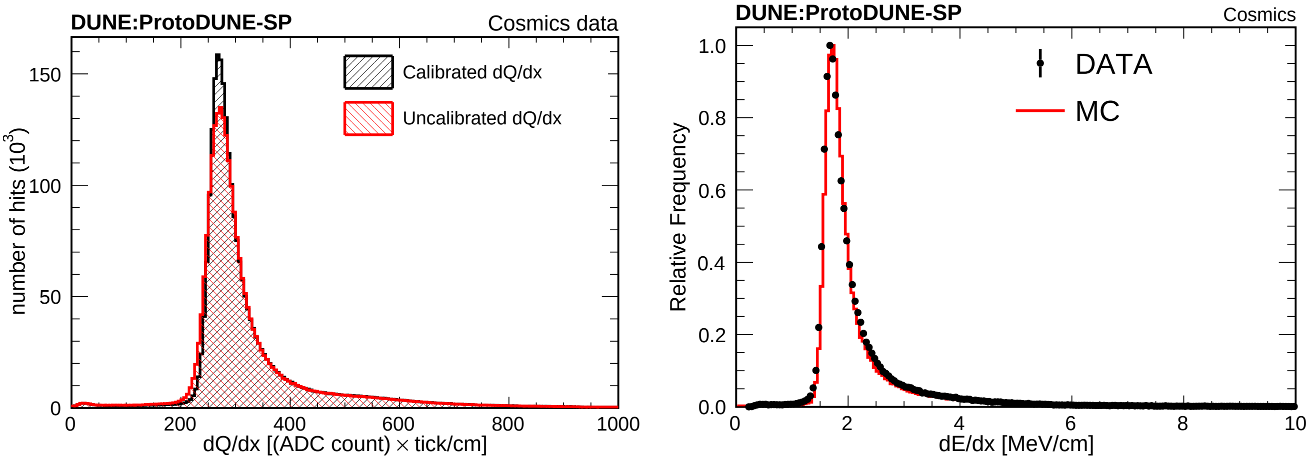

(a) dQ/dx calibration

(b) dE/dx data and simulation comparison

Figure 4.11: Calibration of the charge deposition for the stopping muon sample which is then used to derive the calibrated dE/dx using the modified Box model. The calibrated dE/dx shows data and simulations in comparison. The peaks have been normalised to one and the agreement is excellent. Taken from [72].

This chapter has described thoroughly the signal processing and data preparations of ProtoDUNE-SP data. An overview of the strong SCE effects has been given, however, apart from spatial distortions and trajectory squeezing for ProtoDUNE-SP beam particles the electric field distortions are luckily comparably small in the beam region and thus will have little influence on the local recombination factor for the energy measurement of beam particles. A quantitative estimate of the influences will be discussed in Section 6.4. Finally, the detector calibration to convert the measured ADC signals to charge signals and finally energy in the units of MeV has been discussed. The presented calibration procedures, as well as an in-depth understanding of those, lay the foundation for ProtoDUNE-SP beam particle or cosmic ray analysis which heavily rely on particle identification and energy measurements for the different steps.

5 SIMULATION, IDENTIFICATION AND SELECTION OF PION ABSORPTION EVENTS

In the present chapter I first describe the beam events of ProtoDUNE-SP and the MC simulations with the underlying models Section 5.1. Next, I specify the signals and backgrounds, as well as the event selection strategy in Section 5.2, Section 5.3, Section 5.4 and Section 5.5. Finally, I describe the performance of the event selection algorithm and irreducible background and reconstruction failures in Section 5.6 and Section 5.7.

5.1 SIMULATION OF EVENTS

Particle physics experiments use MC simulations to predict particle behaviour based on theoretical models and the detector model. Simulations are based on previously conducted measurements, the knowledge of the detector geometry and medium, particle interactions with matter, and theoretical models that are tested with the experiment. In this thesis, the simulations are used to predict the expected pion flux in ProtoDUNE-SP and study the effect of cuts in certain observables of the detector. Finally, a comparison between the measured and predicted pion cross-section in the theoretical models is done.

The simulation, reconstruction, and analysis framework used in ProtoDUNE-SP are based on the LArSoft [94] software tool kit. It is a kit widely used in LArTPC neutrino experiments based on C++ and ROOT[95]. It consists of a commonly used core and specific developed parts for the different experiments. It is commonly used for data analysis and interfaces with the event generators for beam particles. ProtoDUNE-SP MC simulations include the generation of the particle, their propagation in the beamline and the detector simulation.

The generation of the primary beam particles in the H4 beamline, their propagation, and possible interactions before the detector is done by the GEANT4 [96] based G4Beamline [97] tool and FLUKA [98]. The beamline was described in Section 3.9. A comparison between the estimated trigger rates by the event generators and data measurements is shown in Figure 5.1. So far, the discrepancies at higher momenta are not understood. The agreement for beam particles at 1 GeV/c momentum (considered for this analysis) is satisfactory.

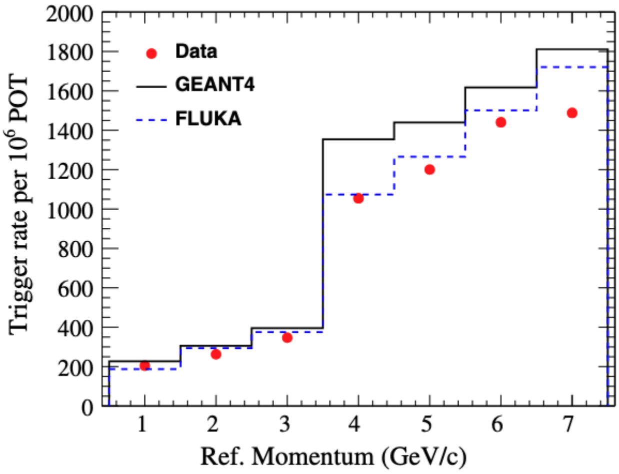

Figure 5.1: Comparison of ProtoDUNE-SP beam trigger rate predictions from GEANT4 and FLUKA event generators with measured data for all the momenta. Simulations and data agree for the lower momenta. Taken from [84].

The detector simulation includes the propagation of the particles in LAr, their energy deposition, and detector effects. The three main sources of particles in ProtoDUNE-SP are the particles from the incident beam referred to as *primary particles*, cosmic rays, and beam halo particles coming from the beamline and upstream sources. Cosmic rays are simulated by CORSIKA [99] and CRY [100] generators.

Primary beam particle propagation is simulated by GEANT4 with a particle tracking step size of 300 μm. This is much smaller than the detector resolution $\mathcal{O}$(cm) and is important in order to understand the particle processes at each propagation step. Furthermore, a small step size allows to accurately simulate small-scale processes like showers. The energy deposition, *i. e.* propagation of the particles through ionisation electrons and scintillation light are simulated. For example, a minimum ionising particle (MIP) will deposit thousands of electrons and photons per cm, releasing 2 MeV/cm.

The detector simulation takes care of drifting the ionisation electrons to the wire planes of the APA and simulates the generated signals including wire response, gain, and electronics noise. Detector effects like electron-ion recombination, longitudinal and transversal diffusion, as well as electric field distortions, and electron capture on impurities are simulated. The generation and propagation of beam particles provided by GEANT4 before reconstruction is referred to as the MC-truth level. For real data, the analyzer has only access to the reconstruction level provided by Pandora. It is often referred to as MC-reco, *i. e.* the measured quantities. MC-reco should replicate reconstructed ProtoDUNE-SP data as close as possible and include aforementioned detector effects, reconstruction efficiencies, and resolution. MC simulations include the MC-truth and reco level and allow to understand certain detector effects and estimate the quality of certain observables as is explained in the following paragraph. On a regular time basis, new MC simulation samples, with refined and better understood detector effects are produced in order to validate the ProtoDUNE-SP data results.

Beam Particle Reconstruction and Back Tracking

Detector signals, both real and simulated, are reconstructed using the Pandora framework [88]. Signals from the wires are grouped to hits and clustered. Dedicated algorithms reconstruct the particle trajectory, energy, interaction points, and associate outgoing particle daughters.

Initially, clusters of hits are reconstructed under the cosmic ray hypothesis. Tracks entering from the top and leaving the detector at the bottom including timing information that is out of phase with a beam trigger are clear cosmic ray candidates that are removed for beam particle analysis. After the cosmic ray removal, the detector is divided in several spatial regions through a 3D slicing algorithm. The division is done in a way such to isolate all hits originating from single particles. They can contain beam particles as well as cosmic rays that were not removed previously. Test-beam candidates are tested with the cosmic ray and test-beam assumption based on the position and direction of the trajectories. A boosted decision tree (BDT) determines the reconstructed objects of test-beam origin. For correct determination of the beam particle, topological information of the reconstructed track is used. Furthermore, the interaction vertex is determined and daughter particles after interaction are associated to the parent beam particle as shown in Figure 5.2. The reconstruction does not always determine the correct vertex position. Angles of daughter particles with respect to their parent beam particle may be too small to find an interaction point as is further elaborated in Section 5.7.

Within the LArSoft framework, there is the possibility to use a BackTracker service that associates the reconstructed particle track to the MC-true particle that was responsible for its generation. The service comes with a set of ambiguities, as it matches the reconstructed hits to the simulated charge deposits which may have originated from several particles. Pragmatically, reconstructed particle tracks are matched to MC-truth particles based on the largest contribution of the truth particle to the reconstructed track. The service is a useful tool to understand and assess the reconstruction quality of certain observables and evaluate the effect of cuts within the model uncertainties.

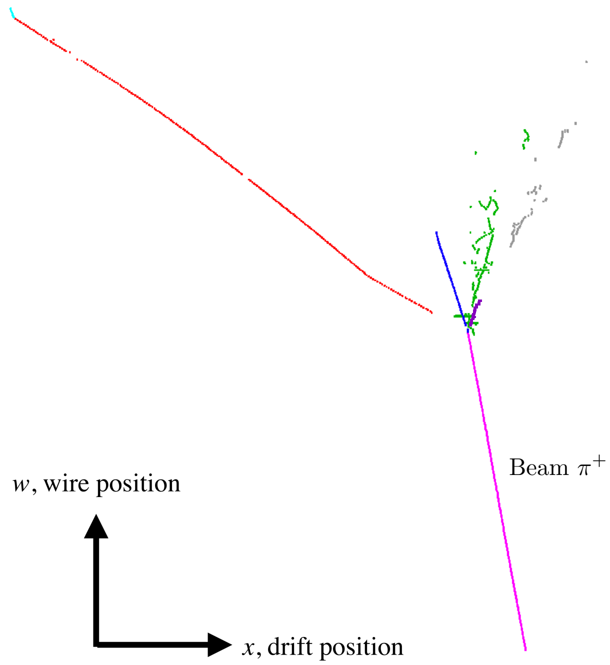

Figure 5.2: π^+ beam particle event reconstructed by Pandora [88] and tagged as beam particle candidate. Daughters / secondaries of the parent beam particle (magenta) after interaction are also associated to the original test beam particle. Different daughter particles are marked with different colors. Taken from [72].

5.2 SELECTION STRATEGY AND SIGNAL TOPOLOGY

To perform a data analysis aiming to measure a specific process in a detector, a careful signal definition and background classification are necessary. For the π^+ absorption interaction, the signal definition follows as a baseline the in Section 2.5 defined π^+ interactions based on the outgoing daughter particles. For the background classification and signal classification, certain detector characteristics like reconstruction efficiency depending on the energy resolution or vertex identification capabilities have to be kept in mind. These effects are addressed further in Chapter 6. After defining the signal topology, a strategy for signal selection is developed maximising efficiency and purity of the selected sample which are defined as:

$$Purity = \frac{N_{trueSelected}}{N_{totalSelected}} \qquad Efficiency = \frac{N_{trueSelected}}{N_{trueAvailable}}, \tag{5.1}$$

where $N_{trueSelected}$ is the number of true selected signal events. $N_{totalSelected}$ is the total number of selected events after a cut including background and signal events and $N_{trueAvailable}$ is the number of true available signal events from the beam either before the cut or at the very beginning of the event selection.

It is important to keep the event selection cuts simple and low in numbers as each cut on an observable can act as a source of systematic uncertainty in the measurement. The distributions from simulations and data are overlaid in the plots to verify that MC represents data well for the chosen observables. Throughout the sections, secondary particles may also be referred to as daughter particles with respect to the primary or parent beam particle. Signal and background types are defined in Table 5.1 and were discussed in detail in Section 2.5. All definitions require an incoming beam pion. Candidate events from ProtoDUNE-SP for the interaction topologies are shown in Figure 5.3.

	Secondary Particles		
	π^+	π^0	p^+ or n
Pion Absorption Signal	✗	✗	✓
Pion Charge Exchange Background	✗	✓	✓
Pion Inelastic Background	✓	✗	✓

Table 5.1: Definition of π^+ inelastic interactions as a function of outgoing secondary particles. The event selection follows this signal definition in order to isolate pion absorption interactions.

The event selection of signal candidates is generally based on four reconstructed observables:

- Reconstructed position and direction of beam event candidates
- Track-, shower- or Michel-like topology of the reconstructed objects by using a Convolutional Neural Network (CNN) [101]
- Energy loss per unit distance of the reconstructed objects to perform Particle Identification (PID)
- Reconstructed number of hits

Seven serial cuts on the observables are performed to extract π^+ absorption event candidates and are listed in their following order below. Each cut will be described separately in the subsequent sections. The effect of each cut will be shown on the reconstructed z position of the beam particle candidates for data and simulations. The observable is chosen as it is directly tied to the estimation of the pion kinetic energy which is the variable the cross-section measurement is performed with. Cuts 1 through 5 isolate the primary particle to be a beam π^+ candidate interacting within the fiducial detector volume. The boundaries in the

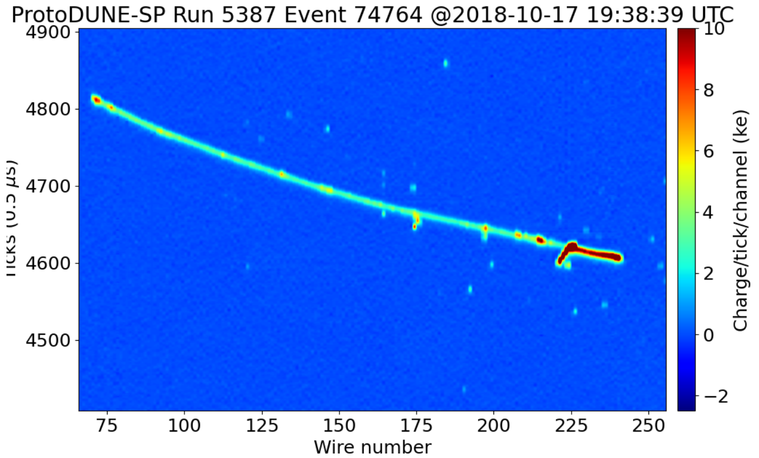

(a) Pion absorption signal candidate.

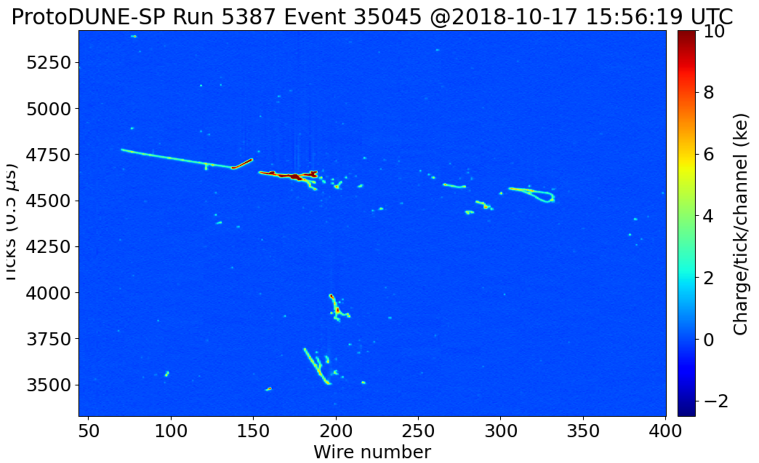

(b) Pion charge exchange candidate.

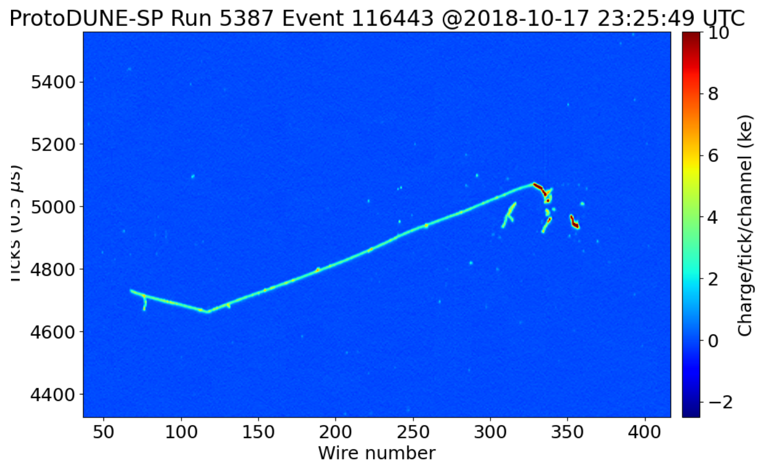

(c) Pion inelastic candidate with elastic kink.

Figure 5.3: ProtoDUNE-SP Run 5387 at 1 GeV/c beam momentum data event displays before reconstruction. Candidates for pion absorption, pion charge exchange and pion inelastic interaction. At the pion interaction vertex in Figure 5.3a two protons coming from the pion absorption process as secondary particles are visible. In the pion charge exchange process Figure 5.3b a π^0 is emitted decaying in two photons γ's. The γ produce a cascade of e^+/e^- pairs and more γ's, also called electromagnetic showers. Pion inelastic interactions can result in nuclear break ups with emission of several nucleons and electrons producing energy depositions and tracks around the interaction vertex as shown in Figure 5.3c.

fiducial volume are set by the end of the first wire plane (APA) of the TPC from the beam entry. Cut 6 and 7 extract the pion absorption interaction channel by rejecting secondary charged π^+ and showers coming from π^0 decays. The performance of the event selection is discussed in Section 5.6.

1. Select from the beam line instrumentation trigger logic π^+ (and μ^+) candidates (Section 5.3)
2. Require the primary track to be identified as a track-like beam particle from Pandora reconstruction (Section 5.4)
3. Select candidate beam π^+ with reconstructed initial position corresponding to the beam window region (Section 5.4)
4. Fiducial volume cut on beam π^+ candidates to interact within the first APA of the TPC (Section 5.4)
5. Remove background events from beam μ coming from pion decay upstream of the detector by identifying Michel electrons from μ-decay (Section 5.4)
6. Reject events with secondary $\pi^\pm$ candidates (Section 5.5)
7. Identify shower candidates within the secondary particles and reject them in order to isolate the π^+ absorption candidate events (Section 5.5)

The PDSP Analyzer Module for Beam Particles

The PDSP Analyzer module [102] is a LArSoft module producing a ROOT flat tree for beam particle analysis by extracting relevant information of the reconstructed entities. For MC simulations it also extracts the corresponding true and the BackTracker matched entities for each event. The module was developed on purpose for this analysis and is now widely used in the ProtoDUNE-SP analysis group.

The PDSP Analyzer module was the key tool for the development of the event selection and cut optimisation. Each entry in the flat tree corresponds to a beam particle. Several branches store important information on the beam particle such as:

- Metadata like the run number, event number, and a flag whether the event is from MC simulation or data
- Beam instrumentation information such as the measured momentum and the beamline PID info

- Reconstructed information of the primary beam particles. *E.g.* track start coordinates, end coordinates, energy deposits, CNN score values, number of deposited hits, etc.

- Vectors with reconstructed information on the associated secondary (daughter) particles of the beam particles. Again, information like daughter track start, end, energy deposits, and CNN values are saved

- If the events are from MC simulation the underlying MC-true (at the generator-level) is stored

- The information of the BackTracker service is saved

The event selection and pion absorption cross-section measurement can be carried out with the ROOT flat tree produced with the PDSP Analyzer module. Swift and easy data analysis and handling is done by using the rDataFrame classes and functions within ROOT [103]. The analysis code used for the event selection can be retrieved here [104].

5.3 PARTICLE IDENTIFICATION WITH BEAM INSTRUMENTATION

Section 3.9 described the BI and its capability to provide a reliable sample of beam pion and muon candidates with a momentum measurement on a particle-by-particle basis. Table 5.2 shows the recorded triggers and expected triggers issued by the beam instrumentation for the different particle types and momenta. The expected triggers are compiled from the MC simulations of the beam line. The analysis presented in this thesis uses the data of π^+ at 1 GeV/c. The measured momentum distribution for π^+ (and μ^+) like triggers from the beam instrumentation is shown for data and MC simulations in Figure 5.4. Figure 5.5 shows the selected beam particle candidates from the beam instrumentation as a function of the beam particle reconstructed end position in the z-coordinate. The purity for the initial sample estimated from the simulations is noted in Table 5.3.

5.4 SELECTION OF PRIMARY PION EVENTS

The beam line sample π^+ (μ^+) triggers is now further filtered by selecting Pandora beam particle candidates the effect of the cut is shown in Figure 5.6.

The beam position cuts ensure that the primary beam particle entered in the region of the beam plug where the energy loss is minimised with respect to outside of the beam plug and can properly be taken into account.

Momentum GeV/c	Trig Rec. $\times 10^3$	Trig Exp. $\times 10^3$	Exp. π^+ $\times 10^3$	Exp. p^+ $\times 10^3$	Exp. e^+ $\times 10^3$	Exp. K $\times 10^3$
0.3	269	242	0	0	242	0
0.5	340	299	1.5	1.5	296	0
1	1089	1064	382	420	262	0
2	728	639	333	128	173	5
3	568	519	284	107	113	15
6	702	689	394	70	197	28
7	477	472	299	51	98	24
Total	4173	3924	1693.5	777.5	1381	72

Table 5.2: Recorded and expected triggers of the ProtoDUNE-SP beam line instrumentation. For the analysis subject of this thesis the data of pions at 1 GeV/c has been used [105].

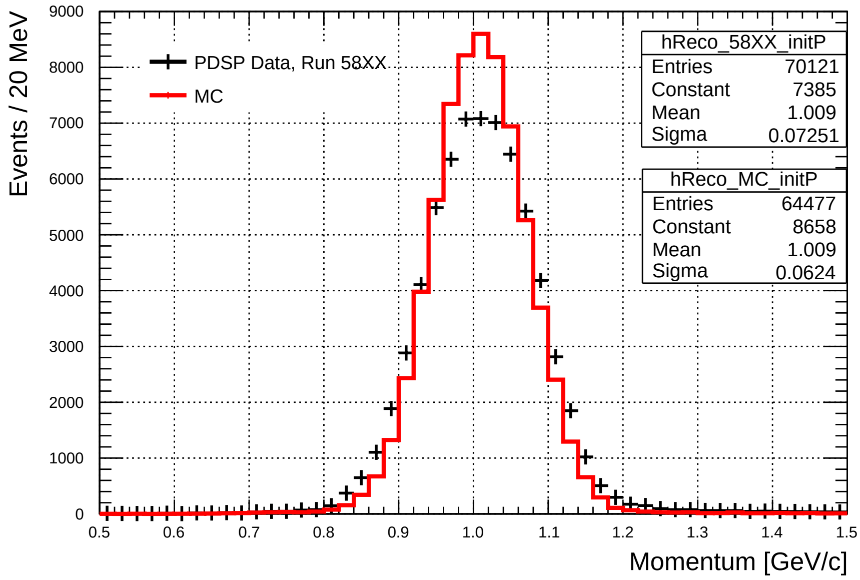

Figure 5.4: Momentum from the beam instrumentation for π^+-like triggers at 1 GeV for data and simulation. The MC distribution is area normalised to data. The fit parameters for a gaussian fit on the data and simulation distributions are noted in the boxes. The width of the MC momentum distribution (red) is 0.062 GeV/c and for data it is 0.0725 GeV/c. Thus, the simulations are underestimating the distribution width. This will be further discussed in Section 6.1.

The reconstructed distributions for the xyz-coordinates of the beam particle track start positions are shown in Figure 5.7 for data and simulations. For data and mc the spatial SCE corrections (Section 4.4) have been applied. For each distribution, a Gaussian fit has been performed. The values of the fits are noted in Table 5.4.

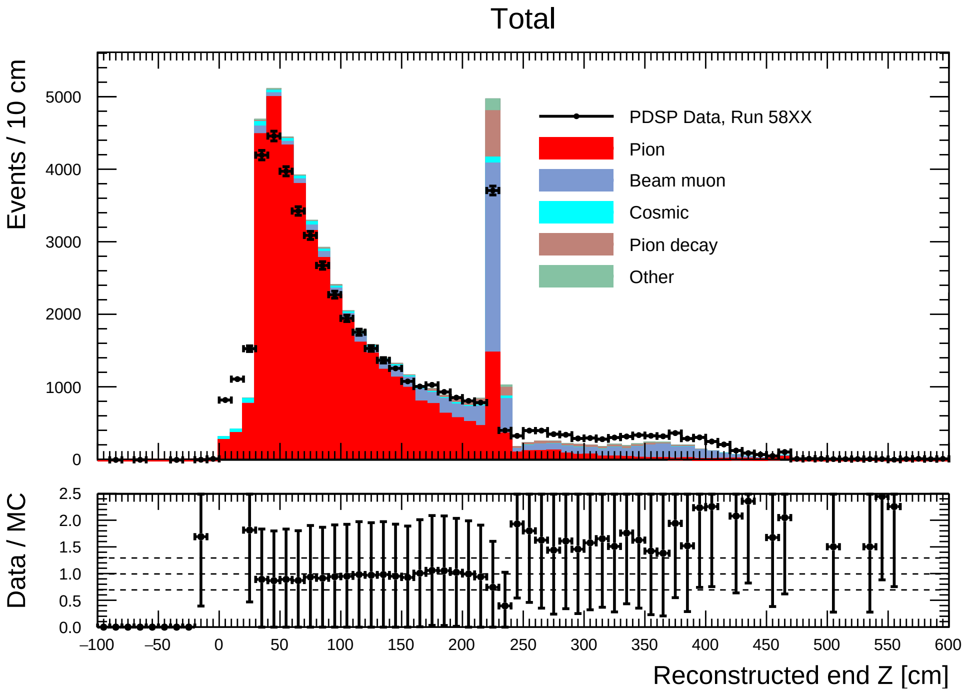

Figure 5.5: Distribution of all available simulation and data events for beam instrumentation pion and muon triggers. The agreement of data and simulation is good until the APA boundary at 228 cm.

	Incident π^+		**π^+ Absorption**	
	Purity	Efficiency	Purity	Efficiency
Total	0.81	1	0.24	1

Table 5.3: Efficiency and Purity for initial sample from the beam instrumentation pion triggers.

Two peaks on the data y-coordinate distribution are visible at higher y-values. This effect has been investigated and found to be due to E-field distortions that are not accounted for in the simulations which also is the reason for the mismatch in the estimated σ in the coordinate. The E-Field distortions arise from the charging up effect of the end wall FR4 box beams that are above the beam plug (see Figure 3.3). The electrically insulating FR4 box beams accumulate charge and visibly distort the E-field above the beam plug region. The E-field distortions are such that the field lines terminate on the box beams and make an enhanced amount of beam particles appear to start there. Investigations were reported in [106].

Data MC differences in the z-coordinate arise from the fact that SCE effects. They are not precise enough simulated especially in the beam entry region and thus corrections in data do not return the particle starting point to $z = 0$ at the beam entry point. If there were no SCE effects, the reconstructed track start position in z should be found around $z = 0$.

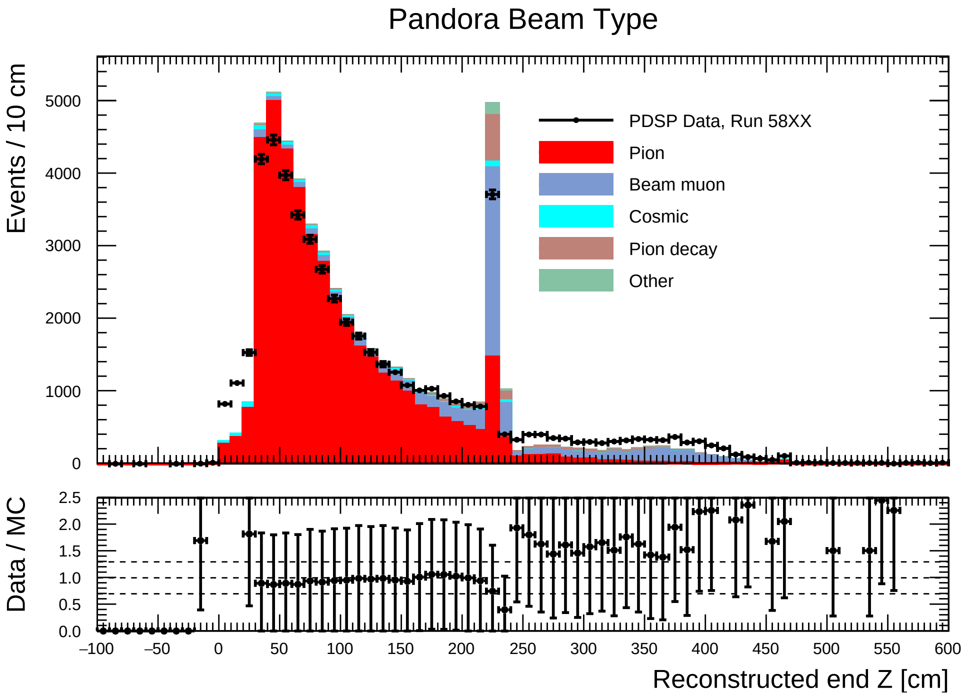

Figure 5.6: Reconstructed end Z distribution after selecting Pandora beam particle candidates.

	Data X	MC X	Data Y	MC Y	Data Z	MC Z
Mean	-28.6	-30.86	424.6	422.4	2.707	0.1151
Sigma σ	4.888	4.944	5.397	4.406	1.215	0.2223

Table 5.4: Fit values of the track start distributions shown in Figure 5.7. The shifts are due to discrepancies between simulation and data as for example the SCE effects in the beam entry region.

The *beam position cuts* do not act on absolute xyz-coordinate values as agreement of data and MC simulations is not representative. Thus, the fit values of the mean and standard deviation σ of the Gaussian distributions are used to compute a cut observable as shown in Figure 5.8. The observable reflects the relative shift of the reconstructed beam particle position with respect to the standard deviation of the distribution for all pion trigger beam particles in the detector coordinates. On a particle-by-particle basis it is assessed whether the beam pion candidate satisfies the beam position requirements as described in Equation 5.2.

$$\text{Beam Position Cut} \qquad \sqrt{\left(\frac{\Delta x}{\sigma_x}\right)^2 + \left(\frac{\Delta y}{\sigma_y}\right)^2} < 3 \quad \text{AND} \quad \left|\frac{\Delta z}{\sigma_z}\right| < 3, \tag{5.2}$$

where Δxyz is the difference between the reconstructed start position of the concerned particle and the mean xyz of either data or simulation as noted in Table 5.4.

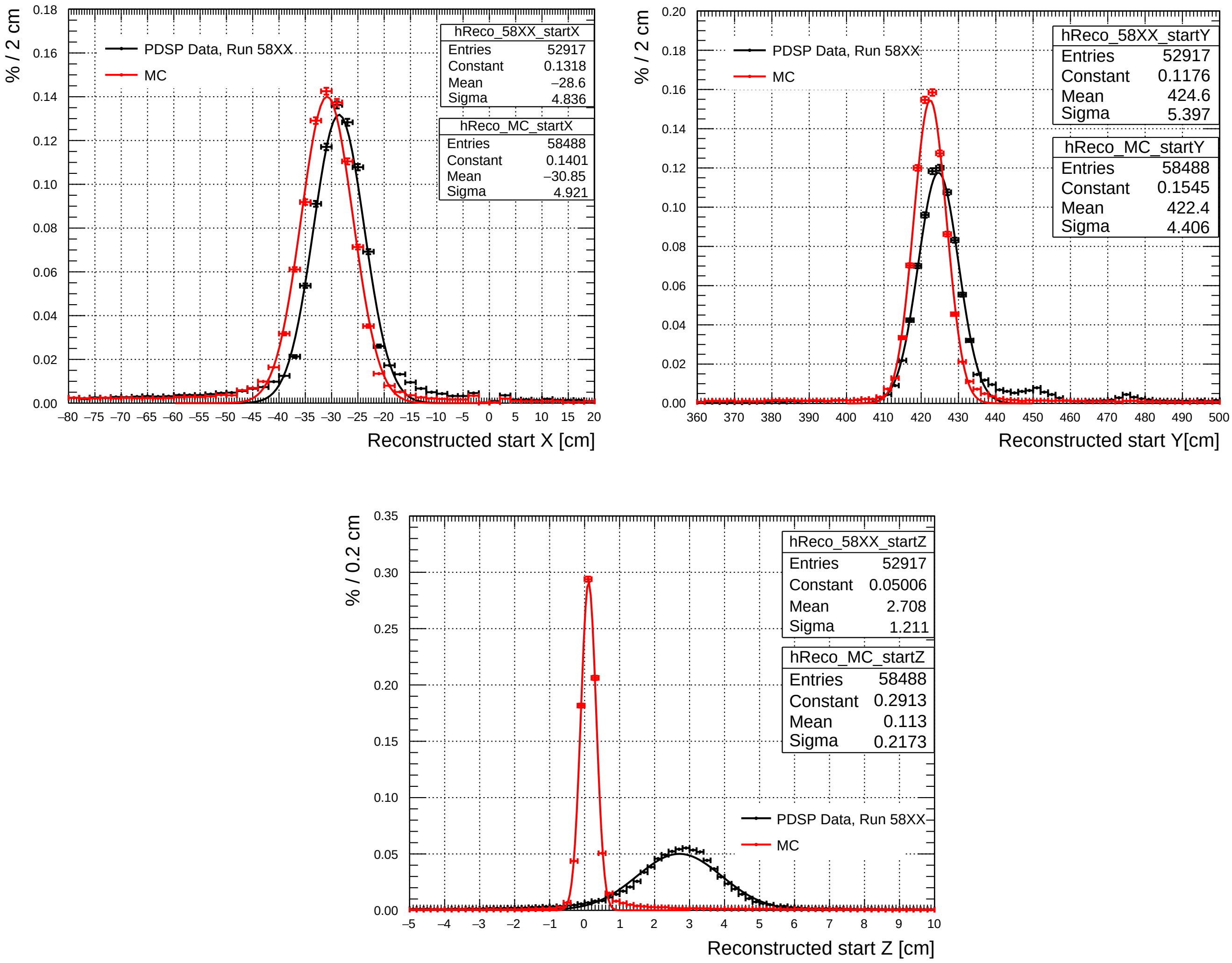

Figure 5.7: Data vs simulation Pandora beam track start coordinates corrected for SCE effect. In x the agreement of data and simulations are reasonable apart from a slight shift of the mean. The yz coordinates show less agreement. In y two emerging bumps are visible in data. Investigations showed that this is due to a charging up effect of the box beams (support structure) of the FC endwalls. The box beams are located above the beam plug. The effect causes Efield lines to end on these box beams and thus makes more beam tracks appear starting there. The start position in z is broader in data than simulations and also shifted by $\sim$2.5 cm. The differences arise from the simulated SCE effect that does not represent data well yet. This will be addressed in upcoming simulation campaigns for ProtoDUNE-SP.

The distributions of $\frac{\Delta xyz}{\sigma_{xyz}}$ both for data and simulations are shown in Figure 5.8. The general agreement is reasonable. However, the previously pointed out discrepancies in the observable of the z-coordinate are still visible (see Figure 5.8c). The beam position cut effect on the pion sample is shown in Figure 5.9 and the associated efficiencies and purities for the Pandora reconstruction and beam position cuts are listed in Table 5.5.

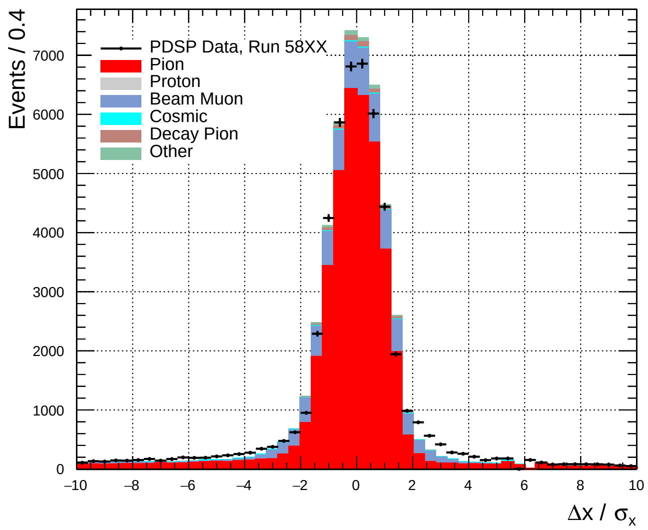

(a) Beam cut observable in x

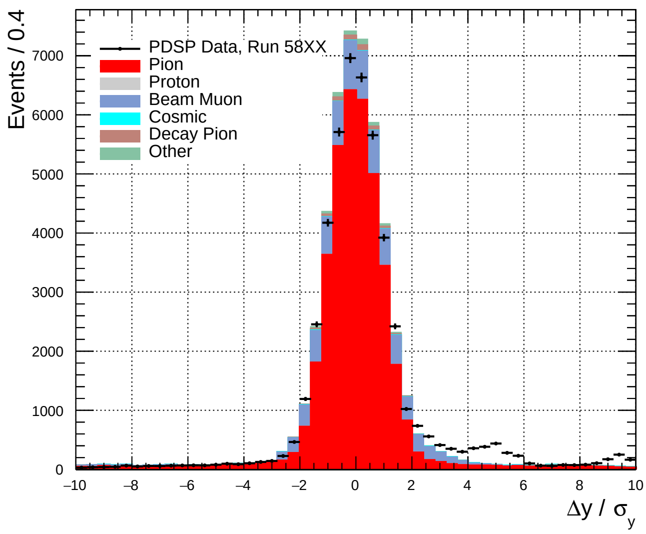

(b) Beam cut observable in y

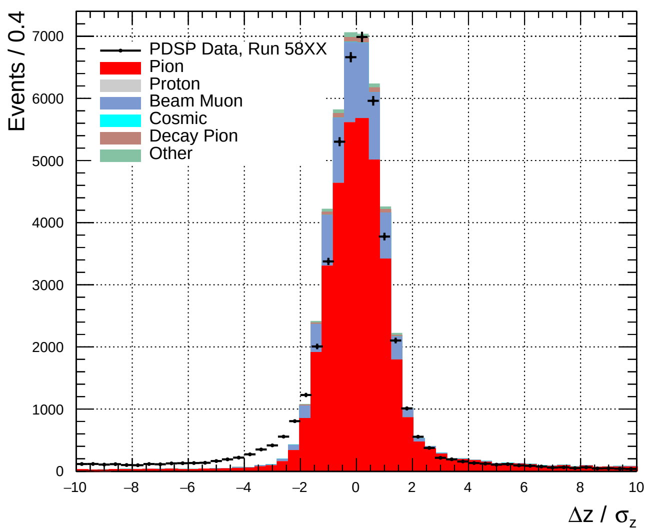

(c) Beam cut observable in z

Figure 5.8: Beam position cut observables in xyz. The cut observables are computed for each beam particle as $\frac{\Delta xyz}{\sigma_{xyz}}$, where Δ is the difference between the mean-xyz and the beam particle reconstructed start position xyz for data and MC respectively. MC is normalised to data. The agreement for negative components of Figure 5.8c is not entirely satisfactory for the currently used simulation. It is due to the mis-estimation of the SCE effects. The mean and standard deviations used for the beam quality observable computation are listed in Table 5.4. The cut values are noted in Equation 5.2.

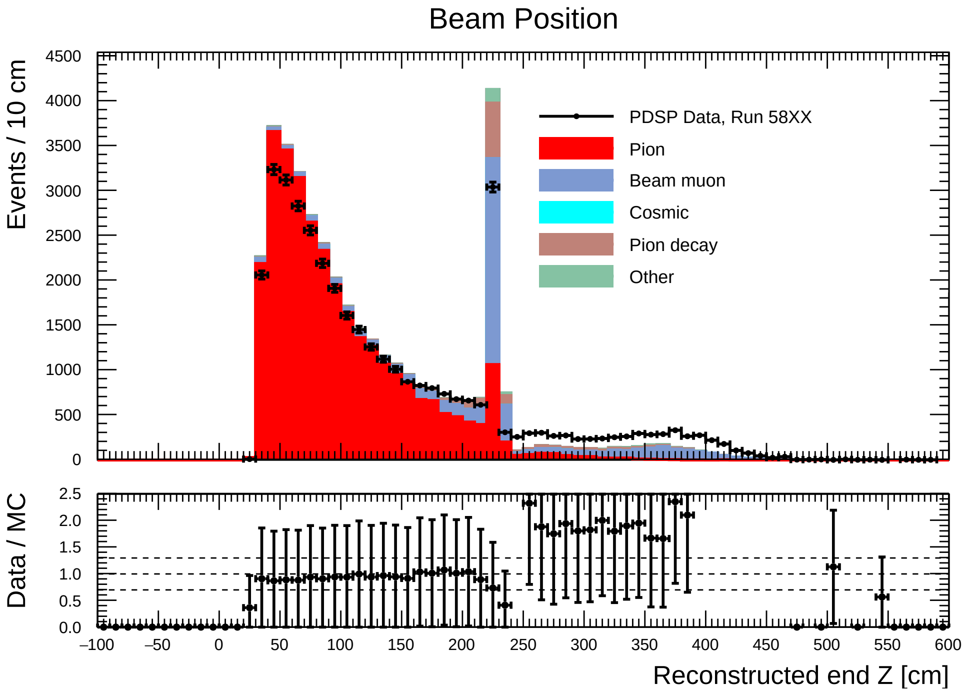

Figure 5.9: Reconstructed end Z distribution after beam position cuts.

	Incident π^+		**π^+ Absorption**	
	Purity	Efficiency	Purity	Efficiency
Pandora	0.80	0.84	0.24	0.88
Beam Position	0.80	0.63	0.26	0.71

Table 5.5: Cut efficiencies and purities for the Pandora beam particle reconstruction and the beam position cuts. The beam position cuts reduce the efficiency for the incident pions, however the purity is maintained.

Beam Muon Background and APA Boundary Issue

A major source of background to the pion absorption cross-section measurement are primary beam muons. They are a source of π^+ decays in the beamline or inside the LArTPC. Within the beamline instrumentation, the μ^+ cannot be distinguished from π^+ as has been pointed out in Section 5.3. The beam position cuts already reduce some of the beam background contributions. However, a large fraction of beam μ^+ remains present (see Figure 5.8). The μ^+ do not undergo hadron interactions but propagate further in the LArTPC than π^+ and will decay in the following channel: $\mu^+ \rightarrow e^+ + \nu_e + \overline{\nu}_\mu$. A further limiting factor to the pion absorption cross-section measurement and especially its range is the simulation of the boundaries between APAs. Electric field distortions at the APA boundaries come from electron diverters (ED). The ED were originally installed to divert electrons that would be lost in the APA gap onto the wire planes. However, their purpose was not effective.

Unfortunately, the ED distort the electric field at the APA boundary and cause the reconstruction algorithms to break apart beam particle tracks that cross from one APA to the next. Currently, the electric field distortions at the boundary of the APAs are not well simulated. In consequence, the track-breaking behaviour of the reconstruction is not comparable between data and simulations. The two following cuts that are discussed address the issues mentioned.

Fiducial Volume Cut at APA Boundary

In order to reduce the beam μ^+ content and remove particles that cross the APA boundary, a fiducial volume cut at the APA boundary is applied referred to as cut 4 in the previously given list or *APA*3 *cut*.

$$\text{APA3 Cut} \qquad \text{reco endZ} < 220\text{cm} \tag{5.3}$$

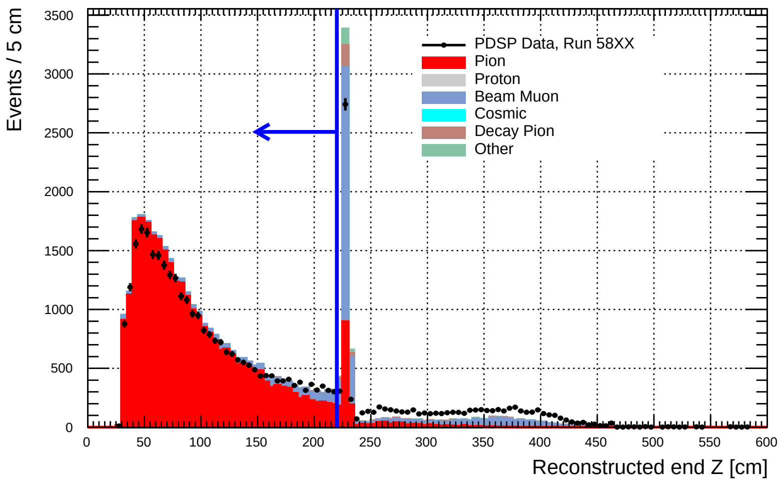

Figure 5.10: Overlay of data and MC simulations for beam particles passing the Pandora and beam position cuts. The distribution shows the z-coordinate of the beam particle end point. At 228 cm the amount of tracks ending is excessive. This is due to the fact that in this region the beam tracks cross the APA boundary and electric field distortions from the electron diverters are present. Simulating the distortions in that region is not trivial. The mis estimation of the distortions in MC is the source of the discrepancy between data and MC for endZ $>$ 228 cm. A fiducial volume cut is applied and only particles with endZ $<$ 220 cm are kept for the data analysis as indicated by the green line. Furthermore the cut reduces the beam muon background component.

Figure 5.10 shows the distribution of the beam particle end points in the z-coordinate. The track-breaking effect for simulation and data at the APA boundary is visible at 228 cm. Note how the data sample has fewer track end points than the simulations in that bin. The MC simulations estimate a higher track breaking with respect to data, which is wrong. In consequence, for endZ $>$ 228 cm the data points are systematically higher than the simulated distribution. Data shows that the track breaking is overestimated in the simulations. The cut value at 220 cm is placed where data and estimations of the beam particle track end points still agree. It is marked with a blue line in Figure 5.10. The electric field distortions caused by the APA boundary extend down to 223 cm. For this reason, the cut value was conservatively placed at 220 cm. The APA3 limits the pion absorption cross-section measurement range in energy as the track breaking at the APA boundary and beyond is not well understood. However, it also efficiently reduces the μ^+ background component as beam muons decay mostly in the region beyond APA3 (see Figure 5.10). The effect of the APA3 cut on the reconstructed primary end z-distribution is shown in Figure 5.11. The efficiency and purity estimates of the cut are summarised in Table 5.6.

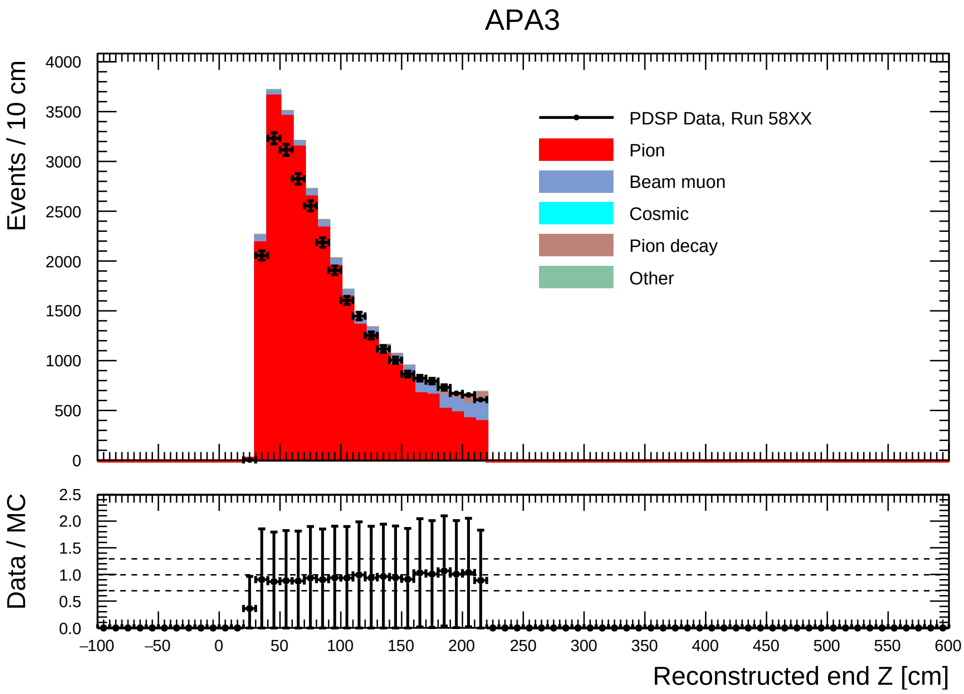

Figure 5.11: Reconstructed end Z distribution after APA3 cut at 220 cm.

CNN Michel Score

A further cut to reduce the μ^+ background component in the selected beam pion candidate sample uses the output of a Convolutional Neural Network (CNN) [101] for ProtoDUNE-SP data. CNN's are artificial networks based on Machine Learning (ML) techniques. They are well suited for pattern recognition in images. As LArTPCs provide high spatial resolution images of particle interactions, ML-based approaches for classification of interaction types and energy reconstruction are well suited for data analysis purposes [107]. The CNN algorithm specifically developed for ProtoDUNE-SP data provides a classification of different track topologies. The CNN output is a score between 0 and 1 for charge depositions (hits) of primary beam particles or beam particle daughters, as well as hits around an interaction vertex. The available classifications are:

- Michel Score

  Michel electrons from muon decay leave a distinctive signature in LArTPCs of short $\sim$5 cm tracks with a kink away from the long muon track and surrounded by photonic energy deposits as shown in Figure 5.13. A CNN Michel score close to 1 at the primary particle vertex indicates a Michel electron candidate from muon decay.

- Track - Shower separation, Track Score

  The CNN can classify hits coming from a track-like or shower-like topology. In ProtoDUNE-SP, the showers dominantly come from electromagnetic cascades of photons and electron-positron pairs. *E.g.* a π^0 decaying to two photons producing each an electromagnetic shower as shown in Figure 5.3b. A track score close to 1 indicates a track-like topology. If close to 0 it is a shower-like topology. The track score will be used to remove pion charge exchange candidates from the pion absorption sample. The cut is described in Section 5.5.

A background reduction of primary beam μ^+ is achieved by using the Michel score output of the charge deposits at the vertex of the beam particle. The cut is applied as follows:

$$\text{MICHEL SCORE} \qquad \text{Michel Score at primary vertex} < 0.55, \tag{5.4}$$

and the distribution of the CNN Michel Score is shown in Figure 5.13 for data and simulations. The effect of the Michel Score cut on the reconstructed end Z distributoin is shown in Figure 5.14 and the purity and efficiency estimate of the

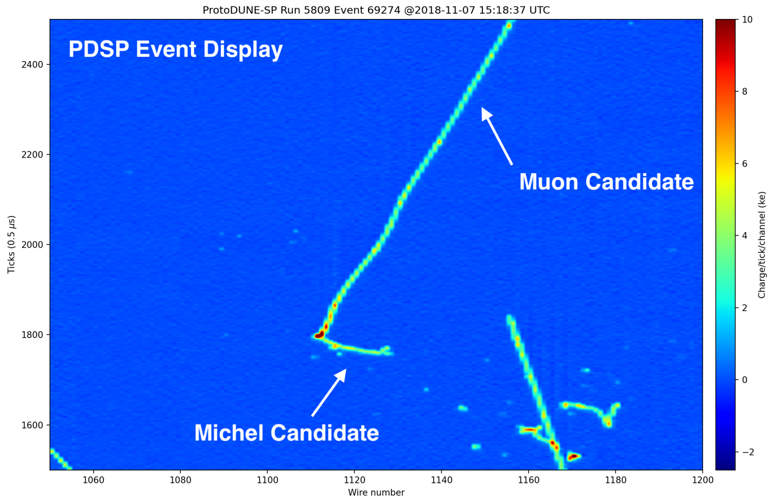

Figure 5.12: ProtoDUNE-SP event display. Candidate muon decay with Michel electron.

cut are given in Table 5.6. The purity and efficiency listed for the incident beam pion sample after the Michel Score cut are the final values for the beam pion selection.

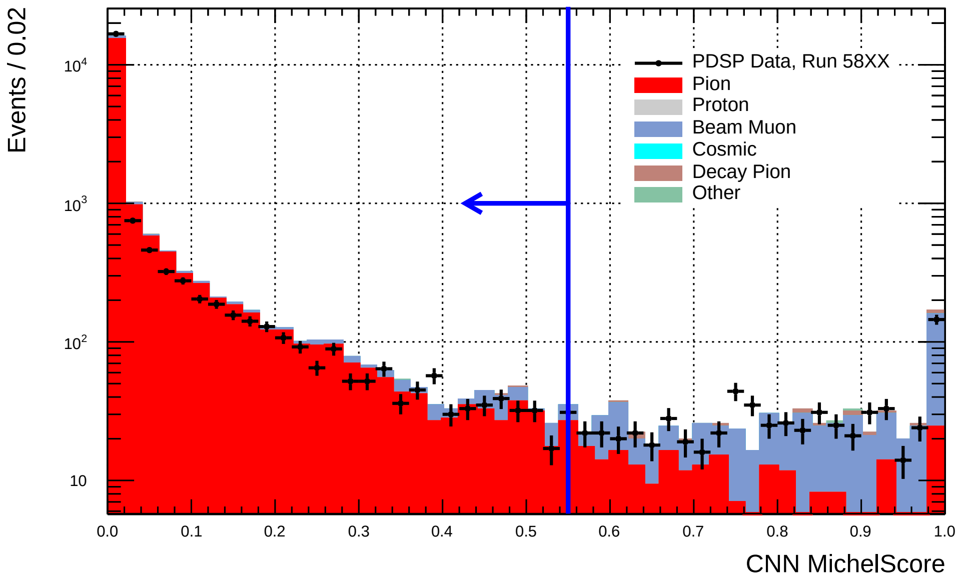

Figure 5.13: CNN Michel Score distributions for charge depositions at the beam particle vertex. A michel score close to 1 indicates that the topology of the charge deposits resembles a muon decay Michel electron. Primary beam μ^+ are a background for the π^+ selection. After selecting Pandora beam particles, passing the beam position cuts and ending before the APA3 boundary, events with a Michel score > 0.55 are removed as they are likely to be μ^+ events from the beam.

	Incident π^+		**π^+ Absorption**	
	Purity	Efficiency	Purity	Efficiency
APA3	0.93	0.59	0.30	0.65
Michel Score	0.94	0.59	0.31	0.65

Table 5.6: Efficiency and purity changes for the APA3 and Michel Score cut. After the Michel Score cut the selection of the incident beam pion candidates is complete.

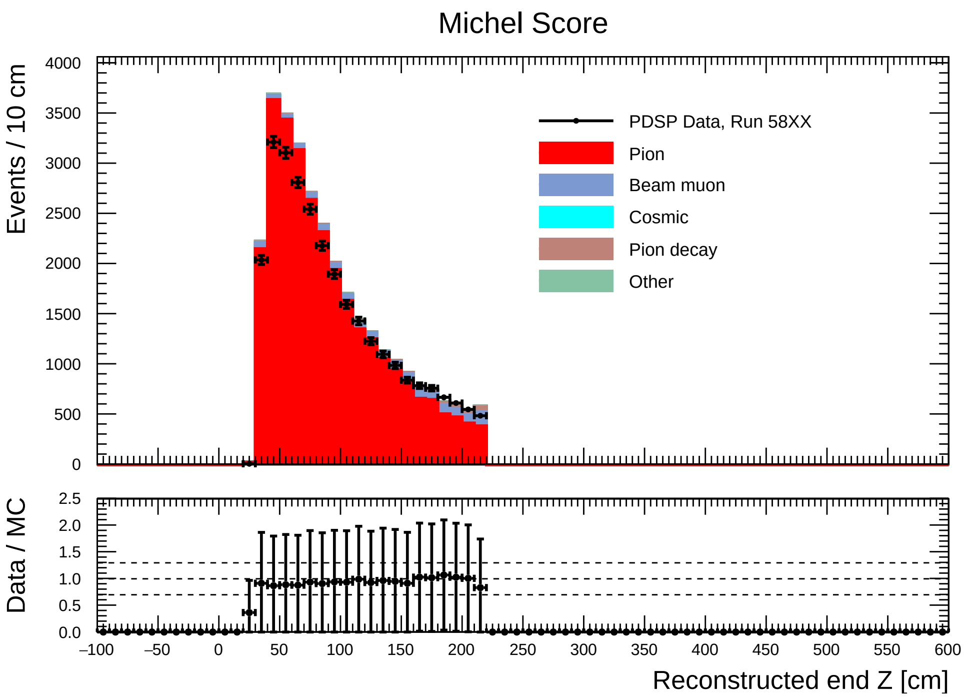

Figure 5.14: Reconstructed end Z distribution after the Michel score cut.

5.5 SELECTION OF PION ABSORPTION EVENTS FROM SELECTED PRIMARY PION SAMPLE

Isolating pion absorption events requires rejecting pion interactions with secondary pions or secondary electromagnetic showers coming from the π^0 decay produced by a pion charge exchange interaction. In the first step, the reconstructed secondary particles of a beam pion candidate are separated into two categories of shower-like and track-like daughters. The separation of track and shower candidates is done with a categorisation of the CNN [101] output described in Section 5.4.

Figure 5.15 shows the distribution of the CNN TrackScore for the daughter particles of selected primary pion candidates. Photons and electrons have a shower-like topology. Therefore, their track score is low. Protons, pions, and muons leave track-like trajectories in the LArTPC. The CNN output shows their track score to be higher. The separation of track and shower daughters is done in the following way and the value was chosen to optimise the selection efficiency and purity.

$$\text{Daughter Track Candidate} \qquad \text{daughter Track Score} > 0.3 \qquad (5.5)$$

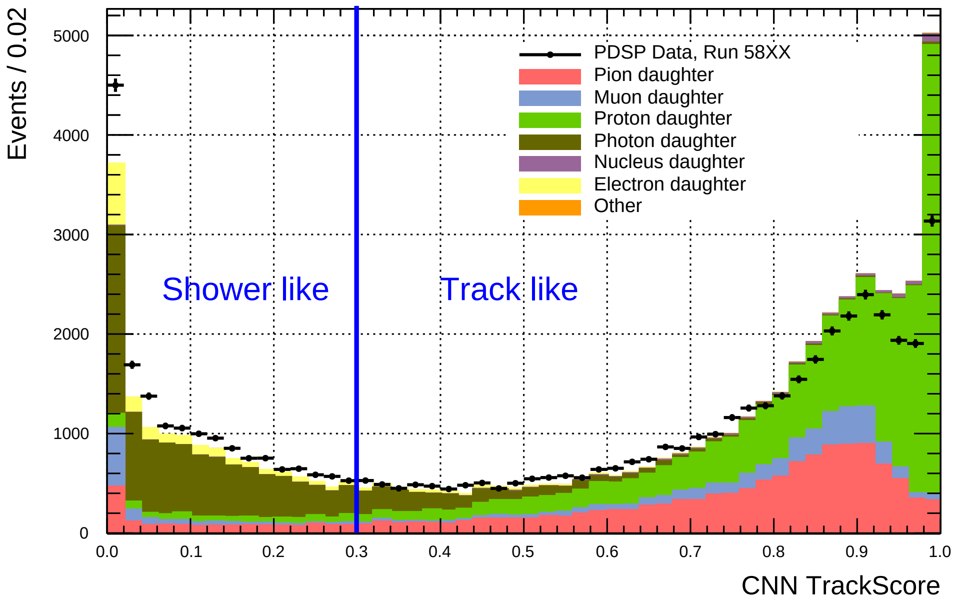

Figure 5.15: CNN track score of selected beam pion daughters. In order to isolate pion absorption interactions from the selected beam pions, the reconstructed secondary particles are classified with the CNN to be either of track or shower type. The separation works well with a cut value at 0.3. The categorisation then permits to isolate events with shower daughter candidates and pion daughter candidates with further cuts and reject such events.

Separation of Pion (Muon) and Proton Daughter Candidates / Pion Rejection

Two distributions are used to reject any pion candidate daughters. The distributions are based on the mean energy loss per unit distance (dEdx) and dEdx vs the residual range on a particle-by-particle basis. The dEdx as a function of particle momenta in liquid argon according to the Bethe Bloch equation was shown in Figure 2.6. Secondary particles of the sample used will have momenta in the sub-GeV range. Figure 2.6 shows a good separation of π^+ / p in that range as expected. Performing a χ^2-test of a ProtoDUNE-SP secondary dEdx vs residual range with the proton expectation as null hypothesis is commonly used to separate protons and muons (pions).

Similarly one can look at the distribution of the energy loss dEdx vs the residual range with respect to the end point of a particle trajectory as shown for ProtoDUNE-SP data in Figure 5.16. A separation between protons and muons is possible as their energy depositions close to the end of the particle trajectory (low residual range) differ considerably. Due to their similar mass ($m_\pi = 139$MeV and $m_\mu = 105.7$MeV) pions and muons show comparable behaviours for their mean energy loss rate.

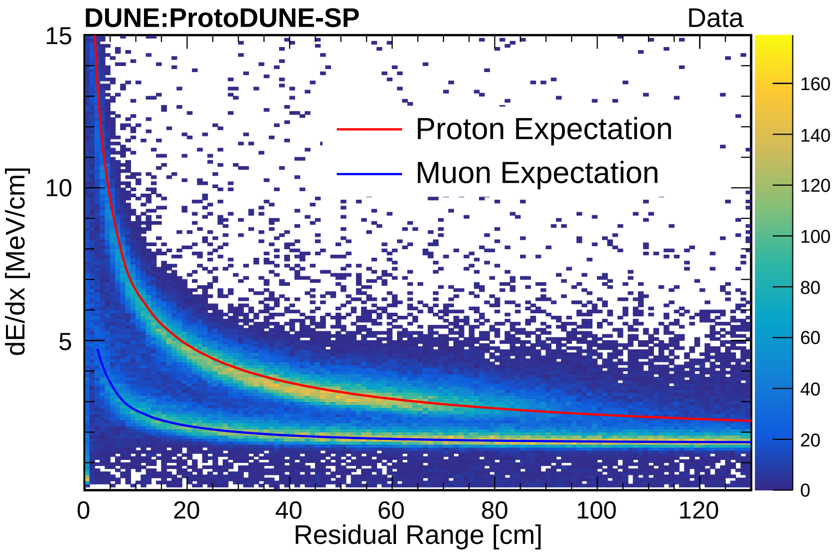

Figure 5.16: ProtoDUNE-SP secondary particles have a momentum distribution in the sub-GeV range. It can be used to separate π^+ from p^+ candidates. The stopping protons and muons vs their residual range in ProtoDUNE-SP are shown. The residual range is defined as the distance to the particle end-point. In overlay are the theoretical expectations for protons and muons. Performing a χ^2-test of a ProtoDUNE-SP secondary dEdx vs residual range with the proton expectation as null hypothesis is commonly used to separate protons and muons (pions). Taken from [72].

Cut optimisation studies have found a combination of evaluating mean energy loss rate for the secondary particles and comparison of the energy loss vs residual range to be the most effective way of separating secondary pions from protons. The PDSP Analyzer Module saves for each reconstructed object a vector containing the measured energy deposition per unit length for each hit. Therefore the cut observables are computed as follows:

1. Truncated mean of dEdx

   For each track-like secondary object, the mean of the dEdx distributions lying within 1σ is computed. It is referred to as the truncated mean dEdx and with the truncation method outlier values and fluctuations are rejected. Higher dEdx values could be from overlapping hits originating from other daughter particles as particle multiplicity can be high at the vertex. If the calculated dEdx value lies within the range of 0.5 and 2.8 MeV/cm the particle is considered to be a pion candidate. The distribution of dEdx for different secondary particles of the ProtoDUNE-SP simulation is shown in Figure 5.17 with the cut values indicated in the blue lines.

2. dEdx vs residual range

   For each track-like secondary object, the distribution of dEdx vs its residual range is computed and a χ^2 test is performed with the proton expectation (Figure 5.16) as the null hypothesis. If a secondary particle has a truncated mean of dEdX <3.4 and the χ^2/ndof >70 (*i. e.* disagreement with the null hypothesis) it is also considered to be a pion candidate. Figure 5.18 shows the distribution of χ^2/ndof for the secondary particles in ProtoDUNE-SP. The cut value at 70 is indicated by the blue line. The cut value for the dEdx is indicated with a blue line in Figure 5.17.

Equation 5.6 describes the cut rejecting primary pion candidates with associated secondary pion candidates. If any of the associated daughter objects fulfill the criterion, the event is rejected and does not enter the pion absorption selection. Studies showed, that the single criteria are not able to reach the purity in the sample (Table 5.7) as is obtained when combining both cuts. The effect on the selected sample for the end Z distribution is shown in Figure 5.19.

$$\begin{gathered}\text{Secondary Pion Candidate Rejection}\\ \left(0.5 < \text{mean dEdx} < 2.8\right) \vee \left(\text{mean dEdx} < 3.4 \;\&\&\; \chi^2/\text{ndof} > 70\right)\end{gathered} \tag{5.6}$$

Rejecting Events with π^0- Shower Candidates

If secondary particles present a shower-like topology (Figure 5.15) and if their number of hits exceeds a value larger than 40, they are considered π^0- shower candidates. Secondary particles with a hit number lower than 40 can be protons with a shower-like topology as is visible in Figure 5.20. Shower candidate events are rejected for the final absorption selection as they are pion charge exchange candidates. The hit distribution for secondary shower-like candidates is shown in Figure 5.20. The data and simulation agreement for shower-like daughters of selected beam particles is excellent. The end Z distribution of the final selected pion absorption candidate sample is shown in Figure 5.21. The purities and efficiencies for the two cuts on the secondary beam particles are listed in Table 5.7. The back-

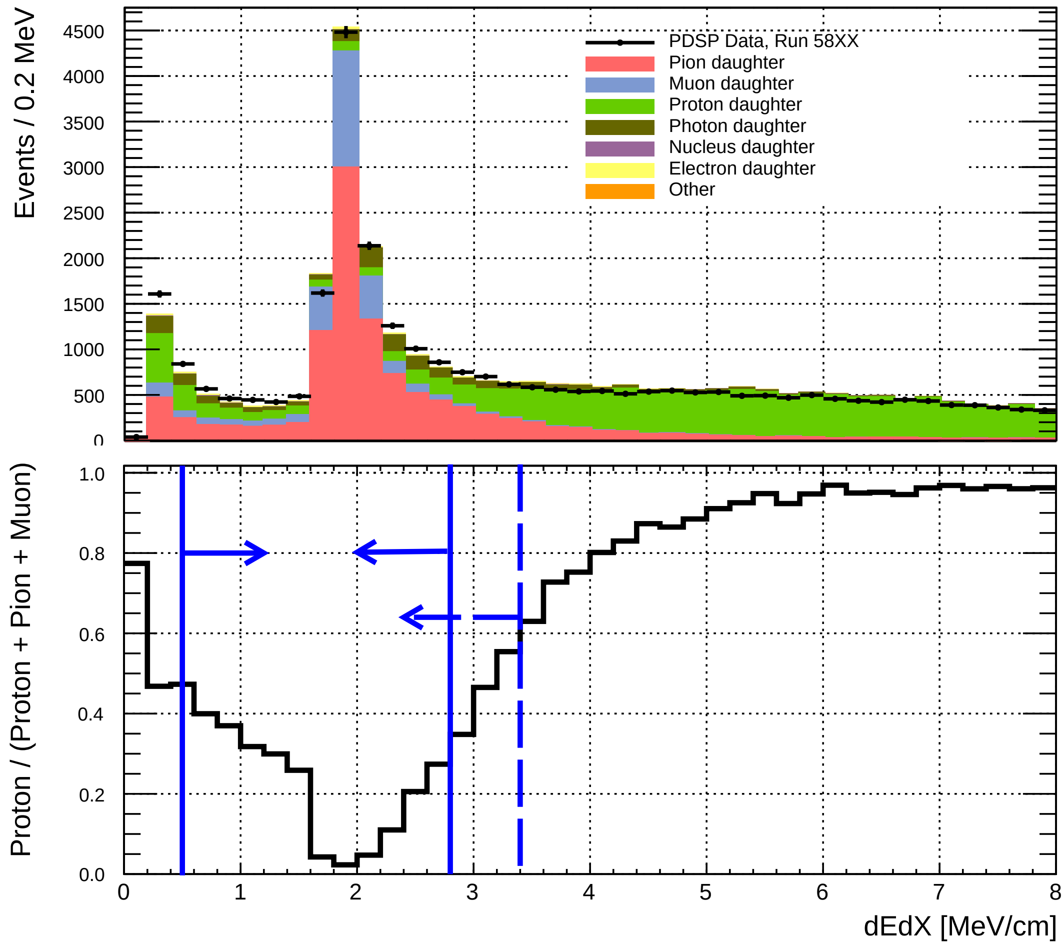

Figure 5.17: Distribution of the truncated mean of dEdx for track-like daughters of selected beam pions. The truncated mean dEdx is computed on a particle-by-particle basis. The mean is computed from the dEdx values lying within 1σ of the distribution. As expected protons (green) deposit more energy per unit length than pions (red). The lower plot shows the fractional ratio of protons along with the dEdx distribution values. The blue lines are the cut values to classify a secondary particle as a pion candidate just with the dEdx values. The dashed blue line indicates the cut value used in combination with Figure 5.18. The agreement of data and simulations is excellent.

ground contributions are dominated by pion inelastic interactions and pion charge exchange events.

Secondary π^0- Shower Candidate Rejection

$$(\text{nHits} > 40 \ \wedge \ \text{CNN trackScore} < 0.3) \tag{5.7}$$

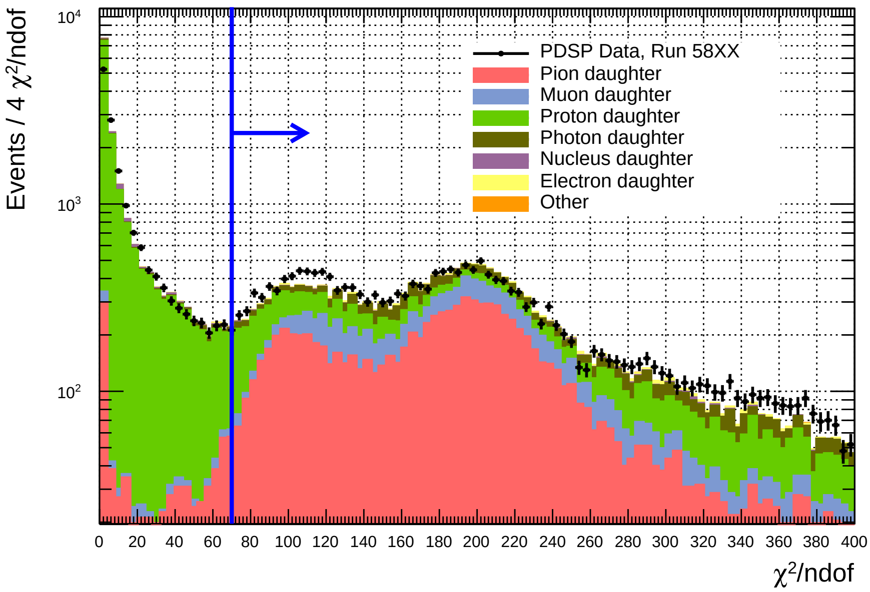

Figure 5.18: Distribution of the χ^2/ndof. It is obtained by performing a χ^2-test on dEdx vs residual range for each secondary track-like particle. The null-hypothesis is the expectation for protons as show in Figure 5.16. Low values indicate the agreement of the secondary particle in question under the proton hypothesis. If secondary particles have a χ^2/ndof value above 70 and their truncated mean dEdx is < 3.4 MeV/cm they are considered as pion candidates. Thus, the event is rejected from the pion absorption selection.

	π^+ **Absorption**	
	Purity	Efficiency
Secondary Pion Rejection	0.45	0.47
Secondary π^0 Showers	0.59	0.45

Table 5.7: Efficiencies and purities from the simualtions for the final cuts on the secondary particles to isolate pion absorption event candidates.

5.6 EVENT SELECTION EFFICIENCY & PURITY

Table 5.8 gives an overview of the simulation estimates on the composition of the selected events and the number of selected data events. The total number is the number of events available after the beam instrumentation selection. A pion is considered as a signal event up until the cut on the Michel score to build the incident pion sample. The cuts on the secondary particles are in order to isolate pion absorption events from the selected pion sample. Thus, for these distributions

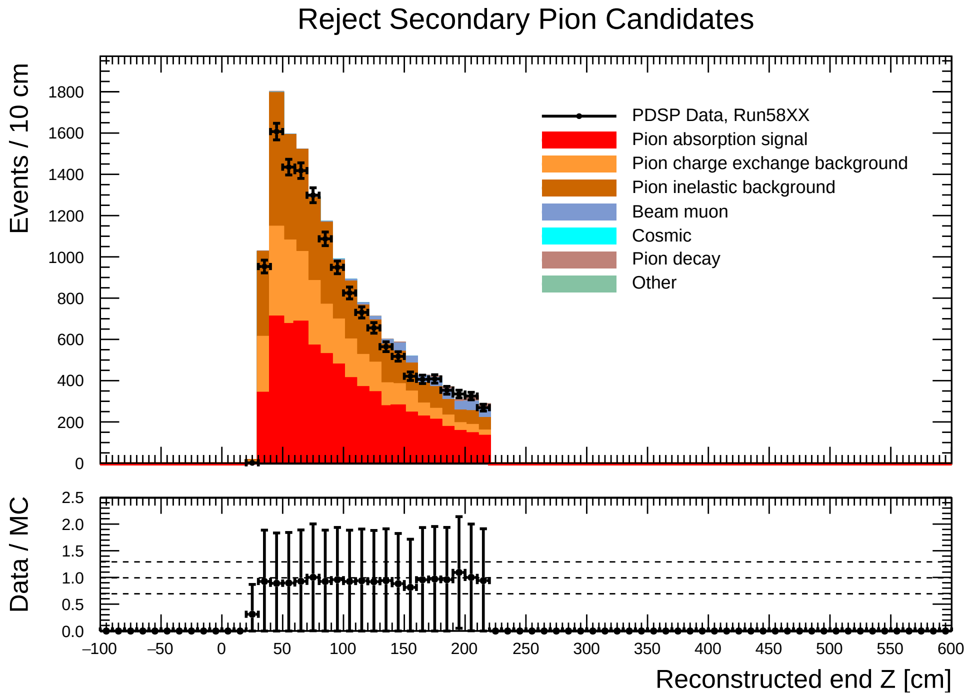

Figure 5.19: Reconstructed end Z distribution after rejecting secondary π^+ candidates. Note, the legend has changed and now shows the different π^+ interaction types.

only pion absorption topologies are considered as signal and pion inelastic or charge exchange interactions are now a background.

	Data	MC	Expected Signal		Expected Background				Fraction	
			Total π^+	π^+ Abs	Total	μ	Decay π^+	π^+	Data	MC
Total	70000	70000	56747	16706	13253	9679	1777	–	1	1
Pandora	52827	59613	47717	14721	11896	9562	1770	–	0.75	0.85
Beam Position	37981	44308	35606	11831	8702	6665	1587	–	0.72	0.74
APA3	29547	36053	33634	10886	2419	1890	401	–	0.78	0.81
Michel Score	28863	35352	33397	10831	1955	1536	293	–	0.98	0.98
Secondary Pion Rejection	14606	17674	–	7899	9775	465	100	9205	0.51	0.50
Secondary π^0 Showers	9619	12727	–	7495	5232	445	73	4787	0.66	0.72

Table 5.8: Summary of the number of selected events after each cut with classification of signal and background. The fractions for data and MC agree for all cuts but the Pandora reconstruction step. The disagreement can be explained through the mis-modelling of the SCE effect at the beam entry point. The SCE effect impacts the event reconstruction efficiency as it squeezes particle tracks. In consequence less hits are available per track and the reconstruction efficiency depends on the number of hits.

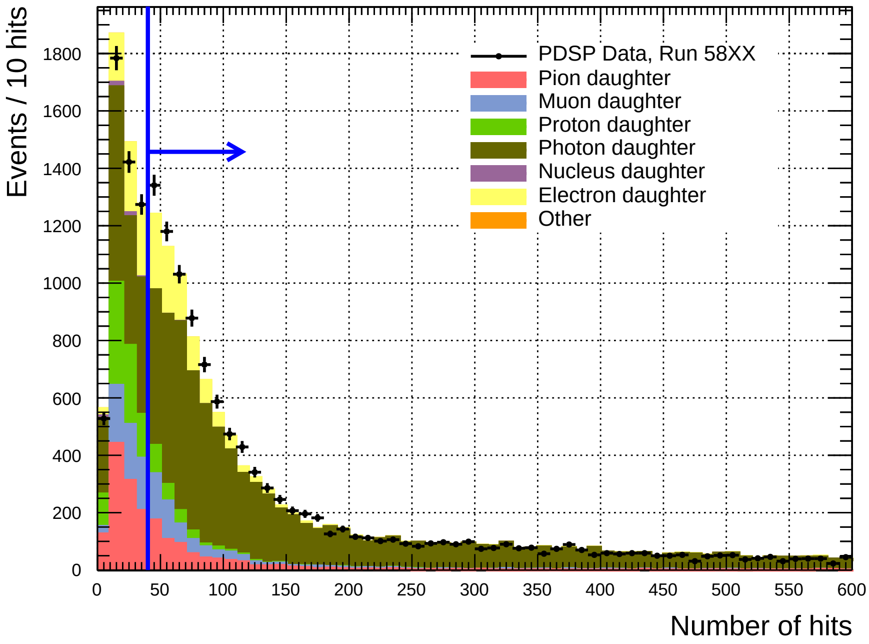

Figure 5.20: Distribution of the number of Hits for each reconstructed shower-like secondary particle. A secondary particle is considered shower-like if its CNN track score is < 0.3 as shown in Figure 5.15. A secondary beam particle is considered a shower candidate if the track score criterion is full filled and the number of reconstructed hits exceeds 40, as indicated by the blue line in the distribution.

Table 5.8 also shows the fraction of events after each cut for data and MC. The fraction of selected events is calculated with respect to the previously available events. The fraction of events available in data and MC after Pandora reconstruction is discrepant. A larger fraction of the MC-generated events remains after reconstruction than in data. This can result from underestimating the SCE effects at the beam entry point. It results in a squeezing effect on particle tracks and this is the reason for a smaller number of hits per track in the beam entry region. The Pandora reconstruction efficiency depends on the number of reconstructed hits. Therefore, if in simulation the SCE effect is underestimated, the squeezing effect is smaller. In consequence, tracks are more likely to be reconstructed as more hits are available per track. Future simulations will aim to take care of this discrepancy and better model the SCE effects at the beam entry point. The fractions noted of the other applied cuts are comparable. The cut on secondary showers is also slightly discrepant and could be due to the track score discrepancy between data and MC for low values as shown in Figure 5.15.

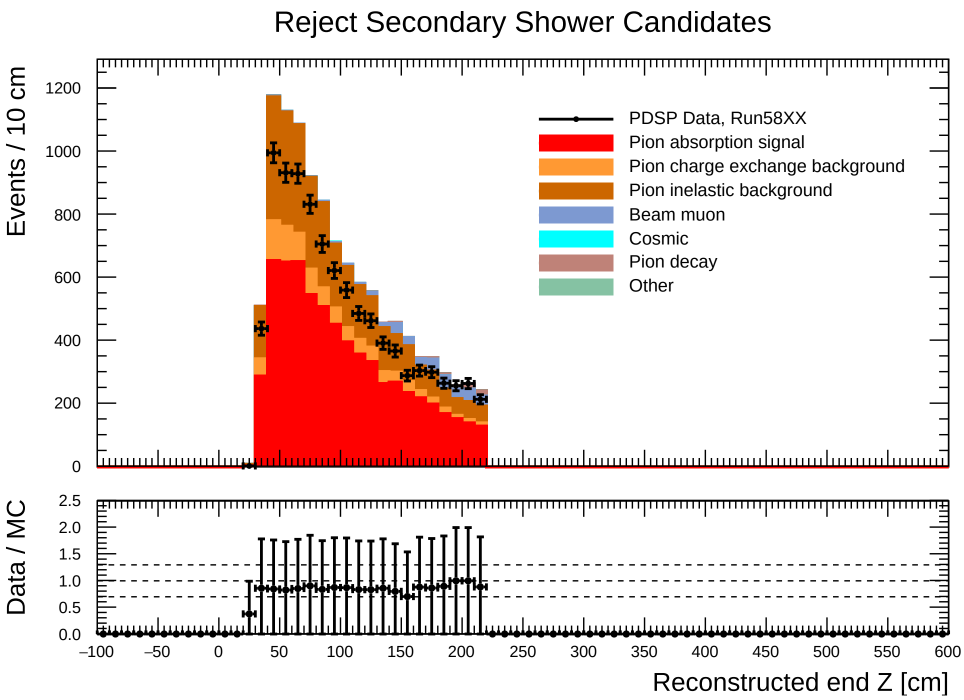

Figure 5.21: Reconstructed end Z distribution after rejecting secondary shower candidates. This is the final selected pion absorption sample.

It is important to balance purity and efficiency well when performing event selections. It is possible to achieve high purity samples with very low efficiency. If event statistics are high, low efficiencies can be accepted. However, the available events from simulation and data of ProtoDUNE-SP low efficiencies increase statistical errors of the measurements. Thus a compromise between efficiency and purity has to be found. Several studies have been performed to improve the purities and efficiencies of the applied cuts.

The purity of the incident π^+ sample after the Michel score cut on primary beam particles is 94% with an efficiency of 59% with respect to to the available π^+ signal events before Pandora reconstruction. The final selection purity of π^+ absorption events is 59% with an efficiency of 45% with respect to to the initially available π^+ absorption events. Table 5.9 summarises how the purity of the event samples improves after each cut while the efficiency decrease is attempted to be kept low after each applied cut. The efficiency drop after the beam position cuts is significant. This is acceptable as the aim of the beam position cut is to select for beam particles that have passed through the beam plug and thus, the estimate of their energy deposit before entering the LArTPC is well estimated. A further significant efficiency drop happens at the cut where secondary pions are rejected. This is because a pion *elastic* kink can be classified by reconstruction as an event vertex. If that is the case, the secondary particle saved in the reconstruction, in reality, is the primary pion and the secondary pion rejection cut will reject the event. If such an event undergoes an absorption process after, thus it is a rejected signal event that is reflected in the cut efficiency. Event selection failures are discussed in Section 5.7.

	Incident π^+		**π^+ Absorption**	
	Purity	Efficiency	Purity	Efficiency
Total	0.81	1	0.24	1
Pandora	0.80	0.84	0.24	0.88
Beam Position	0.80	0.63	0.26	0.71
APA3	0.93	0.59	0.30	0.65
Michel Score	0.94	0.59	0.31	0.65
Secondary Pions	–	–	0.45	0.47
Secondary Showers	–	–	0.59	0.45

Table 5.9: Event selection efficiencies and purities for each cut. The purity is calculated from the selected true signal events with respect to to all selected events at each step. The efficiency is calculated as the ratio of the selected true signal events with respect to the true available events after the BI selection, *i. e.* the *Total* line. Both values of efficiency and purity are noted for the full incident pion sample and the pion absorption sample. Balancing purity and efficiency of event selections is important. The goal is to increase purity while keeping the efficiency decrease low. An efficiency decrease increases the statistical error if the amount of available data and simulation events is finite.

5.7 IRREDUCIBLE BACKGROUND AND RECONSTRUCTION ISSUES

For the incident pion sample, the purity is very high at 94% as shown in Table 5.9. The 6% selected background events are mainly coming from beam muons (see Table 5.8) where the Michel electron has not been reconstructed or properly identified by the Michel score variable. The π^+ absorption sample is lower in purity and has 41% of background events. The contaminating events for the selected absorption sample come from π^+ inelastic interaction with a secondary pion on the MC-true generation level. The cause can lie in reconstruction problems limiting the performance. The main problems are:

- Mis-reconstruction of the interaction vertex position
- Reconstruction missing or partially missing secondary particles

Figure 5.22 illustrates four different reconstruction issues that can arise from the aforementioned problems. They can cause the event selection to fail at the secondary cuts. The blue trajectory in Figure 5.22 represents the truth level of the simulated beam pion. It is a pion with a low angle elastic scatter (marked by a circle) which is later absorbed (at the star) under emission of a proton (p). The green drawings show different possible behaviours of the reconstruction. Due to electric field and spatial distortions in ProtoDUNE-SP, a vertex found anywhere within a $\Delta R \sim 5$ cm, reflecting the resolution of the reconstruction, is accepted as ideal reconstruction. The first drawing for the reconstruction is the ideal case.

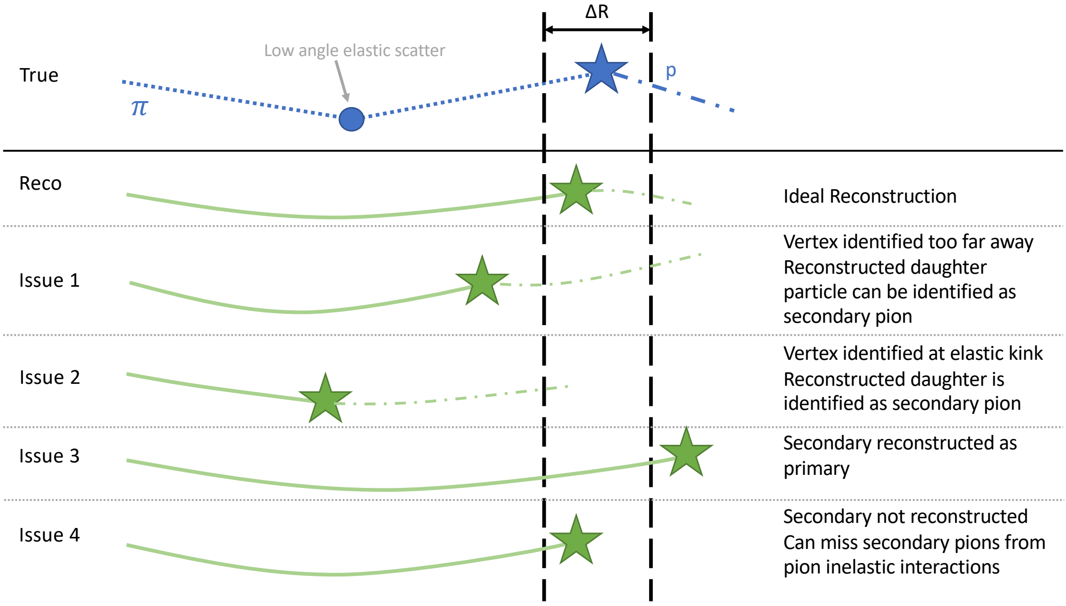

Figure 5.22: Schematic for different reconstruction issues causing event selection failures. The reconstruction issues contribute to select background events or reject signal events when applying the event selection cuts. The blue drawing refers to the simulated truth and the green drawings refer to the ideal and possible failures of reconstruction. The different issues are described in detail in the text.

- Issue 1

  The reconstruction identifies the vertex before the true vertex position. A secondary particle is found too. The reconstructed secondary particle can be identified as a secondary pion, thus the event may be refused by the event selection which causes an efficiency drop.

- Issue 2

  An elastic kink is wrongly identified as an interaction vertex. An example is shown in Figure 5.23. If reconstruction identifies the rest of the original pion as secondary this event will be rejected which affects the efficiency of the selection. If the daughter is not identified as a secondary pion it would still be selected as an absorption event but with a misestimated interacting energy.

- Issue 3

  The interaction vertex is placed further than the true vertex and true secondary particles now are part of the reconstructed primary particle. In consequence, a true secondary pion may be part of the reconstructed primary particle and therefore, a π^+ inelastic interaction is misidentified as absorption and selected. This is the main reason for the contamination.

- Issue 4

  The interaction vertex is correctly identified, however, outgoing secondary particles are missed by the reconstruction. This can happen if they are low energetic particles or deposit very few hits. If secondary pions from inelastic interactions are missed or π^0 showers these events are selected as absorption and contribute to the background.

A breakdown of the contributions to the background is given in Table 5.10. The largest contribution comes from π^+ inelastic events (30%), *i. e.* beam π^+ with a secondary π^+. The event selection is not able to reject these events due to reconstruction issue 3. In fact, for a large fraction of the selected background events, the secondary π^+ was not reconstructed as is shown in Figure 5.24. The not reconstructed secondary pions do not deposit enough hits at the interaction vertex to be reconstructed, *i. e.* they are emitted at low energies. Another reason is, that their hit depositions are associated with other daughter particles if the multiplicity at the vertex is high. As is visible from the purity values for the secondary pion rejection cut, not all reconstructed secondary pions will be rejected. Some have similar dEdx values as protons. This again is an effect of high multiplicity at the interaction vertex and the reconstruction is not able to resolve the different track objects. The selected charge exchange background is due to π^0 showers not associated with the primary particle vertex. Improvements of the reconstruction algorithms at particle vertices and for a low number of hits can help reduce the selected backgrounds in future analyses.

The cut selection presented within this thesis is the best compromise that has been found with a constrained amount of time for the analysis. For each cut, the agreement of the cut observable prediction from simulations and data was checked. The effect of all cuts was shown on the distribution of the beam particle interaction coordinate in z and the efficiency and purity for each cut were discussed. The obtained final event selection efficiencies and purities are sufficient to perform the first measurement on the pion absorption cross-section. In the future, more

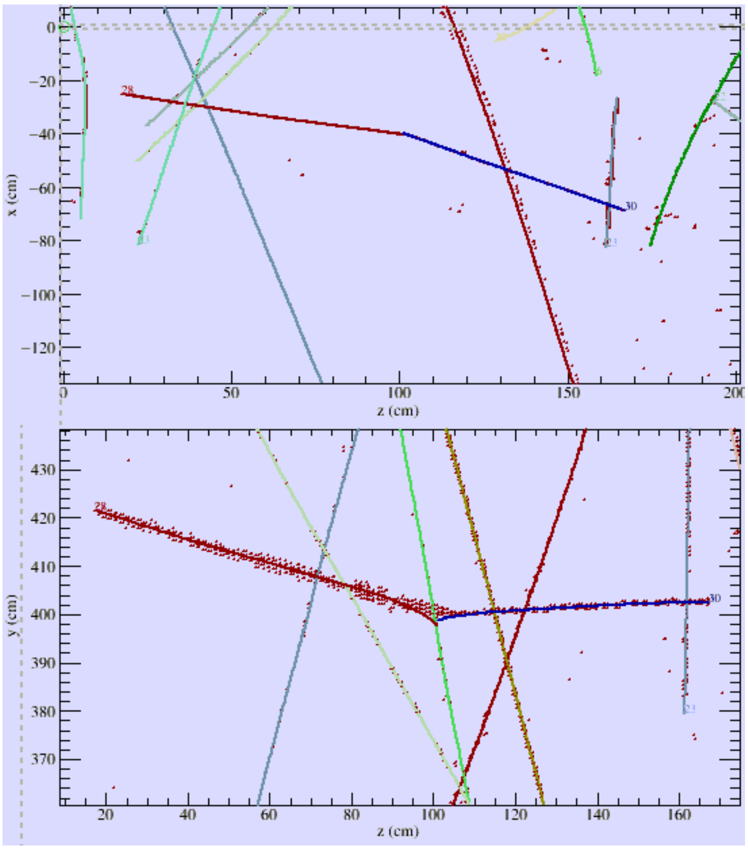

Figure 5.23: Pandora event display of a pion event. The $x - z$ and $y - z$ projections are shown. The simulated true pion elastically scatters with a visible kink ($z \sim 100$) and interacts at $z \sim 160$. The reconstruction algorithm identifies the interaction vertex at the elastic kink. The reconstructed primary beam particle is visible in red and the reconstructed secondary is visible in blue. This corresponds to Fail 2 in Figure 5.22. The reconstructed tracks crossing steeply crossing the views are cosmic rays.

ABSORPTION EVENT CANDIDATES	[%]
Total BG	41%
π^+ inelastic *without* reconstructed secondary π^+	22%
π^+ inelastic *with* reconstructed secondary π^+	8%
π^+ charge exchange	8%
Other	3%

Table 5.10: Detailed split of the background contributions for the pion absorption selection. The major background contribution comes from π^+ inelastic events with a secondary π^+ at the truth level. Figure 5.24 shows that within the π^+ inelastic events many times the secondary π^+ is missed by the reconstruction.

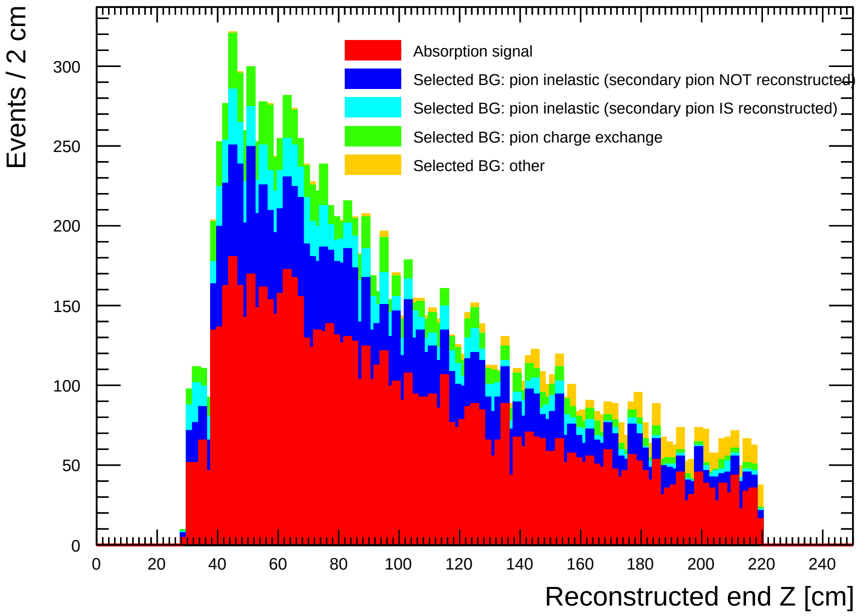

Figure 5.24: Selected π^+ absorption signals. The contributions of the background signals are split by their interaction type. The biggest background contribution coming from the π^+ inelastic interactions is further split (blue and cyan) in events based on whether the secondary π^+ was reconstructed or not. A secondary particle can be missed by the reconstruction if not enough hits are deposited in the LArTPC, *i.e.* it does not have enough energy.

detailed studies, simulation improvements, and new possibilities for the classification of observables will be useful to improve the here presented event selection. Improved selection efficiency will reduce the statistical uncertainties of the measurement and improved purity is less prone to background misestimations from simulation.

6 SYSTEMATIC UNCERTAINTIES

All uncertainties that are not directly related to statistical uncertainties in a measurement are systematic. Typical systematic uncertainties in particle physics measurements arise from the detector model, the physics model used in the generators, and the statistical uncertainties of the simulations. This chapter discusses the dominant systematic uncertainties for the pion absorption cross-section measurement. It is important to evaluate the influence of systematic uncertainties on the distributions of the pion initial kinetic energies and their kinetic energy at the interaction point, as these are the necessary distributions to perform the cross-section measurement. Section 6.1 discusses the beam-related systematic uncertainties and Section 6.2 the uncertainties from the physics model of the cross-section, as well as the event selection uncertainties. Uncertainties arising from the event reconstruction, for example, the vertex resolution, are discussed in Section 6.3. Errors on the detector model, detector response, and calibration are discussed in Section 6.4.

6.1 BEAM ASSOCIATED SYSTEMATIC ERRORS

The beam momentum measurement from the beam instrumentation and the energy loss until the TPC entry point give the initial kinetic energy of the beam pions when they enter the detector fiducial volume. From the relation of energy, momentum, and mass in natural units, one derives the pion initial kinetic energy to be

$$E_{KE\ initial} = \sqrt{p^2 + m_\pi^2} - m_\pi - E_{deposited\ BeamLine}. \tag{6.1}$$

The pion kinetic energy at its interaction point is then calculated by estimating the energy deposit inside the detector as

$$E_{KE\ interacting} = E_{KE\ initial} - \Delta E_{deposited}. \tag{6.2}$$

For the cross-section measurement, any uncertainties on the initial energy of the beam pions have to be taken into account when propagating systematic uncertainties of the measurement.

There are three sources of beam-related associated uncertainties discussed in this section: The first is a slight discrepancy between the simulated and reconstructed momentum distribution from the beam instrumentation measurements which directly influences the initial kinetic energy measurement and of course the interacting kinetic measurement in consequence. A data-driven reweighting of the simulated distribution has been performed to correct this issue. The particle-by-particle uncertainty of the beam momentum measurement from the beam instrumentation and the uncertainty on the energy loss of the particles within the beam plug before entering the LAr detector volume are the two other sources of uncertainty. The beam instrumentation uncertainty is the largest.

Data Driven Beam Momentum Reweight

It is shown in Figure 5.4 that the data distribution of the pion initial kinetic energy slightly deviates from the simulated beam instrumentation momentum. Using Equation 6.1 the distributions from data and simulations for the initial kinetic energy are plotted with their fit values from a Gaussian fit in Figure 6.1a. The widths of the fitted distributions between data (black) and MC (red) differ by ∼10 MeV with the simulated distribution having a smaller width. The simulated beam instrumentation values are reweighted in a data-driven way to reproduce the Gaussian shape of the beam instrumentation data. The reweighted initial kinetic energy is obtained by adding a random generated value from a Gaussian distribution with $\mu = 0$ and $\sigma = \sqrt{\sigma_{data}^2 - \sigma_{MC}^2}$. The reweighted distribution for the initial kinetic energy is shown in Figure 6.1b. The reweighted values in simulations are also used for the estimation of the interacting kinetic energy.

Beam Momentum Measurement Uncertainty

The XBPF spectrometers (Section 3.9) measure the position of the beam particles to infer the momentum on a particle-by-particle basis. Given the fiber width of 1 mm, the resolution for the momentum measurement is of ∼2.5% on a particle-by-particle basis as estimated in [84]. Thus, for ∼1 GeV/c pions the uncertainty on the momentum measurement of the single particle is ±25 MeV/c. In consequence, the uncertainty on the measured initial kinetic energy of a beam particle is also of ±25 MeV. Due to the resolution of the initial kinetic energy of each beam pion, the bin width of the cross-section measurement was chosen to be 50 MeV as the beam momentum uncertainty does not allow for a smaller binning.

Energy Loss in the Beam Line

The momentum of the beam particles is measured before they enter through the beam plug in the LArTPC. The estimated total material budget in between the

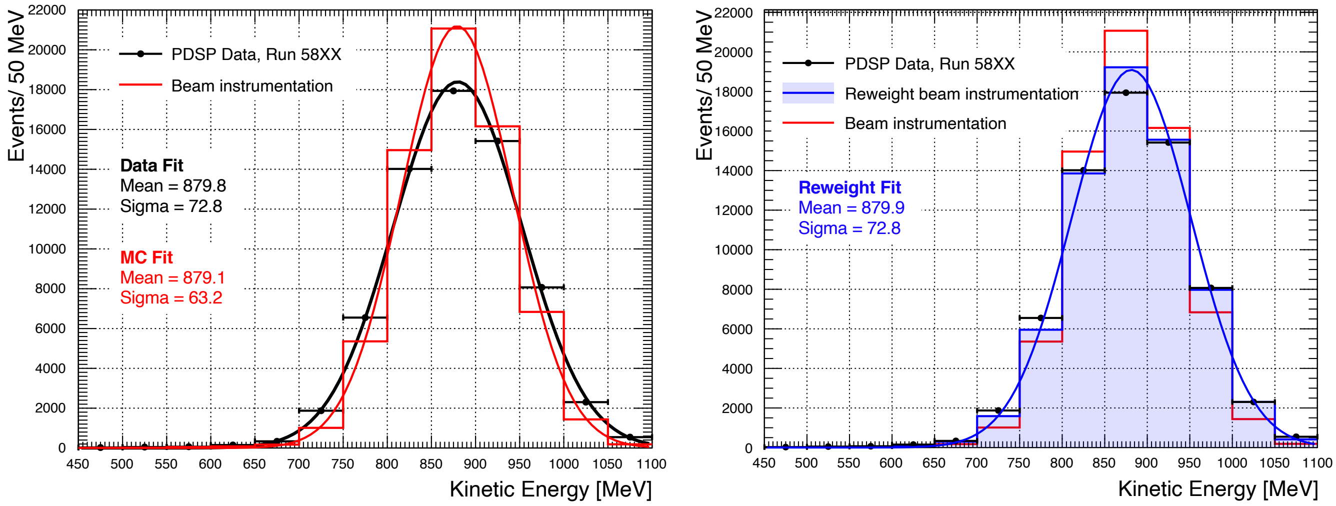

(a) Beam Instrumentation Kinetic Energy

(b) Reweight Beam Instrumentation Kinetic Energy

Figure 6.1: Left: Simulated and measured initial kinetic energy from the beam instrumentation momentum. The simulated distribution has a width that is ∼10 MeV smaller than data. Right: Data driven correction of the beam instrumentation measurement for the initial kinetic energy in order to reproduce the observed Gaussian distribution in data.

point of momentum measurement and the detector active volume is 9±1 g/cm^2 corresponding to an equivalent of ∼18±2 MeV for minimum ionizing particles [108]. The main material contributors are the beam instrumentation (2 g/cm^2), the cryostat beam window (2.5 g/cm^2), and the beam plug filled with nitrogen gas (4-5 g/cm^2). Estimates from simulations suggest that the most probable value for the energy loss for pions at 1 GeV/c momentum is of ∼13±2 MeV [108]. From the two estimates, the energy lost between the beam momentum measurement point and the detector entry point is assumed to be 15±5 MeV.

Finally, Table 6.1 summarises the estimates for the beam-related errors of the three sources on the pion energy measurement.

Uncertainty	Pion Initial KE [MeV]	Pion interacting KE [MeV]
Momentum measurement	±25	±25
Beam line energy loss	±5	±5

Table 6.1: Impact of beam momentum uncertainties and estimated energy loss within the beam line.

6.2 THEORETICAL AND EVENT SELECTION UNCERTAINTIES

Uncertainties on the implemented cross-section model (Figure 2.13) do not influence the pion kinetic energy but influence the measured signal distribution shapes. Uncertainties in the underlying cross-section model implementation can be evaluated by using different event generators and comparing them to each other. For ProtoDUNE-SP however, simulations from different event generators are not available. Thus, in the present case, the effect of a variation of the pion absorption cross-section is tested by reweighting the cross-section in the available simulations and performing the measurement with the reweighted simulations. The effects of varying the absorption cross-section by ±20 % are tested in Section 7.5. Varying the global cross-section by 20% is in agreement with the expected model uncertainties [54, 55]. The impact of this variation of the pion absorption probability influences the total number of available pion absorption signals in the simulations.

Variations of the pion absorption event selection are directly reflected in the signal selection efficiency and purities. The measurement of the pion absorption cross-section is corrected for event selection efficiencies and purities. Thus, by varying those values individually in the simulations, the impact of the variations can be studied in the final measurement. Effects of varying efficiencies and purities by ±10% with respect to their nominal values are tested in Section 7.5. The variations that will be tested are noted in Table 6.2.

VARIATION	[%]
Pion Absorption GEANT4 Cross-Section	±20%
Pion Absorption Selection Purity	±10%
Pion Absorption Selection Efficiency	±10%

Table 6.2: In order to study the effect of uncertainties in the pion absorption cross-section model and the estimated event selection purity and efficiency for the pion absorption cross-section measurement, the values are varied individually by 10 or 20%.

6.3 UNCERTAINTIES FROM EVENT RECONSTRUCTION

Issues with the vertex identification from reconstruction have been discussed in Section 5.7. The beam particles in ProtoDUNE-SP travel in the direction of the z-coordinate in the detector. The measurement of the deposited energy beam particles inside ProtoDUNE-SP is done by determining the wire (parallel to z) of interaction. Thus, another uncertainty on the measurement of the deposited energy depends on the resolution of the final particle position in the z-coordinate and only affects the interacting energy of the beam particle. The MC simulations are used to determine the $\Delta z = z_{reco} - z_{true}$ at the interaction point for reconstructed true beam pions. A vertex resolution of ± 5 cm was found in the simulations, with a slight tendency to reconstruct the particle interaction vertex at higher z than in the true phase space as shown in Figure 6.2. This happens if the reconstruction associates daughter particles as beam particles with a small angle with respect to the beam particle as was pointed out in Section 5.7.

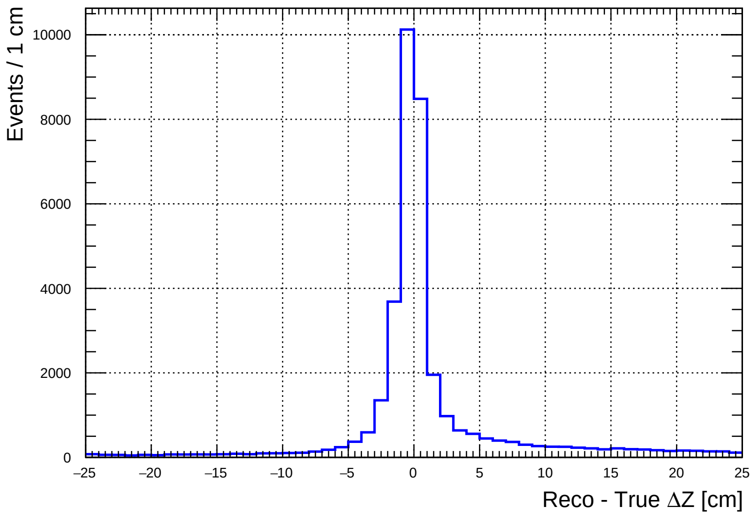

Figure 6.2: Simulation: the resolution of the beam particle end point in the z-coordinate for reconstructed true beam pions. $\Delta z = z_{reco} - z_{true}$ shows a slight tendency for reconstruction of the end point in z at higher values. This happens if (parts of) daughter particles are associated as beam particles which is more likely in values of high z, *i.e.* along the beam direction. The general uncertainty of the beam particle reconstructed position in z is ± 5 cm corresponding to an energy deposit of ~ 10 MeV.

To verify the estimated resolution of the z-coordinate 300 data events of the ProtoDUNE-SP 1 GeV/c Run 5387 were scanned by eye: from raw ProtoDUNE-SP event displays it is possible to identify the wire of interaction. This is compared to the reconstructed wire of interaction by taking the reconstructed z-coordinate and dividing it by the wire pitch distance of 4.79 mm. An example event display with the observed and reconstructed wire of interaction is shown in Figure 6.3. The differences of the observed wire with respect to the reconstructed wire are logged in a histogram shown in Figure 6.4. The result shows that the wire discrepancy for the reconstructed vertex in data is ± 10 wires. This corresponds to ~ 5 cm and is consistent with the results from simulations in Figure 6.2. An example event from data where a daughter is also identified as part of the beam particle is shown in Figure 6.5. Table 6.3 shows the final uncertainty on the beam particle interacting energy due to the interaction vertex resolution in the z-coordinate.

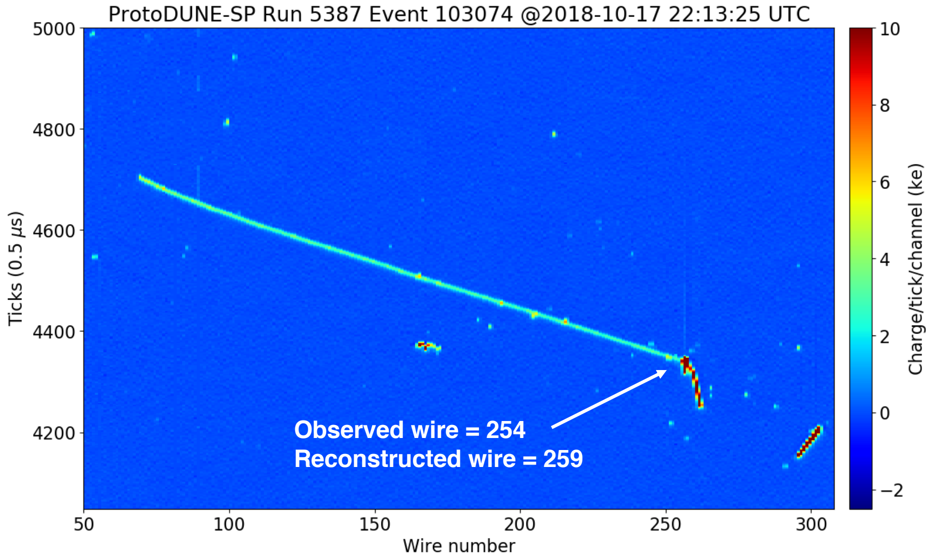

Figure 6.3: ProtoDUNE-SP beam data run 5387: Python event display in order to determine the *observed* wire of interaction and compare it to the reconstructed wire of interaction. For this example the discrepancy is 5 wires. With a wire pitch of 4.79 mm this corresponds to ∼2.4 cm.

Uncertainty	Pion Initial KE [MeV]	Pion interacting KE [MeV]
Vertex resolution z-coordinate	–	±10

Table 6.3: Uncertainty from the resolution on the interaction point of beam particles. The uncertainty was estimated with simulations and confirmed by studies on ProtoDUNE-SP beam data.

6.4 DETECTOR MODEL, RESPONSE AND CALIBRATION SYSTEMATIC ERRORS

Several systematic uncertainties are related to the detector model and its simulated response. The uncertainties can come from the models of the SCE effects for the electric field and spatial corrections, the dE/dx calibration, the simulated transversal and longitudinal charge diffusion, the value of electron-ion recombination as a function of the electric field, and mismodeling of electric field distortions in the APA boundary regions. For the current analysis, it is necessary to evaluate the first-order effects of the uncertainties on the beam pion kinetic energy measurement.

Electric Field Uncertainty and Impact on Recombination

The electron-ion recombination factor describes the fractions of ionisation electrons lost to reattachment to ions before being available for detection. The recombination depends on the electric field as described earlier in Section 2.3 [49, 110] Uncertain-

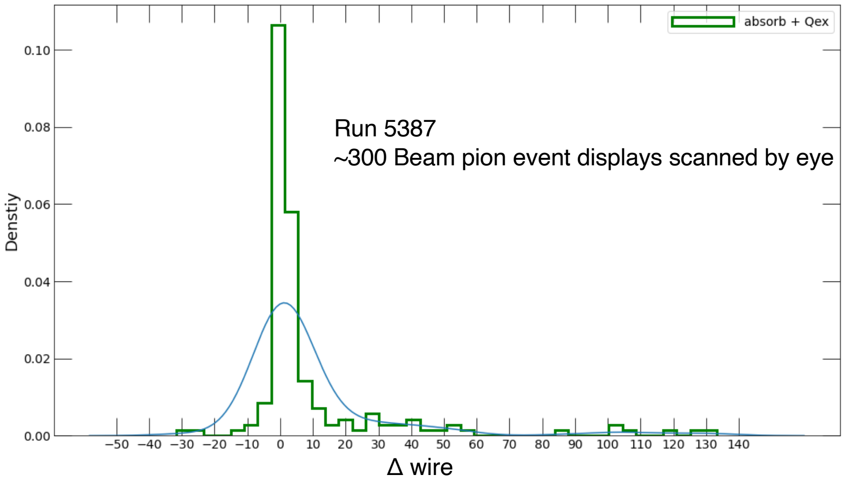

Figure 6.4: ProtoDUNE-SP beam data: 300 beam pion events. The difference of the observed wire and reconstructed wire are compared. The uncertainty on the wire resolution from data is ± 10 wires $\simeq 5$ cm which is consistent with the results from the MC simulations. Taken from [109].

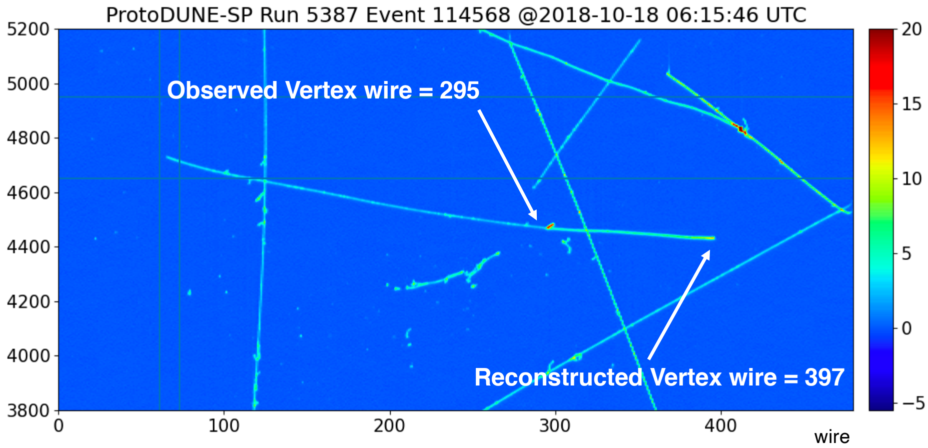

Figure 6.5: ProtoDUNE-SP beam data run 5387: Python event display in order to determine the *observed* wire of interaction and compare it to the reconstructed wire of interaction. For this example the discrepancy is 102 wires. With a wire pitch of 4.79 mm this corresponds to ~ 49 cm. In this case the reconstruction did not recognise an outgoing secondary pion as daughter but continued associating it to the primary beam particle.

ties in the electric field intensity distortions from SCE effects lead to uncertainties on the recombination factor used in the detector model and subsequently to uncertainty in the available charge for detection, *i. e.* the measured dE/dx. In the specific case of this measurement, the deviation of the electric field intensity from the nominal value due to SCE effects is of interest as it reflects the change of the recombination factor in that region. In [72] a relative change of 10% with respect to the nominal field value (500 V/cm) in the beam entry region as shown in Figure 6.6 is reported. The maximum change of the recombination factor for a 10% larger electric field intensity is 1.2% as calculated from the tables in [111]. Thus, the uncertainties on the recombination factor are smaller than 1% and do not impact the energy measurement significantly. The impact on the energy deposition inside the detector by varying the recombination factor is described in the calibration uncertainties.

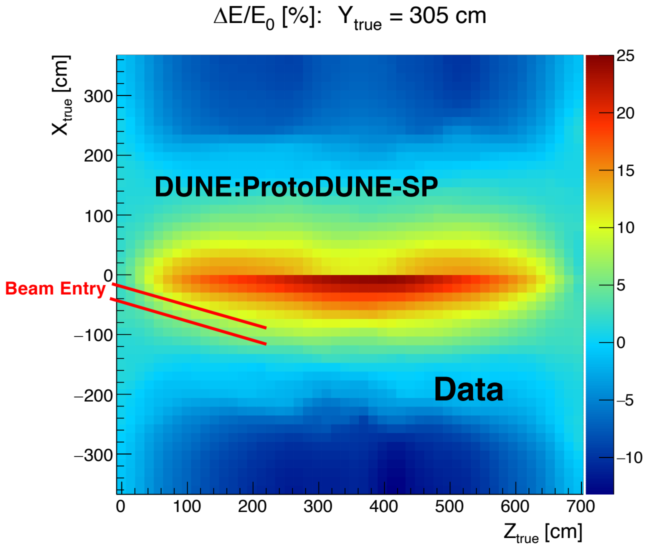

Figure 6.6: xz-view of the relative change of the electric field intensity for ProtoDUNE-SP at $y = 305$ cm. The beam entry region is marked in red. Taken from [72]. Uncertainties on the recombination are smaller than 1%.

Electric Field Intensity [V/cm]	Recombination Factor
500 (nominal)	0.698
550	0.706

Table 6.4: Recombination factor calculated from [111] for the nominal field intensity of ProtoDUNE-SP and a 10% deviation. The change of the recombination factor in the beam entry region is maximally 1.2%.

Calibration Uncertainty

The ProtoDUNE-SP calibration for the deposited energy per unit track length (dE/dx) has been discussed in Section 4.4 and is detailed in [112]. As the calibration scheme is similar to the one used in the MicroBooNE experiment [48], the evaluation strategy for systematic uncertainties on the energy calibration from MicroBooNE [93] can be used for ProtoDUNE-SP: The calibration sample of cathode crossing and anode crossing muons is divided into four samples by angular regions and spatial corrections (yz and x) are applied. Comparison of the subsamples to the full sample allows for the evaluation of statistical fluctuations and the dependence on the track angle for the measured energy depositions. The relative differences for subsamples in the angular region similar to the beam track angles are below ±1% for corrections in the x-direction and around ±3% for the yz-corrections [113]. For standard yz- and x-corrections the recombination factor was varied in order to study the effect on C_{cal} which is used for the calculation of dE/dx. The difference of after variation is $\mathcal{O}(1\%)$.

Uncertainties on the deposited charge dQ/dx coming from uncertainties on the measured electron lifetime corrections from the purity monitors are evaluated by studying the effect on the calibrated values of dQ/dx. The relative difference to the central value of the calibrated dQ/dx is $\mathcal{O}(0.02\%)$. Therefore, the smearing of dQ/dx as a function of drift distance eliminates discrepancies that may arise from the measured electron lifetime uncertainties [113]. The overall systematic uncertainties on the simulated and measured dE/dx were estimated to be

$$\begin{aligned} \text{Data} \qquad & \sigma_{\text{dE/dx MIP}} = 1.68\% \\ \text{MC} \qquad & \sigma_{\text{dE/dx MIP}} = 1.5\%. \end{aligned}$$

The deposited energy of beam particles inside the detector is the product of dE/dx× track pitch. In consequence, the uncertainty from the calibration on the measured total deposited energy is the same. The range of the beam pions used in this analysis is up to APA3, *i.e.* around ∼220 cm. A 1 GeV/c beam pion will deposit in average ∼2.1 MeV/cm and therefore deposit ≲500 MeV. A 1.6% uncertainty on dE/dx from the calibration transfers to a maximum uncertainty of ±8 MeV for the deposited energy by beam particles. This assumption for the calibration uncertainty effect is taken rather conservatively. The calibration uncertainty is comparable to the vertex resolution in the z-coordinate noted in Table 6.3.

Different sources of uncertainties were discussed in this chapter and how they specifically impact the pion energy measurements. Uncertainties in the energy measurement will shift around the measured bins. All uncertainties on the pion kinetic energy are listed again in Table 6.5 including the resulting total uncertainty, *i.e.* the square root of the sum of the squares of all contributions on the pion initial and interacting kinetic energy. Uncertainties coming from the event selection or the theoretical model of the cross-section will be varied globally.

UNCERTAINTY	PION INITIAL KE [MeV]	PION INTERACTING KE [MeV]
Momentum measurement	± 25	± 25
Beam line energy loss	± 5	± 5
Vertex resolution z-coordinate	–	± 10
Calibration uncertainty	–	± 8
TOTAL	± 25.5	± 28.5

Table 6.5: Summary of all uncertainties on the pion initial and interacting kinetic energy. The total uncertainty is the square root of the sum of the squares.

7 MEASUREMENT OF THE PION ABSORPTION CROSS-SECTION

The final chapter of the thesis presents the measurement of the pion absorption cross-section with ProtoDUNE-SP data for beam pions with an initial momentum distribution of 1 GeV/c. The proof of principle of the E-Slice method on simulated true quantities as well as the construction of the interacting and incident histogram are presented in Section 7.1. The measurement of the reconstructed kinetic energy of a pion is detailed in Section 7.2. Section 7.3 shows the distributions of the measured incident and interacting histograms. The iterative Bayesian unfolding technique to obtain the underlying truth distribution of the measured incident and interacting histograms introduced in Section 7.4. The final measurement of the cross-section is presented in Section 7.5 with its uncertainties. The uncertainties listed in Chapter 6 are propagated through the measurement by varying the simulations for each uncertainty and performing the unfolding with the varied simulation. The initially measured distributions, therefore, remain unchanged.

7.1 ENERGY SLICE METHOD VALIDATION

This section shows the validation of the energy slicing method with the true quantities of the simulated ProtoDUNE-SP events. The aim is to use the simulated truth quantities of the pion kinetic energies and the true interaction types to reproduce the input model GEANT4 cross-sections shown in Figure 2.13 with the equation for the cross-section extraction as a function of the true pion kinetic energy. The only uncertainties included in this step are statistical. For this purpose, the full simulation of the so-called MC-Prod4a RITM1115963 [114] for 1 GeV/c beam pions has been used. The derivation of the equation to extract the pion absorption cross-section with the E-Slice method has been discussed in Section 2.6. The equation for the final cross-section extraction is noted again here as a reminder

$$\sigma(E_i) = \frac{A}{N_A \rho \Delta E} \frac{dE}{dx}(E_i) \ln\left(\frac{N_{\pi Incident}(E_i)}{N_{\pi Incident}(E_i) - N_{\pi Interacting}(E_i)}\right). \tag{7.1}$$

The values used for the constants are noted in Table 7.1. Following assumptions are made for the cross-section measurement with the E-Slice method:

- The energy slice ΔE thickness is chosen to be constant. Each slice has a width of 50 MeV. The choice comes from the momentum uncertainty of 2.5% on a particle-by-particle basis resulting in ± 25 MeV for 1 GeV/c momentum particles. Details are given in Chapter 6.
- Each energy slice is considered as an independent experiment
- For low statistics in an energy slice, its thickness could be varied
- The energy slice thickness is mostly insensitive to SCE effects as recombination variation is negligible in the beam particle region Section 6.4
- All pions have the same energy when reaching a particular slice
- dE/dx is derived from the Bethe Bloch formula for the mean energy loss at the corresponding pion momentum (1 GeV/c). This is reasonable as the dEdx vs residual range agreement is excellent for ProtoDUNE-SP data (see Figure 5.16).

CONSTANTS	VALUE
Atomic mass A	39.948 u
Avogadro number N_A	6.02×10^{23}
Density ρ	1.4 g/ml
Energy bin width ΔE	50 MeV

Table 7.1: Constant values used for the extraction of the cross-section as described in Equation 7.1.

The validation of the E-Slice method is done by using the true particle interaction information and classifying the interaction type based on the true secondary particles of a pion interaction as defined in Table 5.1. For each pion, the initial kinetic energy is derived from the simulated true momentum of the beam instrumentation using the relation of energy, momentum, and mass of a particle in natural units. It is given as

$$E^2 = p^2 + m_\pi^2, \tag{7.2}$$

where E is the total energy, *i.e.* the sum of the energy at rest $E_0 = m_\pi$ and the kinetic energy of the pion. p is the momentum of the pion from the beam instrumentation and the mass of the pion $m_\pi = 139$ MeV. The estimated energy loss in the beam plug is taken into account for the derivation of the initial pion kinetic energy.

The true pion kinetic energy at its interaction point is computed in the following way: Compute the distribution of the mean energy loss as a function of traveled distance (energy lost) in LAr for 1 GeV/c momentum pions. The cumulative sum of the distribution gives the total energy lost in LAr as a function of the pion track length. Thus, with the information of the true initial kinetic energy of the pion and its true track length, the interacting energy can be estimated $E_{KEinteracting} = E_{KEinitial} - \Delta E_{deposited}$. An overlay of the dEdx vs true track length and its cumulative are shown in Figure 7.1.

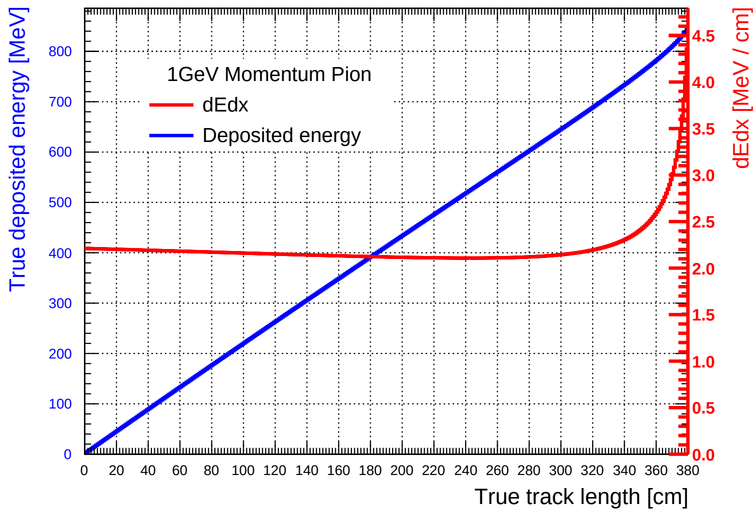

Figure 7.1: Red: dEdx vs true track length for a π^+ at 1 GeV momentum. Blue: Cumulative sum of the red curve, *i. e.* the deposited energy in the LArTPC as a function of true pion track length.

The incident and interacting histograms, necessary for the cross-section extraction as shown in Equation 7.1 are constructed as a function of the pion kinetic energy. Instead of constructing the incident histogram on a particle-by-particle basis, it is constructed from the distribution of the pion *initial kinetic energy* at the TPC entry point and the distribution of the *interacting kinetic energy* at the interaction energy. The reason for building the incident histogram from the start- and interacting distribution lies in the procedure of unfolding. It is impossible to unfold the incident histogram as each pion contributes multiple times to the distribution. Therefore, it is necessary to unfold the distribution of the initial and interacting pion histograms separately, as for these two distributions each pion only contributes once. Detector smearing effects then are removed by unfolding and after the unfolding procedure, the incident histogram is computed. More details will be given in Section 7.4. From the two distributions for all beam pions the bins of the incident histogram are filled as

$$N_{incident}(i) = \sum_{j=0}^{i-1} N_{KE\ initial}(j) - \sum_{j=0}^{i-1} N_{KE\ interacting}(j), \tag{7.3}$$

where $i = 0$ corresponds to the last bin with the highest kinetic energy of the distribution and $i = nBin$ to the lowest bin of the distribution with $E = 0$. It is useful to look at Figure 7.2 to best understand this. The number of incident pions in bin i is the difference between the sum of the pions that entered the LArTPC (*initial*) and the sum of the pions that interacted before the corresponding bin (*interacting*). Only pions that cross from at least one bin to the next can be considered relevant for the measurement. Pions that are incident and interact in the same bin would not appear in the incident histogram, as is clear from Equation 7.3 and would be miscounted in the interacting histogram. These events are removed and considered as a background of the measurement.

Figure 7.2 shows the kinetic energy distributions for the incident pions. Figure 7.2a shows the true initial kinetic energy of the beam pions derived from the simulated true beam instrumentation momentum and the energy lost prior to the TPC entry. The distribution of the true kinetic energy at the pion interaction points is shown in Figure 7.2b. With Equation 7.3, Figure 7.2a, and Figure 7.2b the resulting true incident pion at the true kinetic energy distribution is shown in Figure 7.2c. The histogram in Figure 7.2c is used as the denominator in Equation 7.1 for the validation of the E-Slice method.

Figure 7.3 shows the distribution of the kinetic energies for truly absorbed pions. It is the distribution used as the nominator of Equation 7.1 for the calculation of the cross-section. The results of the E-Slice Method validation for the pion absorption and the total inelastic cross-section are shown in Figure 7.4. The agreement is excellent and the E-Slice method can fully reproduce the model input cross-section by using the underlying truth simulated values.

The statistical error for each bin is binomial as the outcome for every bin of energy is whether a pion interacted in the corresponding process or not with the probability $P_{int} = n_{Int}/n_{Inc}$. The systematic error on each bin is derived through error propagation of the statistical bin error of the incident and interacting histograms as shown in Equations 7.4 to 7.6. At low kinetic energy bins there are less statistics (see Figure 7.3) thus, the errors increase.

The E-Slice method is validated for the pion absorption and total inelastic interaction types. From now on the thesis will only focus on the pion absorption cross-section measurement.

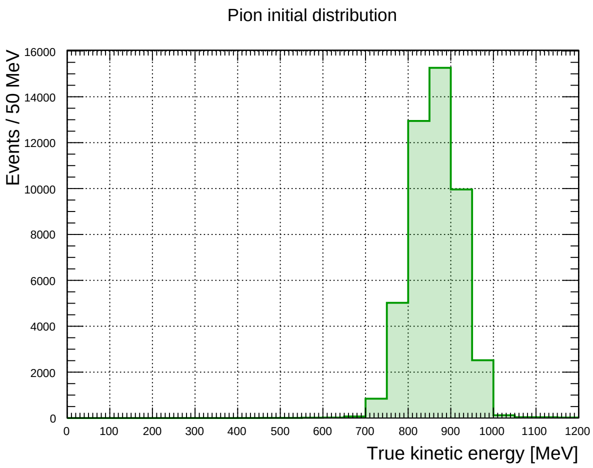

(a) True beam pions true initial kinetic energy distribution.

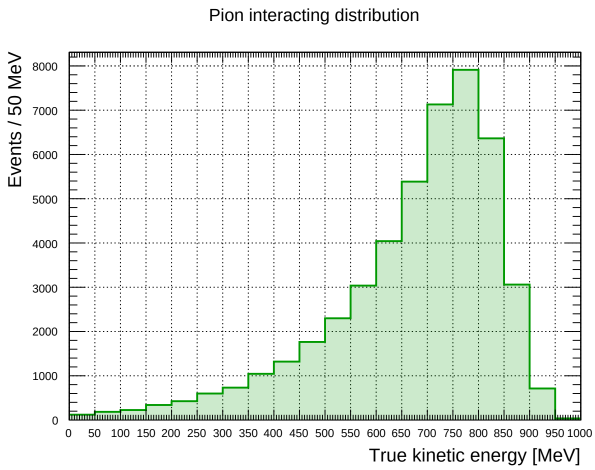

(b) True beam pions true interacting kinetic energy distribution.

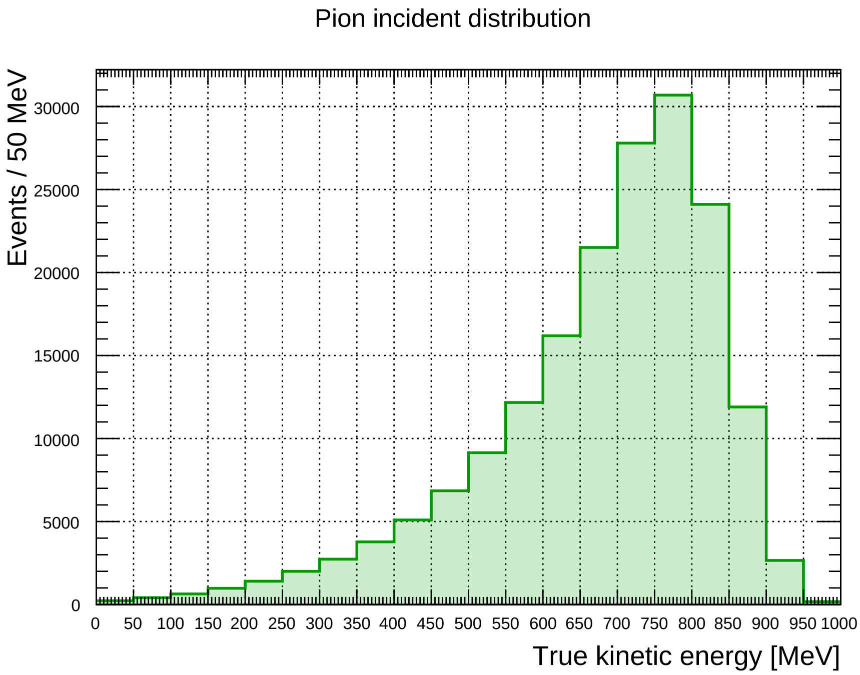

(c) True beam pions incident histogram built from initial and interacting distributions

Figure 7.2: Distributions of the true kinetic energy for simulated true beam pions in ProtoDUNE-SP. Figure 7.2a and Figure 7.2b are used to compute the histogram of the incident pions Figure 7.2c with Equation 7.1. The incident pion distribution is the denominator used for the validation of the E-Slice method with Equation 7.1.

$$\sigma^2_{xs\ Validation} = \delta^2_{statistical} + \delta^2_{systematic} \tag{7.4}$$

$$\delta_{statistical} = \sqrt{\frac{p(1-p)}{n_{Inc}}} \tag{7.5}$$

$$\delta_{systematic} = \frac{1}{n_{Inc} - n_{Int}} \sqrt{\delta^2_{Inc} + \delta^2_{Int}} \tag{7.6}$$

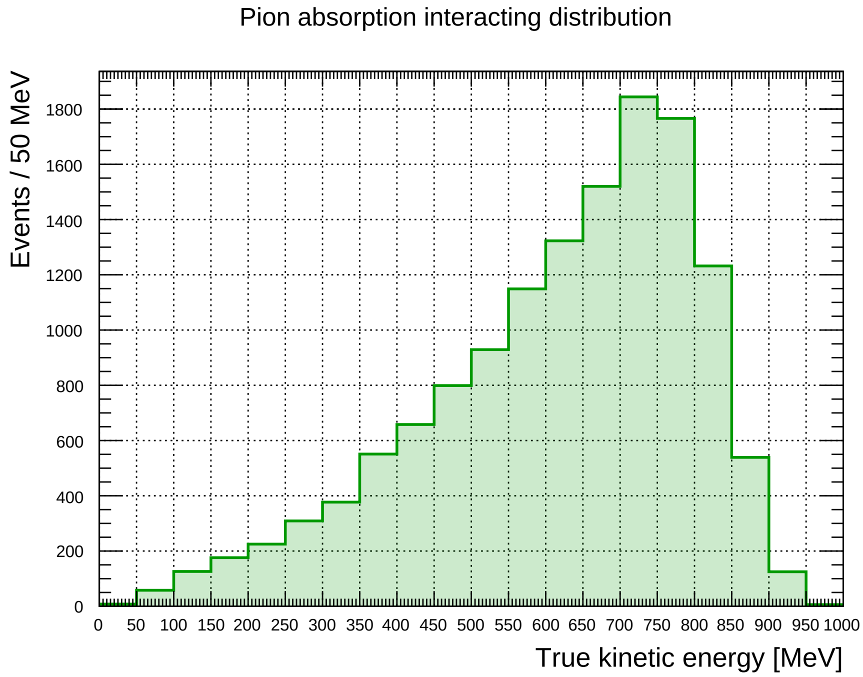

Figure 7.3: Distribution of the pion kinetic energy of true absorption events. This histogram recieves one entry per absorption event at the interacting kinetic energy. It is used as the nominator in Equation 7.1 for the calculation of the cross-section.

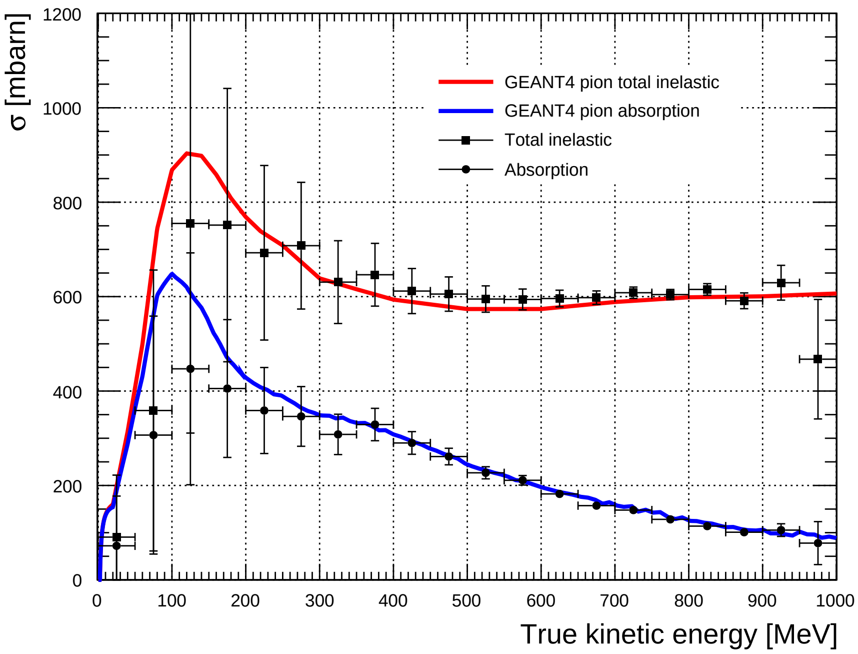

Figure 7.4: Validation of the E-Slice Method for the cross-section extraction. The blue and red curves are the GEANT4 input models for the pion total inelastic (red) and pion absorption (blue) cross-section. The validation has been done using the histograms in Figure 7.2 and Figure 7.3 computed from the truth values of the simulation for 1 GeV beam pions. The computed cross-sections agree with the predictions. The errors are of statistical nature. At low energies less events are available, thus the errors increase. The binning is of 50 MeV in the true kinetic energy phase space.

7.2 PION ENERGY MEASUREMENT

In this section now the pion energy measurement is discussed for the reconstructed observables. However, but the approach with the cumulative energy lost as a function of the interaction point of the track remains the same as presented in Section 7.1.

The pion initial kinetic energy is estimated for the reconstructed momentum of the pion (muon) triggers from the beam instrumentation and the energy lost in the beamline with Equation Equation 6.1. The distribution of the beam instrumentation momentum measurements for data and reconstructed simulation was shown in Figure 5.4. Note, as explained in Section 6.1 the initial beam momentum for simulations is re-weighted to better match the data distribution of the beam instrumentation measurements. The reconstructed interacting kinetic energy is computed as stated in Equation 6.2. The deposited energy is a sum of the energy lost in the beamline (Section 6.1) and the reconstructed deposited energy inside the detector.

Reconstructed Deposited Energy

As was done with the simulated true quantities in Figure 7.1, the goal is to produce a map from reconstructed data that allows estimating the energy deposited by a beam pion at its interaction point, *i.e.* the corresponding collection wire within the TPC. ProtoDUNE-SP measures for each beam particle its energy deposition dE/dx and the track pitch at each wire. The track pitch is the distance traveled between two wires which is slightly longer than the wire pitch due to the beam angle. The product of reconstructed dE/dx$\times$track pitch results in a map of the deposited energy as a function of the collection wire.

Ideally, the dE/dx and track pitch for each beam pion is measured and its deposited energy is computed on a particle-by-particle basis. As a benefit, this would directly include variations in the distribution of dE/dx values for the beam pions. However, ProtoDUNE-SP is subject to constantly passing through cosmic rays, it happens that a crossing cosmic ray trajectory adds hits on the beam particle trajectory. Thus, a false, higher energy deposition would be measured. To avoid this, the distribution of the reconstructed dE/dx for all pions and the reconstructed track-pitches for all pions are used. It is legitimate to do so as all beam pions have a similar momentum and enter ProtoDUNE-SP at the same angle.

Simulated SCE effects are not accurate in the beam entry region with respect to the distortions observed in data. The track squeezing from SCE affects the measured track pitch and dE/dx in the beam entry region. However, their product *i.e.* the deposited energy is not affected by the spatial distortions. The reconstructed dE/dx and track pitch values which are not corrected for SCE effects, but are calibrated and corrected for electron lifetime are used.

The reconstructed track pitches for all pions are fitted to their mean value with a Gaussian fit for each track pitch value at each collection wire. The distribution of reconstructed dE/dx values for each wire follows a Landau distribution and the most probable value (MPV) is fitted at each wire and corrected for the electron lifetime. When considering many beam pions, it is necessary to use the mean value of dE/dx value. The mean value of a Landau distribution is not well defined due to its long tail and the errors on a fitted mean value would be large. However, the mean value can be obtained by applying the ratio of the Bethe Bloch mean and MPV for 1 GeV/c pions and the corresponding wire pitch after the lifetime correction $C_{lifetime}$ as described in Equation 7.7.

$$\frac{dE}{dx}_{Mean\ Fit} = \frac{dE}{dx}_{MPVFit} \times C_{lifetime} \times \left(\frac{dEdx_{Mean\ BetheBloch}}{dEdx_{MPV\ BetheBloch}} \right) \tag{7.7}$$

An example of the fitting procedure on the reconstructed dE/dx values for wire 163 is shown in Figure 7.5.

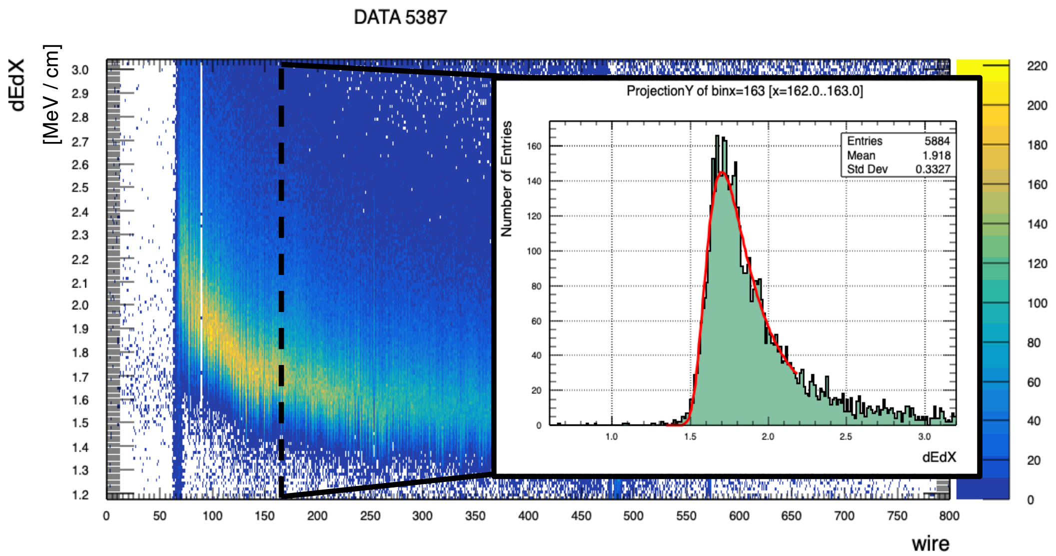

Figure 7.5: Example of fitting procedure for reconstructed dE/dx values of beam pions from ProtoDUNE-SP data. For each wire a Landau fit is performed on its dE/dx distribution and the most probable value is found. The SCE effect is well visible as data points only start at wire 68 corresponding to the Δz shift of about 30 cm from the boundary (wire 0) of ProtoDUNE-SP. In consequence and due to the track squeezing the values of dE/dx are higher.

The 2D distributions of the reconstructed dE/dx vs collection wire and the track pitch vs collection wire are shown in Figure 7.6 and Figure 7.7 for data and simulations, respectively. The fit values for each projection on the corresponding wire are shown in the overlay.

The data distributions directly show the effects of SCE on the track pitch and the deposited energy in Figure 7.6. The squeezing effect from the detector boundary inwards increases the deposited energy on the initial wires. The effect stabilises from wire 200 upwards as the particles reach the bulk region of the detector where the spatial distortions of the SCE effects decrease.

In Figure 7.7 the simulated data-driven SCE effect is shown. The simulated effect represents the general tendency of the observed SCE effects from data. However, in the beam entry region, the squeezing is underestimated. This can be appreciated by comparing the measured track pitches from data and simulation on the initial wires. Furthermore, a distinctive S-shape can be seen for the simulated dE/dx distribution in the wire region of 100 to 150 in Figure 7.7a. It is expected that the inaccuracies in the simulation and understanding will be improved in future ProtoDUNE-SP simulation campaigns.

The map of the deposited energy as a function of the collection wire is produced by multiplying the reconstructed dE/dx value with the corresponding track pitch resulting in the total deposited energy at each wire. The cumulative sum of this distribution is the total deposited energy for 1 GeV/c pion beam particles until their interaction at a wire X. The energy deposition maps are shown in Figure 7.8. The APA3 boundary is visible in the region of wires 480 where there is a small plateau in the reconstructed deposited energy. After the APA boundary data and simulations slightly diverge. Otherwise, the general agreement for data and simulation is excellent. The interacting kinetic energy of the reconstructed beam particle is estimated by subtracting the deposited energy retrieved from the map from the initial kinetic energy measurement of each beam pion.

7.3 INTERACTING AND INCIDENT PION EVENTS

This section shows the incident and interacting histograms for selected beam pions and pion absorption events with the event selection discussed in Chapter 5. The presented histograms are the input distributions that will be corrected for event selection inefficiencies and purities and for the final measurement are unfolded.

Incident Beam Pion Histogram

As introduced in Section 2.5 and Section 7.1, the events for the incident histogram, should all be selected beam pions. The necessary event selection cuts in order to isolate a sample of beam pions were introduced in Section 5.4. The selected

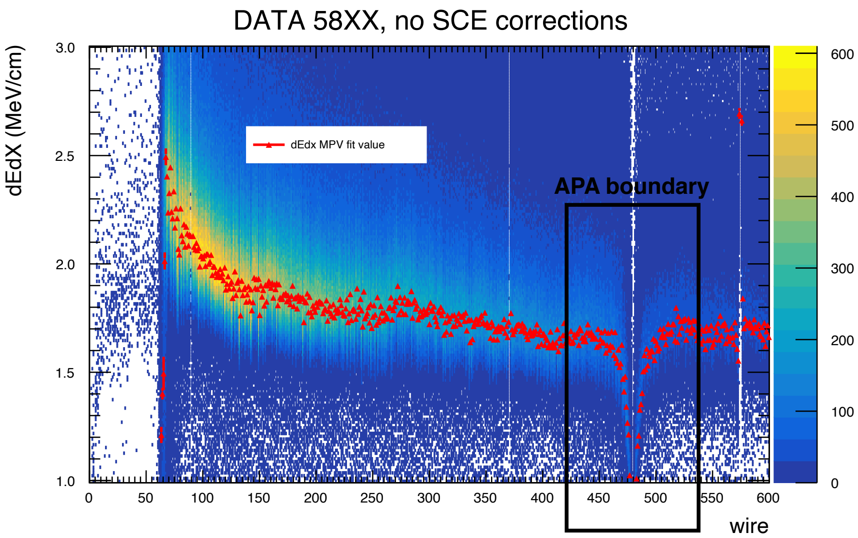

(a) Data dEdx MPV fit

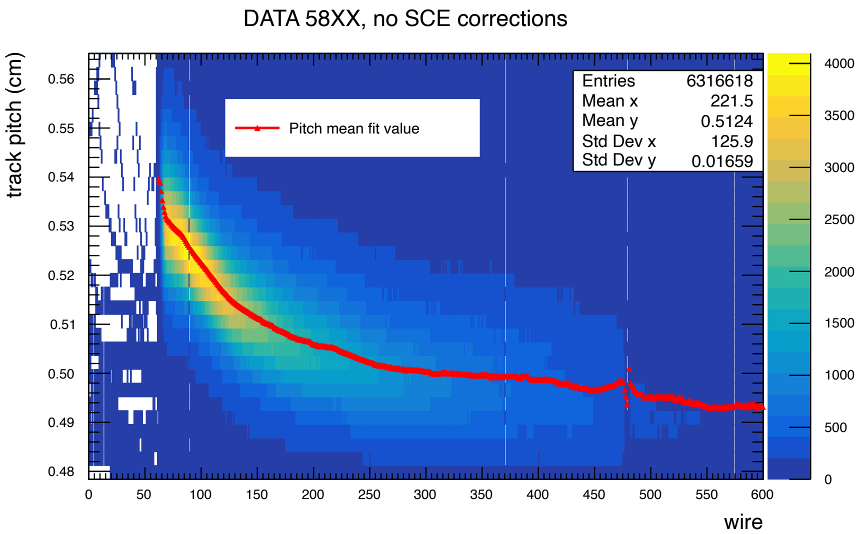

(b) Data track pitch fit.

Figure 7.6: 2D histograms of reconstructed dEdx vs wire and track pitch vs wire for ProtoDUNE-SP 1 GeV beam data from several runs. The distributions for dE/dx on each wire are fitted with a Landau function and the track pitch distributions with a Gaussian. The MPV and mean of the fits are overlaid in red onto the 2D distributions. Distortions from the electron diverters in the APA3 boundary are well visible in the wire region 450 – 500.

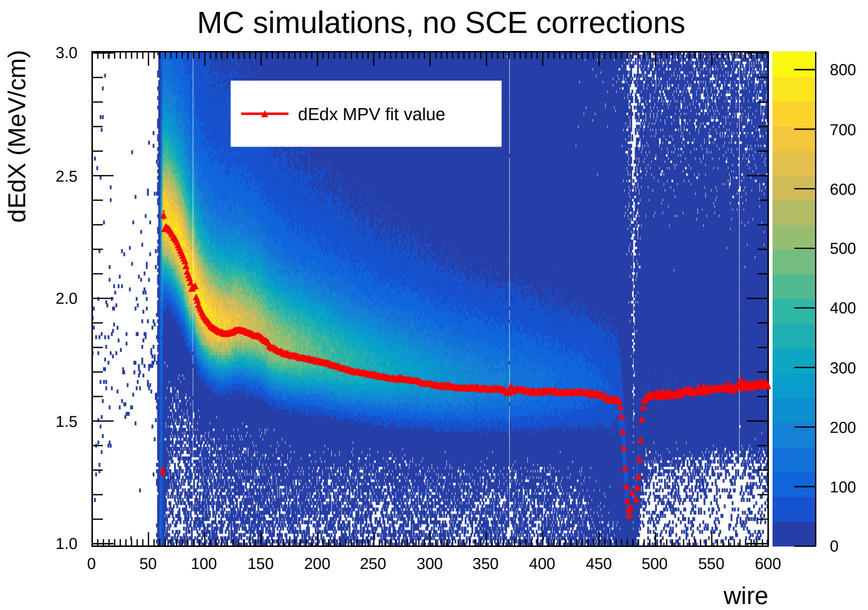

(a) MC dEdx MPV fit

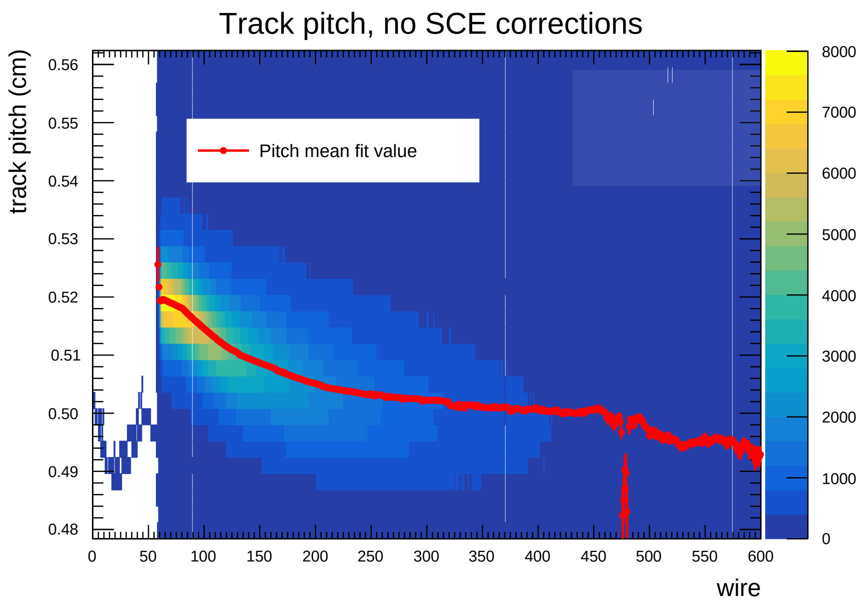

(b) MC track pitch fit.

Figure 7.7: 2D histograms of the reconstructed dEdx vs wire and track pitch vs wire distribution for simulated 1 GeV pions in ProtoDUNE-SP. As done in data, the dEdx distribution for every wire is fitted with a Landau and the MPV value is estimated. For the track pitch a Gaussian fit is applied. The obtained fit values are overlaid in red. The distinctive S-shape in the dEdx distribution around wire 100 – 150 is due to inaccurate simulations of the SCE effects in ProtoDUNE-SP. This will be improved in future simulations.

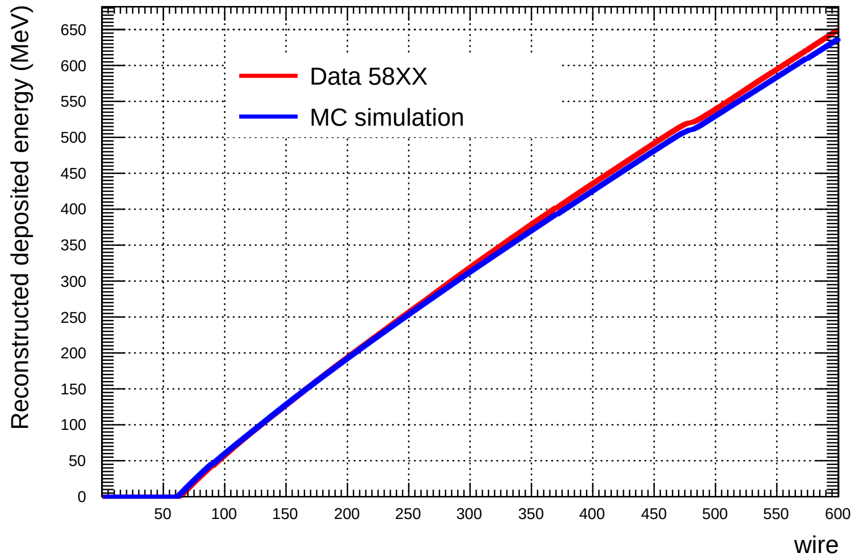

Figure 7.8: Cumulative sum of the product of the fit values in Figure 7.6a and Figure 7.6b for data in red vs mc in blue from Figure 7.7a and Figure 7.7b. This is the distribution used to determine the deposited energy in the LArTPC for each beam particle if the collection wire at the interaction point is known. The APA boundary region is visible at wire 480. The agreement for data and simulations is excellent.

sample of primary beam pion candidates is used to compute the distribution of the reconstructed initial and interacting kinetic energy of the selected events. The selection purity and efficiencies for primary beam pions were estimated from the simulations and discussed in Section 5.6. They are summarised again in Table 7.2.

PRIMARY BEAM PION SELECTION	VALUE
Purity	94 %
Efficiency	59 %

Table 7.2: Summary of efficiency and purity results for selected primary beam pions.

Figure 7.9 shows the initial and interacting kinetic energy distributions for the selected beam pion events in data and MC in bins of 50 MeV. The initial kinetic energy of the simulated events is re weighted as explained in Section 6.1. The general agreement for data and simulations is good. However it seems that the number of interacting pions in the kinetic energy range of 200 to 600 MeV is underestimated for simulations, see Figure 7.9b. This is due to the fact that beam pions interacting at lower kinetic energies are found to be in the APA boundary region where the track breaking is overestimated in the simulations with respect to data. Despite the cut at the APA boundary, the mismatch leaves some data MC discrepancy.

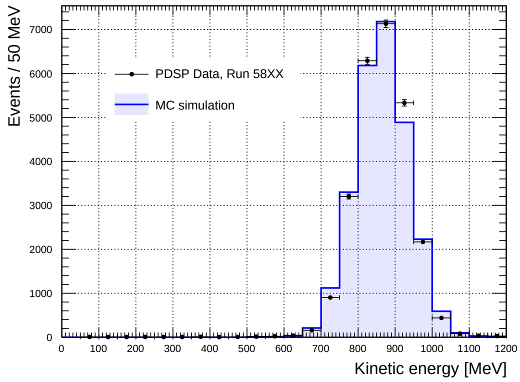

(a) Selected beam pions reconstructed initial kinetic energy

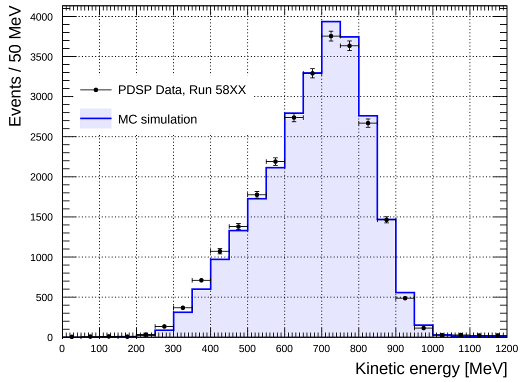

(b) Selected beam pions reconstructed interacting kinetic energy

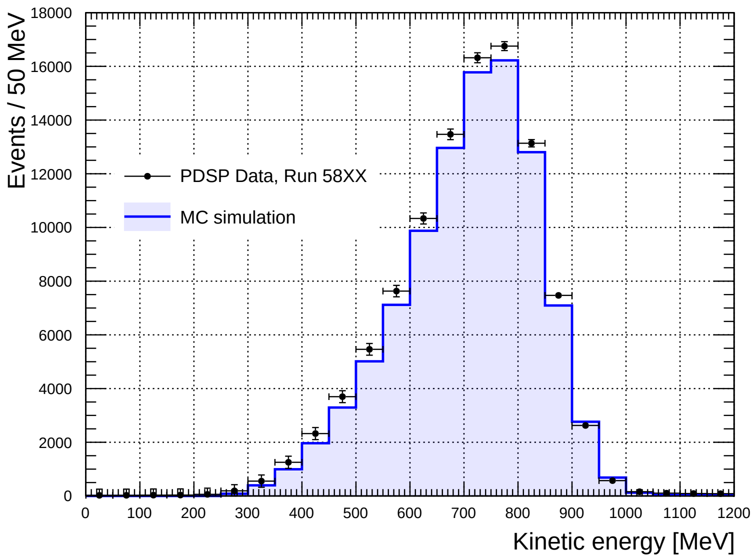

(c) Selected beam pions reconstructed incident distribution

Figure 7.9: Distributions of the reconstructed kinetic energy for selected beam pions data vs MC. Figure 7.9a and Figure 7.9b are used to compute the histogram of the incident pions Figure 7.9c with Equation 7.1. The MC dsitributions are scaled to data.

Interacting Pion Absorption Histogram

The sample of selected pion absorption event candidates is used to compute the distribution of the reconstructed interacting kinetic energy shown in Figure 7.10. The estimated purity and efficiency for the pion absorption selection is summarised in Table 7.3. A drop in number of events after the 400 MeV interacting energy bin can be seen. This is due to the APA3 boundary cut in the event selection. Furthermore, at lower kinetic energy values the statistics for the measurement start becoming scarce. This will introducing some limits to the unfolding procedure and the final measurement of the pion absorption cross-section, which is explained in the upcoming section.

PION ABSORPTION SELECTION	VALUE
Purity	59 %
Efficiency	45 %

Table 7.3: Summary of efficiency and purity results for selected pion absorption event candidates.

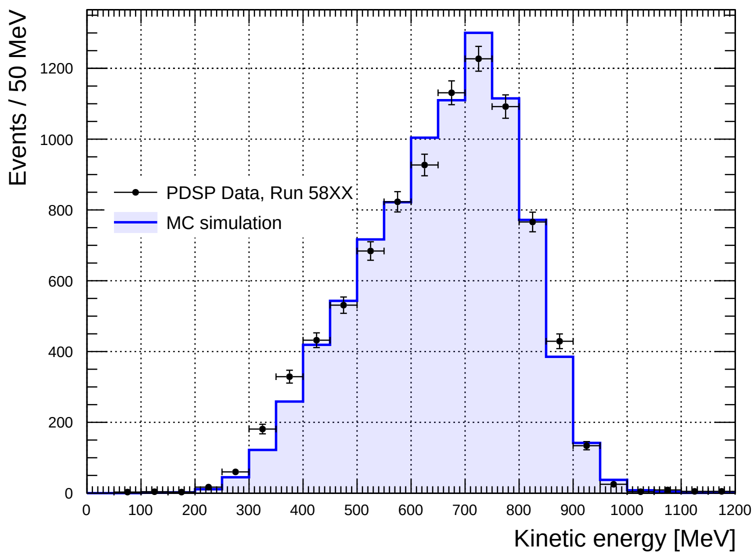

Figure 7.10: Distribution of the reconstructed kinetic energy for selected pion absorption events data vs MC. The MC dsitributions is scaled to data. The visible drop in events below the 400 MeV bin is due to the APA boundary cut.

7.4 UNFOLDING PROCEDURE

The ultimate goal of experimental physicists is to provide results that are independent of the experiment and can be used as input or constraints on theoretical models. However, measured distributions never are free of distortions arising from detector effects, physical or instrumental background, and statistical fluctuations. In the present case, the measured distributions of the interacting and incident histograms are expressed in terms of the reconstructed kinetic energy which is affected by distortions and smearing. The smearing from true kinetic energy to reconstructed kinetic energy can be removed employing unfolding procedures. The mathematical problem can be expressed as

$$m_i = \sum_{j=1}^{M} \mathbf{R}_{ij} t_j, \quad i = 1, ..., N \tag{7.8}$$

where the measured distributions are the bin contents m_i of the pion initial, interacting and absorption interacting histograms. $\mathbf{R}_{ij}$ is the response matrix and t_j the bin contents of the true distribution of the kinetic energy as shown in Section 7.1. The response matrix maps the true distribution to the measured/reconstructed distribution. If $N = M$ the response matrix is a square matrix. It becomes clear that MC simulations carry out the job of the response matrix. In consequence, the quality of the response matrix is tied to the quality of the MC simulations, its underlying physics models, and the statistics. The easiest approach to derive the truth distribution is to invert the response matrix. This is not trivial, as often smearing matrices can be singular, *i. e.* non-invertible or non-linear with large off-diagonal contributions. The inverted matrix will have large oscillations on off-diagonal entries with negative contributions and thus is not able to handle any large statistical fluctuations in measured distributions. Results of inverted matrices are very unstable and cannot provide reasonable unfolded measurement results.

The problem of retrieving truth distributions is more complex and different approaches with their limits are used in particle physics. The measurement presented here uses an *unfolding method* proposed by G. D'Agostini in 1993 [115, 116]. The method is based on Bayes' Theorem and is a powerful tool for statistical inference. The method has several advantages such as applicability to multidimensional problems, variable bin width between true and measured distributions, any smearing and bin migration can be accounted for, different background sources can be considered, it does not rely on matrix inversion, and a correlation matrix can be computed from the results. It was implemented within the ROOT framework and is accessible ready to use in several classes of code.

The Bayes' Theorem makes the following statement for several independent causes C_i and effects E_j. The causes can be compared to the truth and the effects on the measured distributions. A cause can influence different effects but the exact cause of an observed effect remains unknown. Thanks to detector simulations, the knowledge of particle behaviour in matter, and theoretical models of interactions, estimates can be made on bin migration, efficiency, and resolution. In consequence, the probability for an observed effect produced by a defined cause $P(E_j|C_i)$ is estimated by simulations. The purpose of unfolding is to estimate the probability of different causes responsible for an observed effect, namely, find an estimate for $P(C_i|E_j)$. The estimation is done by using Bayes' Theorem: if an observation of an effect E has occurred, the probability that the cause C_i was responsible can be noted as shown in Equation 7.9

$$P(C_i|E) = \frac{P(E|C_i) \cdot P(C_i)}{\sum_{l=1}^{n_C} P(E|C_l) \cdot P(C_l)}. \tag{7.9}$$

Thus, the probability of cause C_i producing an the observed E is proportional to the initial probability of the cause $P(C_i)$ multiplied by the probability of the cause to produce the effect $P(E|C_i)$. For experimental distributions the following statement can be made: $n(E)$ observed events are assigned to several causes. The expected number of events corresponding to one cause $\widehat{n}(C_i)$ can be written as

$$\widehat{n}(C_i) = n(E) \cdot P(C_i|E). \tag{7.10}$$

As several effects are possible E_j, $j = 1, ...n_E$, the Bayes formula holds for each probability $P(C_i|E_j)$ and Equation 7.9 and 7.10 are rewritten as

$$P(C_i|E_j) = \frac{P(E_j|C_i) \cdot P_0(C_i)}{\sum_{l=1}^{n_C} P(E_j|C_l) \cdot P_0(C_l)}, \tag{7.11}$$

$$\widehat{n}(C_i) = \frac{1}{\epsilon_i} \sum_{j=1}^{n_E} n(E_j) \cdot P(C_i|E_j) \qquad \epsilon_i \neq 0, \tag{7.12}$$

where $P_0(C_i)$ are the initial probabilities and ϵ_j the efficiencies of the i-th cause having an effect. From the unfolded events $\widehat{n}(C_i)$ the final probability of the causes and and an overall efficiency can be estimated as follows

$$\widehat{N}_{true} = \sum_{i=1}^{n_C} \widehat{n}(C_i), \tag{7.13}$$

$$\widehat{P}(C_i) = \frac{\widehat{n}(C_i)}{\widehat{N}_{true}}, \tag{7.14}$$

$$\widehat{\epsilon} = \frac{N_{obs}}{\widehat{N}_{true}}. \tag{7.15}$$

It is possible that the initial probability $P_0(C_i)$ is not consistent with the data and does not agree with $\widehat{P}(C_i)$. With simulations, this can be verified and an iterative approach to estimate the final $\widehat{n}(C)$ and $\widehat{P}(C)$ can be taken by comparing the χ^2 of the estimated number of causes at each iteration step. After a certain number of iterations, the unfolded distribution of $\widehat{n}(C)$ is obtained. The necessary number of iterations is estimated by observing the change of the χ^2 values for the unfolded distributions stopping when the value is significantly low and does not change a lot from one iteration to the next. As iterative unfolding in the limit of infinity becomes matrix inversion, a too high number of iterations can lead to unwanted oscillatory behaviour in the unfolded distributions.

Bayesian unfolding can also take into account the presence of background as a background simply is another cause responsible for the effects. Finally, the result of an unfolding process is an estimator for the truth distribution with a corresponding covariance matrix. Bin-to-bin correlations are retrieved from the covariance matrix.

In the present measurement, the software package RooUnfold [117] has been used as it implements D'Agostini unfolding with Bayes' Theorem. The number of iterations can be set by the user and the prior probabilities for the effects E_j due to causes C_i, are implemented from the MC simulations in a response matrix as they provide a prior map from truth to measured observables. Background events can also be included and the framework can take care of selection and reconstruction efficiencies. The implementation of the reco-true relations for the kinetic energy observable, as well as the selection purities and efficiencies is called the training process.

The built-in error propagation of RooUnfold is not used. Instead, I vary the training distributions for the unfolding process according to estimated systematic uncertainties, as discussed in Chapter 6). The measured distribution from data then is unfolded with the varied training sets to estimate the effect on the measured cross-section through the varied training samples. This has the advantage, that the data to be unfolded remains unchanged. Limits to the unfolding technique used here, are the estimate of how many iterations to consider, the estimate of the error from unfolding, and the underlying initial bias from the MC simulations by favoring them in the training process through the prior assumed probabilities for a pion absorption interaction which is intrinsically present in the cross-section model of the simulations. Testing different numbers of iterations, varying the response matrices, or using MC simulations from different generators are means to reduce and understand the limitations. Furthermore, comparisons to other measurement methods are useful for sanity checks.

Unfolding Validation with MC Simulations

Validation of the unfolding procedure is done on the measured simulated distributions. The unfolding of the incident histogram is done for the distributions of the initial pion kinetic energy and interacting pion kinetic energy (Figure 7.9a and Figure 7.9b). The unfolded incident histogram is obtained from the two underlying unfolded distributions. Thus, three distributions are unfolded to obtain the unfolded estimate of the cross-section: the selected beam pion initial kinetic energy and interacting kinetic energy distribution and the selected pion absorption interacting distribution are all separately unfolded.

In the RooUnfold package, the events from the simulation are classified into three types. They contribute either to the response matrix, missed events, or fake events with their true and/or reconstructed values for the pion interacting (initial) kinetic energy. Table 7.4 shows the conditions for events in the categories.

Thus, the response matrix is filled with selected true signal events. Furthermore, only events are assigned to the response matrix if they do not start and interact in the same bin of kinetic energy in the reconstructed as well as in the true phase space. The response matrix is the prior probability to reconstruct a pion of a certain true interacting kinetic energy in a certain reconstructed kinetic energy bin.

Events that are categorized as missed are true signals that were not selected by the event selection, not reconstructed or reconstructed to be starting and interacting in the same kinetic energy bin but do not in the truth phase space. The missed events represent inefficiencies.

Fake events are background events that made it into the selection or signal events that in the true phase space start and interact in the same bin. Within the unfolding procedure, backgrounds are subtracted before unfolding from the reconstructed to the true phase space.

Depending on the distribution that is unfolded, the categorization of the events changes. For example, if the measured distribution of selected pion absorption events is unfolded, the true signal is the pion absorption signal and the selection is the one for isolating pion absorption events. If the measured distributions of the full ensemble of beam pions are unfolded, the selection is composed of the initial cuts for the beam pion selection and the true signal is a beam pion regardless of its interaction process.

It is important to be unfolding in a reasonable range of the distribution, especially in the range where data and simulations agree. It was shown in Section 5.4 and Section 6.4 that the agreement of data and simulations is discrepant in the region of the APA3 boundary. Furthermore, it is important to remember that the ensemble of the selected beam pion events was subject to a fiducial volume cut at 220 cm of the reconstructed end position in the z-coordinate for each primary particle. According to Figure 7.8 particles reaching the APA boundary have up to $\sim$ 500 MeV along their trajectory. The distribution of the reconstructed initial kinetic energy of selected beam pions peaks at 865 MeV. This back-of-the-envelope estimation already suggests that unfolding the measured distributions below the interacting kinetic energy bin at 400 MeV could be problematic.

Figure 7.11 shows side-by-side the normalised 2D distributions of the reconstructed end Z position vs the interacting kinetic energy for beam pion candidates before the APA3 cut. The cut is indicated with a red line on the distributions. It is visible by comparing the data and simulation distributions that for the interacting kinetic energy bins 200-450 MeV the behaviour differs. This leads to problems with the unfolding procedure and is a limiting factor for the measurement. Low

RESPONSE MATRIX $\mathbf{R}[E_{reco}\|E_{true}]$	MISSED $\mathbf{m}[E_{true}]$	FAKE $\mathbf{f}[E_{reco}]$
$\wedge$ True Signal Event	$\wedge$ True Signal Event	$\wedge$ Selected Event
$\wedge$ Reco init. KE bin $\neq$ reco inter. KE bin	$\wedge$ True init. KE bin $\neq$ true inter. KE bin	$\wedge$ ($\neg$ True Signal $\vee$ true init. KE bin == true inter. KE bin)
$\wedge$ True init. KE bin $\neq$ reco inter. KE bin	$\wedge$ (Reco init. KE bin == reco inter. bin $\vee$ $\neg$ Selected Event)	
$\wedge$ Selected Event		

Table 7.4: For the unfolding procedure of a measured distribution the events are assigned into three categories according to certain criteria, represented by logic symbols (and = $\wedge$, or = $\vee$, not = $\neg$) in the table. If an event is of true signal type, has been selected by the underlying event selection and does not start and interact within the same energy bin in the true and reconstructed phase space, it contributes to the response matrix. The response matrix is a map projecting the true phase space onto the reconstructed phase space and representing the energy smearing. A true event that was not selected (or reconstructed) or wrongly reconstructed by starting and ending in the same reco kinetic energy bin, is considered a missed event. Such an event contributes to the efficiency consideration in the unfolding procedure. Fake events are background events that sneak in the selection or events that in the true space started and interacted in the same energy bin (they cannot be considered for the incident and interacting histograms). They are subtracted prior to unfolding.

statistics in bins above 1000 MeV limit the unfolding at higher energies. Thus, the conservative range of 450 -1000 MeV in interacting kinetic energy is chosen for the unfolding procedure.

In future simulations, the APA3 boundary region is expected to be better modeled. This will allow extending the energy range for the unfolding procedure to lower energies. For now, the issues of the simulations limit the unfolding procedure, and thus, unfolded results below 450 MeV are not reliable.

The validation of the unfolding procedure is done in the following way: Two-thirds ($\sim 45 \times 10^3$ events) of the available 1 GeV/c beam pion simulations are used to create the response matrix, the missed events, and the fake events. The other $\sim 20 \times 10^3$ events of the MC statistics are used to test the unfolding algorithm: the measured distributions for the beam pion selection initial and interacting histogram as well as the measured distribution for the pion absorption selection are used as *pesudo data* input to the unfolding framework. The underlying truth distributions for the *pseudo data* MC are available and can be compared for accuracy to

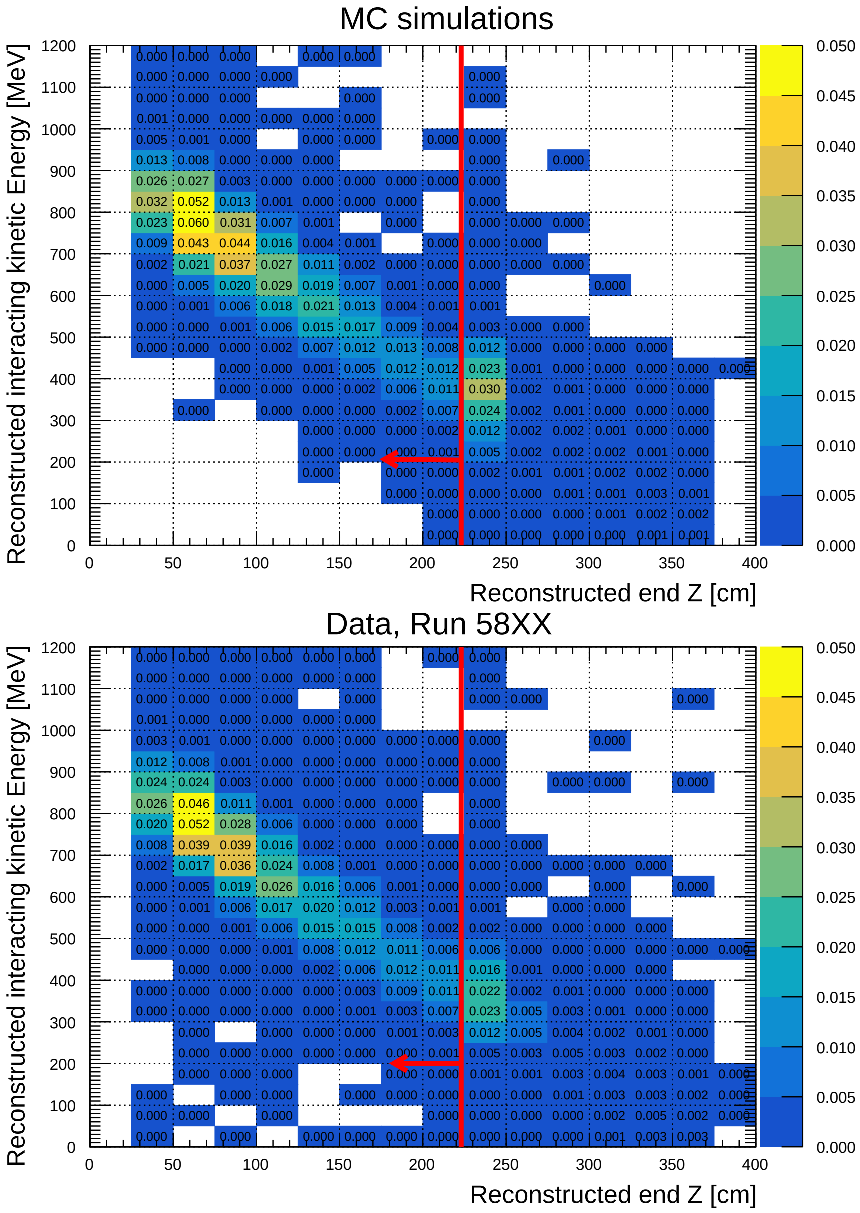

Figure 7.11: Normalised 2D distributions of the reconstructed end z-coordinate vs interacting kinetic energy of reconstructed beam pion candidates before the APA3 cut. On the left the simulations and on the right the results from data are displayed. The disagreement of simulations and data in the APA3 boundary region is visible. Due to the discrepancy the range of unfolding is chosen conservatively only for kinetic energy bins in the range of 450 to 1000 MeV.

the unfolded distributions. For validation of the framework and implementation, the unfolded distributions should agree with the truth distributions.

The unfolded distributions are shown for the beam pion selection initial kinetic energy and interacting energy, as well as for the pion absorption selection interacting kinetic energy in Figure 7.12a, Figure 7.12c and Figure 7.12e, respectively. The bin-to-bin correlations are shown for each unfolded distribution on the right-hand side. The implementation of the unfolding algorithm reproduces the underlying truth distributions well for the beam pion sample. Discrepancies in the unfolding of the higher energy part for the pion interacting energy Figure 7.12c are compensated when computing the incident histogram as can be seen in Figure 7.13. Since it is an integral of the beam pions it is less sensitive to the fluctuations from unfolding.

The unfolding on the absorption histogram shows some discrepancies in the higher energy bins. This is a cumulated effect of low statistics in those energy bins and the *background contribution* due to being located in the beam pion initial kinetic energy rise and thus having a larger likelihood of pions starting and interacting in the same energy bin. With a smaller bin width than 50 MeV, this apparent background contribution would decrease, however, the bin-to-bin migration would increase and the reasons for the 50 MeV choice have been already explained.

Figure 7.14 shows the extraction of the cross-section with the unfolded distribution in comparison to the underlying truth distribution of the simulation sample used for validating the framework. The errors in the unfolded distribution are just the statistical and systematic errors of the cross-section measurement as described in Equation 7.4. The error of unfolding is not taken into account. Above 950 MeV the errors increase due to the very low statistics in those energy bins. The entry of the energy bin at 1000 MeV of the unfolded incident histogram is 0. Therefore, the unfolding procedure gives reliable results in the energy range of 450 to 950 MeV of pion kinetic energy.

Table 7.5 gives a rundown of the χ^2 of change results after each iteration. The χ^2 of change describes the convergence of the unfolded distribution with respect to the previous step. The initial energy histogram is unfolded during 4 iterations, the interacting histograms for beam pions and pion absorption are unfolded with 6 iterations. The response matrices used for training will be shown in Section 7.5 as they are the same response matrices as used for the final unfolding on data, but with fewer statistics as one-third of the available simulations was used for validation.

ITERATION	PION INIT E χ^2	PION INTER E χ^2	ABS INTER E χ^2
0	0.141	19.212	6.658
1	0.096	4.558	2.534
2	0.074	1.507	1.403
3	0.062	0.749	0.882
4	–	0.479	0.616
5	–	0.341	0.465

Table 7.5: Values for the χ^2 of change after each iteration of the unfolding algorithm where the unfolded distribution is compared to the previous.

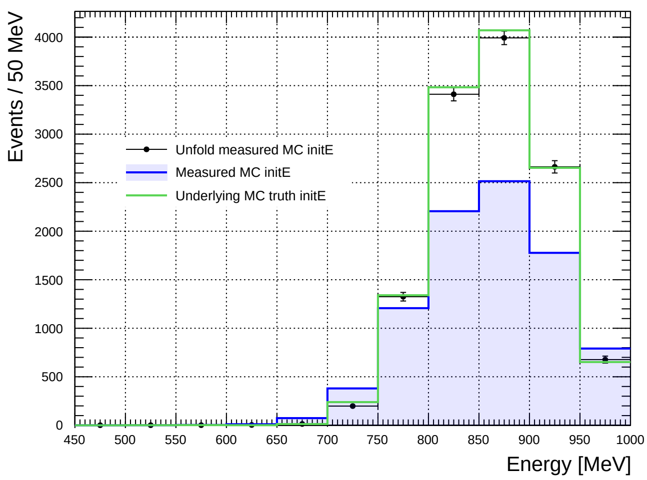

(a) Selected beam pions initial energy distribution

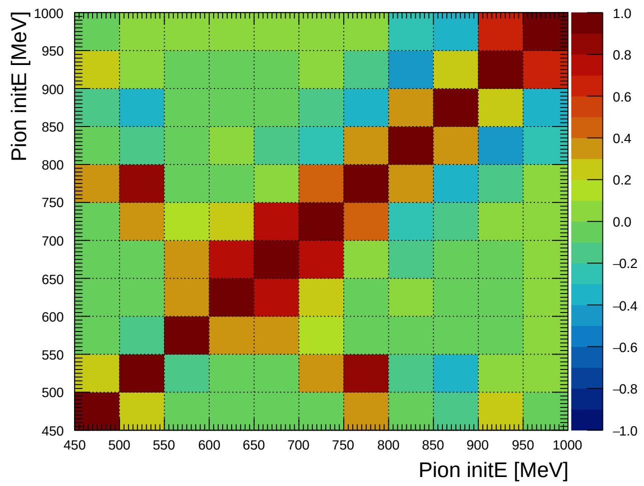

(b) Bin-to-bin correlations

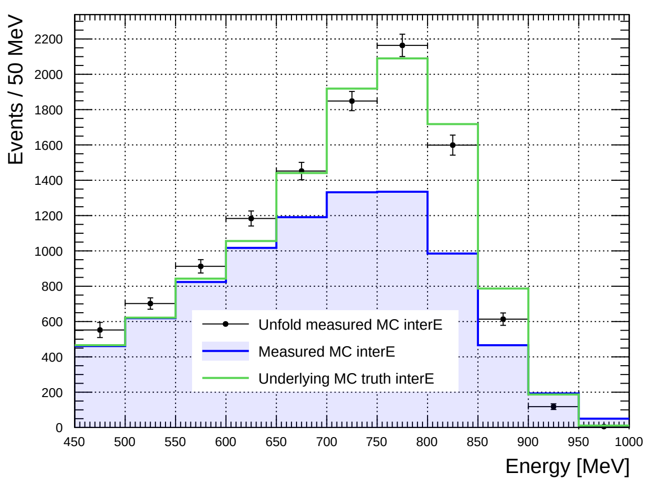

(c) Selected beam pions interacting energy distribution

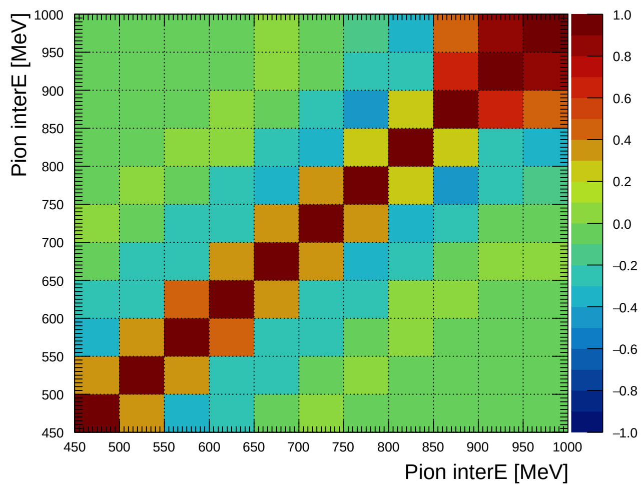

(d) Bin-to-bin correlations

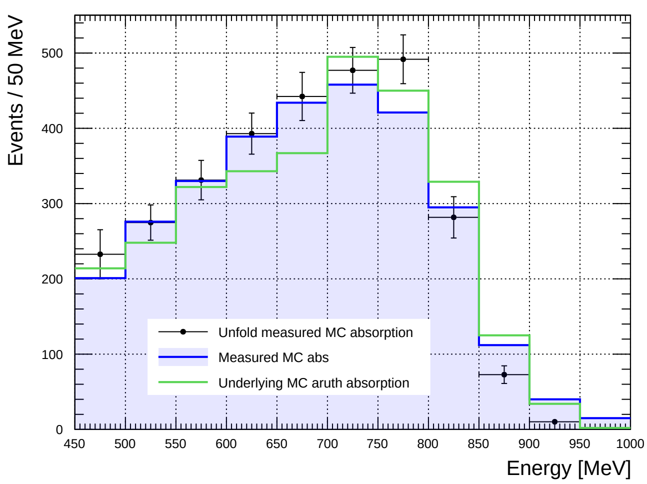

(e) Selected pion absorption interacting energy distribution

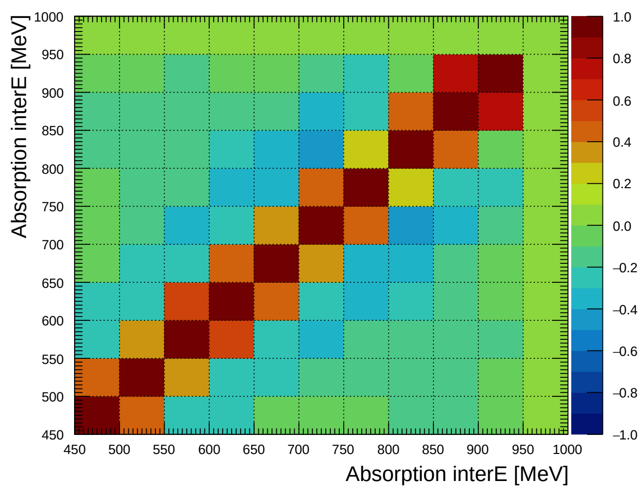

(f) Bin-to-bin correlations

Figure 7.12: Validation of the unfolding procedure. Two thirds of the available beam simulations are used to create the response matrix and estimate the backgrounds. The remaining third is used to test the unfolding frame work with a *pseudo data* measured distribution. The unfolded distribution is compared to the underlying truth distribution. For the interacting samples the results of the unfolding for energy bins above 850 MeV is less well behaved. The bin-to-bin correlations are shown for all unfolded distributions. For the interacting samples at higher energies the off-diagonal correlations are stronger. In general always three adjacent bins are strongly correlated due to the bin migrations.

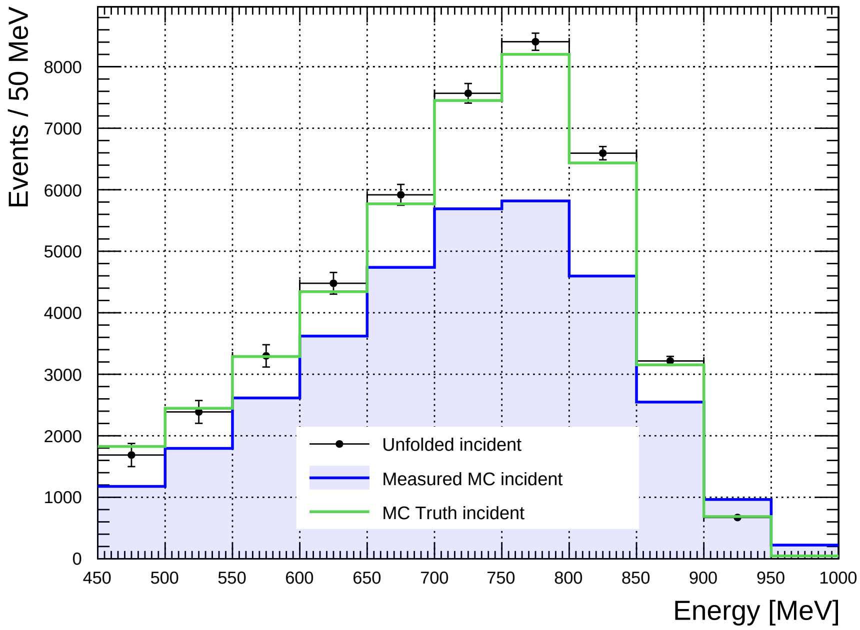

Figure 7.13: Unfolded incident distribution built from Figure 7.12a and Figure 7.12c. The incident histogram is less sensitive to the discrepancies at higher energies as shown in the unfolded interacting energy histogram in Figure 7.12c).

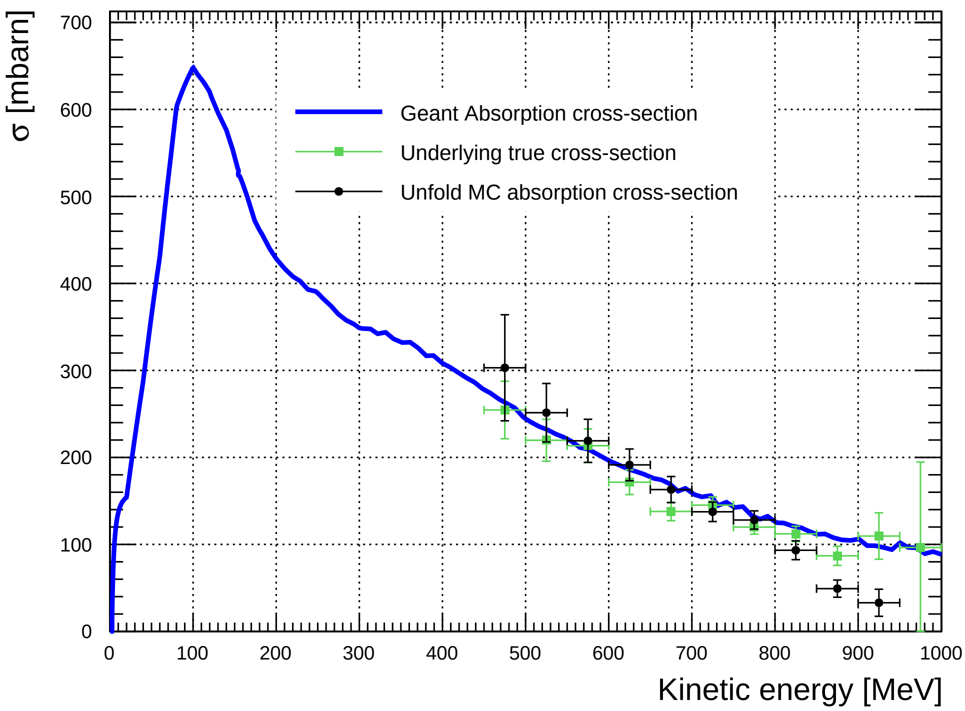

Figure 7.14: Closure test on the unfolding procedure: Extraction of the cross-section with the unfolded distributions form Figure 7.12e and Figure 7.13. The cross-section extraction for the underlying truth distributions is shown in green. The estimated errors include the statistical errors from the E-Slice method as described in Equation 7.4. The error arising from unfolding is not taken into account. The results are reliable in the range of 450 to ∼950 MeV true pion kinetic energy. Lack of events above 950 MeV produces large errors.

7.5 DETERMINATION OF THE CROSS-SECTION

This section discusses the unfolding of the data distributions and the final extraction of the cross-section with the propagated uncertainties. The uncertainties are propagated by varying the training samples for the unfolding, *i.e.* the MC events according to the systematic uncertainties. The measured data distributions, remain unchanged and are unfolded with all the varied training samples one by one. The variations in the extracted cross-section reflect the effect of the uncertainties and allow to provide a final cross-section measurement with propagated uncertainties. Table 7.6 is the list of the runs used for the analysis. They have been properly calibrated and were taken during stable detector conditions with an electron lifetime larger than 25 ms.

RUN NUMBER	BEAM MOMENTUM [GeV/c]	PION TRIGGERS
5809	1	7501
5810	1	3391
5814	1	3994
5816	1	7987
5817	1	19246
5842	1	22572
5844	1	5430

Table 7.6: List of *good runs* at beam momentum 1 GeV/c with calibration used for analysis.

Unfolding the Data Distributions

With the response matrices shown in Figure 7.15, the estimates of missed signals and selected backgrounds in the iterative Bayesian unfolding is applied to the measured distributions from ProtoDUNE-SP 1 GeV/c beam momentum data in the range of 450–1000 MeV pion kinetic energy. The three response matrices are shown in Figure 7.15. The data are unfolded with the same amount of iterations as used in the MC validations. Table 7.7 shows the values of the χ^2 of change after each iteration. Figure 7.16 shows the unfolded data distributions. The unfolding process shown here is trained with the nominal MC simulations.

A preliminary test on the resulting cross-section from the unfolded distributions is shown in Figure 7.18. The errors on the distributions are estimated according to Equation 7.4. The effects of systematic errors are propagated in the next sections. The general behaviour of the preliminary cross-section measurement tends to systematically be lower than the Geant absorption cross-section predictions. The

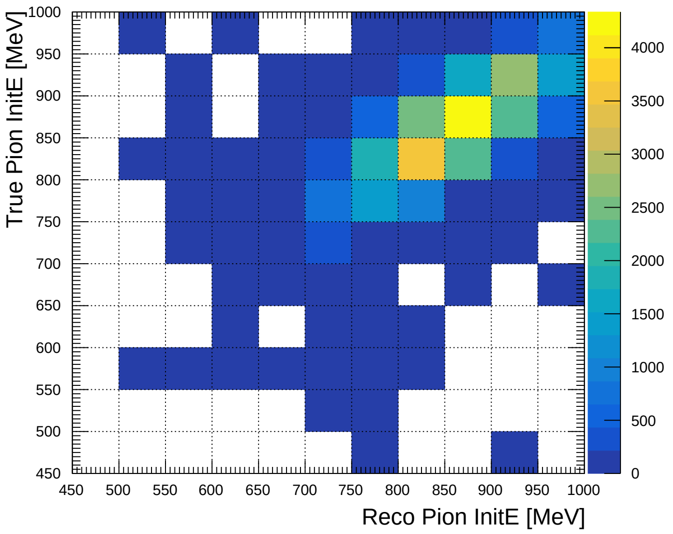

(a) Response matrix pion initial energy

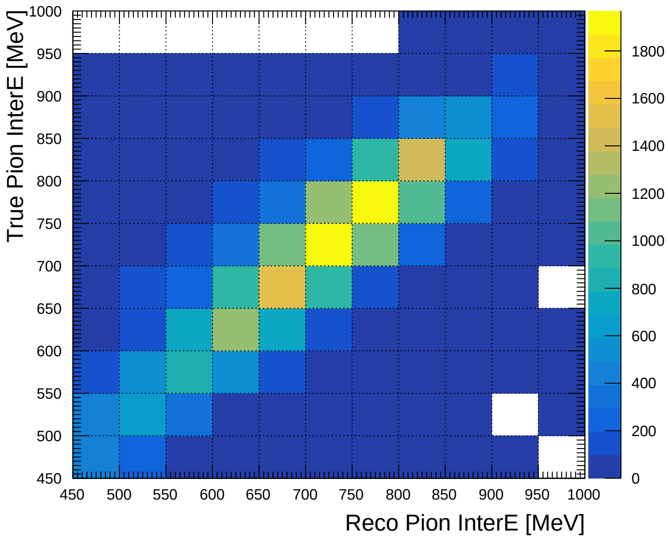

(b) Response matrix pion interacting energy

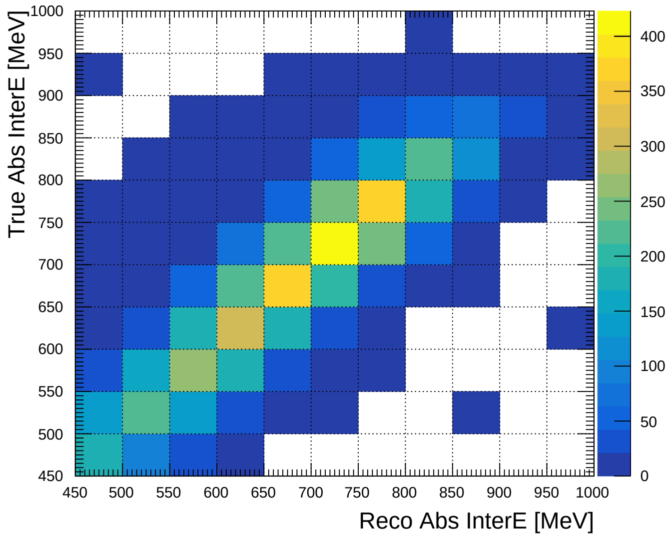

(c) Response matrix pion absorption

Figure 7.15: Response matrices used for the unfolding procedure of the three reconstructed distributions: the pion initial kinetic energy, the pion interacting kinetic energy and the pion absorption interacting kinetic energy distribution. The matrices describe the initial probability of the observed effects being produced by the defined causes, *i. e.* the energy smearing from a true energy distribution to a reconstructed energy distribution due to detector effects, statistical fluctuations and backgrounds.

extraction of the errors from the systematic uncertainties and the effect of those on the final measurement are discussed in the next section.

ITERATION	DATA PION INIT E χ^2	DATA PION INTER E χ^2	DATA ABS INTER E χ^2
0	18.592	55.113	1.196
1	6.508	15.025	0.852
2	2.938	5.67	0.639
3	1.727	2.957	0.499
4	–	1.861	0.405
5	–	1.285	0.337

Table 7.7: Unfolding Data: Values for the χ^2 of change after each iteration of the unfolding algorithm where the unfolded distribution is compared to the previous.

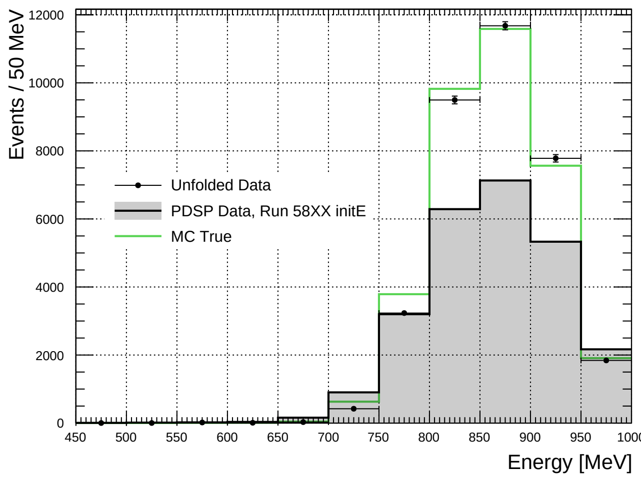

(a) Data: selected beam pions

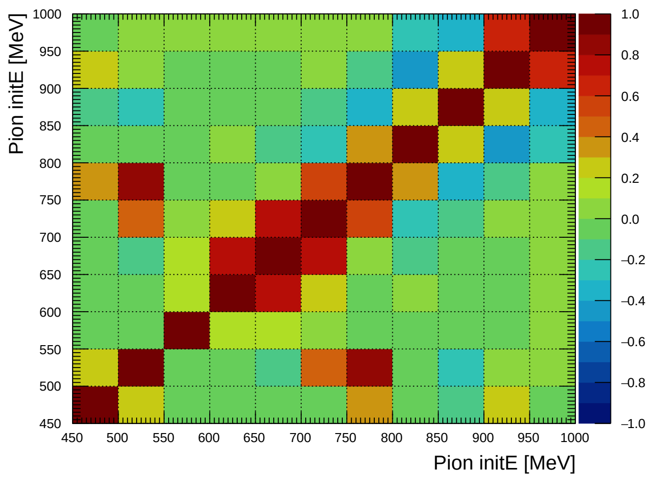

(b) Bin-to-bin correlations

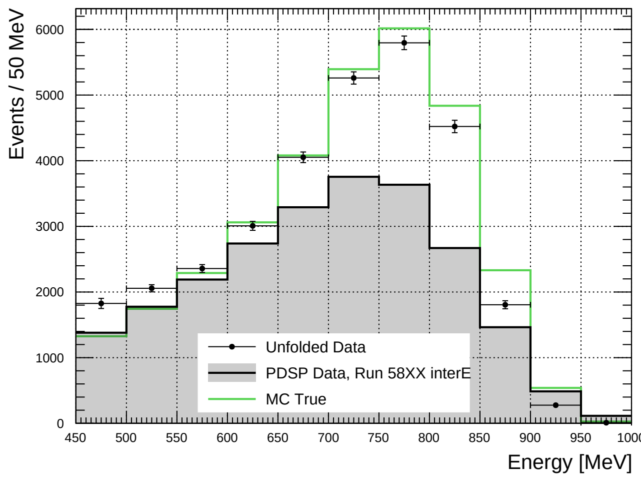

(c) Data: selected beam pions

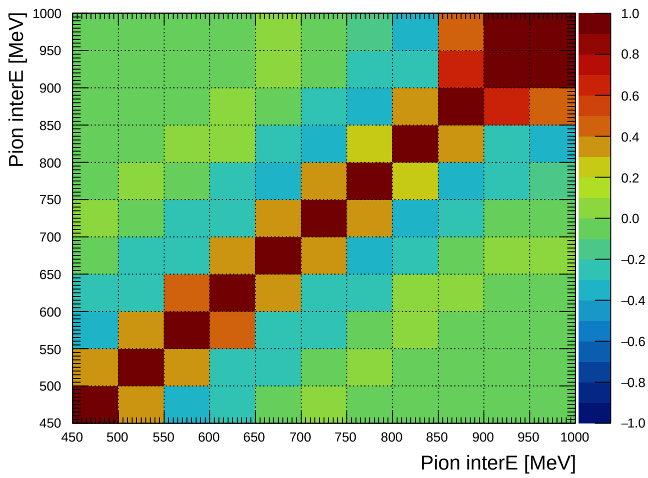

(d) Bin-to-bin correlations

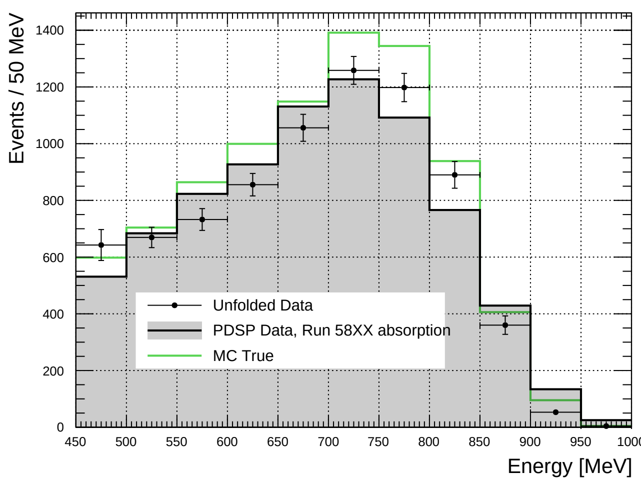

(e) Data selected pion absorption

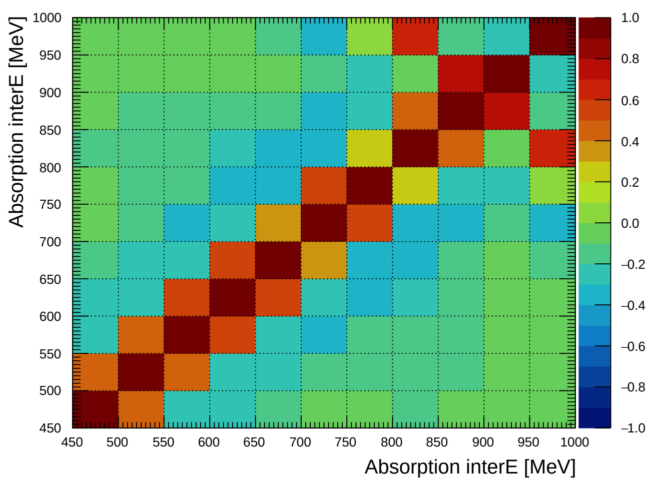

(f) Bin-to-bin correlations

Figure 7.16: For each measured distribution (gray histogram) the results of unfolding (black points) and the MC truth predictions (green) are shown. The corresponding bin-to-bin correlations are shown for each unfolded distribution on the right-hand side. Compared to the MC validation the off diagonal correlations at the higher energy bins are stronger. The unfolded distributions are comparable to the MC truth distributions. In the lowest energy bin at 450 MeV there is a slight rise in the unfolded pion sample and more pronounced in the absorption sample. Figure 7.16c shows less pions interacting at higher energies for the unfolded distribution.

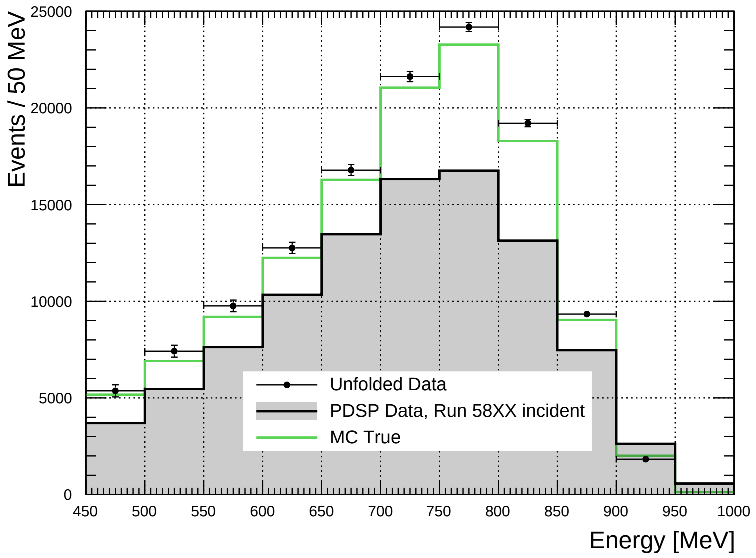

Figure 7.17: Resulting unfolded incident distribution for data from Figure 7.16a and Figure 7.16c with respect to the measured distribution in gray and the MC truth distributon in green. In data a slight excess of pions is measured at lower kinetic energy. This is a relic of the fact that in the unfolded distribution in Figure 7.16c less pions interact at higher energies with respect to the truth distribution.

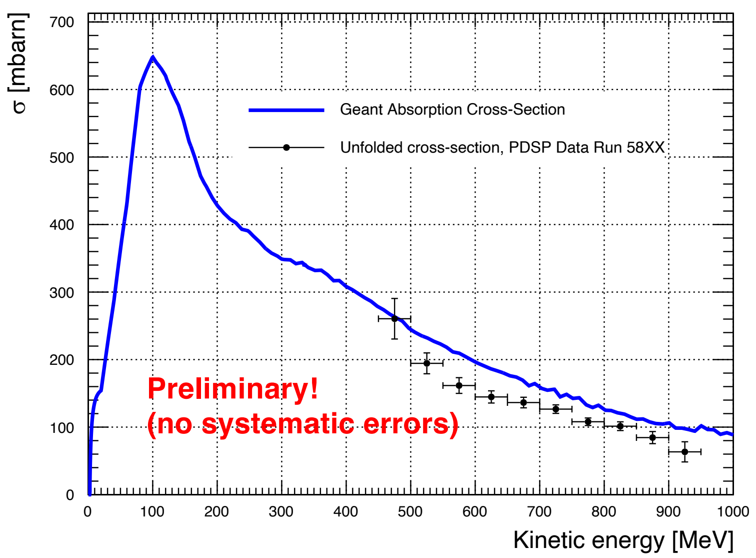

Figure 7.18: Preliminary unfolded cross-section from the unfolded data distributions in Figure 7.16e and Figure 7.17. The errors do not include the systematic uncertainties. The rising behaviour of the GEANT cross-section agrees with the unfolded results from data. However, the preliminary unfolded measurement tends to show a lower measured cross-section than the model prediction.

7.6 PROPAGATION OF SYSTEMATIC UNCERTAINTIES

Chapter 6 detailed several uncertainties on the measurement that are taken into consideration and propagated for the final computation of the cross-section measurement. For the propagation of the uncertainties, the measured distributions from data are not varied. However, the MC simulations that are used to train the unfolding framework are globally varied according to the uncertainty. This results in *new* prior probabilities according to the variation that is done. Depending on the type of variation the response matrices may change, the total number of events, the number of background events, or the efficiencies of the selection. The measured data distributions are unfolded multiple times with differently trained frameworks. In this way, the effect of each uncertainty can be studied in the unfolded measured cross-section with the corresponding framework with respect to the central values of the unfolded data in the non-varied nominal MC case.

Table 7.8 summarises the four main uncertainties that are varied in the training sample for the unfolding. The variation of the four uncertainties leads to eight differently trained unfolding frameworks. Thus, the measured distributions from ProtoDUNE-SP data are unfolded eight times each with a different unfolding framework resulting in variations of the cross-section according to the varied prior probabilities. The resulting error on the cross-section from the variations are measured on a bin-by-bin basis and finally listed for each variation in Table 7.9. Furthermore, the error on the cross-section from the calculation is listed and finally, the total error on the cross-section measurement for each bin is computed in the table as the square root of the sums of the squares of each error.

UNCERTAINTY	VARIATION
Energy	initial kinetic energy $\pm$25.5 MeV
	interacting kinetic energy $\pm$28.5 MeV
Pion Absorption cross-section model	$\pm$20 %
Absorption Selection Purity	$\pm$10 %
Absorption Selection Efficiency	$\pm$10 %

Table 7.8: Summary of the uncertainties that are propagated in the measurement of the pion absorption cross-section. The uncertainties are varied on a global basis and not bin-by-bin.

Pion Kinetic Energy Variation

The distribution of the reconstructed kinetic energies for simulated MC events are changed in two ways as described by Equation 7.16. When adding ΔE to the reconstructed kinetic energies, the pions are simulated to be incident and interact at higher energies. When subtracting ΔE, the opposite is the case. The change of the reconstructed particle kinetic energy affects the shape of the response matrix and the background shape.

$$\begin{aligned} E_{initial\ KE} &= E_{initial\ KE} + \Delta E_{initial} & E_{interacting\ KE} &= E_{interacting\ KE} + \Delta E_{interacting} \\ E_{initial\ KE} &= E_{initial\ KE} - \Delta E_{initial} & E_{interacting\ KE} &= E_{interacting\ KE} - \Delta E_{interacting} \end{aligned} \tag{7.16}$$

Figure 7.19 shows the results after unfolding the measured distributions from data with the varied unfolding frameworks. It is well visible that the variations of the cross-section with a shift in energy have the most impact on the higher and the lower energy bins. This can be understood because the number of events in those bins is smaller and thus the distribution shifts have more impact, see Figure 7.15. Furthermore, a global uncertainty on the reconstructed kinetic energy of the pion candidates impacts the various energy bins differently. When increasing the pion kinetic energies the unfolding reveals a steepening of the measured cross-section prediction (darker colored squares), if energy is subtracted from the reconstructed central values then the unfolded cross-section distribution flattens out (light red squares).

Pion Absorption Cross-Section Model Variation

The implemented pion absorption cross-section model is varied by $\pm 20\%$. In consequence, the total number of pion absorption events is increased/decreased, *i. e.* a pions chance to interact in the absorption channel is higher/lower. The variation changes the number of signal events contributing to the response matrix and missed events. As the pion absorption cross-section in this way is changed globally the bin to bin variations are not expected to be very different from each other.

Figure 7.20 shows the unfolded distributions with MC simulations that include more/less pion absorption events. The shape of the unfolded distributions from the varied MC is the same as the central values of the unfolded data. Increasing the model cross-section leads to an increase of the unfolded distributions and vice versa for the decrease. For energy bins above 550 MeV, the bin-to-bin variations of the unfolded distributions are similar. At the lower energy bins, where the cross-section increases the variations are slightly larger. While the cross-section is changed by 20% in the simulations, the change in the unfolded data distributions is smaller and around 10%. In consequence, enough decrease in the cross-section model will converge with the unfolded distributions of data. This is something to keep in mind for future work on the present analysis.

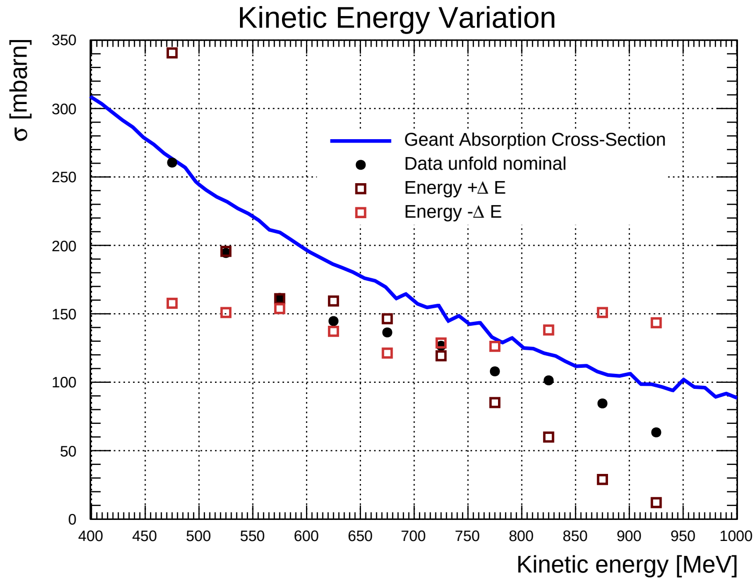

Figure 7.19: Unfolded cross-section measurement with unfolding frame works including the uncertainties on the reconstructed kinetic energy. The MC simulations are varied for their reconstructed kinetic energy and the unfolding framework is trained with the varied MC sample. The data remains unchanged and is unfolded with the varied MC samples. The plot shows the central values of the unfolded data (black dots) and the new unfolded distributions for the energy variations on the beam particle reconstructed kinetic energy. A global variation of the reconstructed particle energy impacts the energy bins differently. The uncertainties at low and high energy bins of the unfolding are larger than in the range of 550 to 750 MeV.

Pion Absorption Event Selection Purity Variation

As was shown in Chapter 5, the event selection relies on cut variables where simulation and data agreement is mostly well behaved. However, the estimates of the purity (and efficiency) of the event selection completely rely on the simulations. The central value of the purity estimated from the pion absorption event selection is 59%. The impact of variations in purity of ±10% is explored here. The selected background distribution is characterised by the *Fake* container in the unfolding training. Before unfolding, the background contributions are subtracted from the measured distribution in each bin. A change in purity increases / decreases the background contributions. As is visible in Figure 7.21 an increase in purity increases the unfolded cross-section measurement and a decrease in purity reduces the unfolded cross-section with respect to the central values. The simulations may include a misestimate of the backgrounds. This needs further investigation and should be constrained by independent control samples from data facili-

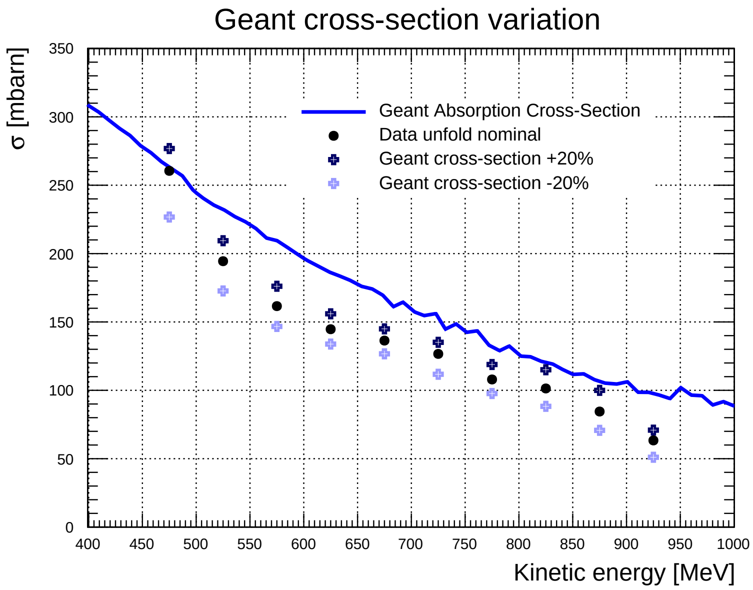

Figure 7.20: Unfolded cross-section measurement with varied pion absorption cross-section models. The total number of pion absorption signals is varied in order to reflect an increase / decrease of the pion absorption cross-section. The data distributions remain unchanged and are unfolded with the varied MC samples. The general shape of the unfolded central values is maintained in the unfolded variations. As expected with a higher cross-section model as prior assumptions for unfolding the unfolded cross-section is moved up and vice versa for a decrease of the pion absorption cross-section model. The change of the unfolded distributions is of around 10% with respect to the central values of the unfolded distribution. This is smaller than the cross-section model change. Eventually convergence can be reached by exploring the decrease of the cross-section model.

tating background constraints for the unfolding procedure. A separate selection of background events was not possible within the timeline of this thesis.

Pion Absorption Event Selection Efficiency Variation

As the event selection purity, also the efficiency of the event selection relies on the estimates of the simulations. The efficiency is a value for how many true signal events were *missed* by the event selection or reconstruction. The efficiency of the event selection was estimated to be 45%, which is varied by $\pm 10\%$ to see the impact of the variation. The efficiency can be controlled in the unfolding framework by either increasing or decreasing the *Miss* distribution and at the same time decreasing or increasing the events contributing to the *Response Matrix* accordingly.

Figure 7.22 shows that an increase in the efficiency just very slightly lowers the unfolded cross-section distribution. This suggests the systematically lower central values of the unfolded data might be stable. A decrease in efficiency, *i. e.* less pion

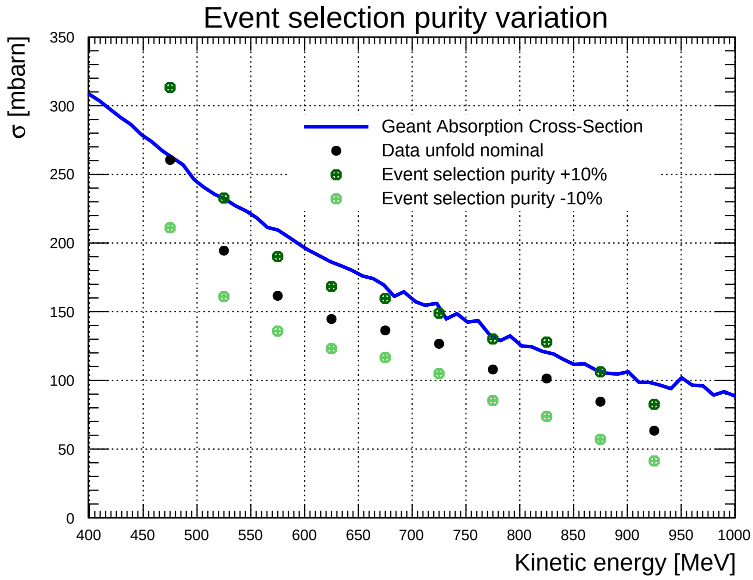

Figure 7.21: Unfolded distributions for varied event selection purity by ±10%. The event selection purity is varied by globally changing the number of selected background events in the event selection. As the purity estimation of the event selection relies on the simulations it is possible that certain background contributions are under or over estimated. As an addition to this measurement and to constrain the background uncertainty, in future independent control samples should be used in order to constrain the backgrounds of the measurement and not rely only on the simulations for the estimate.

absorption events detected pulls up the unfolded cross-section measurement. Improved versions of the event selection will strive for better efficiency and purity.

Given the tests with the current event selection, the unfolded cross-section values can be expected to confirm the region of their central values with reduced systematic errors. The contribution of each systematic uncertainty to each energy bin is listed in Table 7.9 and the total uncertainty is computed.

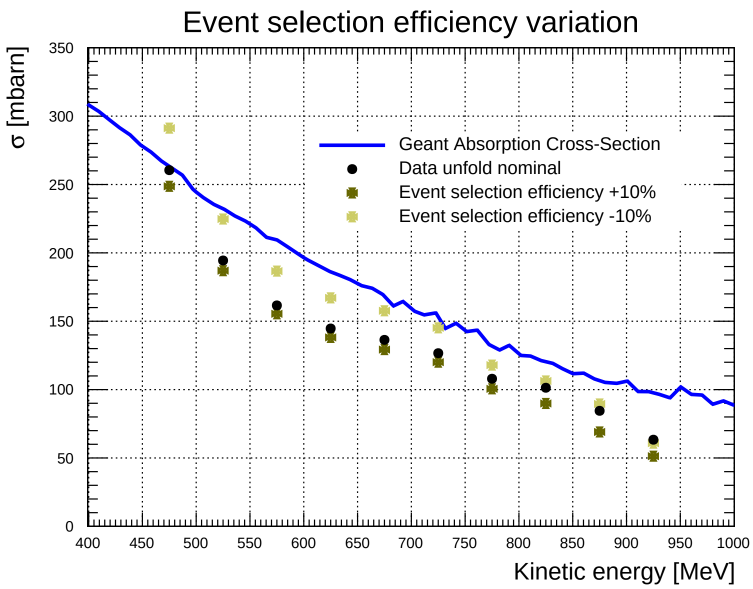

Figure 7.22: Unfolded distributions for varied event selection efficiency by ±10%. The variation of the efficiency is done by shifting missed events to the response matrix for an efficiency increase or the other way around for an efficiency decrease. An efficiency increase leads to very similar results on the unfolded cross-section as the central values. An efficiency decrease shifts the unfolded results upwards. Improved event selections are expected to have improved efficiency.

Bin central value [MeV]	475	525	575	625	675	725	775	825	875	925	975
Cross-Secion central value [mbarn]	260.1	194.4	161.6	144.8	136.3	126.3	107.6	102.2	90.8	78.5	0
$\delta_{+\Delta E}$	+80.5	+1.2	-0.6	+14.5	+10.0	-7.0	-22.5	-42.3	-61.8	-66.4	–
$\delta_{-\Delta E}$	-102.4	-43.5	-7.8	-7.6	-15.1	+2.4	+18.6	+35.9	+60.1	+ 65.0	–
$\delta_{+\ cross-section\ model}$	+16.7	+15.01	+14.5	+11.1	+8.6	+8.8	+11.2	+12.8	+9.2	+7.5	–
$\delta_{-\ cross-section\ model}$	-33.4	-21.7	-14.9	-11.0	-9.7	-14.6	-10.0	-13.9	-20.0	-27.4	–
$\delta_{+\ event\ selection\ purity}$	+53.1	+38.3	+28.5	+ 23.5	+23.3	+22.6	+22.5	+25.7	15.4	+4.1	–
$\delta_{-\ event\ selection\ purity}$	-49.0	33.4	-25.7	-21.7	-19.7	-21.4	-22.4	-28.5	-33.7	-37.1	–
$\delta_{+\ event\ selection\ efficiency}$	-11.4	-7.4	-6.2	-6.7	-7.1	-6.2	-7.1	-12.4	-21.8	-27.1	–
$\delta_{-\ event\ selection\ efficiency}$	+31.1	+30.4	+25.1	+22.3	+21.3	+18.9	+10.3	+ 4.1	-1.3	-17.6	–
Total $\delta_{syst\ high}$	102.7	53.5	40.6	37.2	34.3	30.9	32.9	46.2	62.8	65.1	–
Total $\delta_{syst\ low}$	-118.9	-59.4	-31.3	-26.4	-27.5	-27.5	-34.0	-54.3	-76.4	-.87.4	–
$\delta_{xs\ calculation}$	±30.0	±14.5	±11.6	± 9.0	±7.8	±6.3	±5.6	± 6.5	±9.5	±17.6	–
Total $\sigma_{xs\ high}$	107.0	53.5	42.3	38.3	35.1	31.5	33.4	46.6	63.5	67.5	–
Total $\sigma_{xs\ low}$	-122.7	-61.4	-33.4	-27.9	-28.6	-28.2	-34.5	-54.7	-77.0	-89.2	–

Table 7.9: Summary of the induced bin-by-bin errors from varying the reconstructed energy, the cross-section model, the event selection purity and efficiency in the MC simulations. The second row summarises the obtained central values (CV) of the unfolded data distributions. The final three rows list the total systematic high and low errors and the error on the cross-section extraction as introduced in Equations 7.4, 7.5, and 7.6. Due to the different bin-to-bin errors for the high and low values the final errors on the cross-section measurement are asymmetric.

7.7 FINAL CROSS-SECTION RESULTS WITH SYSTEMATIC UNCERTAINTIES AND DISCUSSION

This chapter has discussed in detail the steps included in the measurement of the pion absorption cross-section on liquid argon for 1 GeV/c beam pions in the range of 450 to 950 MeV kinetic energy with data from ProtoDUNE-SP. The measurement is performed with the newly developed energy slicing method including an unfolding procedure to remove detector effects and correct for event selection inefficiencies and purities. The dominant uncertainties have been discussed and their effects on the final measurement were evaluated. The final result of the unfolded cross-section measurement with ProtoDUNE-SP data is shown in Figure 7.23 and compared to the GEANT model prediction and the existing LADS data for pion absorption interactions on argon.

For each bin of the measurement, the total uncertainty is included as calculated in Table 7.9. The cross-section estimation is in agreement with the LADS results suggesting a lower cross-section than estimated by the GEANT predictions. The

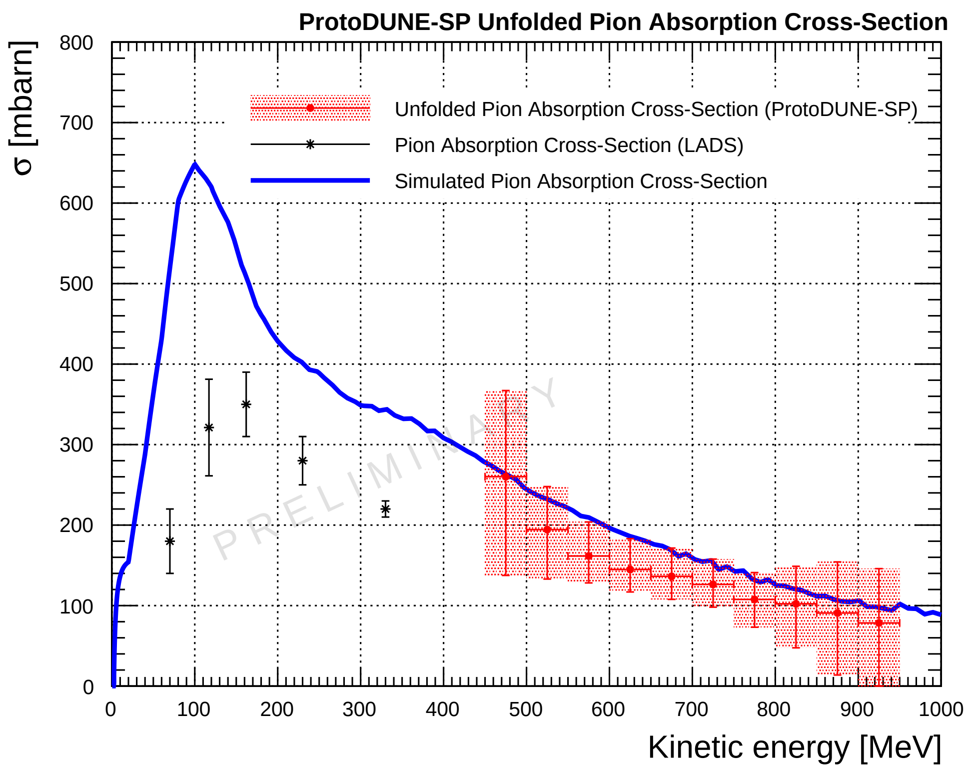

Figure 7.23: Final measurement of the pion absorption cross-section on liquid argon for pions at 1 GeV/c momentum. The results are shown with their statistical and systematic uncertainties in the pion kinetic energy range of 450 to 950 MeV. For comparison, the data of the LADS experiment [66] is shown, and the GEANT model predictions (blue-8) were used in the simulations for ProtoDUNE-SP data.

ProtoDUNE-SP pion absorption cross-section measurement agrees within 15–20% of the GEANT predictions. However, the central values of the measurement indicate a lower cross-section. The physics model agrees with the general trend.

The result of the pion absorption cross-section agrees with the LADS data suggesting a lower cross-section than used in the GEANT predictions. Nevertheless, it is important to understand the systematically lower cross-section value of the measurement. Different causes can lead to this result.

Firstly, the estimated background may be too low. The variation of the purity uncertainty showed that the unfolded cross-section values rise with increasing purity. Defining an independent control sample to constrain the backgrounds of this measurement can give more insight into the predicted backgrounds from the underlying physics model. Beam muons will go beyond the APA boundary region and can be used in the future as an independent control sample for the muon background estimation.

Secondly, it was also shown in the uncertainty evaluation that a global variation of the model cross-section leads to an increase/decrease of the unfolded cross-section. In the next step, the GEANT cross-section model should be reweighted to better match data and the measurement can be done again to verify that the model predictions converge with the results from data.

The current measurement is limited in its energy range from 450 to 950 MeV kinetic energy. The limitation in the lower energy part is due to the fiducial volume cut at the APA boundary. Beyond, the discrepancies of data and simulations are too significant to continue the measurement. The maximum energy deposition within the first wire plane is $\mathcal{O}$(500 MeV), thus 1 GeV/c pions will at most reach values of around 450 MeV before crossing the APA boundary. Future improvements of the simulations will allow us to explore the cross-section at pion kinetic energies below 450 MeV. The measurement can be extended and more statistics can be added by including beam momentum data runs (2 – 7 GeV).

CONCLUSIONS AND OUTLOOK

Liquid Argon Time Projection Chambers are powerful detectors for neutrino oscillation physics experiments, supernovae neutrino observations, and proton decay searches. Next-generation experiments such as DUNE are based on this technique. They require high sensitivity for a broad spectrum of science goals. The main science drivers for DUNE are the measurement of the CP-violating phase in the oscillation parameters and the determination of the neutrino mass hierarchy. The CP-violation search will reveal the yet unknown reasons for the matter-dominated universe we live in. To meet the required goals a strong effort in R&D is necessary to pave the way for large-scale LArTPC detectors such as DUNE.

This PhD thesis was dedicated to the construction and operation of the largest LArTPC built to date: ProtoDUNE-SP, the first DUNE far detector prototype containing $\mathcal{O}(700\ \mathrm{t})$ liquefied argon. The detector was operated from September 2018 to July 2020 at CERN collecting hadron beam data in the momentum range of 0.5 to 7 GeV/c. The ProtoDUNE-SP performance for calorimetry and its imaging resolution are excellent and were published in [72].

During the first two years of my PhD, as part of my experimental work, I was a member of the large core team building, commissioning, and running the ProtoDUNE-SP detector. I became one of the experts on the high voltage system and the field cage which are the heart of any LArTPC detector. In the beamtime period, I provided essential contributions to the data-taking campaign of the experiment assuring high-quality data taking. Further, I performed the first studies on space charge effects showing the direct dependence of the liquid argon fluid flow from the purification system with the asymmetric distribution of the accumulated space charge. An extensive paper on the design, construction, and operation of ProtoDUNE-SP was published in August 2021 [40]. Thanks to my extensive involvement in the completion of the detector I was appointed as one of the five editorial board members for this publication.

I dedicated the second half of my PhD thesis to the development of a hadron interaction cross-section measurement with ProtoDUNE-SP beam data. Charged pions are common products of neutrino interactions. Therefore, precise knowledge of their behaviour and interactions with argon nuclei is crucial to control systematic uncertainties on neutrino oscillation parameters at the percent level. To measure CP-violation, oscillation analyses rely on simulations from event generators to understand and interpret the results from the experiments. Only scarce data on interaction cross-sections of pions with nuclei exist in literature. So far, the implemented predictions for pion interactions with argon nuclei have been interpolated from measurements with heavier and lighter nuclei than argon. If pions undergo a *pion absorption* process they are absorbed by an argon nucleus and will not be detected. Pion absorption can make a charged current resonant neutrino interaction look like a quasi-elastic neutrino interaction and thus presents a significant background for the latter. Therefore, I decided to measure the pion absorption cross-section on argon for 1 GeV/c beam pions with ProtoDUNE-SP. This measurement provides the neutrino community with data on this specific interaction that can then be fed into prediction models.

To perform the measurement I developed an event selection procedure to isolate pion absorption events from the total sample of pion events. The event selection algorithms were thoroughly tested and optimised in order to maximise purity and efficiency. The measurement methodology is based on an original energy slice method that I developed. The new method is not sensitive to spatial distortions in the detector which were measured to be significant due to space charge accumulation. I concluded the pion absorption cross-section measurement in the energy range of 450 to 950 MeV pion kinetic energy. To compare the measurement with predictions of pion absorption models, the measured results were unfolded in order to remove smearing effects from the detector and account for impurities and inefficiencies from the event selection and reconstruction. I found the model predictions to lie within the systematic uncertainties of the final results. However, my measurement suggests a systematic underestimation of the model predictions for the cross-section. This is in agreement with pion absorption on argon measurements in the energy ranges from 90 to 330 MeV obtained by the former LADS experiment.

Currently, the presented measurement is limited in its energy range due to a mismatch of data and simulations on the wire plane boundary region. As the measurement relies on purity and efficiency corrections from the simulations, the measurement was restricted to a fiducial volume region of the first 220 cm of ProtoDUNE-SP from the beam entry point. Here, distributions for the relevant observables between data and simulations agree remarkably well. If the simulations are improved, the measurement range can be extended in the lower kinetic energy region and fully compared to the LADS measurements. In the higher energy range, the measurement can be extended by including the higher pion momentum runs above 1 GeV/c. Due to lack of calibration for the high beam momentum runs, it was not possible to include them in the scope of my thesis.

The currently used method of removing the detector smearing through iterative unfolding can be biased as the estimates of the prior probabilities come from the model predictions. I included a global systematic uncertainty on the implemented pion absorption model. However, I did not modify the implemented cross-section shape. Different possibilities to remove any model biases in the measurement should be explored in the future. The simplest approach would be to vary the current cross-section model in shape and study the effect on the unfolded measurement. Another option would be to vary the measured distributions from the simulations in order to better match data and then extract the model cross-section from the varied distributions. The results of the two methods can then be compared to each other. Within the ProtoDUNE-SP analysis group, other methods will be tested soon to complete the measurement.

The established event selection completely relies on the estimated efficiencies and purities from simulations. In the future, it would be beneficial to reduce uncertainties on the selection purity, if independent samples constraining the background shapes with data were defined. An independent sample could be the beam muon events passing the APA boundary. Other improvements through the implementation of neural networks could be made to the event selection. However, a well-researched guess on possible systematic uncertainties introduced by such neural networks should be made.

With the here presented first pion absorption cross-section measurement and the suggested further studies, the energy range extension, and a cross-validation with a different cross-section measurement method the pion absorption cross-section measurement will be mature enough to be published in a dedicated physics paper. The results can be fed to the theoretical models in order to improve the model predictions and reduce theoretical systematic uncertainties which propagate to the neutrino oscillation parameter measurements and, ultimately, to the sensitivity on the CP-violating phase determination.

BIBLIOGRAPHY

[1] C. Giunti and C.W. Kim. *Fundamentals of Neutrino Physics and Astrophysics*. OUP Oxford, 2007. ISBN: 9780191523229.

[2] M. Thomson. *Modern Particle Physics*. Modern Particle Physics. Cambridge University Press, 2013. ISBN: 9781107034266.

[3] S.M. Bilenky. "Neutrino. History of a unique particle." In: *The European Physical Journal H* 38.3 (2012), 345–404. ISSN: 2102-6467. DOI: 10.1140/epjh/e2012-20068-9. URL: http://dx.doi.org/10.1140/epjh/e2012-20068-9.

[4] F. Stocker. "A Novel Approach to Liquid Argon Time Projection Chambers." Masterthesis presented in July 2017.

[5] J. Chadwick. "Intensitätsverteilung im magnetischen Spectrum der β-Strahlen von radium B + C." In: *Verhandl. Dtsc. Phys. Ges.* 16 (1914), p. 383. URL: http://cds.cern.ch/record/262756.

[6] C. D. Ellis and W. A. Wooster. "The Average Energy of Disintegration of Radium E." In: *Proceedings of the Royal Society of London Series A* 117.776 (Dec. 1927), pp. 109–123. DOI: 10.1098/rspa.1927.0168.

[7] W. Pauli. "Dear radioactive ladies and gentlemen." In: *Phys. Today* 31N9 (1978), p. 27.

[8] M. Goldhaber, L. Grodzins, and A. W. Sunyar. "Helicity of Neutrinos." In: *Phys. Rev.* 109 (3 1958), pp. 1015–1017. DOI: 10.1103/PhysRev.109.1015. URL: https://link.aps.org/doi/10.1103/PhysRev.109.1015.

[9] G. Danby, J-M. Gaillard, K. Goulianos, L. M. Lederman, N. Mistry, M. Schwartz, and J. Steinberger. "Observation of High-Energy Neutrino Reactions and the Existence of Two Kinds of Neutrinos." In: *Phys. Rev. Lett.* 9 (1 1962), pp. 36–44. DOI: 10.1103/PhysRevLett.9.36. URL: https://link.aps.org/doi/10.1103/PhysRevLett.9.36.

[10] Martin L. et al. Perl. "Evidence for Anomalous Lepton Production in e+ - e- Annihilation." In: *Phys. Rev. Lett.* 35 (1975), pp. 1489–1492. DOI: 10.1103/PhysRevLett.35.1489.

[11] R. Davis, D. S. Harmer, and K. C. Hoffman. "Search for Neutrinos from the Sun." In: *Phys. Rev. Lett.* 20 (21 1968), pp. 1205–1209. DOI: 10.1103/PhysRevLett.20.1205. URL: https://link.aps.org/doi/10.1103/PhysRevLett.20.1205.

[12] John N. Bahcall, Neta A. Bahcall, and Giora Shaviv. "Present Status of the Theoretical Predictions for the ^{37}Cl Solar-Neutrino Experiment." In: *Phys. Rev. Lett.* 20 (21 1968), pp. 1209–1212. DOI: 10.1103/PhysRevLett.20.1209. URL: https://link.aps.org/doi/10.1103/PhysRevLett.20.1209.

[13] S.M. Bilenky and B. Pontecorvo. "Again on Neutrino Oscillations." In: *Lett. Nuovo Cim.* 17 (1976), p. 569. DOI: 10.1007/BF02746567.

[14] S. Fukuda et al. "The Super-Kamiokande detector." In: *Nuclear Instruments and Methods in Physics Research Section A: Accelerators, Spectrometers, Detectors and Associated Equipment* 501.2 (2003), pp. 418–462. ISSN: 0168-9002. DOI: https://doi.org/10.1016/S0168-9002(03)00425-X. URL: https://www.sciencedirect.com/science/article/pii/S016890020300425X.

[15] N. Jelley, A. B. McDonald, and R.G. H. Robertson. "The Sudbury Neutrino Observatory." In: *Annual Review of Nuclear and Particle Science* 59.1 (2009), pp. 431–465. DOI: 10.1146/annurev.nucl.55.090704.151550. eprint: https://doi.org/10.1146/annurev.nucl.55.090704.151550. URL: https://doi.org/10.1146/annurev.nucl.55.090704.151550.

[16] Araki T. et al. "Measurement of neutrino oscillation with KamLAND: Evidence of spectral distortion." In: *Phys. Rev. Lett.* 94 (2005), p. 081801. DOI: 10.1103/PhysRevLett.94.081801. arXiv: hep-ex/0406035 [hep-ex].

[17] M. H. Ahn et al. "Measurement of Neutrino Oscillation by the K2K Experiment." In: *Phys. Rev. D* 74 (2006), p. 072003. DOI: 10.1103/PhysRevD.74.072003. arXiv: hep-ex/0606032.

[18] P. Adamson et al. "Measurement of Neutrino and Antineutrino Oscillations Using Beam and Atmospheric Data in MINOS." In: *Phys. Rev. Lett.* 110 (25 2013), p. 251801. DOI: 10.1103/PhysRevLett.110.251801. URL: https://link.aps.org/doi/10.1103/PhysRevLett.110.251801.

[19] Y. Abe et al. "Indication of Reactor $\overline{\nu}_e$ Disappearance in the Double Chooz Experiment." In: *Phys. Rev. Lett.* 108 (13 2012), p. 131801. DOI: 10.1103/PhysRevLett.108.131801. URL: https://link.aps.org/doi/10.1103/PhysRevLett.108.131801.

[20] F. P. An et al. "Observation of Electron-Antineutrino Disappearance at Daya Bay." In: *Phys. Rev. Lett.* 108 (17 2012), p. 171803. DOI: 10.1103/PhysRevLett.108.171803. URL: https://link.aps.org/doi/10.1103/PhysRevLett.108.171803.

[21] J.K. Ahn et al. "Observation of Reactor Electron Antineutrino Disappearance in the RENO Experiment." In: *Phys. Rev. Lett.* 108 (2012), p. 191802. DOI: 10.1103/PhysRevLett.108.191802. arXiv: 1204.0626 [hep-ex].

[22] A. D. Sakharov. "Violation of CP Invariance, C asymmetry, and baryon asymmetry of the universe." In: *Pisma Zh. Eksp. Teor. Fiz.* 5 (1967), pp. 32–35. DOI: 10.1070/PU1991v034n05ABEH002497.

[23] T2K Collaboration. "Constraint on the matter–antimatter symmetry-violating phase in neutrino oscillationss." In: *Nature* 580 (2020), 339–344. DOI: https://doi.org/10.1038/s41586-020-2177-0.

[24] M. Tanabashi, K. Hagiwara, K. Hikasa, and other. "Review of Particle Physics." In: *Phys. Rev. D* 98 (3 2018), p. 030001. DOI: 10.1103/PhysRevD.98.030001. URL: https://link.aps.org/doi/10.1103/PhysRevD.98.030001.

[25] D. Griffiths. *Introduction to elementary particles*. 2008. ISBN: 978-3-527-40601-2.

[26] P. Gagnon. *The Standard Model: a beautiful but flawed theory*. URL: https://www.quantumdiaries.org/2014/03/14/the-standard-model-a-beautiful-but-flawed-theory/. (accessed: 15.09.2021).

[27] G. Altarelli and K. Winter. *Neutrino mass*. Springer tracts in modern physics. Berlin: Springer, 2003. DOI: 10.1007/b13585. URL: https://cds.cern.ch/record/642521.

[28] I. Esteban et al. *Nufit4.1 at nufit webpage*. 2020. URL: http://www.nu-fit.org/?q=node/228.

[29] I. Esteban, M.C. Gonzalez-Garcia, M. Maltoni, T. Schwetz, and A. Zhou. "The fate of hints: updated global analysis of three-flavor neutrino oscillations." In: *Journal of High Energy Physics* 2020.9 (2020). ISSN: 1029-8479. DOI: 10.1007/jhep09(2020)178. URL: http://dx.doi.org/10.1007/JHEP09(2020)178.

[30] R. N. Cahn, D. A. Dwyer, S. J. Freedman, W. C. Haxton, R. W. Kadel, Yu. G. Kolomensky, K. B. Luk, P. McDonald, G. D. Orebi Gann, and A. W. P. Poon. *White Paper: Measuring the Neutrino Mass Hierarchy*. 2013. arXiv: 1307.5487 [hep-ex].

[31] European Strategy Group. *2020 Update of the European Strategy for Particle Physics*. Geneva: CERN Council, 2020. ISBN: 978-92-9083-575-2. DOI: 10.17181/ESU2020.

[32] S. et al. Ritz. "Building for Discovery: Strategic Plan for U.S. Particle Physics in the Global Context." In: (May 2014). URL: https://inspirehep.net/files/1ba9cc583c35365d810f5d6069611924.

[33] B. Abi et. al. In: 15.08 (2020), T08008–T08008. DOI: 10.1088/1748-0221/15/08/t08008. URL: https://doi.org/10.1088/1748-0221/15/08/t08008.

[34] Dealtry T. et al. *Hyper-Kamiokande*. 2019. arXiv: 1904.10206 [hep-ex]. URL: https://arxiv.org/abs/1904.10206.

[35] Cern Courier. *A portal to new physics*. URL: https://demonstrations.wolfram.com/NeutrinoOscillations/. (accessed: 16.08.2021).

[36] B. Abi et al. *Deep Underground Neutrino Experiment (DUNE), Far Detector Technical Design Report, Volume II: DUNE Physics*. 2020. arXiv: 2002.03005 [hep-ex].

[37] Shinzou Kubota, Masahiko Hishida, Masayo Suzuki, and Jian-zhi Ruan(Gen). "Dynamical behavior of free electrons in the recombination process in liquid argon, krypton, and xenon." In: *Phys. Rev. B* 20 (8 1979), pp. 3486–3496. DOI: 10.1103/PhysRevB.20.3486. URL: http://link.aps.org/doi/10.1103/PhysRevB.20.3486.

[38] S. et al. Amoruso. "Study of electron recombination in liquid argon with the ICARUS TPC." In: *Nucl. Instrum. Meth.* A523 (2004), pp. 275–286. DOI: 10.1016/j.nima.2003.11.423.

[39] W. Walkowiak. "Drift velocity of free electrons in liquid argon." In: *Nuclear Instruments and Methods in Physics Research Section A: Accelerators, Spectrometers, Detectors and Associated Equipment* 449.1 (2000), pp. 288 –294. ISSN: 0168-9002. DOI: https://doi.org/10.1016/S0168-9002(99)01301-7. URL: http://www.sciencedirect.com/science/article/pii/S0168900299013017.

[40] A. Abed Abud et al. *Design, construction and operation of the ProtoDUNE-SP Liquid Argon TPC*. 2021. arXiv: 2108.01902 [physics.ins-det].

[41] C. Thorn. "Properties of LAr." MicroBooNE Document Database. 2009.

[42] W. M. Haynes, ed. *Handbook of Chemistry and Physics*. 94th ed. CRC Press, 2013.

[43] B. L. Henson. "Mobility of Positive Ions in Liquefied Argon and Nitrogen." In: *Phys. Rev.* 135.4A (1964), pp. 1002–1008.

[44] M. Lüthi. "A Novel UV Laser System for Electric Field Calibration in Liquid Argon Time Projection Chambers." PhD thesis. University of Bern (CH), 2019.

[45] Jay N. Marx and David R. Nygren. "The Time Projection Chamber." In: *Phys. Today* 31N10 (1978), pp. 46–53. DOI: 10.1063/1.2994775.

[46] Georges Charpak, R. Bouclier, T. Bressani, J. Favier, and C. Zupancic. "The Use of Multiwire Proportional Counters to Select and Localize Charged Particles." In: *Nucl. Instrum. Meth.* 62 (1968), pp. 262–268. DOI: 10.1016/0029-554X(68)90371-6.

[47] C. Rubbia. "The Liquid Argon Time Projection Chamber: A New Concept for Neutrino Detectors." In: (1977).

[48] R. Acciarri et al. "Design and Construction of the MicroBooNE Detector." In: *JINST* 12.02 (2017), P02017. DOI: 10.1088/1748-0221/12/02/P02017. arXiv: 1612.05824 [physics.ins-det].

[49] L. Onsager. "Initial Recombination of Ions." In: *Phys. Rev.* 54 (8 1938), pp. 554–557. DOI: 10.1103/PhysRev.54.554. URL: https://link.aps.org/doi/10.1103/PhysRev.54.554.

[50] S. Amerio et al. "Design, Construction and Tests of the ICARUS T600 Detector." In: *Nucl. Instrum. Meth.* A527 (2004), pp. 329–410. DOI: 10.1016/j.nima.2004.02.044.

[51] R. Acciarri et al. "A study of electron recombination using highly ionizing particles in the ArgoNeuT Liquid Argon TPC." In: *JINST* 8 (2013), P08005. DOI: 10.1088/1748-0221/8/08/P08005.

[52] J.B. Birks. *The theory and practice of scintillation counting*. International series of monographs on electronics and instrumentation. Macmillan, 1964.

[53] J. L. Hewett et al. *Fundamental Physics at the Intensity Frontier*. 2012. arXiv: 1205.2671 [hep-ex].

[54] F. Vannucci. "Interactions of neutrinos with matter." In: *Progress in Particle and Nuclear Physics* 95 (2017), pp. 1–47. ISSN: 0146-6410. DOI: https://doi.org/10.1016/j.ppnp.2017.03.003. URL: https://www.sciencedirect.com/science/article/pii/S0146641017300340.

[55] L. Alvarez-Ruso et al. "NuSTEC White Paper: Status and challenges of neutrino–nucleus scattering." In: *Progress in Particle and Nuclear Physics* 100 (2018), 1–68. ISSN: 0146-6410. DOI: 10.1016/j.ppnp.2018.01.006. URL: http://dx.doi.org/10.1016/j.ppnp.2018.01.006.

[56] C. Andreopoulos et al. "The GENIE Neutrino Monte Carlo Generator." In: *Nucl. Instrum. Meth. A* 614 (2010), pp. 87–104. DOI: 10.1016/j.nima.2009.12.009. arXiv: 0905.2517 [hep-ph].

[57] P. de Perio, S. K. Singh, J. G. Morfin, M. Sakuda, and K. D. Purohit. "NEUT Pion FSI." In: (2011). DOI: 10.1063/1.3661590. URL: http://dx.doi.org/10.1063/1.3661590.

[58] T. Golan, J. T. Sobczyk, and J. Zmuda. "NuWro: the Wroclaw Monte Carlo Generator of Neutrino Interactions." In: *Nucl. Phys. B Proc. Suppl.* 229-232 (2012). Ed. by George S. Tzanakos, pp. 499–499. DOI: 10.1016/j.nuclphysbps.2012.09.136.

[59] O. Buss, T. Gaitanos, K. Gallmeister, H. van Hees, M. Kaskulov, O. Lalakulich, A.B. Larionov, T. Leitner, J. Weil, and U. Mosel. "Transport-theoretical description of nuclear reactions." In: *Physics Reports* 512.1 (2012). Transport-theoretical Description of Nuclear Reactions, pp. 1–124. ISSN: 0370-1573. DOI: https://doi.org/10.1016/j.physrep.2011.12.001. URL: https://www.sciencedirect.com/science/article/pii/S0370157311003619.

[60] A M Heikkinen, N Stepanov, and J P Wellisch. *Bertini intra-nuclear cascade implementation in Geant4*. Tech. rep. Geneva: CERN, 2003. URL: https://cds.cern.ch/record/619377.

[61] T. Golan. "What is inside MC generators... and why it is wrong." NuSTEC Conference, Okayma. 2015. URL: http://www.ift.uni.wroc.pl/~tgolan/talks/NuSTEC_MC_Generators.pdf.

[62] A. S. Carroll, I. H. Chiang, C. B. Dover, T. F. Kycia, K. K. Li, P. O. Mazur, D. N. Michael, P. M. Mockett, D. C. Rahm, and R. Rubinstein. "Pion-nucleus total cross sections in the (3,3) resonance region." In: *Phys. Rev. C* 14 (2 1976), pp. 635–638. DOI: 10.1103/PhysRevC.14.635. URL: https://link.aps.org/doi/10.1103/PhysRevC.14.635.

[63] E. Gramellini et al. "Measurement of the (π^-, Ar) total hadronic cross section at the LArIAT experiment." In: (July 2021). arXiv: 2108.00040 [physics.ins-det].

[64] et al. K. Ieki. "Measurement of absorption and charge exchange of π^+ on carbon." In: *Phys. Rev. C* 92 (2015), p. 035205. DOI: 10.1103/PhysRevC.92.035205. arXiv: 1506.07783 [hep-ex].

[65] R. Acciarri et al. "The Liquid Argon In A Testbeam (LArIAT) experiment." In: *Journal of Instrumentation* 15.04 (2020), P04026–P04026. ISSN: 1748-0221. DOI: 10.1088/1748-0221/15/04/p04026. URL: http://dx.doi.org/10.1088/1748-0221/15/04/P04026.

[66] Kotliński et al. "Pion absorption reactions on N, Ar and Xe." In: *European Physical Journal A* 9.4 (Jan. 2000), pp. 537–552. DOI: 10.1007/s100500070010.

[67] C. Anderson et al. "The ArgoNeuT detector in the NuMI low-energy beam line at Fermilab." In: *Journal of Instrumentation* 7.10 (2012), P10019–P10019. ISSN: 1748-0221. DOI: 10.1088/1748-0221/7/10/p10019. URL: http://dx.doi.org/10.1088/1748-0221/7/10/P10019.

[68] BSI Corporate. *BS EN 10025-4:2004 Hot rolled products of structural steels.* https://shop.bsigroup.com/ProductDetail?pid=000000000030027418.

[69] B. Abi et al. *The Single-Phase ProtoDUNE Technical Design Report*. 2017. arXiv: 1706.07081 [physics.ins-det].

[70] DuPont Specialty Products USA, LLC. *D11261075 Kapton polyimide film 100XC10E7*. https://www.dupont.com/content/dam/dupont/amer/us/en/products/ei-transformation/documents/EI-10142-Kapton-Summary-of-Properties.pdf. 2017.

[71] B. Abi et al. *Deep Underground Neutrino Experiment (DUNE), Far Detector Technical Design Report, Volume III: DUNE Far Detector Technical Coordination*. 2020. arXiv: 2002.03008 [physics.ins-det].

[72] B. Abi et al. "First results on ProtoDUNE-SP liquid argon time projection chamber performance from a beam test at the CERN Neutrino Platform." In: *Journal of Instrumentation* 15.12 (2020), P12004–P12004. DOI: 10.1088/1748-0221/15/12/p12004. URL: https://doi.org/10.1088/1748-0221/15/12/p12004.

[73] R. Jerry, L. Winslow, L. Bugel, and J. M. Conrad. *A Study of the Fluorescence Response of Tetraphenyl-butadiene*. 2010. arXiv: 1001.4214 [physics.ins-det].

[74] Z. Moss, J. Moon, L. Bugel, J. M. Conrad, K. Sachdev, M. Toups, and T. Wongjirad. *A Factor of Four Increase in Attenuation Length of Dipped Light-guides for Liquid Argon TPCs Through Improved Coating*. 2016. arXiv: 1604.03103 [physics.ins-det].

[75] H da Motta et al. "ARAPUCA light trap for large liquid argon time projection chambers." In: *Journal of Physics: Conference Series* 1143 (2018), p. 012003. DOI: 10.1088/1742-6596/1143/1/012003. URL: https://doi.org/10.1088/1742-6596/1143/1/012003.

[76] R. Herbst et al. "Design of the SLAC RCE Platform: A General Purpose ATCA Based Data Acquisition System." In: (Jan. 2015). URL: https://www.osti.gov/biblio/1168437.

[77] J. Anderson et al. "FELIX: a PCIe based high-throughput approach for interfacing front-end and trigger electronics in the ATLAS Upgrade framework." In: *Journal of Instrumentation* 11.12 (2016), pp. C12023–C12023. DOI: 10.1088/1748-0221/11/12/c12023. URL: https://doi.org/10.1088/1748-0221/11/12/c12023.

[78] Gaztransport & Technigaz SA (GTT). *GTT membrane technologies*. https://www.gtt-training.co.uk/gtt-membrane-technologies.

[79] Y. Li et al. "Measurement of longitudinal electron diffusion in liquid argon." In: *Nuclear Instruments and Methods in Physics Research Section A: Accelerators, Spectrometers, Detectors and Associated Equipment* 816 (2016), 160–170. ISSN: 0168-9002. DOI: 10.1016/j.nima.2016.01.094. URL: http://dx.doi.org/10.1016/j.nima.2016.01.094.

[80] B Rossi et al. "A prototype liquid Argon Time Projection Chamber for the study of UV laser multi-photonic ionization." In: *Journal of Instrumentation* 4.07 (2009), P07011–P07011. ISSN: 1748-0221. DOI: 10.1088/1748-0221/4/07/p07011. URL: http://dx.doi.org/10.1088/1748-0221/4/07/P07011.

[81] M. Adamowski et al. "The Liquid Argon Purity Demonstrator." In: *JINST* 9 (2014), P07005. DOI: 10.1088/1748-0221/9/07/P07005. arXiv: 1403.7236 [physics.ins-det].

[82] S C Delaquis, R Gornea, S Janos, M Lüthi, Ch Rudolf von Rohr, M Schenk, and J L Vuilleumier. "Development of a camera casing suited for cryogenic and vacuum applications." In: *Journal of Instrumentation* 8.12 (2013), T12001–T12001. DOI: 10.1088/1748-0221/8/12/t12001. URL: https://doi.org/10.1088/1748-0221/8/12/t12001.

[83] M. Auger, A. Blatter, A. Ereditato, D. Goeldi, S. Janos, I. Kreslo, M. Luethi, C. Rudolf von Rohr, T. Strauss, and M.S. Weber. "On the electric breakdown in liquid argon at centimeter scale." In: *Journal of Instrumentation* 11.03 (2016), P03017–P03017. DOI: 10.1088/1748-0221/11/03/p03017. URL: https://doi.org/10.1088/1748-0221/11/03/p03017.

[84] A C Booth, N Charitonidis, P Chatzidaki, Y Karyotakis, E Nowak, I Ortega-Ruiz, M Rosenthal, and P Sala. "Particle production, transport, and identification in the regime of 1-7 GeV/c." In: *Phys. Rev. Accel. Beams* 22 (2019), 061003. 12 p. DOI: 10.1103/PhysRevAccelBeams.22.061003. URL: http://cds.cern.ch/record/2688289.

[85] Inaki Ortega Ruiz. "Accurate Profile Measurement of the low Intensity Secondary Beams in the CERN Experimental Areas." Presented 23 Feb 2018. 2018. DOI: 10.5075/epfl-thesis-8278. URL: https://cds.cern.ch/record/2307347.

[86] B. Baller. "Liquid argon TPC signal formation, signal processing and reconstruction techniques." In: *Journal of Instrumentation* 12.07 (2017), P07010–P07010. ISSN: 1748-0221. DOI: 10.1088/1748-0221/12/07/p07010. URL: http://dx.doi.org/10.1088/1748-0221/12/07/P07010.

[87] F. Cavanna. *NP04/ProtoDUNE-SP Status Report 2019*. Tech. rep. Geneva: CERN, 2019. URL: https://cds.cern.ch/record/2669536.

[88] MicroBooNE Collaboration. "The Pandora multi-algorithm approach to automated pattern recognition of cosmic-ray muon and neutrino events in the MicroBooNE detector." In: *The European Physical Journal C* 78.1 (2018), p. 82. ISSN: 1434-6052. DOI: 10.1140/epjc/s10052-017-5481-6. URL: https://doi.org/10.1140/epjc/s10052-017-5481-6.

[89] S. Palestini et al. "Space charge in ionization detectors and the NA48 electromagnetic calorimeter." In: *Nuclear Instruments and Methods in Physics Research Section A: Accelerators, Spectrometers, Detectors and Associated Equipment* 421.1 (1999), pp. 75 –89. ISSN: 0168-9002. DOI: https://doi.org/10.1016/S0168-9002(98)01193-0. URL: http://www.sciencedirect.com/science/article/pii/S0168900298011930.

[90] Sandro Palestini. "Space Charge Effects in Noble-Liquid Calorimeters and Time Projection Chambers." In: *Instruments* 5.1 (2021). ISSN: 2410-390X. DOI: 10.3390/instruments5010009. URL: https://www.mdpi.com/2410-390X/5/1/9.

[91] The MicroBooNE Collaboration. *Study of Space Charge Effects in MicroBooNE*. Tech. rep. MICROBOONE-NOTE-1018-PUB. 2016. URL: http://microboone.fnal.gov/wp-content/uploads/MICROBOONE-NOTE-1018-PUB.pdf.

[92] F. Stocker. *SCE studies: Recirculation OFF and HVscan*. URL: https://indico.fnal.gov/event/18681/contributions/48644/attachments/30313/37302/CM_SCE_parallel_stocker.pdf. (accessed: 28.09.2021).

[93] C. Adams et al. "Calibration of the charge and energy loss per unit length of the MicroBooNE liquid argon time projection chamber using muons and protons." In: *Journal of Instrumentation* 15.03 (2020), P03022–P03022. ISSN: 1748-0221. DOI: 10.1088/1748-0221/15/03/p03022. URL: http://dx.doi.org/10.1088/1748-0221/15/03/P03022.

[94] LArSoft Collaboration. *Software for LArTPCs*. URL: https://larsoft.org/. (accessed: 16.08.2021).

[95] R. Brun et al. *ROOT data analysis framework*. URL: https://root.cern.ch. (accessed: 16.08.2021).

[96] S. Agostinelli et al. "Geant4—a simulation toolkit." In: *Nuclear Instruments and Methods in Physics Research Section A: Accelerators, Spectrometers, Detectors and Associated Equipment* 506.3 (2003), pp. 250 –303. ISSN: 0168-9002. DOI: https://doi.org/10.1016/S0168-9002(03)01368-8. URL: http://www.sciencedirect.com/science/article/pii/S0168900203013688.

[97] T. J. Roberts, K. B. Beard, S. Ahmed, D. Huang, and D. M. Kaplan. "G4beamline Particle Tracking in Matter Dominated Beam Lines." In: *Conf. Proc. C* 110328 (2011). Ed. by Todd Satogata and Kevin Brown, pp. 373–375.

[98] T. T. Böhlen, F. Cerutti, M. P. W. Chin, A. Fassò, A. Ferrari, P. G. Ortega, A. Mairani, P. R. Sala, G. Smirnov, and V. Vlachoudis. "The FLUKA Code: Developments and Challenges for High Energy and Medical Applications."

In: *Nucl. Data Sheets* 120 (2014), 211–214. 4 p. DOI: 10.1016/j.nds.2014.07.049. URL: https://cds.cern.ch/record/2109973.

[99] D. Heck, J. Knapp, J. N. Capdevielle, G. Schatz, and T. Thouw. "CORSIKA: A Monte Carlo code to simulate extensive air showers." In: (Feb. 1998).

[100] C. Hagmann, D. Lange, and D. Wright. "Cosmic-ray shower generator (CRY) for Monte Carlo transport codes." In: *2007 IEEE Nuclear Science Symposium Conference Record*. Vol. 2. 2007, pp. 1143–1146. DOI: 10.1109/NSSMIC.2007.4437209.

[101] A. Reynolds. "Evaluating the low-energy response of the ProtoDUNE-SP detector using Michel electrons." PhD thesis. University of Oxford (UK), 2020.

[102] J. Calcutt. *PDSPAnalyzer*. URL: https://wiki.dunescience.org/wiki/PDSPAnalyzer. (accessed: 16.08.2021).

[103] Enrico Guiraud, Axel Naumann, and Danilo Piparo. "TDataFrame: functional chains for ROOT data analyses." In: (2017). DOI: 10.5281/zenodo.260230.

[104] J. Calcutt and F. Stocker. *Pion Analysis Repository*. URL: https://github.com/calcuttj/PionStudies. (accessed: 16.08.2021).

[105] F. Cavanna et al. *Report of SPSC Annual Review 2019*. Tech. rep. 2019. URL: https://cds.cern.ch/record/2669536/files/SPSC-SR-252.pdf.

[106] J. Calcutt. "Detector Effect Investigation." DRA Meeting. 2021. URL: https://indico.fnal.gov/event/49430/contributions/217133/attachments/144325/183241/Detector%20Effect.pdf.

[107] B. Abi et al. "Neutrino interaction classification with a convolutional neural network in the DUNE far detector." In: *Physical Review D* 102.9 (2020). ISSN: 2470-0029. DOI: 10.1103/physrevd.102.092003. URL: http://dx.doi.org/10.1103/PhysRevD.102.092003.

[108] P. Madigan. *Upstream energy losses*. URL: https://indico.fnal.gov/event/22908/contributions/70257/attachments/44194/53237/2020-01-26-DUNECollaboration-EnergyLosses.pdf. (accessed: 14.09.2021).

[109] Stocker F. Dolek F. Boran F. *Pion Analysis: Comparing Raw Data and Reconstructed Values*. URL: https://indico.cern.ch/event/1021276/contributions/4286539/attachments/2213978/3747902/Reco2.pdf. (accessed: 14.09.2021).

[110] J. B. Birks. "Scintillations from Organic Crystals: Specific Fluorescence and Relative Response to Different Radiations." In: *Proceedings of the Physical Society. Section A* 64.10 (1951), pp. 874–877. DOI: 10.1088/0370-1298/64/10/303. URL: https://doi.org/10.1088/0370-1298/64/10/303.

[111] Brookhaven National Laboratory. *Liquid Argon Properties (Tables and Calculators)*. URL: https://lar.bnl.gov/properties/. (accessed: 14.09.2021).

[112] R. Diurba. "Energy calibration of the ProtoDUNE-SP TPC." 40th International Conference on High Energy physics - ICHEP2020. 2020. URL: https://pos.sissa.it/390/198/pdf.

[113] R. Diurba. *dQ/dx Calibration Uncertainties Update*. URL: https://indico.cern.ch/event/1034213/contributions/4344541/attachments/2238576/3794998/dQdx_Calibration_AncillaryInputs.pdf. (accessed: 14.09.2021).

[114] DUNE-wiki. *ProtoDUNE-SP datasets*. 2021. URL: https://wiki.dunescience.org/wiki/ProtoDUNE-SP_datasets.

[115] G. D'Agostini. *A multidimensional unfolding method based on Bayes' Theorem*. Tech. rep. Hamburg: DESY, 1994. URL: http://cds.cern.ch/record/265717.

[116] G. D'Agostini. *Improved iterative Bayesian unfolding*. 2010. arXiv: 1010.0632 [physics.data-an].

[117] T. Adye. *Unfolding algorithms and tests using RooUnfold*. 2011. arXiv: 1105.1160 [physics.data-an].

ACKNOWLEDGEMENTS

I gratefully acknowledge Prof. Dr. Antonio Ereditato for establishing the contacts with the CERN Neutrino Platform in order to work on the ProtoDUNE detector, as well as for his guidance and supervision of my dissertation.

I would like to thank my supervisor at CERN Dr. Francesco Pietropaolo for fostering my interest in experimental particle physics, his constant availability, enthusiasm and curiosity. Furthermore, I would like to express my deepest gratitude to Dr. Stefania Bordoni who has guided me through my physics measurement and always offered critical and well reflected thoughts on my work. Her constant presence and provision of indispensable knowledge kept me motivated and curious throughout my PhD.

I convey my special thanks to Jake Calcutt, Prof. Dr. Kendall Mahn, Richard Diurba, Dr. Thomas Junk and Dr. Stephen Pordes for great discussions, team work, guidance, and contributions throughout the development of the physics measurement.

Many thanks to the CERN Neutrino Platform group for offering me invaluable opportunities, full support and trust to work on the ProtoDUNE experiment and contribute to its success. I would like to extend my gratitude to the DUNE Collaboration and the numerous mechanical, electronics, and cryogenic engineers without whom the construction and operation of the detector would have been impossible.

Within the ProtoDUNE group I encountered a very familiar and encouraging working atmosphere, this will always remain in good memory. CERN has been a place where I have met new friends making my four years of PhD unforgettable in many ways.

I wish to thank my sister and friends for all the great times and keeping me sane throughout my studies. Finally, I am deeply grateful to my parents for enabling my studies in the first place, supporting me over the full period of my education and their precious guidance.

Declaration of Consent

on the basis of Article 30 of the RSL Phil.-nat. 18

Name, First Name: Stocker, Francesca

Matriculation Nr: 12-104-238

Study Program: Physik

Bachelor ☐ Master ☐ Dissertation ☒

Title of Thesis: Measurement of the Pion Absorption Cross-Section with the ProtoDUNE Experiment

Supervisor: Prof. Dr. Antonio Ereditato
Dr. Francesco Pietropaolo

I declare herewith that this thesis is my own work and that I have not used any sources other than those stated. I have indicated the adoption of quotations as well as thoughts taken from other authors as such in the thesis. I am aware that the Senate pursuant to Article 36 paragraph 1 litera r of the University Act of 5 September, 1996 is authorized to revoke the title awarded on the basis of this thesis. For the purposes of evaluation and verification of compli-ance with the declaration of originality and the regulations governing plagiarism, I hereby grant the University of Bern the right to process my personal data and to perform the acts of use this requires, in particular, to reproduce the written thesis and to store it permanently in a database, and to use said database, or to make said database available, to enable comparison with future theses submitted by others.

Bern, 22. November 2021

Stocker Francesca